

Doctorate Dissertation

博士論文

Photoevaporation of Protoplanetary Disks and Molecular
Cloud Cores in Star-Forming Regions

(星形成領域中の原始惑星系円盤および分子雲コアの光蒸発)

A Dissertation Submitted for Degree of Doctor of Philosophy
December 2018

平成30年12月 博士（理学）申請

Department of Physics, Graduate School of Science,
The University of Tokyo

東京大学大学院理学系研究科物理学専攻

Riouhei Nakatani

仲谷峻平

ABSTRACT

Galaxies contain a large amount of gas in the form of molecules. The molecules shape gaseous clumps called molecular clouds. They are the parental bodies of stars, and star formation is initiated by the gravitational collapse of the clouds. A protostar forms in the collapsing core, and, at the same time, a gaseous disk surrounds the star. The circumstellar disk is composed of gas and a small amount of solid particles (dust) and is the birthplace of planets, and thus it is named a protoplanetary disk (PPD). The PPD coevolves with the central star and eventually disperses. A young stellar system is left behind as a remnant.

Recent observations have revealed that planets commonly exist around solar-type stars, but many of them have different characters from those of our Solar System's planets. Although the origin of the variety is not yet clear, it can be attributed to some environmental factors that affect the formation and evolutionary processes of stellar systems. In fact, the occurrence of Jupiter-like planets (Jovian planets) is observationally known to decrease with the host star mass and with the host star metallicity, i.e. the amount of heavy elements. Similarly, the observations of the outer Galaxy, where metallicity is low, have proposed a short dispersal time of PPDs. The origins of these trends are also poorly understood, but it explicitly shows that the formation and evolutionary processes of stellar systems are affected by their forming environments. Studying the processes occurring in diverse environments is a necessary step to understand the origins of such varieties and trends, and, ultimately, to construct a universal picture of stellar system formation and evolution.

In this thesis, our main interest is in star and planet formation/evolution in various metallicity environments. Metallicity is one of the important quantities that has the potential to characterize the location of star-forming regions and the period of star-forming activities. For instance, metallicity decreases as going further from the galactic center in the Milky Way, and more importantly, metallicity is increased as a whole, as galaxies evolve from their primordial states. Hence, considering metallicity variation can give essential implications to study the formation and evolution of stellar systems since the birth of galaxies. This is, in turn, indispensable to study the evolution of galaxies, which are an important constituent of the universe.

To this end, in this thesis, we investigate the dispersal processes of PPDs and molecular clouds in star-forming regions with a wide variety of metallicity. PPDs are irradiated by the central stars with their intense ultraviolet (UV) and X-ray radiation. It heats disk surfaces and drives evaporative flows. The dispersal process is termed as photoevaporation and can disperse PPDs within a few million years, which is consistent with the observationally-estimated dispersal time. The disk lifetime limits the available time to form planets, especially for Jovian planets, within PPDs, and is a significantly relevant quantity to determine initial configurations of primordial planetary systems. Hence, the disk lifetime is a particularly important parameter in the context of planet formation. We investigate photoevaporation of PPDs with various metallicities to estimate their lifetimes and to derive, if any, their metallicity dependence. Similarly, in star-forming regions around massive stars, the star's intense radiation drives photoevaporation from the surfaces of molecular clouds and reduces the cloud mass. This negatively affects star formation around massive stars. On the other hand, the

intense radiation is known to drive a strong shock in the interior of clouds. The central density of the clouds is increased to strengthen self-gravity. This process positively affects star formation in star-forming regions nearby massive stars. Whether positive or negative, these processes due to the existence of nearby massive stars contribute to set the efficiency of star formation in the star-forming regions. These processes may be particularly important in high-redshift galaxies and the early time of the Milky Way, where massive stars are considered to be preferentially formed. We study photoevaporation of molecular clouds with various metallicities to discuss the influences of massive stars on the efficiency of star formation.

First, we perform radiation hydrodynamics simulations of photoevaporating PPDs irradiated by far-UV (FUV; $6\text{ eV} \lesssim h\nu \leq 13.6\text{ eV}$) and extreme-UV (EUV; $h\nu > 13.6\text{ eV}$) from the central young star. We solve nonequilibrium chemistry in a self-consistent manner. Dust temperatures are also self-consistently determined by solving radiation transfer for stellar irradiation and dust (re-)emission. We vary the disk metallicity Z in a wide range of $10^{-4} Z_{\odot} \leq Z \leq 10 Z_{\odot}$. We find that FUV photoelectric heating drives dense, neutral photoevaporative flows, and the FUV heating and dust-gas collisional cooling regulate the resulting mass-loss rates. The FUV-driven neutral flows yield a mass-loss rate of the order of $\sim 10^{-8} M_{\odot} \text{ yr}^{-1}$ at solar metallicity. The mass-loss rate increases as metallicity decreases for $10^{-1} Z_{\odot} \lesssim Z \lesssim 10 Z_{\odot}$, because the amount of dust, which is the main absorber of FUV, is reduced. For $10^{-2} Z_{\odot} \lesssim Z \lesssim 10^{-1} Z_{\odot}$, dust-gas collisional cooling becomes efficient compared to FUV heating. This suppresses the FUV-driven photoevaporation, and the resulting mass-loss rates decrease with decreasing metallicity. In the low-metallicity extent of $10^{-4} Z_{\odot} \lesssim Z \lesssim 10^{-2} Z_{\odot}$, EUV-driven ionized flows dominantly contribute to the mass loss. Since the main absorber of EUV is hydrogen, the photoevaporation rates are roughly constant with $\sim 10^{-9} M_{\odot} \text{ yr}^{-1}$. The metallicity dependence of the estimated lifetimes is consistent with those of the observational lifetimes. It directly shows that FUV photoevaporation can be a cause for the observational trend in PPD lifetimes.

Next, we incorporate X-ray ($0.1\text{ keV} \lesssim h\nu \lesssim 10\text{ keV}$) effects into our simulations of photoevaporating PPDs and study the influences of X-ray on photoevaporation and lifetimes. The effectiveness of X-ray on photoevaporation has remained a matter of debate, and for the first time, we directly examine it with radiation hydrodynamics simulations with taking into account the spectral energy distribution of X-ray irradiation. The disk metallicity is varied again to investigate the metallicity dependence of photoevaporation caused by both UV and X-ray. Our results show that X-ray heating is not efficient to drive the dense, neutral photoevaporative flows as FUV, but X-ray ionization can strengthen FUV heating by ionizing the neutral regions of PPDs. The metallicity dependence of photoevaporation rates is again largely regulated by FUV heating and dust-gas collisional cooling, and thus the trend is similar to that in the case of UV photoevaporation. However, the strengthening effect of X-ray boosts the photoevaporation rates in $10^{-2.5} Z_{\odot} \lesssim Z \lesssim 10^{-2} Z_{\odot}$, where FUV hardly drives the neutral photoevaporative flows without the X-ray effect. The resulting photoevaporation rates are of the order of 10^{-8} – $10^{-7} M_{\odot} \text{ yr}^{-1}$ and decreases with decreasing metallicity. At $Z \lesssim 10^{-3} Z_{\odot}$, the neutral photoevaporative flows are hardly driven, and the resulting mass-loss rates are mainly contributed from the EUV-driven flows. The mass-loss rates are roughly constant without FUV heating, because the metallicity-independent EUV-driven flows set the mass-loss rates in this case. The estimated lifetimes are even more consistent with the observations when the X-ray effects are taken into account in the UV photoevaporation model. Although X-ray photoevaporation has been suggested as a key mechanism to explain the metallicity dependence of the observational lifetimes in a few previous studies that employ a simplified method, our direct comparison based on the self-consistent radiation hydrodynamics simulations indicate that X-ray is ineffective to drive a

strong photoevaporation or to directly cause a metallicity-dependent trend in the lifetimes.

Finally, we investigate the evolution of low-mass molecular clouds in star-forming regions with a wide variety of metallicities. We consider molecular cloud cores with $10^{-3} Z_{\odot} \leq Z \leq 1 Z_{\odot}$ exposed to UV field of nearby massive stars in order to derive their lifetimes and discuss star formation efficiency around the massive stars. We perform 3D radiation hydrodynamics simulations, including relevant thermochemical reactions. Again, we simultaneously solve hydrodynamics, radiative transfer, and nonequilibrium chemistry in a self-consistent manner. In our simulations, we observe a strong shock driven by the intense EUV irradiation in the interior of the cores with $Z \gtrsim 10^{-1} Z_{\odot}$. The shock and hot ambient gas compress the cores to form a cometary structure. The cores survive for $\sim 10^5$ yr. Low-metallicity cores ($Z \lesssim 10^{-2} Z_{\odot}$) lack coolants inside, and hence keep high temperatures after compression by the shock. The cores are short-lived and have lifetimes of the order of 10^4 yr. We find that the free fall time, which is an important measure to quantify the collapsing time of cores to form stars, is sufficiently shortened in the higher-metallicity cores to initiate gravitational collapse before completely dispersed. We also study photoevaporation of molecular cloud cores in photodissociation regions (PDRs), where EUV photons are hardly present. It is shown that FUV heating also compresses cores and form a cometary structure for $Z \gtrsim 1 Z_{\odot}$, but the cores with $Z \lesssim 10^{-0.5} Z_{\odot}$ expand rather than shrinking. This makes the free fall time longer and thus suppresses star formation. We conclude that in metal-rich star-forming regions with $Z \gtrsim 10^{-1} Z_{\odot}$, the effects of the intense EUV radiation from massive stars can promote star formation, and if metallicity is sufficiently high ($Z \gtrsim 1 Z_{\odot}$), the gravitational collapse can be also initiated in the PDRs; otherwise, star formation is significantly suppressed or delayed by the effects of FUV and EUV radiation from massive stars. In metal-poor environments ($Z \lesssim 10^{-2} Z_{\odot}$), UV radiation of massive stars generally have effects to suppress or to delay star formation.

Our results suggest that in the local, present-day star-forming regions ($Z \gtrsim 0.1 Z_{\odot}$), star formation is likely to be promoted around massive stars, and in the resulting young stellar systems, gas giant planets may efficiently form as metallicity increases. On the other hand, in low-metallicity environments ($Z \lesssim 0.01 Z_{\odot}$) like protogalaxies, star formation can be significantly suppressed around massive stars. PPDs, if present, have longer lifetimes as metallicity decreases. Planets have a long time to grow and to evolve dynamically through the interaction with the parental disks. The wind profiles and the estimated lifetimes of the low-metallicity PPDs are still expected to be applicable to “evolved” disks, where dust grains have grown to larger bodies and settled to the midplane, and locally realize a low-metallicity environment. Future observations with next-generation telescopes would make a direct comparison possible. In this thesis, we focus on the dispersal processes of low-mass objects. In practice, these bodies have mass spectra. The dispersal processes of high- or even lower-mass molecular clouds and PPDs might have different evolutionary characters. In addition, the luminosities of the radiation sources would be more or less dependent on both the stellar mass and metallicity. In future works, we incorporate these effects to study the evolutionary processes. The results, including those in this thesis, can be broadly applied to many other fields, such as future planet-searching missions and theoretical studies of galaxy formation.

ACKNOWLEDGEMENT

First and foremost, I would like to express my sincere gratitude to my supervisor Prof. Naoki Yoshida for the continuous support and guidance to my study/research and for all his contribution of time, consideration, idea, and funding to make my time in the graduate school this fruitful and productive. I could enhance my strong points while acquiring new skills and pieces of knowledge. He has, both consciously and unconsciously, let me learn not only the ways to conduct researches and to grow as a research scientist but also an attitude to work and to life. I have seen that life is not so long as one expects, and therefore we had better make the most of this very second to contribute to society and nature. His teachings have motivated me not to make compromises during this invaluable fraction of my life. At the same time, I have also learned that being adequately optimistic helps myself in a lot of kinds of situations. The balance of this uncompromising and optimism is one of the most important acquirement during my time in graduate school. He encouraged me when we had a hard time, and he was glad for me when I made achievements. It has been such a great honor of mine to be his Ph.D./Master student for the last five years. I cannot thank him enough with words.

I would also like to express my special gratitude to Takashi Hosokawa for the technical advice and encouragement. Regardless of the physical distance separating our two universities, he always cared about me and frequently verified the progress of our researches. His insightful comments and practical advice also helped me deal with issues and immensely contributed to widening our researches from various perspectives.

My sincere thanks also go to my research collaborators, Hideko Nomura, and Rolf Kuiper. They provided me the observational data and the computational routines used in the simulations for the studies in this dissertation. They also gave me detailed and clear explanations when I had questions. It particularly deepened my understandings of the physics underlying observational results and computational methods in the works of literature.

I am deeply grateful to Neal Turner, Mario Flock, Yasuhiro Hasegawa, and Shigeru Suzuki for their great hospitality during my visit to NASA Jet Propulsion Laboratory from October 16 to December 25, 2017. Their supports and technical advises made my stay productive and fulfilling. The skills, knowledge, and ideas acquired through our discussions are indispensable for our future studies as well as those so far.

I am greatly indebted to my vice-supervisors, Hiromoto Shibahashi and Satoshi Yamamoto, for their continuous assistance and guidance. The helpful discussions not only broadened my knowledge but also developed new viewpoints to our studies. I would like to express my appreciation to the researchers in the field who devoted their time to discuss the results of our researches and provided ideas to make improvements/extensions for them: David Hollenbach, Shu-ichiro Inutsuka, Takeru Suzuki, Uma Gorti, Eiichiro Kokubo, Kengo Tomida, Xuening Bai, Kei Tanaka, Hiroshi Kobayashi, Shinsuke Takasao, Masahiro Machida, Hajime Susa, Nozomu Tominaga, Nathaniel Dylan Kee, Anastasia Fialkov, and Nami Sakai. I would like to thank the committee members for this dissertation: Fujihiko Hamba (chief), Aya Bamba, Noriko Yamasaki, Katsuaki Asano, and Masami Ouchi for their time, interest, and helpful and insightful comments.

With regards to daily life at the Hongo Campus of the University of Tokyo, I thank all the staffs, secretaries, friends belonging to the University of Tokyo Theoretical Astrophysics group (UTAP) and Research Center for Early Universe (ResCEU). Their presence is significant to make my time in the school invaluable and memorable. I am especially thankful to the present/past members: Kazumi Kashiyama, Gen Chiaki, Kento Masuda, Shigeki Inoue, Tilman Hartwig for their time, mentoring, and fruitful discussions.

Last but not least, a special thanks to my family. In particular, I am very grateful to my mother, Yuko, for your devoted support, uninterrupted assistance, powerful encouragement, valuable advice, and supportive care; to my little brothers, Hayato and Reo, for inspiring me and making me motivated to be self-disciplined; to my nieces, Ria and Noa, for your innocent smile comforting and energizing your uncle to work. You all brought me this wonderful, satisfying, enjoyable life and accomplishments. Words cannot sufficiently describe my appreciation and gratitude to you.

I gratefully acknowledge the funding by the grant-in-aid for the Japan Society for the Promotion of Science (16J03534) and also by Advanced Leading Graduate Course for Photon Science (ALPS) of the University of Tokyo. All of the numerical computations were carried out on the Cray XC30 and XC50 at the Center for Computational Astrophysics, National Astronomical Observatory of Japan.

For the rest of my life, I would like to return the favor by continuously improving myself as a scientist and, more importantly, as a man and by contributing to society and nature, with the skills and pieces of knowledge I have obtained thanks to the precious supports from all of the people around me.

Riouhei Nakatani

*Department of Physics,
Graduate School of Science,
The University of Tokyo*

December 2018

Contents

Chapter 1	Introduction	1
1.1	Molecular Clouds in Galaxies	1
1.2	Overview of Stellar System Formation and Evolution	3
1.3	Mass Functions of Clumps and Cores, and Initial Mass Function	5
1.4	Birth and Evolution of Stars	6
1.5	Protoplanetary Disks	7
1.5.1	Protoplanetary Disk Formation	7
1.5.2	Protoplanetary Disk Structure	8
1.5.3	Observations of Protoplanetary Disks	10
1.5.4	Lifetimes of Protoplanetary Disks	11
1.5.5	Metallicity Dependence of Lifetimes	14
1.5.6	Dispersal Mechanisms of Disks	15
1.6	Aims and Structure of the Present Thesis	23
Chapter 2	UV Photoevaporation of PPDs: Metallicity Dependence	26
2.1	Overview	26
2.2	Methods	26
2.2.1	Numerical Setup	27
2.2.2	Basic Formulae	28
2.2.3	Heating and Cooling	31
2.2.4	Chemistry Model	34
2.2.5	Radiative Transfer	36
2.2.6	Initial Conditions	36
2.3	Results	37
2.3.1	Solar-Metallicity Disk Structure	37
2.3.1.1	Structures of Density, Velocity, and Temperature	37
2.3.1.2	Hydrogen-bearing Species	40
2.3.1.3	Metal Species	40
2.3.2	Different Metallicities Disks	42
2.3.2.1	Photoevaporative Flows	42
2.3.2.2	Hydrogen-Bearing Species Distribution	45
2.3.2.3	Metal Species Distribution	46
2.3.3	Photoevaporation Rates and Metallicity Dependence	47
2.3.4	Semi-Analytic Model for Photoevaporation Rates	49
2.4	Discussion	55
2.4.1	Differences from X-Ray Photoevaporation	55
2.4.2	Lifetimes	55
2.4.3	Dust Grain Effects on FUV-Driven Photoevaporation	56

	2.4.4	Spurious Reflection at Outer Boundary	58
	2.4.5	Measurement of Photoevaporation Rates	61
	2.4.6	Collisional Excited Lines in H II regions	62
	2.5	Chapter Summary	62
Chapter 3		UV & X-Ray Photoevaporation of PPDs: the Influences of X-Ray	64
	3.1	Overview	64
	3.2	Methods	65
	3.2.1	X-Ray Heating/Ionization	67
	3.2.1.1	Cross Section	67
	3.2.1.2	X-Ray Ionization	67
	3.2.1.3	X-Ray Heating	69
	3.2.2	Chemistry Model	69
	3.3	Results	70
	3.3.1	Solar Metallicity Disk	70
	3.3.2	Photoelectric Heating in Disks with Low-Metallicities	72
	3.3.3	X-Ray Ionization Effect	74
	3.3.4	Mass-Loss Profile	77
	3.3.5	Lifetimes	82
	3.4	Discussion	82
	3.4.1	Spectral Hardness of X-ray	83
	3.4.2	Heating Efficiency	85
	3.4.3	Input Parameter Uncertainties	88
	3.5	Chapter Summary	91
Chapter 4		Photoevaporation of Molecular Clumps with Various Metallicities	92
	4.1	Overview	92
	4.2	Background	92
	4.3	Methods	94
	4.4	Results	96
	4.4.1	Solar-Metallicity Core	96
	4.4.1.1	Core Evolution and Lifetime	96
	4.4.1.2	The Rocket Effect	99
	4.4.2	Low-Metallicity Cores	100
	4.4.2.1	EUV Effects	100
	4.4.2.2	Photoevaporation Driven by FUV	104
	4.5	Discussions	104
	4.5.1	Core Photoevaporation with Weaker UV fluxes	104
	4.5.2	The Rocket Effect and Star Formation	107
	4.5.3	Gravity Effects	108
	4.5.4	Implications to Star Formation	109
	4.5.5	Metallicity Dependence in the Spectra of High-Energy Radition	111
	4.6	Chapter Summary	112
Chapter 5		Summary and Concluding Remarks	114
References			119

Chapter 1

Introduction

The big bang model describes that the universe has been in a hot, dense state at an early time. As the universe expands, it cools, and several light elements such as hydrogen, deuterium, helium, and lithium are produced from protons and neutrons, which have not yet formed elements, through nuclear reactions (so-called primordial nucleosynthesis). The light elements form the first stars, and other heavy elements, or metals, are produced inside them via nuclear fusion. When the stars die, the heavy elements are scattered into space by the explosion. These materials are then used to form next-generation stars. There, nuclear fusion takes place to produce metals again. The stars assemble to shape galaxies, enriching their environments with metals by repeating the processes. This generally increases the amount of metals in the universe and metallicity of stars, as the universe evolves. The production of the metals is indispensable to build planets, especially for terrestrial planets like Earth. Metallicity is thus a key quantity that associates the formation of stars and planets, which are the constituents of galaxies, with the evolution of the universe. It is clearly an essential step to study formation/evolution of stars and planets in various metallicity environments to understand the evolutionary history of galaxies and the universe from their births, and the origins of our galaxy and solar system.

In the present thesis, we discuss the formation and evolutionary stages of star-planet systems in physically different environments, supposing star-forming regions in the inner/outer regions of the Milky Way and molecular complexes in distant galaxies. Particularly, our main interest is in the dispersal processes of young stellar systems with a wide variety of metallicities, as we will see in the following chapters.

1.1 Molecular Clouds in Galaxies

A galaxy is a self-gravitating body composed of stellar objects, interstellar medium (ISM), and dark matter. Dark matter is responsible for the majority of the total mass ($\sim 90\%$), and the rest mass belongs to the other objects. A galaxy contains about 10^7 – 10^{14} stars, and the interspace between the stars is filled with ISM. These components rotate around the galactic center, forming a geometrically thin disk with the typical diameter of 1–100 kpc.

ISM is the birthplace of stars and consists of gas and small solid particles called dust. A dense region of ISM is referred to as an interstellar cloud. Hydrogen is the most dominant element of ISM and is present in chemically different forms: atomic hydrogen H I, molecular hydrogen H₂, and ionized hydrogen H II. In the Milky Way, H I exists in rarefied gas as well as distinct clouds in ISM and has the largest total mass among the chemical species. Molecular hydrogen H₂ is found throughout our galaxy and are known to concentrate on the galactic plane more than H I. Ionized hydrogen H II is relatively small in the total mass compared to H₂ or H I in the Milky Way and is

often found around massive OB stars. The Lyman continuum photons (LyC; $h\nu > 13.6$ eV) from such stars ionize surrounding H I, and an H II region consequently forms with a typical radius of several parsecs. Recombinations between ions and electrons followed by level transitions produce a number of lines at, for instance, the optical wavelengths (e.g., Balmer lines) and centimeter wavelengths followed by transitions between high levels. These lines are used as a tracer of massive stars.

Most of the gas in the Milky Way is in distinct agglomerations called H I clouds. The clouds typically have hydrogen nuclei number density n_{H} of $10\text{--}10^2$ cm^{-3} , the radius of $\sim 1\text{--}10^2$ pc, and a temperature of $\sim 10^2$ K. Similarly, most of the H_2 molecules exist in discrete clouds known as molecular clouds. The physical properties of the clouds such as the size, morphology, optical thickness, density, temperature, and total mass are different one by one, but they are often categorized into several kinds: diffuse clouds, dark clouds, giant molecular clouds, molecular cloud clumps, molecular cloud cores, and globules. Note that the categorization of molecular clouds is not completely distinct. There can exist a molecular cloud that is sorted into two of the kinds according to, for instance, its size.

Diffuse molecular clouds account for only a small portion of ISM. They are relatively optically thin molecular clouds with the typical visual extinction of $A_{\text{V}} \simeq 1$. This allows much of the lights from background stars to penetrate the clouds and to be observed with absorption lines. The clouds have typical masses of tens of solar masses and the typical size of a few parsecs, and the structure of the clouds are maintained by the confining pressure due to a surrounding warm and rarefied gas. Star formation is never seen in these clouds. The ζ Ophiuchi cloud is an example of diffuse clouds.

Dark clouds are originally defined as invisible clouds in optical wavelengths, but at present, they are instead defined as the nearby clouds with the typical mass of $\lesssim 10^4 M_{\odot}$ where massive star formation does *not* take place. The clouds have a large A_{V} of the order of 10 and hence show a significant absorption of optical photons. The Taurus-Auriga molecular cloud is one of such molecular clouds. There, hundreds of low-mass stars are newly forming.

Molecular clouds of the larger-mass counterpart ($\gtrsim 10^4 M_{\odot}$) are referred to as giant molecular clouds (GMCs). GMCs are the largest self-gravitating bodies in galaxies and have the typical size, density, and mass of ~ 50 pc, $\sim 10^5\text{--}10^6 M_{\odot}$, and $n_{\text{H}} \sim 10^2$ cm^{-3} , respectively. The mass even reaches $\sim 10^7 M_{\odot}$ at the highest in the central molecular region of the Milky Way (Oka *et al.* 2001). Most of the molecular ISM are contained in GMCs (e.g., Blitz 1993, Williams *et al.* 2000). It has been revealed through molecular line surveys at millimeter and submillimeter that GMCs have clumpy and inhomogeneous substructures with broad ranges of size ($\sim 0.1\text{--}10$ pc) and mass ($\sim 1\text{--}10^3 M_{\odot}$) (Bally *et al.* 1987, Bertoldi and McKee 1992, Blitz 1993, Evans 1999, Williams *et al.* 2000, Muñoz *et al.* 2007). The structured clouds are called molecular cloud clumps, and have a higher density (several times of $n_{\text{H}} \sim 10^2$ cm^{-3}) than the average density of the surrounding medium. Some of the most massive clumps are sites of star and planet formation; young stellar systems form with materials contained in the cores inside the clumps. Further, molecular cloud clumps often contain even higher-density regions ($n_{\text{H}} \sim 10^5$ cm^{-3}) called molecular cloud cores. The typical core density is higher than the average clump density by about an order or two orders of magnitude. Formation of individual stellar systems is associated with a molecular core. Note that in GMCs massive OB stars form in several massive clumps, whereas only low-mass stars ($M_{*} \lesssim M_{\odot}$) form in dark clouds. The massive stars ionize the interclump medium, and thus H II regions are often found in GMCs. The region where molecular clouds, young clusters, and H II regions are mixed is referred to as a molecular cloud complex.

Globules are small, isolated molecular clouds with a typical mass of $\sim 1 M_{\odot}$. Massive globules ($\sim 10^1\text{--}10^2 M_{\odot}$) is referred to as Bok globules (Bok and Reilly 1947). Stars also form in these

globules.

In this thesis, our focus is on the formation and evolutionary processes of young stellar systems that are supposed to occur in star-forming molecular clouds: namely, GMCs and dark clouds.

1.2 Overview of Stellar System Formation and Evolution

Stellar system formation begins with gravitational contraction of molecular cloud cores in a molecular cloud clump (Figure 1.1 (b)). Star “seeds” form there, while surrounding medium accretes to feed the seeds. The star seed gains mass and grows as the contraction proceeds (see also Section 1.4 for a detailed description of protostar formation). A geometrically thin Keplerian disk forms around the protostar as a natural consequence of angular momentum transfer (Figure 1.1 (c)). The disk is the birthplace of planets and thus is named a protoplanetary disk (PPD). In this earlier stage of stellar system formation, the envelope surrounds the young star-disk system. The envelope continuously falls onto the disk, and the disk, in turn, accretes to the star. The star gains mass through this accretion process.

The envelope finally disappears by the mass loss due to the accretion and/or dispersal by winds (Figure 1.1 (d)). The disappearance of the envelope makes the central star optically visible. The central star in this stage is referred to as a pre-main-sequence (PMS) star. PMS stars radiate photons with releasing its gravitational energy through the quasi-static contraction. The starlight is absorbed and scattered by circumstellar gas and dust. This significantly affects the structure and evolution of a PPD dynamically, thermally, and chemically. In the interior of a PPD, protoplanets are formed out of the gas and dust grains contained in the disk. Protoplanets grow to planets, while the disk loses the mass owing to disk winds and accretion.

After the disk dispersal, a planetary system and/or a debris disk may be left as a remnant of a PPD (Figure 1.1 (e)). The central PMS star becomes a zero-age main-sequence star (ZAMS) when the central density becomes high enough to burn hydrogen nuclei. At this point, the stellar system is composed of a main-sequence star and a planetary system as the solar system.

The timescale with which a protostar evolves to a main-sequence star is an important parameter to quantify a characteristic time of stellar system evolution. The gravitational energy of the star is radiated away during the quasi-static contraction. Thus,

$$\begin{aligned} \frac{d}{dt} \frac{GM_*}{R_*} &\simeq L_* \\ \frac{d}{dt} \ln R_* &\simeq -t_{\text{KH}}^{-1} \end{aligned} \quad (1.1)$$

where G is the gravitational constant, M_* , R_* , and L_* are stellar mass, radius, and luminosity, respectively. The right-hand-side of Eq.(1.1) is the inverse of the Kelvin-Helmholtz (KH) time

$$\begin{aligned} t_{\text{KH}} &= \frac{GM_*^2}{R_*L_*} \\ &= 3 \times 10^7 \text{ yr} \left(\frac{M_*}{M_\odot} \right)^2 \left(\frac{R_*}{R_\odot} \right)^{-1} \left(\frac{L_*}{L_\odot} \right)^{-1}. \end{aligned} \quad (1.2)$$

It gives a rough measure for the decrease of R_* due to contraction. The KH time gets longer as the radius decreases by contraction. This indicates that the decrease of R_* slows down; young stars have stellar parameters close to the main-sequence values during a large portion of the time, until it evolves to the main-sequence star. Thus, t_{KH} with the main-sequence values of M_* , R_* , and L_*

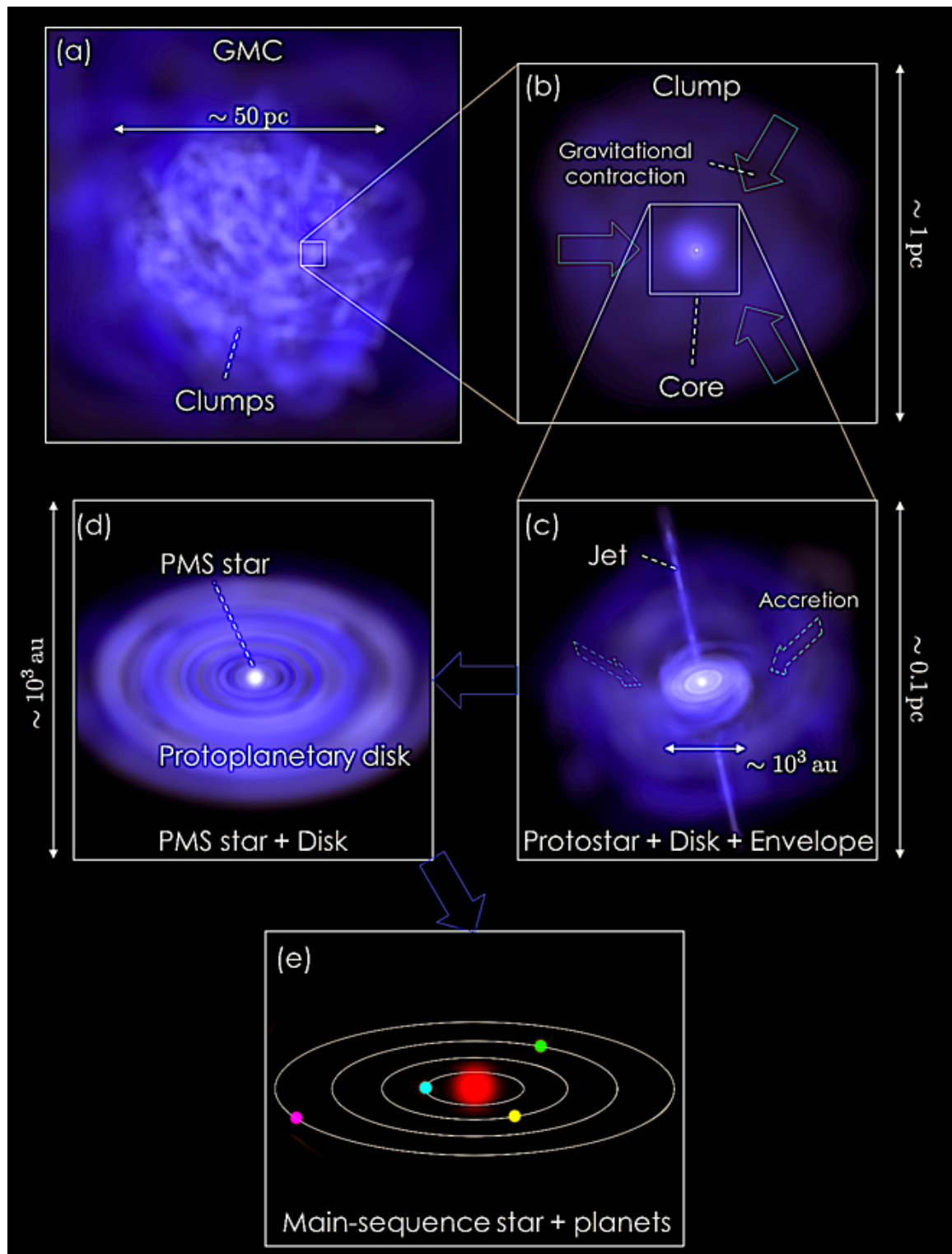


Fig. 1.1 Schematic picture of low-mass stellar system evolution. (a) GMC with clumpy substructures. (b) Close-up view of a molecular cloud clump in the GMC. The clump is gravitationally contracting in the central region, forming a molecular cloud core. (c) Close-up view of a molecular cloud core inside the clump. A disk forms around the central star, and the envelope falls onto the disk. A jet is observed in this system. (d) Young stellar system with PMS star and a surrounding PPD. Most of the envelope has disappeared by the time at which the system reaches this stage. Disk materials are accreting to the star and are forming protoplanets inside. (e) Disk has dispersed, and a young planetary system is left behind.

provides an approximate time with which a young star evolves to a main-sequence star. Note that the KH time is much longer than the crossing time of the star, which is of the order of hours. This guarantees the quasi-static evolution of PMS stars.

Eq.(1.2) shows that the evolution time of young stars depends on the mass. Since less massive stars tend to have smaller effective temperatures T_{eff} , they take a longer time to evolve to main-sequence stars. This indicates that the evolutionary time of a young stellar system depicted in Figure 1.1 differs according to the mass of the stellar system. Although not necessarily related to the evolution time of stars, dispersal time of PPDs, which also quantifies evolutionary time of young stellar systems, has been observationally found to be shorter around Herbig stars with a few solar masses than solar-type stars (see Section 1.5.4). This directly shows that the evolution time of the young stellar system depends on the mass. The evolutionary time of young stellar systems might be also affected by other factors, such as metallicity, the multiplicity of central stars, and the existence of nearby luminous stars.

To summarize, some of the mass in the original molecular cloud core goes into the star, some of the other mass forms into planets, and the other is dispersed by jets and winds. Note that not all of the materials in the parental molecular core goes into constituent objects in the resulting stellar system. The evolutionary time of young stellar systems may depend on the physical properties of the system itself and external environmental factors.

1.3 Mass Functions of Clumps and Cores, and Initial Mass Function

Molecular cloud clumps are the formation site of molecular cloud cores, and the cores are the parental bodies of stellar systems. The mass spectra of clumps and cores are thus significant to determine the initial mass function (IMF) of the resulting stellar systems and hence star formation efficiency. The IMF and star formation efficiency give many important implications to various fields of astrophysics, such as galaxy evolution and planet formation. Investigating these mass functions has been a subject of great importance.

Molecular line surveys have revealed that GMCs have self-similar structures, and the mass spectra of associated clumps commonly follow a power law relation $dN/d \log M \propto M^{-x}$ with $x = 0.6-0.8$ in a wide mass range of $10^{-4} M_{\odot} < M < 10^5 M_{\odot}$ (Blitz 1993, Heithausen *et al.* 1998, Heyer and Terebey 1998, Kramer *et al.* 1998, Muñoz *et al.* 2007). The index x is notably different from that of the Salpeter IMF $x = 1.35$ (Salpeter 1955). This suggests that there exists a departure from the self-similarity during star formation.

Continuum surveys have found steeper spectra of core mass functions (CMFs) than the clump mass function (Testi and Sargent 1998, Motte *et al.* 1998, André *et al.* 2010). The power law index of CMFs is estimated to be $x = 1.1-1.5$ for $\gtrsim M_{\odot}$ and fairly resembles the stellar IMF, in contrast to the clump mass function. The resemblance of CMFs to stellar IMFs holds to a lower mass extent $\sim 0.3 M_{\odot}$ (André *et al.* 2010), providing direct evidence of the connection between molecular cloud cores and star formation. It is suggested that the core formation process may ultimately control the resulting mass spectra of stars.

Note that although the clump mass function is different from the IMFs, they do not necessarily have to be similar; not all molecular cloud clumps form stars inside them. Most of the contribution to star formation originates from star clusters forming in several of the most massive clumps in a molecular cloud. In order to reveal the origin of IMFs and the resulting mass spectra of young stellar systems, it would be necessary to understand the formation process of star-forming clumps and their evolution to individual star-forming cores.

1.4 Birth and Evolution of Stars

A star forms in a gravitationally-contracting molecular cloud core. As the contraction proceeds, the internal density of the core increases to become optically thick to infrared radiation. The core can not radiate away its internal energy anymore at this point. The internal temperature increases, and the pressure eventually balances with the gravity, when the central density reaches $n_{\text{H}} \sim 10^{11} \text{ cm}^{-3}$. This (quasi-)hydrostatic gas sphere is a protostar core (the first core). The first core has a typical size of $\sim 1 \text{ au}$, the mass of $\sim 10^{-2} M_{\odot}$, and the temperature of $\sim 10^3 \text{ K}$. The main component is molecular hydrogen.

The first core continuously grows in mass by accretion. The internal temperature also continuously increases. After $\sim 10^4 \text{ yr}$, it gets high enough ($\sim 2000 \text{ K}$) to dissociate hydrogen molecules by collisions. The endothermic reaction allows the protostar core to resume a *hydrodynamical* contraction.

The contracting protostar core reaches hydrostatic equilibrium again when it shrinks to several solar radii. The hydrostatic gas sphere is now a protostar (the second core). The typical temperature, density, and mass are $\sim 4000 \text{ K}$, $n_{\text{H}} \sim 10^{16} \text{ cm}^{-3}$, and $\sim 0.01 M_{\odot}$, respectively, at this point, and the main component is ionized hydrogen H II.

Circumstellar materials accrete to feed the protostar. Dimensional analysis provides a typical accretion rate of

$$\dot{M}_{\text{acc}} \sim \frac{M_{\text{J}}}{t_{\text{ff}}}, \quad (1.3)$$

where M_{J} is the Jeans mass given with gas density ρ and sound speed c_{s}

$$M_{\text{J}} = \frac{\pi}{6} \rho \left(\frac{c_{\text{s}}}{\sqrt{\rho G}} \right)^3, \quad (1.4)$$

t_{ff} is the free fall time

$$t_{\text{ff}} = \sqrt{\frac{3\pi}{32\rho G}}. \quad (1.5)$$

Thus, Eq.(1.3) reduces to

$$\begin{aligned} \dot{M}_{\text{acc}} &\sim \frac{c_{\text{s}}^3}{G} \\ &\simeq 6.4 \times 10^{-6} \left(\frac{c_{\text{s}}}{0.3 \text{ km s}^{-1}} \right)^3 M_{\odot} \text{ yr}^{-1}. \end{aligned} \quad (1.6)$$

Note that Eq.(1.6) basically depend only on the temperature of the accreting gas. The validity of Eq.(1.6) is supported by numerical simulations (e.g., Shu 1977, Stahler *et al.* 1980, Masunaga and Inutsuka 2000) and the observations that typical accretion rates in the Taurus-Auriga molecular cloud is $\dot{M}_{\text{acc}} \sim 10^{-6} M_{\odot} \text{ yr}^{-1}$ (e.g., Bertout *et al.* 1988, Hartigan *et al.* 1991).

When the accretion materials fall onto the star surface, it drives a shock with the temperatures of $\sim 10^4 \text{ K}$. The gravitational energy of the falling materials is released at the surface and is converted

to radiation in optical and ultraviolet (UV) wavelengths. The accretion luminosity is estimated as

$$L_{\text{acc}} = \frac{GM_*\dot{M}_{\text{acc}}}{R_*} \simeq 3.1 \times 10^1 \left(\frac{M_*}{M_\odot}\right) \left(\frac{R_*}{R_\odot}\right)^{-1} \left(\frac{\dot{M}_{\text{acc}}}{10^{-6} M_\odot \text{ yr}^{-1}}\right) L_\odot. \quad (1.7)$$

Since protostars are embedded in optically thick clouds to optical and UV lights, the emitted photons can be only seen as infrared (re-)emitted by dust, which reprocesses the optical and UV photons.

The typical accretion rate in Eq.(1.6) indicates that protostars grow to a solar-type star on the timescale of $\sim 10^5$ – 10^6 yr, while the accretion rate decays with time. The protostar finally shrinks to a few solar radii and has the central temperature of $\sim 10^6$ K. The mass growth has almost completed at this point, and the protostar proceeds to the pre-main-sequence phase.

PMS stars quasi-statically contract and radiate away its own gravitational energy. When the radius of a PMS star shrinks to $\sim R_\odot$, the central temperature reaches $\sim 1.5 \times 10^7$ K that is sufficiently high temperature to burn hydrogen. The nuclear fusion energy sustains high internal pressure of the star, and it halts the quasi-static gravitational contraction. Hydrogen burning is the onset of the main-sequence phase of stars. Main-sequence stars survive until they burn out all hydrogen fuel in the central region. Note that the overview of stellar system evolution described in this section holds for low- and intermediate-mass stars ($M_* \lesssim 8 M_\odot$). Massive stars with a few tens of solar masses evolve in a different manner. ^{*1}

1.5 Protoplanetary Disks

In the formation process of stellar systems, a PPD forms around the central star and coevolves with it. The disk is composed of gas and dust, and is the parental body of a planetary system. Thus, physical properties of PPDs have a direct link to the formation and evolution of stars and planets. Understanding their properties and formation/evolution processes is essential to understand those of stellar systems. Especially, dispersal of PPDs is our focus of interest in Chapter 2 and Chapter 3. Here, we review their basic characters in detail.

1.5.1 Protoplanetary Disk Formation

Molecular clouds are inhomogeneous in both density and velocity, i.e. they have turbulent structure (Larson 1981, Ostriker 2007). This indicates that a star-forming core has angular momentum as a whole. The azimuthal motions of the circumstellar medium yield the centrifugal force and weaken the radial component of the gravity. The circumstellar medium thus flattens during the collapse and forms disk structure. An angular-momentum-conserved matter has a circular orbit with the radius R_{eq} at which the centrifugal force and gravity balance. The circular radius of a core with the specific angular momentum l and mass M_c is approximately

$$\frac{l^2}{2R_{\text{eq}}^2} = \frac{GM_c}{R_{\text{eq}}} \\ R_{\text{eq}} = \frac{l^2}{2GM_c}.$$

^{*1} We omit to review the formation process of high-mass stars because our focus is on low-mass stellar systems in the present thesis.

The specific angular momentum of a core with radius R_c and rotational energy E_{rot} is roughly $l \simeq \sqrt{2R_c^2 E_{\text{rot}}/M_c}$. Thus, the circular radius is

$$R_{\text{eq}} = \frac{R_c^2 E_{\text{rot}}}{GM_c^2}. \quad (1.8)$$

Observationally, an typical ratio of the rotational energy E_{rot} to the gravitational energy $E_{\text{grav}} = GM_c^2/R_c$ of molecular cloud cores is $\chi \equiv E_{\text{rot}}/E_{\text{grav}} \sim 10^{-2}$ (Goodman *et al.* 1993). The circular radius of Eq.(1.8) is reduced to

$$R_{\text{eq}} \sim 10^2 \left(\frac{R_c}{0.05 \text{ pc}} \right) \left(\frac{\chi}{10^{-2}} \right)^{1/2} \text{ au}. \quad (1.9)$$

Hence, the collapse of a turbulent molecular cloud core results in the formation of a PPD with a typical radius of 10^2 au. Note that a typical specific angular momentum of a molecular cloud core is

$$\begin{aligned} l &\simeq \sqrt{\frac{2R_c^2 E_{\text{rot}}}{M_c}} \\ &\sim 10^{21} \left(\frac{R_c}{0.05 \text{ pc}} \right) \left(\frac{M_c}{M_\odot} \right)^{-1/2} \left(\frac{\chi}{10^{-2}} \right)^{1/2} \text{ cm}^2 \text{ s}^{-1}, \end{aligned} \quad (1.10)$$

which is several orders of magnitude larger than the mean specific angular momentum of the solar system; a large fraction of the total angular momentum of parental cores might be lost during the formation process.

1.5.2 Protoplanetary Disk Structure

The dynamical time of a Keplerian disk is of the order of 10^3 yr at 10^2 au. It is several orders of magnitude smaller than the dispersal time of PPDs, which will be discussed later in Section 1.5.4. This assures that as a first approximation, PPDs can be assumed to be in hydrostatic equilibrium (HSE).

PPD mass is typically $M_{\text{disk}} \sim 0.01 M_\odot$ and at most $M_{\text{disk}} \sim 0.1 M_\odot$. The self-gravity of a PPD is relatively weak, compared to the stellar gravity. In the cylindrical polar coordinates (R, ϕ, z) , the radial and vertical force balances of an axisymmetric Keplerian disk are described as

$$0 = -\frac{1}{\rho} \frac{\partial P}{\partial z} - \frac{GM_*}{R^2 + z^2} \frac{z}{\sqrt{R^2 + z^2}} \quad (1.11)$$

$$0 = -\frac{1}{\rho} \frac{\partial P}{\partial R} - \frac{GM_*}{R^2 + z^2} \frac{R}{\sqrt{R^2 + z^2}} + \frac{v_\phi^2}{R}, \quad (1.12)$$

where ρ , P , and v_ϕ are gas density, pressure, and azimuthal velocity, respectively. The equation of state (EOS) for the ideal gas is given by

$$P = \rho \frac{k_B T}{\mu m_u}. \quad (1.13)$$

In the EOS, k_B is the Boltzmann constant, μ is mean molecular weight, and m_u is the atomic mass unit. Given that the mid-plane density is $\rho_{\text{mid}} = \rho_{\text{mid}}(R)$, Eq.(1.11) is analytically solved for a

vertically isothermal disk

$$\rho = \rho_{\text{mid}} \exp \left[\frac{v_{\text{K}}^2}{c_{\text{s}}^2} \left(\frac{1}{\sqrt{1 + z^2/R^2}} - 1 \right) \right], \quad (1.14)$$

where $v_{\text{K}} = \sqrt{GM_*/R}$ is the Keplerian velocity and $c_{\text{s}} = \sqrt{k_{\text{B}}T/\mu m_{\text{u}}}$ is the isothermal sound speed. These quantities and the mid-plane temperature T_{mid} define the scale height of the disk H as

$$\begin{aligned} H &\equiv \frac{c_{\text{s}}}{v_{\text{K}}} R \\ &\simeq 3.1 \times 10^{-2} \left(\frac{M_*}{M_{\odot}} \right)^{-1/2} \left(\frac{R}{\text{au}} \right)^{1/2} \mu^{-1/2} \left(\frac{T_{\text{mid}}}{10^2 \text{ K}} \right)^{1/2} R. \end{aligned} \quad (1.15)$$

The scale height H is notably much smaller than R at any distance. This indicates that $\rho/\rho_{\text{mid}} \ll 1$ holds for $z \gtrsim R$ in Eq.(1.14), and the bulk of the mass resides in the $z \lesssim R$ region. For the region, Eq.(1.14) is approximated by

$$\rho \simeq \rho_{\text{mid}} \exp \left[-\frac{z^2}{2H^2} \right], \quad (1.16)$$

and the disk surface density Σ is calculated as

$$\begin{aligned} \Sigma &= \int_{-\infty}^{\infty} \rho \, dz \simeq \sqrt{2\pi} \rho_{\text{mid}} H \\ &\sim 10^3 \left(\frac{n_{\text{H, mid}}}{10^{15} \text{ cm}^{-3}} \right) \left(\frac{H}{10^{-2} \text{ au}} \right) \text{ g cm}^{-2}, \end{aligned} \quad (1.17)$$

where $n_{\text{H, mid}}$ is the number density of hydrogen nuclei in the midplane. For comparison, the so-called minimum mass Solar Nebula model (Weidenschilling 1977) of Hayashi (1981) gives the surface density distribution of

$$\Sigma = 1.7 \times 10^3 \left(\frac{R}{1 \text{ au}} \right)^{-3/2} \text{ g cm}^{-2}, \quad (1.18)$$

for the gas component.

Eq.(1.12) describes force balance in the radial direction. Substituting Eq.(1.14) reduces Eq.(1.12) to

$$v_{\phi}^2 = v_{\text{K}}^2 \left\{ 1 + \frac{\partial \ln T_{\text{mid}}}{\partial \ln R} \left[1 - \left(1 + \frac{z^2}{R^2} \right)^{-3/2} \right] + \frac{H^2}{R^2} \left(\frac{\partial \ln T_{\text{mid}}}{\partial \ln R} + \frac{\partial \ln \rho_{\text{mid}}}{\partial \ln R} \right) \right\}. \quad (1.19)$$

Supposing that Σ and T_{mid} have power-law dependences on R of

$$\begin{aligned} \Sigma(R) &\propto R^{-\alpha} \\ T_{\text{mid}}(R) &\propto R^{-\beta}, \end{aligned}$$

Eq.(1.19) reduces to

$$\begin{aligned} v_{\phi}^2 &= v_{\text{K}}^2 \left\{ 1 - \beta \left[1 - \left(1 + \frac{z^2}{R^2} \right)^{-3/2} \right] - \frac{H^2}{R^2} \left(\alpha + \frac{\beta}{2} + \frac{3}{2} \right) \right\} \\ &\simeq v_{\text{K}}^2 \left[1 - \frac{H^2}{R^2} \left(\alpha + \frac{\beta}{2} + \frac{3}{2} + \frac{3\beta}{2} \frac{z^2}{H^2} \right) + \mathcal{O} \left(\frac{z^4}{R^4} \right) \right] \quad (\text{for } R \gg z). \end{aligned} \quad (1.20)$$

PPDs generally have $\alpha > 0$, $\beta > 0$, and, most importantly, $H/R \ll 1$. Therefore, the azimuthal

velocity of PPD gas is sub-Keplerian. The sub-Keplerian motion has an important effect especially on dust dynamics in PPDs and, ultimately, on planet formation. Pressureless dust particles can orbit the central star with Keplerian velocity. Such dust particles move against the headwind by the sub-Keplerian gas. They transfer the angular momentum through aerodynamical friction to gas and migrate inward. The migration time of meter-sized planetesimals is the shortest, and it falls to the star on a much shorter time than planet formation timescale. This implies that such planetesimals cannot grow to a larger-size body in PPDs, which clearly contradicts the existence of the planets. This is one of the biggest issues in the field of planet formation theory. In order to form planets, planetesimals are necessary to grow fast before it falls to the star, or some mechanisms should work to stop the migration. Formation of fluffy dust aggregates is proposed as one of the potential solutions for the problem (Kataoka *et al.* 2013).

1.5.3 Observations of Protoplanetary Disks

By the beginning of the pre-main-sequence phase in the stellar system formation, the envelope has dispersed, and it makes the star-disk system visible in the optical and near-infrared wavelengths. The first direct observation of protoplanetary disks conducted by optical surveys with *Hubble Space Telescope* (HST) in the mid-90s (McCaughrean and O'dell 1996). Its highly-resolved ($\sim 0.1''$) observations captured direct images of PPDs, most of which are evaporating disks exposed to the intense radiation of nearby massive stars^{*2} or so-called silhouette PPDs. Those images show the central luminous stars and surrounding dark disks with a size of ~ 100 au.

Before the direct observation by HST, *Infrared Astronomical Satellite* (IRAS) performed surveys of the entire night sky at mid- and far-infrared (IR) wavelengths ($12 \mu\text{m}$, $25 \mu\text{m}$, $60 \mu\text{m}$, and $100 \mu\text{m}$). IRAS revealed that IR excess of PMS stars visible in optical light (See also Section 1.5.4) is ubiquitous in many molecular clouds and is originated from the reprocessed emission of the circumstellar medium. In the mid-90s, adaptive optics technique was applied to ground-based telescopes and made it possible to perform ground-based observations with resolutions as high as that of HST. High-resolution IR surveys have directly observed the near-IR lights of young stars scattered by the circumstellar disks. Those surveys have revealed that circumstellar disks have various morphology.

The development of bolometer array detectors greatly contributed to the studies of the young stellar system at submillimeter and millimeter wavelengths in the 80s and 90s. Since dust opacity is generally smaller in the submillimeter/millimeter wavelengths than in the ultraviolet, optical, or IR wavelengths, the submillimeter/millimeter wavelength lights are particularly useful to observe dense regions where A_V is so high that their interiors cannot be seen even at IR wavelengths. One example is the highly-dense, midplane region of circumstellar disks. The region is optically thick to the thermal emission of dust at the IR wavelengths but is optically thin to that at the submillimeter/millimeter wavelengths. Thus, the emission is useful to systematically estimate the total mass of the disks. The submillimeter/millimeter lights are also used for the observations of protostars, which are generally embedded deep in the circumstellar medium. Thermal emission of protostars and surrounding medium cannot be seen even at the near-IR wavelengths. Submillimeter/millimeter surveys first succeeded to detect protostars that were hardly detected by IRAS. It is also noteworthy that the recent development of interferometer arrays permits the observations of young stellar systems with even higher resolutions. *Atacama Large Millimeter/submillimeter Array* (ALMA) achieves the highest resolution of $\sim 0.01''$. The detailed observations with that high resolution have discovered many unexpected properties in young stellar systems. The discovery of the multiple rings in the

^{*2} Such evaporating PPDs by the intense irradiation of nearby massive stars are termed “proplyds”.

HL Tau disk is a representative one. Since the detection of the rings in the HL Tau disk, ring/gap structure has been found in tens of PPDs. There also exist disks with a spiral structure of dust and with nonaxisymmetric structure. The recent discoveries of such detailed structure are changing our understanding of PPDs such that rather than a smooth density distribution, PPDs commonly have substructures: rings, gaps, spirals, nonaxisymmetries, and etc. In the 2020s, several other infrared and submillimeter/millimeter telescopes are planned to be in operation. Observations with these telescopes are expected to deepen our systematic understandings about the structure and properties of PPDs.

1.5.4 Lifetimes of Protoplanetary Disks

Materials of a PPD accrete onto the stellar surface in the region close to the star, while those apart from the star are dispersed by thermally- and/or magnetically-driven winds. Therefore, PPDs have the lifetimes. They are often estimated by observing the number fractions of disk-bearing members in young clusters. UV, optical, and IR lights are used for the observations. The optical and UV lights originate from the accreting gas driving a shock on the stellar surface, while the IR is from the reprocessed emission of dust on the surfaces of PPDs.

UV and optical photons of the central star are absorbed by the circumstellar materials. The circumstellar dust absorbs the UV and optical photons from the central star, reprocesses the photons, and thermally (re-)emits photons at IR wavelengths. A typical spectral energy distribution (SED) of a young stellar system is thus composed of two components: the stellar component whose wavelength ranges from ultraviolet to optical, and the circumstellar material component which significantly contributes to an observed intensity at the IR bands of the SED (Figure 1.2). The IR contribution from the circumstellar dust is referred to as the *infrared excess* (IR-excess), which is a direct indicator of the existence of a circumstellar disk around a PMS. Note that young stellar systems with embedded protostars, which are in the early stage of the evolution, are not visible at the optical or near-IR wavelengths in contrast to the young systems hosting PMS stars. The thin geometry of PPDs allows photons to be observed in a wide variety of wavelengths.

Although the IR-excess is defined as the excessive infrared above the stellar component, it does not mean that multiwavelength observations ranging from UV to IR are always necessary to find the IR-excess. The infrared colors $J - H$ and $H - K$ derived from J -, H -, and K -bands ($1.25 \mu\text{m}$, $1.65 \mu\text{m}$, and $2.2 \mu\text{m}$) photometric data provides a tool to detect the IR excess. Given that JHK photometric data is obtained for an infrared source, the infrared colors set the position of the source on the infrared color-color diagram. The position gives information about the magnitude of reddening due to the circumstellar and/or interstellar dust. Lada and Adams (1992) systematically showed that a young star surrounded by the circumstellar medium presents a significant $H - K$ color excess on the color-color diagram, compared to stars without the circumstellar medium; such evolved objects are seen as main-sequence stars reddened by the interstellar extinction in the diagram. Applying these diagnostics to the members of a cluster yields the disk fraction, which is defined as the number ratio of the disk-bearing members to all the members. Observationally, it has been found that the disk fractions of the nearby clusters exponentially decrease as the cluster ages, and typically fall below 10% for the cluster age of $\gtrsim 6$ Myr (Haisch *et al.* 2001, Hernández *et al.* 2007, Meyer *et al.* 2007, Mamajek 2009, Ribas *et al.* 2014). Thus, typical disk lifetimes are estimated to be ~ 3 – 6 Myr for PPDs in the nearby clusters (Alexander *et al.* 2014, Gorti *et al.* 2016, Ercolano and Pascucci 2017).

The lifetimes are estimated by deriving the disk fractions as a function of cluster age but not the age of a single star. One of the advantages using cluster ages to estimate the lifetimes is that

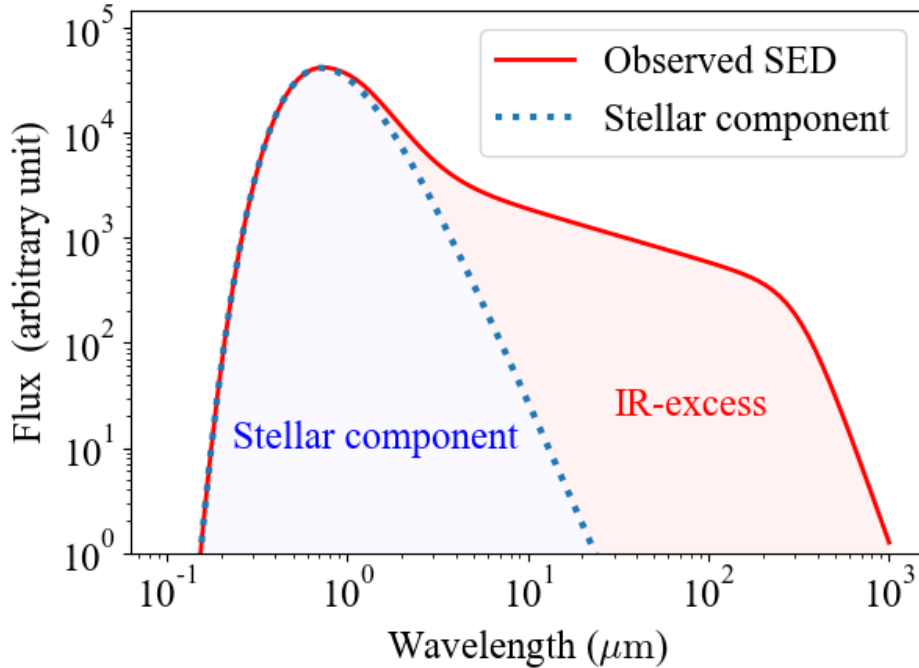


Fig. 1.2 Typical SED of a young star with a PPD. The red line shows the observed SED. The dotted blue line indicates the contribution from the stellar radiation, and the residual (the red area) are the contribution from the circumstellar dust.

broadband photometric data is not always necessary to determine their ages in contrast to the case of single stars. Using an evolutionary model of PMS stars, we can model the near-IR functions of a cluster with a given IMF. Lada and Lada (1995) showed that the slope of the power-law portion of the K -band luminosity function (KLF) significantly changes as clusters age. Thus, cluster ages can be inferred by comparing the slopes of the model and observations. Both of cluster ages and the disk fractions, which are the necessities to estimate the lifetimes, are provided with the near-IR photometric data of clusters. Nevertheless, it is important to estimate the lifetimes as a function of the single star's age because all members of a cluster may not necessarily have exactly the same age, and the environmental difference between single-star- and cluster-forming regions could yield a difference in their lifetimes. Takagi *et al.* (2014) investigated the disk lifetimes in single-star-forming regions. The ages of single stars are determined by the surface gravities derived with high-resolution optical and near-IR spectroscopy. The near-IR colors of the single stars are shown to decrease with increasing stellar ages. The dispersal time of PPDs is thus estimated to be $\sim 3\text{--}4$ Myr, which is in good agreement with the lifetimes of PPDs estimated for the nearby clusters. It is concluded that PPDs have the lifetimes of a few Myr in general.

Although the IR-excess due to warm and small circumstellar dust gives a tool to estimate the PPD lifetimes, dust is the minor component of PPDs in mass and evolves in a dynamically different manner from the gas component. The lifetimes derived with the IR-emission would not always coincide with those of gas disks. Gas disks could exist even after the disappearance of the IR-excess. Fedele *et al.* (2010) used $H\alpha$ (656.28 nm) line emission from young stars to examine the lifetimes of the gas disks. It is empirically known that accreting stars have a larger equivalent width of $H\alpha$

(EW [H α]) than the chromospheric values of EW [H α] (Barrado y Navascués and Martín 2003, White and Basri 2003). Similarly, the width of H α at 10% of the line peak is systematically known to be large ($> 270 \text{ km s}^{-1}$; Natta *et al.* (2004)) for accreting stars (White and Basri 2003, Natta *et al.* 2004, Jayawardhana *et al.* 2006, Flaherty and Muzerolle 2008). These diagnostics are applied to the nearby young clusters, and the gas disk fractions are shown to decrease as the cluster age increases. The typical lifetimes of the gas disks are derived to be 2.3 Myr; the gas component of PPDs also disperses on almost the same time as the dust component.

The near-IR traces the warm dust residing in the inner region ($\lesssim 0.1 \text{ au}$) of a PPD. Therefore, the lifetime of $\sim 3 \text{ Myr}$ estimated by the near-IR observations is not necessarily applicable to the dispersal time of the outer dust. Mid-IR ($\simeq 3 \mu\text{m}$) and far-IR ($\simeq 20 \mu\text{m}$) are used as tracers for the dust component at the outer radius of $\sim 1 \text{ au}$ and $\sim 10 \text{ au}$, respectively. Ribas *et al.* (2014) studied the decay of the disk fractions with these longer-wavelength IR, and showed that the e-folding time of the decay is similar for the disk fractions derived by near-IR and mid-IR (2–3 Myr) and is slightly longer for those estimated with far-IR (4–6 Myr). This suggests that a whole dust disk completely disperses within 10 Myr. Similarly, H α is an accretion indicator which traces the gas component very close to the star. Millimeter transitions of ^{12}CO and [O I] $63 \mu\text{m}$ are used to probe the cold outer disk. Although the number of the samples is limited, it has been found that the bulk of gas in the outer disk ($\sim 10\text{--}10^2 \text{ au}$) disperse within $\sim 10 \text{ Myr}$ (Pascucci *et al.* 2006, Dent *et al.* 2013). Hence, both gas and dust components in a PPD are considered to disappear on the timescale of 10 Myr.

Multiwavelength IR observations have found a subgroup of PPDs that show lack of near- and/or mid-IR excess but have excess in mid- and far-IR wavelengths (e.g., Strom *et al.* 1989, Espaillat *et al.* 2014). These objects are termed *transitional disks*, and are inferred to be caught in the act of disk clearing. The fraction of transitional disks is only $\sim 10\%$ of detected PPDs. This statistically implies a much shorter transitional time, of the order of 10^5 yr , than the disk lifetimes (e.g., Skrutskie *et al.* 1990). The existence of transitional disks and the aforementioned observational results indicate that PPDs abruptly disperse in an inside-out manner at the last stage of disk clearing. SEDs of some PPDs show a homogeneous depletion in the IR-wavelengths; the IR-excess emission is smaller than those of primordial (full) PPDs (for example, the average SED of the PPDs in Taurus star-forming region) but is larger than that of debris disks (Currie *et al.* 2009), which are the remnant objects after disk dispersal. However, recent radiative transfer studies showed that most of these homogeneously depleted disks may be optically thick disks with dust well settled in the midplane (Ercolano *et al.* 2011), and the dominant channel of disk dispersal is the inside-out clearing (Koeperl *et al.* 2013).

In the literature above, the lifetimes are estimated for young low-mass stars with $M_* \lesssim M_\odot$. However, the different physical properties of high-mass stars can affect the lifetimes of PPDs. Ribas *et al.* (2015) examine the PPD lifetimes around young stars with a wide range of mass covering a high-mass regime $M_* \geq 2 M_\odot$. The disk fractions are found to decrease for both low-mass stars ($M_* < 2 M_\odot$) and high-mass stars ($M_* \geq 2 M_\odot$) at older ages. It is also found that PPDs are present around the low-mass stars more frequently than around the high-mass stars at any age of stars. The mass dependence of the disk fractions is statistically robust enough to conclude that PPDs evolve faster and/or earlier around the high-mass stars. The physical reason for the mass dependence is still an open question but photoevaporation (Section 1.5.6) may be a key dispersal mechanism; higher luminosities of high-mass stars can potentially shorten the dispersal time of PPDs.

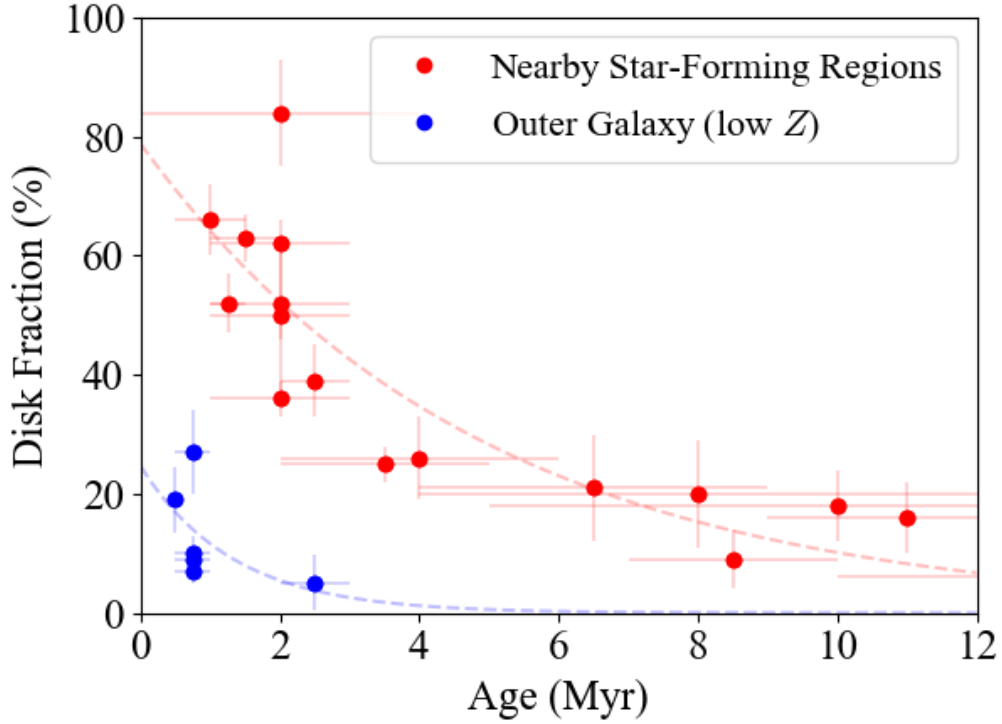


Fig. 1.3 Disk fractions of the nearby star-forming regions (red) and the clusters in the outer Galaxy (blue), where metallicity is significantly low, approximately $Z \sim 10^{-0.7} Z_{\odot}$. The data is taken from Ribas *et al.* (2014) and Yasui *et al.* (2010) for the disk fractions in the nearby regions and in the low-metallicity environments, respectively. The dashed lines fit the observational disk fractions to the exponential function given by Eq.(1.21). The best-fit e-folding times, or typical lifetimes, are $\tau_{\text{lif}} = 4.9 \pm 1.1$ Myr for the nearby star-forming regions and $\tau_{\text{lif}} = 1.3 \pm 1.9$ Myr for the clusters in the outer Galaxy. (See also Table 1.1 for the best-fit parameters.)

1.5.5 Metallicity Dependence of Lifetimes

Dust grains and metal species are important as the absorbers of photons as well as coolants in star-forming regions. The amount of them significantly matters in the formation and evolutionary processes of stars, disks, and planets. The amounts of metal species and dust are associated with metallicity Z . Higher-metallicity environments correspondingly have a large amount of dust and metal species.

In the Milky Way, it is well known that the metallicity is the highest near the galactic center, where the stellar density is high and declines as it gets distant from the center. Star-forming regions also exist in the extreme outer regions, and the environmental difference can cause different PPD lifetimes from those of the nearby star-forming regions. Since PPD lifetimes directly links to the formation time of planets, it is essential to investigate PPD lifetimes in different metallicity environments in order to understand the stellar system formation in general.

The near-IR observations have been conducted for the star-forming regions in the extreme outer Galaxy, where the metallicity is significantly lower than in the solar neighborhood, to estimate the

disk lifetimes (Yasui *et al.* 2009, 2010, 2016a,b). Interestingly, the disk fraction there declines steeply with increasing cluster age and becomes $\lesssim 10\%$ at the cluster age of $\lesssim 1$ Myr. In Figure 1.3, we compare the disk fractions in the nearby star-forming regions and in the low-metallicity environments. The data are compiled from Ribas *et al.* (2014) for the nearby clusters and from Yasui *et al.* (2010) for those in the outer Galaxy. We fit the disk fractions f_{disk} as functions of cluster age t_{age} to

$$f_{\text{disk}} = f_0 \exp[-t_{\text{age}}/\tau_{\text{life}}], \quad (1.21)$$

where f_0 is the disk fraction at $t_{\text{age}} = 0$, and τ_{life} is the typical lifetime. Note that the fitting function goes to zero with $t_{\text{age}} \rightarrow \infty$, implying the assumption that any disk eventually disappears. We use the least squares method to fit the disk fractions. The best-fit parameters are listed in Table 1.1. It appears that a PPD in low metallicity environments disperses earlier and/or faster

Table 1.1 Best-Fit Parameters for the Observed Disk Fractions.

	Nearby clusters ($Z \simeq 1 Z_{\odot}$)	Outer Galaxy ($Z \simeq 0.2 Z_{\odot}$)
f_0 (%)	78 ± 9	4.9 ± 1.1
τ_{life} (Myr)	25 ± 19	1.3 ± 1.9

than in nearby environments. The causes of the metallicity dependence have also been unclear but again, photoevaporation (Section 1.5.6) is proposed as a key dispersal mechanism that can potentially yield the metallicity dependence (Ercolano and Clarke 2010). The metallicity dependence of PPD photoevaporation is discussed in Chapter 2 and Chapter 3.

1.5.6 Dispersal Mechanisms of Disks

It has been observationally confirmed that the lifetime of PPDs is of the order of several million years in general, depending on metallicity and the stellar mass. Since not all materials might go into forming planets, some mechanisms should work to disperse PPDs within the time. Several dynamical processes such as accretion (Shakura and Sunyaev 1973, Lynden-Bell and Pringle 1974), photoevaporation (e.g., Hollenbach *et al.* 1994), magnetohydrodynamics (MHD) wind (e.g., Suzuki and Inutsuka 2009), stellar wind (e.g., Elmegreen 1979), and giant planet formation (Rice *et al.* 2003) have been proposed to be effective on disk dispersal. In particular, disk evolution models in which a viscous PPD evolves under the effects of the winds driven by photoevaporation and/or MHD effects appear to well explain both the lifetime and the formation of the transitional disks (Clarke *et al.* 2001, Alexander *et al.* 2006, Owen *et al.* 2010, Gorti *et al.* 2015). Thus, accretion, photoevaporation, and MHD wind are considered to be key dispersal mechanisms of PPDs at present. We briefly review these processes in this section.

Accretion

PPDs lose the mass mainly via accretion, especially at the early stage of disk evolution. The angular momentum of a PPD is transferred and redistributed within the disks. The angular momentum of an inner annulus is transferred to the adjacent outer annulus via viscous friction. The governing

equations of motion for viscous gas are

$$\frac{\partial \rho}{\partial t} + \nabla \cdot \rho \mathbf{v} = 0 \quad (1.22)$$

$$\rho \frac{d\mathbf{v}}{dt} = \nabla \cdot \mathbf{S} + \rho \mathbf{K}, \quad (1.23)$$

where \mathbf{S} is the stress tensor and \mathbf{K} is body force. Let μ be the coefficient of the shear viscosity in this section. The stress tensor is given as

$$S_{ij} = -P\delta_{ij} + 2\mu \left(e_{ij} - \frac{1}{3} e \delta_{ij} \right), \quad (1.24)$$

where e is the rate of straining tensor

$$e_{ij} \equiv \frac{1}{2} \left(\frac{\partial v_i}{\partial x_j} + \frac{\partial v_j}{\partial x_i} \right), \quad (1.25)$$

and e is its trace. The bulk viscosity is neglected in Eq.(1.24) because it is generally small compared to the pressure or shear stress. Hereafter in this section, we use the cylindrical polar coordinates, and we assume that the viscous gas has a rotational axis and is axisymmetric around it, and that the variables are symmetric along the z -direction. Galilean invariance allows us to set $v_z \simeq 0$. Thus, Eq.(1.22) and the ϕ -component of Eq.(1.23) reduce to

$$\frac{\partial \Sigma}{\partial t} + \frac{1}{R} \frac{\partial}{\partial R} R \Sigma v_R = 0 \quad (1.26)$$

$$\frac{\partial}{\partial t} \Sigma R^2 \Omega + \frac{1}{R} \frac{\partial}{\partial R} R^3 \Sigma v_R \Omega = \frac{1}{2\pi R} \frac{\partial}{\partial R} \left(2\pi R^3 \nu \Sigma \frac{\partial \Omega}{\partial R} \right), \quad (1.27)$$

where $\nu \equiv \mu/\rho$ is the coefficient of kinematic viscosity and $\Omega \equiv v_\phi/R$ is the angular velocity. Eq.(1.27) is the transfer equation of angular momentum. The right-hand-side describes the net shear stress exerted by the adjacent annulus. We further assume that Ω is independent of time. ^{*3} Eq.(1.26) and Eq.(1.27) are then rewritten as

$$\frac{\partial \Sigma}{\partial t} = -\frac{1}{2\pi R} \frac{\partial}{\partial R} \left[\frac{\frac{\partial}{\partial R} \left(2\pi R^3 \nu \Sigma \frac{\partial \Omega}{\partial R} \right)}{\frac{\partial}{\partial R} R^2 \Omega} \right] \quad (1.28)$$

$$2\pi R v_R \Sigma = \frac{\frac{\partial}{\partial R} \left(2\pi R^3 \nu \Sigma \frac{\partial \Omega}{\partial R} \right)}{\frac{\partial}{\partial R} R^2 \Omega}. \quad (1.29)$$

In the case of an accreting disk around a star, the R -component of Euler equations yields

$$\Omega_K = \sqrt{\frac{GM_*}{R^3}}. \quad (1.30)$$

^{*3} This assumption is justified when $R\Omega \gg v_R$ and $R\Omega \gg R \frac{\partial v_R}{\partial R}$, according to the R -component of Euler equations.

Substituting Eq.(1.30) into Eq.(1.28) and Eq.(1.29), we obtain

$$\frac{\partial \Sigma}{\partial t} = \frac{3}{R} \frac{\partial}{\partial R} \sqrt{R} \frac{\partial}{\partial R} \sqrt{R} \nu \Sigma \quad (1.31)$$

$$2\pi R v_R \Sigma = \frac{\frac{\partial}{\partial R} \left(2\pi R^3 \nu \Sigma \frac{\partial \Omega_K}{\partial R} \right)}{\frac{\partial}{\partial R} R^2 \Omega_K}. \quad (1.32)$$

Eq.(1.31) describes the surface density evolution of viscous Keplerian disks, and Eq.(1.32) sets the accretion rate. Let $x = 2\sqrt{R}$ and $f = (3/2)\Sigma x$; the continuity equation Eq.(1.31) is transformed to a diffusion equation

$$\frac{\partial f}{\partial t} = D \frac{\partial^2 f}{\partial x^2},$$

where $D = 12\nu/x^2$ is the diffusion coefficient. Hence, the surface density evolution of a viscous disk is a diffusion process. The timescale with which the viscosity smooths out the gradient of f within an interval Δx is given by $\sim \Delta x^2/D$, and thus the diffusion time of an accreting disk with a size of R is

$$t_\nu \simeq \frac{R^2}{\nu}. \quad (1.33)$$

Considering the fact that the near-IR observations suggest the disk lifetime of a few million years, we can set the viscous timescale Eq.(1.33) of PPDs to be of the order of 10^6 yr at the distance of $\lesssim 1$ au. This results in the viscous timescale of $\sim 10^7$ yr at several tens of astronomical units and even longer time at further distant regions (Hollenbach *et al.* 2000, Armitage 2011), though the choice of ν is arbitral. Nevertheless, the very long viscous timescale clearly contradicts the observational PPD lifetimes. Moreover, Eq.(1.31) predicts that the surface density should decrease with time in a power-law manner as $\Sigma \propto t^{-p}$ (Lynden-Bell and Pringle 1974). It also contradicts the existence of transitional disks (Andrews and Williams 2005) and the much shorter transitional time than the PPD lifetime (e.g., Skrutskie *et al.* 1990, Kenyon and Hartmann 1995, Alexander *et al.* 2014). In order to explain the timescale of disk dispersal and the existence of transitional disks, some other dispersal processes should work with accretion; photoevaporation and MHD wind are proposed as such processes.

The evolution of viscous disks is significantly affected by the profile of ν . It is necessary to understand the origin of the viscosity to obtain the profile. The molecular collision is one of the candidates. Collisions between molecules in a shear flow cause a viscosity which is called molecular viscosity. The molecular viscosity is given as

$$\nu_{\text{mol}} = \frac{c_s}{n_{\text{H}} \sigma_{\text{mol}}},$$

where σ_{mol} is the collision cross section of molecules. The cross section is roughly equivalent with the size of molecules $\sim 10^{-15}$ cm². The viscous time for molecular collisions is estimated to be

$$t_{\nu, \text{mol}} \sim 10^7 \left(\frac{R}{\text{au}} \right)^2 \left(\frac{n_{\text{H}}}{10^{14} \text{ cm}^{-3}} \right) \left(\frac{\sigma_{\text{mol}}}{10^{-15} \text{ cm}^2} \right) \left(\frac{c_s}{0.3 \text{ km s}^{-1}} \right)^{-1} \text{ Myr}.$$

The viscous timescale is much longer than the lifetime of PPDs, and therefore the molecular viscosity is unlikely to be the origin. Although ν_{mol} is small, it can yield a large Reynolds number in the

interior of PPDs

$$\begin{aligned} \text{Re} &\simeq \frac{c_s H}{\nu_{\text{mol}}} \\ &\sim 10^{10} \left(\frac{H}{10^{-2} \text{ au}} \right) \left(\frac{n_{\text{H}}}{10^{14} \text{ cm}^{-3}} \right) \left(\frac{\sigma_{\text{mol}}}{10^{-15} \text{ cm}^2} \right). \end{aligned} \quad (1.34)$$

This indicates that a physical instability generates turbulence with dissipative motions on a smaller scale than H . The turbulent motions mix gas with the adjacent annulus, and it effectively works as viscosity. If the turbulence is isotropic, the scale height H limits the scale of the turbulent motion. Similarly, since supersonic flow leads to driving shock and dissipating rapidly, the turbulence velocity is limited to be less than c_s . Hence, the turbulent viscosity can be represented by a dimensionless parameter α (Shakura and Sunyaev 1973)

$$\nu_{\text{tur}} = \alpha c_s H. \quad (1.35)$$

The parameter α is referred to as the Shakura-Sunyaev α parameter and is estimated to be of the order of 10^{-2} – 10^{-4} from the disk lifetimes. Note that α does not have to be a constant but can depend on physical variables such as density, temperature, and magnetic field. Nonetheless, α is often treated as a constant in calculations of viscous disk evolution just for simplicity.

Photoevaporation

PPDs are irradiated by ultraviolet and X-ray emitted from the central star and/or nearby massive stars. The atoms and dust absorb the photons and are photoionized. The ejected electrons thermalize to increase gas temperatures in optically thin regions. The “hot” gas flows out of the disk, which causes a considerable mass loss. The mass loss process is referred to as photoevaporation (Figure 1.4). Far ultraviolet (FUV; $6 \text{ eV} < h\nu < 13.6 \text{ eV}$), extreme ultraviolet (EUV; $13.6 \text{ eV} < h\nu < 0.1 \text{ keV}$), and X-rays ($h\nu > 0.1 \text{ keV}$) are effective to drive photoevaporative flows.

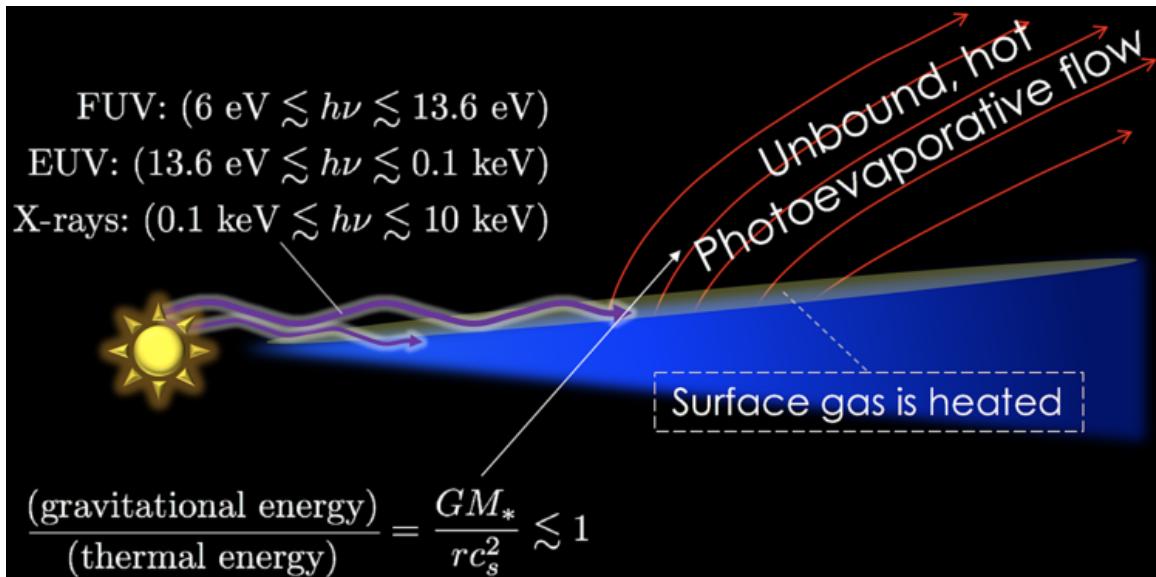


Fig. 1.4 Schematic picture of photoevaporation. The disk surface is irradiated by FUV, EUV, and X-ray from the central star. Photoevaporative flows are driven from the heated region. Note that in the inner region, the heated gas is bound by the central star’s gravity.

EUV photoevaporation first started to be investigated, before FUV or X-ray was proposed as the important heating sources that can cause strong photoevaporation. Hollenbach *et al.* (1994) performed 1+1D EUV radiative transfer calculations, where the disk is divided into two physically different regions in the radial direction at the gravitational radius

$$R_g = \frac{GM_*}{c_s^2} \quad (1.36)$$

$$\simeq 7.5 \left(\frac{M_*}{M_\odot} \right) \left(\frac{T}{10^4 \text{ K}} \right)^{-1} \left(\frac{\mu}{0.7} \right) \text{ au.}$$

It is assumed from dimensional analysis that the disk achieves hydrostatic equilibrium in the inner region $R < R_g$, while steady photoevaporative flows are driven in the outer region $R > R_g$ at the velocity of the sound speed for the ionized gas ($\simeq 10 \text{ km s}^{-1}$). The vertical density distribution of the disk is taken into account for the inner region, but it is set to $H = 0$ in the outer region, i.e. the disk is infinitesimally thin there. The density profile $n_H(R)$ is determined 1+1D radiative transfer calculation for EUV. The resulting profile scales as $R^{-3/2}$ for $R < R_g$ and $R^{-5/2}$ for $R > R_g$, and the photoevaporation rate is estimated to be $\dot{M}_{\text{ph}} \sim 10^{-10} - 10^{-9} M_\odot \text{ yr}^{-1}$. Font *et al.* (2004) performed 2D hydrodynamics simulations, using the density profile of Hollenbach *et al.* (1994) as the boundary condition at the midplane. The resulting photoevaporation rate is smaller than that of Hollenbach *et al.* (1994) by a factor of 2–3. The small difference is originated from the launch velocity; Hollenbach *et al.* (1994) assumed the sound speed, while the launch velocities are 30–40% of the sound speed in the simulations of Font *et al.* (2004). It is concluded that photoevaporative flows are launched at the subsonic speed rather than the sonic speed. Recently, Tanaka *et al.* (2013) studied EUV photoevaporation of PPDs with 2D radiative transfer calculations, using a disk model that also has a nonzero scale height for $R > R_g$ as well as $R < R_g$. Tanaka *et al.* (2013) concluded that the direct EUV component is dominant in the flow region rather than the diffuse EUV component, which contradicts the conclusion of Hollenbach *et al.* (1994), and this results in $R^{-3/2}$ dependence of the density profile even for the flow region $R > R_g$ in contrast to Hollenbach *et al.* (1994). The large contribution from the distant regions yields a higher photoevaporation rate ($\sim 10^{-9} M_\odot \text{ yr}^{-1}$) by a factor than that of Hollenbach *et al.* (1994). Yorke and Welz (1996) and Richling and Yorke (1997) performed radiation hydrodynamics simulations of photoevaporating PPDs around the central massive star with $M_* = 8.4 M_\odot$, taking into account the diffuse EUV generated by radiative recombinations (Yorke and Welz 1996) and the scattered EUV by dust (Richling and Yorke 1997). For the disk model, the results of the cloud collapse simulations in Yorke *et al.* (1995) was used. The disk has a hole in the $R \lesssim 40 \text{ au}$ regions. Although the scattering EUV is concluded as an important component to drive photoevaporation in the outer regions, it appears to mainly result from the geometrical structure of the adopted disk. Hence, the causes of the different conclusions in the studies above might be the differences in the adopted methods and disk models. It is still under debate which of the direct, diffuse, and scattering EUV components is dominant to drive photoevaporation. Self-consistent radiation hydrodynamics simulations that have the inner boundary close to the stellar surface is necessary to investigate it. Unfortunately, this is beyond the limitation of the currently available numerical methods.

The main absorber of EUV is atomic hydrogen. The absorption cross section is of the order of $\sigma_{\text{HI}} \sim 10^{-17} \text{ cm}^2$. In contrast, the main absorber of FUV photons are dust grains, and the cross section is about four orders of magnitude smaller than that of atomic hydrogen. FUV is typically attenuated at the column density of $\sim 10^{21} \text{ cm}^{-2}$; FUV can reach a denser region inside PPDs than EUV in general. As a result, FUV-driven flows have a higher density than EUV-driven

flows, and thus FUV photoevaporation generally yields higher mass loss rates by more than an order of magnitude compared to EUV photoevaporation (Gorti and Hollenbach 2009, Owen *et al.* 2012). The effects of FUV on the photoevaporation of PPDs are first investigated in the context of photoevaporation of PPDs illuminated by external nearby massive stars (so-called “proplyds”). Johnstone *et al.* (1998) presented analytic and numerical models for proplyds and showed that the mass loss rate is determined by either of FUV-driven flows or EUV-driven flows; it was concluded that FUV-driven flows dominantly contribute the mass loss for distant proplyds where the EUV photons hardly reach from the external massive stars. However, Johnstone *et al.* (1998) did not perform detailed calculations of chemical/thermal structure in PPDs, and thus it could not be accurately concluded under which conditions FUV-driven flows dominate the mass loss. Störzner and Hollenbach (1998) improved the models of Johnstone *et al.* (1998) by including the results of both equilibrium and nonequilibrium PDR codes, and by setting the launch velocity to be the escape velocity instead of using it as a free parameter. It was shown that with sufficient FUV fluxes $G_0 \simeq 5 \times 10^4 - 2 \times 10^7$, FUV-driven flows are dominant to cause the mass loss. The models can explain the observed sizes of the ionization fronts of many proplyds in the Orion Nebula. In Johnstone *et al.* (1998) and Störzner and Hollenbach (1998), it has been assumed that the disks have a spherical structure and steady photoevaporative winds spherically flow out of the disks. In contrast, as a continuous study of Richling and Yorke (1998) where only EUV effects are incorporated, Richling and Yorke (2000) performed two-dimensional radiation hydrodynamics simulations of proplyds illuminated by both FUV and EUV from external stars. The thermal structure and radiation field are self-consistently calculated to determine the density and flow structure, although a simplified cooling function is used. The results of the simulations show that FUV photons heat the gas up to 5000 K and drive photoevaporative flows on the surface of the proplyds. The FUV-driven flows are also launched on the disk surface in the shaded region from the external star owing to the effects of the diffuse FUV. The launched flows interact with EUV photons, developing a head-tail configuration. The heads have bright emission lines with a crescent shape, and the tails are elongated in the direction opposite to the external star. The properties of the head-tail shaped proplyds explain the observational results of proplyds in the star-forming regions such as the Orion Nebula, M8, NGC 2024, and NGC 3603. Gorti and Hollenbach (2009) first developed a model for photoevaporation driven by FUV emitted from the central young star instead of external massive stars. The thermal and chemical structures of PPDs are determined without solving hydrodynamics to estimate FUV photoevaporation rates. Photoevaporative flows are assumed to be launched at sound speed from the surface where the local thermal energy of the gas is equal to the gravitational energy. The photoevaporation rates are estimated by integrating the mass flux over the surface. Resulting FUV photoevaporation rates are of the order of $\sim 10^{-8} M_\odot \text{ yr}^{-1}$ for typical young low-mass stars. The photoevaporation rates are $10-10^2$ times larger than those of EUV photoevaporation rates (Hollenbach *et al.* 1994, Font *et al.* 2004, Tanaka *et al.* 2013). In Chapter 2, we perform the first radiation hydrodynamics simulations to investigate disk photoevaporation driven by FUV emitted from the central star. Radiative transfer and detailed chemistry are solved in a self-consistent manner to derive photoevaporation rates.

As well as FUV and EUV, significant X-ray emission is observed from young stars. The X-rays heat disk medium to a large column comparable to FUV and hence have a potential to yield a significantly larger mass loss rate compared to EUV. Photoevaporation excited by X-ray irradiation from central young stars has also been studied (Alexander *et al.* 2004, Ercolano *et al.* 2008, Gorti and Hollenbach 2008, Ercolano *et al.* 2009, Gorti and Hollenbach 2009, Owen *et al.* 2010, 2012, Wang and Goodman 2017). Alexander *et al.* (2004), Ercolano *et al.* (2008, 2009), and Gorti and Hollenbach (2009) adopt a similar hydrostatic method; photoevaporation rates are estimated by determining the

thermal and chemical structure of PPDs without solving hydrodynamics. However, the conclusions are divergent regarding the significance of X-ray on photoevaporation. Alexander *et al.* (2004) and Gorti *et al.* (2009) have shown that X-ray is ineffective or, at least, has only a minor effect to drive photoevaporation compared to FUV or EUV, while Ercolano *et al.* (2008, 2009) have concluded that X-ray can cause a significant mass loss comparable to FUV photoevaporation rates. Owen *et al.* (2010, 2012) performed hydrodynamics simulations based on the chemistry calculations of Ercolano *et al.* (2009). The temperatures of gas heated by X-rays are given as a function of the ionization parameter. The resulting X-ray photoevaporation rate is of the order of $10^{-8} M_{\odot} \text{ yr}^{-1}$ and is consistent with that estimated in Ercolano *et al.* (2009). Note that the most effective component on driving photoevaporation appears to be the photons with $\lesssim 0.1 \text{ keV}$ according to Table 1 of Ercolano *et al.* (2009), although X-ray is defined as $0.1 \text{ keV} < h\nu < 10 \text{ keV}$ photons in Ercolano *et al.* (2009). Unfortunately, none of these studies treat hydrodynamics, radiative transfer, and chemistry in a self-inconsistent manner. Dynamics can affect radiative transfer and chemistry by varying optical depth and chemical/thermal structure of the disk, and vice versa. Using a self-consistent method is important to investigate photoevaporation of PPDs. Wang and Goodman (2017) first conducted X-ray photoevaporation with self-consistent radiation hydrodynamics simulations, solving nonequilibrium chemistry. There, X-ray has been concluded to be ineffective on driving photoevaporation. However, X-ray energy is assumed to be 1 keV in Wang and Goodman (2017). Since the chemical and thermal effects of X-ray depend on the X-ray energy, considering multi-energy X-ray irradiation is essential to discuss the effectiveness of X-ray. In Chapter 3, we perform the first radiation hydrodynamics simulations with self-consistent thermochemistry, incorporating multi-energy X-ray irradiation.

Photoevaporation works as a mass loss process with accretion at the same time. Photoevaporative winds strip the mass off from the disk surface while disk materials fall onto the central star. The typical dispersal time due to accretion is given by the viscous time, but it is longer than the disk lifetime, especially in the outer region. By contrast, photoevaporation has a sufficiently short dispersal time even in that region, and therefore it is an essential process to explain the observed disk lifetimes and evolution (Hollenbach *et al.* 2000). Several previous studies have taken into account the mass loss effect of photoevaporation in the 1D hydrodynamics simulations of accretion disks. The resulting dispersal time is in good agreement with the observed lifetimes (Clarke *et al.* 2001, Alexander *et al.* 2006, Owen *et al.* 2010, Gorti *et al.* 2015). Besides, in these models, there is a physical transition in the global evolution of the disk, when accretion rates locally drop below photoevaporation rates in the later stage. The disk mass is locally lost by photoevaporation instead of accreting to the inner region at this point. A gap opens at the radius where the accretion rate lowers below the photoevaporation rate, and the disk is separated in the inner and outer disks. The inner disk disperses with the short viscous time due to its small size, leaving the outer disk behind. This can be the formation mechanism of the observed transitional disks. The inner edge of the outer disk is then exposed to the direct irradiation of the central star, and thus the outer disk disperses within a short time of $\sim 10^5 \text{ yr}$ (Clarke *et al.* 2001, Alexander *et al.* 2006, Owen *et al.* 2010, Gorti *et al.* 2015). This is also consistent with the observational fact that the occurrence of transitional disks is about 10% in PPDs. Hence, photoevaporation is an essential mass loss process to explain not only the observed disk lifetimes but also the formation of transitional disks and their short dispersal time.

Furthermore, photoevaporation is proposed as a key mass loss process that also explains the metallicity dependence of the lifetimes (Ercolano and Clarke 2010). The main absorbers of FUV and hard X-rays are dust grains and metal elements, respectively, and their amounts decrease with decreasing

metallicity. The photons, therefore, reach a deep interior of PPDs with low metallicities and have the potential to yield higher mass loss rates as metallicity decreases. Ercolano and Clarke (2010) (hereafter, EC10) derived the metallicity dependence of X-ray photoevaporation rates by hydrostatic calculations. The resulting X-ray photoevaporation rates significantly increase with lowering disk metallicity. The estimated disk lifetimes are correspondingly shorter for lower metallicities and scale as $Z^{0.52}$ for $10^{-2} Z_{\odot} \leq Z \leq Z_{\odot}$. The lifetimes are in good agreement with the observational trend of the disk lifetimes. However, EC10 uses a hydrostatic method and infers photoevaporation rates with assumptions on the launch velocity and base density. The hydrostatic method is shown to result in a different photoevaporation rate from that derived by hydrodynamics simulations (Owen *et al.* 2010), even though it gives a consistent photoevaporation rate within an order of magnitude accuracy. Thus, the calculation method possibly affects the resulting slope of the metallicity-dependent lifetimes. Radiation hydrodynamics studies are necessary to derive the metallicity dependence of the lifetimes directly. In Chapter 2 and Chapter 3, we perform radiation hydrodynamics simulations of photoevaporating PPDs, varying disk metallicity. We investigate the UV effects on photoevaporation of PPDs with various metallicities in Chapter 2, and we additionally implement X-ray effects to examine the variances in the photoevaporation rates and the metallicity dependence from the case of UV photoevaporation in Chapter 3.

Magnetohydrodynamics Winds

Magnetohydrodynamics (MHD) effects also have significant influences on the evolution of PPDs. Magnetorotational instability (MRI) (Balbus and Hawley 1991) is considered to be the most promising origin of the turbulence within the disks (cf. Eq.(1.35)). The turbulence is, in turn, the origin of the viscosity, and thus MRI is relevant in the global evolution of PPDs. MRI is derived from an MHD interaction between the magnetized gas in an accretion disk. Supposing a situation where a weak vertical magnetic field threads disk gas, and some fluid elements are perturbed inward and outward, the magnetic tension acts as a spring that connects the inner elements to the outer ones. In a disk where the angular velocity decreases with increasing the radial distance, the inner annulus moves faster than the outer one. The magnetic tension pulls the inner elements to the direction opposite to the angular velocity, while it accelerates those of the outer ones. The angular momentum is transported outward through this effect. Owing to the loss of the angular momentum, the inner gas moves towards the inner region, while the acquirement of the angular momentum makes the outer gas move even outwards. This unstable process generates a turbulent motion of the gas in the disks.

Besides being the origin of turbulence, MRI has been found to drive vigorous winds from disk surfaces by performing local box simulations of stratified disks (Suzuki and Inutsuka 2009, Suzuki *et al.* 2010). The disks become turbulent by the MRI effect, and large-scale channel flows develop at $z \simeq 1.5-2H$. The channel flows break up by the magnetic reconnection there, the magnetic fields carry the mass to both upward and downward directions. The total mass loss rate is as high as $2.5 \times 10^{-9} M_{\odot} \text{ yr}^{-1}$.

The fact that this picture of MRI above is in an ideal-MHD limit, where the magnetic field strongly couples with the gas, implies that a disk needs to be sufficiently ionized to trigger the turbulent motion. However, PPDs have large column densities and hence are predominantly neutral in large regions ($\sim 0.1-50$ au). MRI may be significantly suppressed especially in the inner, dense regions (so-called “dead zones”; Gammie 1996). The gas would be partially ionized in the surrounding regions of the dead zones. In such a partially ionized gas, the magnetic field indirectly interacts with the neutral component of the gas by collisions between the neutrals and charged species, which

couple with the magnetic field. Ideal-MHD does not hold in the regions; it is required to introduce non-ideal MHD effects: Ohmic dissipation, the Hall effect, and ambipolar diffusion, in order to discuss MRI in a partially ionized gas. Ohmic dissipation accounts for the dissipation of currents, which generates magnetic fields, due to collisions between charged particles and neutrals. The Hall effect describes the deflected motions of charged species by the Lorentz force. This effect yields Hall currents, and the magnetic field is changed by them. Ambipolar diffusion explains decouple of the charged species and neutrals in motion owing to a poor collision rate. The neutrals slip past the magnetic fields with which the charged particles couple. These non-ideal MHD effects are dominant in the regions surrounding the dead zones.

Recent non-ideal MHD studies showed that the low ionization degree of the inner disk indeed suppresses MRI, but winds can be still centrifugally driven from disk surfaces by the magneto-centrifugal force (Bai and Stone 2013, Gressel *et al.* 2015). Since magnetized winds exert a torque on disks in contrast to photoevaporative winds, the winds may have an essential role to extract the disk angular momentum. The loss of the angular momentum is indispensable to cause accretion, and the magneto-centrifugal winds are suggested to be effective as such a mechanism, while hydrodynamics instabilities, including MRI, are often found to be ineffective in PPDs (Bai 2013, Bai and Stone 2013, Simon *et al.* 2013b,a, Turner *et al.* 2014).

Thermal evolution of gas has not yet been considered in the non-ideal MHD simulations above. It affects the wind kinematics and global evolution of PPDs and thus is worth being incorporated. Recent studies developed a global model of the winds with incorporating a simplified external thermal heating (irradiation) as well as the non-ideal MHD effects (Bai 2016, Bai *et al.* 2016). The mass loss rate is actually influenced by both the strength of the magnetic field and thermal heating, and it is characterized by the ratio of sound speed and Alfvén speed at the base. In these studies, it is found that this “magneto-thermal” winds driven by the total pressure gradient are dominant over the magneto-centrifugal winds in PPDs (Bai 2017).

Although MHD winds and photoevaporation have been frequently studied independently, the interplay between photoevaporation and the MHD effects on disk evolution is an important question for realistic modeling of global PPDs. However, it is highly computationally expensive to self-consistently solve radiative transfer and chemistry by taking into account the non-ideal MHD effects. At the time of writing this thesis, Wang *et al.* (2018) presented global MHD simulations where radiative transfer, chemistry, and non-ideal MHD are coupled in a consistent manner. When EUV radiation is disabled in the model, warm molecular flows are driven by the toroidal magnetic pressure generated by winding the poloidal magnetic field, but not by the magneto-centrifugal force. The resulting mass-loss rate is comparable to photoevaporation rate ($\sim 10^{-8} M_{\odot} \text{ yr}^{-1}$). Strengthening the poloidal magnetic field increases both the mass-loss rate and the accretion rate. Ionization due to EUV and X-ray at the base is shown to affect the mass-loss rate strongly. It has been concluded that the dynamical profile of magneto-thermal winds sensitively depends on details of chemistry.

Metallicity effects on the MHD winds remain unknown. The ionization degree of the disk interior would be dependent on the amounts of dust and metal elements, and can change the magnitude of the MHD effects. Considering influences of metallicity on the MHD winds may be thus important for more detailed modeling of the dynamics and thermochemical structure of PPDs.

1.6 Aims and Structure of the Present Thesis

The formation of an astronomical object is always followed by the disappearance of the parental bodies. Molecular cloud cores and PPDs bear stellar systems and planets inside them while they

themselves are dispersing. The dispersal time is an important measure to characterize the formation timescale of the bodies left behind. This holds for the local, present-day star-forming regions but also for those in high- or low-metallicity environments, such as the inner/outer galaxy and high-redshift galaxies. Bearing this in mind, we investigate the dispersal processes of molecular cloud cores and PPDs by photoevaporation in this thesis. We perform a suite of radiation hydrodynamics simulations, varying the metallicities of the objects. In particular, we derive the mass loss rates, and derive, if any, the metallicity dependence of the lifetimes. The results of these studies have the potential to give a number of implications to star and planet formation in the various environments since the early stage of the universe evolution. This is an indispensable step to explore the evolutionary history of galaxies, including the Milky Way, and hence the origin of our solar system. It is noteworthy that our studies are ahead of the operation of the next-generation telescopes, which are currently planned to start operating in the near future, such as the Square Kilometre Array (SKA), Next Generation Very Large Array (ngVLA), James Webb Space Telescope (JWST), and other several planet-searching telescopes. They are designed so that they can observe the objects residing in many different environments. It is expected to obtain brand-new observational results regarding stellar systems. Our studies are meaningful in this context; the results could be available as tools to interpret the observed data and to provide a guide into observations with using the high-performance telescopes.

In Chapter 2, we perform radiation hydrodynamics simulations of photoevaporating PPDs irradiated by UV from the central low-mass star. Metallicity of the disks is varied to investigate the metallicity dependence of photoevaporation rates for giving clues to explain the observational trend of the PPD lifetimes. In our simulations, the effects of FUV and EUV are incorporated as Yorke and Welz (1996) and Richling and Yorke (2000), which followed the evolution of a disk irradiated by a central B star and an external radiation source, respectively, with self-consistent radiation hydrodynamics simulations. These studies, however, focus on the dispersal process around massive stars whose luminosities are significantly higher than low-mass stars by several orders of magnitude. The results would not be directly applicable to photoevaporation of PPDs around low-mass stars. As for photoevaporation of PPDs irradiated by the central star, this is the first study which implements both of FUV and EUV effects of the central low-mass star into hydrodynamics simulations. Our study is also the first for performing self-consistent radiation hydrodynamics simulations. In addition, we solve nonequilibrium chemistry to calculate accurately the relevant heating/cooling rates and to determine the temperature distribution. None of the previous studies has adopted this self-consistent method. Since hydrodynamics, radiative transfer, and chemistry affect each other, using a self-consistent method is important in the study of PPD photoevaporation. Regarding metallicity dependence of photoevaporation rates, EC10 approximately derives that of X-ray photoevaporation with a hydrostatic method. By contrast, we directly perform radiation hydrodynamics simulations with including nonequilibrium chemistry. Simultaneous modeling of dynamical evolution and chemical/thermal structure is essential to accurately model from where and with which speed photoevaporative flows are launched. Furthermore, we calculate dust temperatures with optical and IR radiative transfer, taking account of both of the irradiation component and the diffusion component. There has been no previous study where dust temperatures are determined with self-consistent radiative transfer calculations. In the chapter, we run a set of simulations of a disk with different metallicities and present the resulting photoevaporation rates. Then, the lifetimes are estimated according to the derived photoevaporation rates. We also develop an analytic model which well explains the simulation results.

In Chapter 3, we additionally implement X-ray heating and ionization into the simulations pre-

sented in Chapter 2. As mentioned above, it has been under debate whether or not X-ray heating is significant to drive photoevaporation; several previous studies have proposed it as an important heating source to excite photoevaporation (Ercolano *et al.* 2008, 2009, Owen *et al.* 2010, 2011a, 2012), while other studies have concluded it to be minor as a photoevaporation driver (Alexander *et al.* 2004, Gorti *et al.* 2009). However, all of these studies adopt a hydrostatic method to estimate photoevaporation rates, but hydrodynamics simulations are necessary to determine the launch velocity and the base density directly. Wang and Goodman (2017) perform hydrodynamics simulations with self-consistent thermochemistry, including both UV and X-ray effects. X-ray is concluded to be minor to drive the winds. However, X-ray is assumed to have single photon energy of 1 keV to simplify the radiative transfer in the simulations. Since X-ray heating and ionization rates depend on the photon energy, it is essential to take account of X-ray energy distribution in a thermochemistry model to rightly discuss the effectiveness of X-ray on photoevaporation. In the chapter, we explore the significance of X-ray heating and ionization for driving photoevaporation with considering X-ray energy distribution, and, particularly, we investigate how the X-ray effects change the metallicity dependence of the UV photoevaporation rates presented in Chapter 2.

In Chapter 4, we extend our scope to the early stage of the stellar system formation; we investigate the evolution of low-mass molecular cloud cores in GMCs. Such cores are exposed to the intense UV radiation field by nearby massive OB stars formed in the associated GMC, as observed in the Orion star-forming regions. The radiation field drives photoevaporation from the surface of the cores and can dissipate the molecular cloud cores. At the same time, the radiation can drive shocks in the interior of the cores, compress them, and potentially trigger star formation inside the cores. We follow these hydrodynamical processes in the chapter. We adopt almost the same computational methods as those used for PPD photoevaporation in Chapter 2 and Chapter 3, and perform sets of 3D radiation hydrodynamics simulations of cloud photoevaporation caused by UV irradiation from external massive stars. We aim to derive the cloud lifetimes and their metallicity dependence. The results can give a number of implications to star formation efficiency and CMFs/IMFs in galaxies. Especially, we aim to derive the lifetimes of the cores with low metallicities that are applicable to star-forming regions in high-redshift galaxies.

In Chapter 5, we give the summary and concluding remarks of the thesis.

Chapter 2

Photoevaporation of Protoplanetary Disks Due to Ultraviolet Irradiation by the Central Star: Metallicity Dependence

2.1 Overview

Protoplanetary disks are considered to have lifetimes of several million years in the solar neighborhood, but recent observations propose that the disk lifetimes are shorter in low-metallicity environments. We perform a suite of radiation hydrodynamics simulations of photoevaporation of protoplanetary disks with a wide range of $10^{-4} Z_{\odot} \leq Z \leq 10 Z_{\odot}$ to examine their long-term evolution of ~ 10000 years, and the metallicity dependence of photoevaporation rates. Our simulations self-consistently follow hydrodynamics, extreme- and far-ultraviolet radiative (FUV) transfer, and nonequilibrium chemistry. We solve the radiative transfer for the stellar irradiation and dust (re-)emission to determine dust temperatures. We find that since a large amount of dust can efficiently reduce FUV photons reaching and heating the dense regions of the disk, higher metallicity results in a lower photoevaporation rate in the range of $10^{-1} Z_{\odot} \lesssim Z \lesssim 10 Z_{\odot}$. In $10^{-2} Z_{\odot} \lesssim Z \lesssim 10^{-1} Z_{\odot}$, dust-gas collisional cooling is efficient compared to FUV heating. This suppresses photoevaporation from the neutral regions, and the resulting photoevaporation rates strongly decrease with decreasing metallicity. EUV heating associated with H I photoionization dominantly heats disk gas at $10^{-4} Z_{\odot} \leq Z \lesssim 10^{-2} Z_{\odot}$, and thus photoevaporation rates are largely independent of metallicity. The derived lifetimes are consistent with observations, implying FUV photoevaporation can be a cause to produce a metallicity-dependent trend in disk lifetimes. We develop a semi-analytic model that accurately describes the profile of photoevaporative flows and the metallicity dependence of the mass-loss rates.

The contents in this chapter are based on the published paper, Nakatani et al., the *Astrophysical Journal*, Volume 857, p.57–78, 2018 (Nakatani *et al.* 2018a).

2.2 Methods

We implement radiative transfer and multispecies chemistry into the publicly available code PLUTO (version 4.1; Mignone *et al.* 2007) so that we can calculate hydrodynamics of photoevaporating PPDs with various metallicities. We summarize the implemented processes with reviewing basic physics relevant to the study in this section.

2.2.1 Numerical Setup

We perform radiation hydrodynamics simulations of photoevaporating PPDs illuminated by the UV radiation from the central star. Disk metallicity is varied in a broad range of $10^{-4} Z_{\odot} \leq Z \leq 10 Z_{\odot}$. The central star is a young PMS star with the mass of $M_{*} = 0.5 M_{\odot}$, FUV luminosity $L_{\text{FUV}} = 3 \times 10^{32} \text{ erg s}^{-1}$, and EUV emission rate $\Phi_{\text{EUV}} = 6 \times 10^{41} \text{ s}^{-1}$. The UV luminosities may be also dependent on metallicity, but we do not take into account such variation. Our focus is on the effects of heavy elements and dust amount on photoevaporation and PPD lifetimes. Other stellar parameters are fixed throughout our simulations for the same reason. It has been proposed that X-rays can also drive strong photoevaporation (Alexander *et al.* 2004, Ercolano *et al.* 2008, 2009, Gorti and Hollenbach 2008, 2009, Owen *et al.* 2010, 2012), but X-ray effects are not included in this chapter. Here we discuss the metallicity dependence of photoevaporation caused by UV irradiation from the central star. X-ray photoevaporation is studied in Chapter 3.

We construct a multispecies chemistry model based on Omukai (2000) and Omukai *et al.* (2005, 2010). The chemical network is the same at all metallicities, but we change the amounts of the heavy elements and dust grains contained in the disk medium. The gas is composed of seven chemical species: H I, H II, H₂, O I, C II, CO, and electron. Henceforth, we term H I, H II, and H₂ “H-bearing species”; and CO, O I, and C II “metal species”. We give the amounts of dust grains and the gas-phase heavy elements in proportion to the relative metallicity Z/Z_{\odot} . The ISM values are adopted for the elemental abundances of the gas-phase carbon and oxygen, and for the dust-to-gas mass ratio $\mathcal{D}\mathcal{G}$ at $Z = 1 Z_{\odot}$:

$$y_{\text{C}} = 0.927 \times 10^{-4} Z/Z_{\odot}, \quad (2.1)$$

$$y_{\text{O}} = 3.568 \times 10^{-4} Z/Z_{\odot}, \quad (2.2)$$

$$\mathcal{D}\mathcal{G} = 0.01 \times Z/Z_{\odot}, \quad (2.3)$$

respectively (Pollack *et al.* 1994, Omukai 2000). ^{*1} We list the input parameters in Table 2.1.

Table 2.1 Properties of the Model

<i>Stellar parameters</i>	
Mass (M_{*})	$0.5 M_{\odot}$
Radius (R_{*})	$2 R_{\odot}$
FUV luminosity (L_{FUV})	$3 \times 10^{32} \text{ erg s}^{-1}$
EUV emission rate (Φ_{EUV})	$6 \times 10^{41} \text{ s}^{-1}$
<i>Gas/dust properties</i>	
Gas species	H I, H II, H ₂ , CO, O I, C II, e ⁻
Carbon abundance (y_{C})	$0.927 \times 10^{-4} \times Z/Z_{\odot}$
Oxygen abundance (y_{O})	$3.568 \times 10^{-4} \times Z/Z_{\odot}$
Dust-to-gas mass ratio ($\mathcal{D}\mathcal{G}$)	$0.01 \times Z/Z_{\odot}$

^{*1} The abundance of species i is defined as the ratio of its number density to hydrogen nuclei number density: $y_i \equiv n_i/n_{\text{H}}$. We use chemical symbol notation for elemental abundances and Romanian notation for chemical abundances. For instance, y_{C} and $y_{\text{C I}}$ indicate the elemental abundance of carbon and the chemical abundance of neutral carbon atoms, respectively. This is also the case for density and column density.

2.2.2 Basic Formulae

The simulations are performed on 2D spherical polar coordinates (r, θ) . We follow the time evolution of the gas density ρ ; all the three components of velocity $\mathbf{v} = (v_r, v_\theta, v_\phi)$; the gas internal energy, including relevant heating and cooling; and the chemical abundances \mathbf{y} , including advection and chemical reactions. The governing equations are

$$\frac{\partial \rho}{\partial t} + \nabla \cdot \rho \mathbf{v} = 0, \quad (2.4)$$

$$\frac{\partial \rho v_r}{\partial t} + \nabla \cdot (\rho v_r \mathbf{v}) = -\frac{\partial P}{\partial r} - \rho \frac{GM_*}{r^2} + \rho \frac{v_\theta^2 + v_\phi^2}{r}, \quad (2.5)$$

$$\frac{\partial \rho v_\theta}{\partial t} + \nabla \cdot (\rho v_\theta \mathbf{v}) = -\frac{1}{r} \frac{\partial P}{\partial \theta} - \rho \frac{v_\theta v_r}{r} + \frac{\rho v_\phi^2}{r} \cot \theta, \quad (2.6)$$

$$\frac{\partial \rho v_\phi}{\partial t} + \nabla^l \cdot (\rho v_\phi \mathbf{v}) = 0, \quad (2.7)$$

$$\frac{\partial E}{\partial t} + \nabla \cdot (H \mathbf{v}) = -\rho v_r \frac{GM_*}{r^2} + \rho (\Gamma - \Lambda), \quad (2.8)$$

$$\text{and } \frac{\partial n_{\text{H}} y_i}{\partial t} + \nabla \cdot (n_{\text{H}} y_i \mathbf{v}) = n_{\text{H}} R_i. \quad (2.9)$$

Here P denotes the gas pressure; G is the gravitational constant; E and H are the total energy and enthalpy per unit volume, respectively; Γ is a heating rate per unit mass (specific heating rate), and Λ is a cooling rate per unit mass (specific cooling rate); the chemical abundances are denoted by y_{HI} , y_{HII} , y_{H_2} , y_{CO} , y_{OI} , y_{CII} , and y_e for each of the species; and R_i is the total reaction rate for the corresponding chemical species i . The incorporated chemical reactions are described in Table 2.2. The self-gravity of the disk is not considered because it is generally weaker than the central star's gravity in a cool disk with the typical mass of $M_{\text{disk}}/M_* \sim 10^{-2}$.

Table 2.2: The List of the Chemical Reactions Incorporated in Our Simulations

Label	Reaction	Rate Coefficient	Reference
k1	$\text{H} + \text{e} \longrightarrow \text{H}^+ + 2\text{e}$	$\exp[-32.71396786$ $+13.536556 \ln T_{\text{eV}}$ $-5.73932875 (\ln T_{\text{eV}})^2$ $+1.56315498 (\ln T_{\text{eV}})^3$ $-0.2877056 (\ln T_{\text{eV}})^4$ $+3.48255977 \times 10^{-2} (\ln T_{\text{eV}})^5$ $-2.63197617 \times 10^{-3} (\ln T_{\text{eV}})^6$ $+1.11954395 \times 10^{-4} (\ln T_{\text{eV}})^7$ $-2.03914985 \times 10^{-6} (\ln T_{\text{eV}})^8]$	1
k2	$\text{H}^+ + \text{e} \longrightarrow \text{H} + \gamma$	$\exp[-28.6130338$ $-0.72411256 \ln T_{\text{eV}}$	1

Continued

Table 2.2 Continued

Label	Reaction	Rate Coefficient	Reference
		$-2.02604473 \times 10^{-2} (\ln T_{\text{eV}})^2$	
		$-2.38086188 \times 10^{-3} (\ln T_{\text{eV}})^3$	
		$-3.21260521 \times 10^{-4} (\ln T_{\text{eV}})^4$	
		$-1.42150291 \times 10^{-5} (\ln T_{\text{eV}})^5$	
		$+4.98910892 \times 10^{-6} (\ln T_{\text{eV}})^6$	
		$+5.75561414 \times 10^{-7} (\ln T_{\text{eV}})^7$	
		$-1.85676704 \times 10^{-8} (\ln T_{\text{eV}})^8$	
		$-3.07113524 \times 10^{-9} (\ln T_{\text{eV}})^9]$	
k12	$\text{H}_2 + \text{e} \longrightarrow 2\text{H} + \text{e}$	$4.4 \times 10^{-10} T^{0.35} \exp(-1.02 \times 10^5/T)$	1
k13	$\text{H}_2 + \text{H} \longrightarrow 3\text{H}$	$k_{\text{H}}(k_{\text{L}}/k_{\text{H}})^a,$ $k_{\text{L}} \equiv 1.12 \times 10^{-10} \exp(-7.035 \times 10^4/T),$ $k_{\text{H}} \equiv 6.5 \times 10^{-7}/\sqrt{T} \exp(-5.2 \times 10^4/T)(1 - \exp(-6000/T))$ $\log n_{\text{cr}} \equiv 4 - 0.416 \log(T/1.0 \times 10^4) - 0.327(\log(T/1.0 \times 10^4))^2,$ $a \equiv (1 + n_{\text{H}}/n_{\text{cr}})^{-1}$	1
k19	$3\text{H} \longrightarrow \text{H}_2 + \text{H}$	$5.5 \times 10^{-29}/T$	1
k20	$2\text{H} + \text{H}_2 \longrightarrow 2\text{H}_2$	$R_{\text{k19}}/8$	1
k21	$2\text{H}_2 \longrightarrow 2\text{H} + \text{H}_2$	$k_{\text{H}}(k_{\text{L}}/k_{\text{H}})^a,$ $k_{\text{L}} \equiv 1.18 \times 10^{-10} \exp(-6.95 \times 10^4/T),$ $k_{\text{H}} \equiv 8.125 \times 10^{-8}/\sqrt{T} \exp(-5.2 \times 10^4/T)(1 - \exp(-6000/T)),$ $\log n_{\text{cr}} \equiv 4.845 - 1.3 \log(T/1.0 \times 10^4) + 1.62(\log(T/1.0 \times 10^4))^2,$ $a \equiv (1 + n_{\text{H}}/n_{\text{cr}})^{-1}$	1
k22	$2\text{H} \longrightarrow \text{H}^+ + \text{e} + \text{H}$	$1.7 \times 10^{-4} R_{\text{k1}}$	1
k23	$2\text{H} \xrightarrow{\text{dust}} \text{H}_2$	$6.0 \times 10^{-17} \sqrt{T/300} f_a (Z/Z_{\odot})$ $\times [1.0 + 4.0 \times 10^{-2} \sqrt{T + T_{\text{dust}}} + 2.0 \times 10^{-3} T + 8.0 \times 10^{-6} T^2]^{-1},$ $f_a \equiv [1.0 + \exp(7.5 \times 10^2(1/75 - T_{\text{dust}}^{-1}))]^{-1}$	1
p1	$\text{H} + \gamma \longrightarrow \text{H}^+ + \text{e}$	R_{ionize} (cf. Eq.(2.21))	-
p2	$\text{H}_2 + \gamma \longrightarrow 2\text{H}$	$R_{\text{H}_2, \text{diss}}$ (cf. Appendix 2.2.4)	2
p3	$\text{CO} + \gamma \longrightarrow \text{C}^+ + \text{O}$	$R_{\text{CO}, \text{diss}}$ (cf. Appendix 2.2.4)	3
k24	$\text{C}^+ + \text{O} \longrightarrow \text{CO}$	$R_{\text{CO}, \text{form}}$ (cf. Appendix 2.2.4)	4

Note: Here T_{eV} is the gas temperature in eV, T is the gas temperature in K, and T_{dust} is the dust temperature in K; **References:** (1) Omukai (2000), (2) Draine and Bertoldi (1996), (3) Lee *et al.* (1996), (4) Nelson and Langer (1997)

The azimuthal component of the hydrodynamics equations is discretized in an angular momentum conserving form. This apparently distinguishes the divergence operator of the component from those of other components, as Eq.(2.7). Let \mathbf{F} an arbitrary vector. The divergence operators are calculated as

$$\nabla \cdot \mathbf{F} = \frac{1}{r^2} \frac{\partial}{\partial r} r^2 F_r + \frac{1}{r \sin \theta} \frac{\partial}{\partial \theta} \sin \theta F_\theta, \quad (2.10)$$

$$\nabla^l \cdot \mathbf{F} = \frac{1}{r^3} \frac{\partial}{\partial r} r^3 F_r + \frac{1}{r \sin^2 \theta} \frac{\partial}{\partial \theta} \sin^2 \theta F_\theta. \quad (2.11)$$

The angular momentum transfer due to the viscous stress is not included. The viscous timescale is much longer than the dynamical timescale within which we solve the time evolution.

The governing equations are closed by giving the equation of state (EOS). We use the EOS for an ideal gas

$$e = \frac{kT}{\mu m_u (\gamma - 1)}, \quad (2.12)$$

$$P = \frac{\rho kT}{\mu m_u}, \quad (2.13)$$

where e is the specific energy of the gas, γ is the adiabatic index, k is the Boltzmann constant, T is the gas temperature, μ is the mean molecular weight, and m_u is the atomic mass unit. The adiabatic index is given by

$$\gamma = 1 + \frac{y_{\text{HI}} + y_{\text{HII}} + y_{\text{H}_2} + y_e}{\frac{3}{2}y_{\text{HI}} + \frac{3}{2}y_{\text{HII}} + \frac{5}{2}y_{\text{H}_2} + \frac{3}{2}y_e}. \quad (2.14)$$

The contribution from the heavy elements can be neglected in Eq.(2.14) because of their negligible abundances. The EOS provides the explicit form of E and H

$$E = \frac{1}{2} \rho \mathbf{v}^2 + \rho e = \frac{1}{2} \rho \mathbf{v}^2 + \frac{P}{\gamma - 1}, \quad (2.15)$$

$$H = E + P = \frac{1}{2} \rho \mathbf{v}^2 + \frac{\gamma P}{\gamma - 1}. \quad (2.16)$$

The computational domain spreads on $r = [1, 400]$ au and $\theta = [0, \pi/2]$ rad. The outer radial extent is set to be larger compared to typical values in previous studies so that we can avoid the spurious reflection of outflows at the boundary (see the discussion in Section 2.4.4). In practice, the disk seamlessly exists in the sink region of our computational domain ($r < 1$ au). The disk medium there absorbs stellar photons to reduce those reaching the $r > 1$ au region. This effect is approximately incorporated in our simulations. We assume that the density is radially uniform in the sink and is equal to the value at the innermost cell. The column densities of the sink is given as $N_i^{\text{sink}} = s n_{i,m}$, where s is the sink size (1 au) and $n_{i,m}$ is the innermost density of the chemical species i . We reduce the stellar fluxes incident on the computational domain by the approximate sink column densities. The disk is axisymmetry around the rotational axis ($\theta = 0$) and is symmetry with respect to the midplane ($\theta = \pi/2$). The computational domain is logarithmically spaced with 128 cells in the radial direction, and is uniformly spaced with 80 cells for each of $\theta = 0-1$ rad and $\theta = 1-\pi/2$ regions in the meridional direction. We use the high-spatial resolution for the $1 \leq \theta \leq \pi/2$ to resolve the small scale-height of PPDs and the launch points of photoevaporative flows (the so-called base).

The effective gravitational radius is $\simeq 1.4(M_*/M_\odot)$ au for an ionized gas with a typical tempera-

ture of $T = 10^4$ K (Liffman 2003). It is smaller than the sink size of our computational domain for a $0.5 M_\odot$ star. Thus, we could miss the mass loss due to photoevaporative flows in the sink region, if excited. However, the base density profile of the ionized flows is anticipated to scale with $\propto R^{-1.5}$ (Tanaka *et al.* 2013), where R is the distance in the cylindrical polar coordinates. (We will show below that the profile actually has a similar scaling.) The outer region has a more contribution than the inner region with this scaling. The contribution from the sink region is a tiny fraction of the total photoevaporation rates. This is confirmed by additional test simulations where the inner boundaries are set to $r_{\text{inner}} = 0.1, 0.35, 0.5$ au; the simulation results have shown that the mass loss from the inner region ($R \leq 10$ au) is responsible for only about a few percents of the total. This justifies using the inner boundary slightly larger than the effective gravitational radius.

Note that the inner (< 1 au) disk could have an important effect on shielding the direct EUV photons. If the inner disk in the sink region were able to completely attenuate the direct stellar photons, only the diffuse photons would reach the outer disk surface in the computational domain. We have found, in the simulations with the smaller inner boundaries, that the direct EUV actually reaches the > 1 au region, and heats/ionizes the gas there as in the simulations with the fiducial value of the inner boundary. The resulting photoevaporation rates thus hardly vary with the sink size, at least for $0.1 \text{ au} \leq r_{\text{inner}} \leq 1 \text{ au}$.

2.2.3 Heating and Cooling

For photoheating sources, we implement photoionization heating associate with EUV absorption by atomic hydrogen, and we also implement grain photoelectric heating followed by FUV absorption of dust grains.

The absorption of the direct EUV from the central star is considered. The radiative transfer equation for the absorption is

$$\frac{1}{r^2} \frac{\partial}{\partial r} (r^2 F_\nu) = -n_{\text{HI}} \sigma_\nu F_\nu, \quad (2.17)$$

where ν is an EUV photon frequency, F_ν is the specific number flux of the direct EUV field, n_{HI} is the atomic hydrogen density, and σ_ν is the absorption cross section of H I. We adopt the approximated absorption cross-section

$$\sigma_\nu = 6.3 \times 10^{-18} \left(\frac{h\nu}{h\nu_1} \right)^{-3} \text{ cm}^2, \quad (2.18)$$

(e.g., Osterbrock and Ferland 2006). In Eq.(2.18), ν_1 is the Lyman limit frequency ($h\nu_1 \simeq 13.6 \text{ eV}$; $\lambda_1 \equiv c/\nu_1 \simeq 91.2 \text{ nm}$). The solution of Eq.(2.17) is analytically calculated as

$$F_\nu(r, \theta, t) = \frac{\Phi_{\text{EUV}}}{4\pi r^2} \exp[-\sigma_\nu N_{\text{HI}}], \quad (2.19)$$

where $N_{\text{HI}} = N_{\text{HI}}(r, \theta, t)$ is the column density of atomic hydrogen measured from the stellar surface

$$N_{\text{HI}}(r, \theta, t) \equiv \int dr' n_{\text{HI}}(r', \theta, t). \quad (2.20)$$

Eq.(2.19) provides the photoionization rate and the associated heating rate

$$R_{\text{Ionize}} = y_{\text{HI}} \int_{\nu_1}^{\infty} d\nu \sigma_{\nu} F_{\nu}, \quad (2.21)$$

$$\Gamma_{\text{EUV}} = \frac{n_{\text{HI}}}{\rho} \int_{\nu_1}^{\infty} d\nu \sigma_{\nu} h(\nu - \nu_1) F_{\nu}, \quad (2.22)$$

respectively. We assume a black body spectrum for the SED of the EUV. The effective temperature is set to $T_{\text{eff}} = 10^4 \text{ K}$, which yields the total stellar EUV emission rate of $\Phi_{\text{EUV}} \simeq 1.5 \times 10^{41} (R_*/R_{\odot})^2 \text{ s}^{-1}$. The frequency-integration range is divided into 81 bins.

In our simulations, the photoelectric heating rate is provided by the analytic formula of Bakes and Tielens (1994) (hereafter BT94). The Mathis-Rumpl-Nordsieck (MRN) distribution (Mathis *et al.* 1977) is assumed for the dust model to derive the heating rates. The size distributions of small carbon grains including polycyclic aromatic hydrocarbons (PAHs) follow the MRN distribution in the model. We note that observations suggest significantly lower PAH abundances around T Tauri stars by typically several tens of times than the ISM value (Geers *et al.* 2007, Oliveira *et al.* 2010, Vicente *et al.* 2013), although there are large uncertainties in the estimated values. We investigate the effects of the PAH abundance on disk photoevaporation rates in Section 2.4.3. The photoelectric heating function is

$$\Gamma_{\text{pe}} = 10^{-24} \text{ erg s}^{-1} \epsilon_{\text{pe}} G_{\text{FUV}} \frac{n_{\text{H}}}{\rho} \frac{Z}{Z_{\odot}}, \quad (2.23)$$

$$\epsilon_{\text{pe}} = \left[\frac{4.87 \times 10^{-2}}{1 + 4 \times 10^{-3} \gamma_{\text{pe}}^{0.73}} + \frac{3.65 \times 10^{-2} (T/10^4 \text{ K})^{0.7}}{1 + 2 \times 10^{-4} \gamma_{\text{pe}}} \right], \quad (2.24)$$

where ϵ_{pe} is the photoelectric effect efficiency and γ_{pe} is the ratio of the dust/PAH photoionization rate to the dust/PAH recombination rate. The ratio is provided by $\gamma_{\text{pe}} \equiv G_{\text{FUV}} \sqrt{\tilde{T}} / \tilde{n}_{\text{e}}$, where $\tilde{T} = (T/1 \text{ K})$ and $\tilde{n}_{\text{e}} = (n_{\text{e}}/1 \text{ cm}^{-3})$. The photoelectric effect efficiency measures the ratio of the gas heating rate to FUV absorption rate of the grains. In Eq.(2.23), G_{FUV} is the FUV flux ($6 \text{ eV} < h\nu < 13.6 \text{ eV}$) normalized by the averaged interstellar flux $F_{\text{ISRF}} = 1.6 \times 10^{-3} \text{ erg cm}^{-2} \text{ s}^{-2}$, and is calculated as $G_{\text{FUV}} = L_{\text{FUV}} e^{-1.8A_{\text{V}}} / (4\pi r^2 F_{\text{ISRF}})$. The last factor Z/Z_{\odot} in Eq.(2.23) accounts for the reduction of the grain amount with decreasing metallicity.

For cooling processes, we include radiative recombination cooling of H II (Spitzer 1978), Ly α cooling of H I (Ammos *et al.* 1997), fine-structure line cooling of O I and C II (Hollenbach and McKee 1989, Osterbrock 1989, Santoro and Shull 2006), molecular line cooling of H₂ and CO (Galli and Palla 1998, Omukai *et al.* 2010), and dust-gas collisional cooling (Yorke and Welz 1996). We neglect other collisional excited lines (CELs) which can be coolants in H II regions. Possible influences this simplification could yield are discussed in Section 2.4.6.

Dust-Gas Collisional Cooling

Heat is transferred via collisions between dust and gas. This effect works as cooling or heating for gas. We use the dust-gas collisional cooling function presented in Yorke and Welz (1996)

$$\Lambda_{\text{dust}} = -4\pi a_{\text{dust}}^2 c_s \frac{n_{\text{H}}}{\rho} \left(\frac{\rho_{\text{dust}}}{m_{\text{dust}}} \right) k(T - T_{\text{dust}}) \frac{Z}{Z_{\odot}}, \quad (2.25)$$

where a_{dust} , ρ_{dust} , m_{dust} , and T_{dust} are the mean dust size, dust density, mean dust mass, and dust temperature, respectively. The parameters are set to $a_{\text{dust}} = 5 \times 10^{-6} \text{ cm}$ and $m_{\text{dust}} = 1.3 \times 10^{-15} \text{ g}$ (Yorke and Welz 1996).

Atomic and Molecular Line Cooling

Radiative recombination cooling of H II, Ly α cooling of H I, C II line cooling, O I line cooling, H₂ line cooling, and CO line cooling are implemented as the coolants of gas.

In H II regions, free electrons recombine to various energy levels of hydrogen. The electrons in excited states quickly go down to lower-energy states with emitting lines (radiative recombination). This works as cooling in H II regions. Approximately two-thirds of the electron energy $\sim kT$ is lost through this process (e.g., Spitzer 1978). In the simulations, the radiative recombination cooling rate is given as

$$\Lambda_{\text{rec}} = 0.67 kT R_{\text{k2}} n_e n_{\text{HII}} \rho^{-1}, \quad (2.26)$$

where R_{k2} is the recombination coefficient (the reaction labeled “k2” in Table 2.2).

In a hot environment where atomic hydrogen exists, the energetic collisions excite neutral hydrogen atoms, and then the atoms de-excite through Ly α photon emission. Hereafter, we simply call it Ly α cooling. We adopt the Ly α cooling function of in Anninos *et al.* (1997)

$$\Lambda_{\text{Ly}\alpha} = \xi_{\text{Ly}\alpha} n_e n_{\text{HI}} \rho^{-1}, \quad (2.27)$$

$$\xi_{\text{Ly}\alpha} = \frac{7.5 \times 10^{-19} e^{-118348/T_{\text{K}}}}{1 + \sqrt{T_{\text{K}}/10^5}} \text{ erg cm}^3 \text{ s}^{-1}, \quad (2.28)$$

where T_{K} is gas temperature in the unit of Kelvin.

Table 2.3 Fine-Structure Line Parameters of C II and O I

Species	$j \rightarrow i$	ν_{ij} (Hz)	A_{ij} (s ⁻¹)	γ_{ij}^e (cm ³ s ⁻¹)	γ_{ij}^{HI} (cm ³ s ⁻¹)	Reference
C II	2 \rightarrow 1	1.9×10^{12}	2.4×10^{-6}	$2.8 \times 10^{-7} T_2^{-0.5}$	$8.0 \times 10^{-10} T_2^{0.07}$	1,2
O I	2 \rightarrow 1	4.7×10^{12}	8.9×10^{-5}	1.4×10^{-8}	$9.2 \times 10^{-11} T_2^{0.67}$	1,3
O I	3 \rightarrow 1	–	1.0×10^{-10}	1.4×10^{-8}	$4.3 \times 10^{-11} T_2^{0.80}$	1,3
O I	4 \rightarrow 1	–	6.3×10^{-3}	1.0×10^{-10}	1.0×10^{-12}	1,3
O I	5 \rightarrow 1	–	2.9×10^{-4}	1.0×10^{-10}	1.0×10^{-12}	1,3
O I	3 \rightarrow 2	2.1×10^{12}	1.7×10^{-5}	5.0×10^{-9}	$1.1 \times 10^{-10} T_2^{0.44}$	1,3
O I	4 \rightarrow 2	–	2.1×10^{-3}	1.0×10^{-10}	1.0×10^{-12}	1,3
O I	5 \rightarrow 2	–	7.3×10^{-2}	1.0×10^{-10}	1.0×10^{-12}	1,3
O I	4 \rightarrow 3	4.7×10^{14}	7.3×10^{-7}	1.0×10^{-10}	1.0×10^{-12}	1,3
O I	5 \rightarrow 3	–	0	1.0×10^{-10}	1.0×10^{-12}	1,3
O I	5 \rightarrow 4	5.4×10^{14}	1.2	0	0	1,3

Note: Here, $T_2 \equiv T/100$ K. The labels i, j indicate the energy levels of the species, the corresponding frequency of the energy difference between levels i and j is represented by ν_{ij} , A_{ij} is an Einstein A coefficient, and γ_{ij}^λ is the rate of collisions with a species λ . We define the labels of energy levels as following: ²P_{1/2} of C II (label 1), and ²P_{3/2} of C II (label 2), respectively. ³P₂ of O I (label 1), ³P₁ of O I (label 2), ³P₀ of O I (label 3), ¹D₂ of O I (label 4), and ¹S₀ of O I (label 5), respectively.

Reference: (1) Osterbrock (1989), (2) Santoro and Shull (2006), (3) Hollenbach and McKee (1989).

Spontaneous emission associated with the fine-structure transitions of C II and O I works as coolants. The total cooling rate of each species is given as

$$\Lambda_X = \frac{n_X}{\rho} \sum_j x_j \sum_{j>i} A_{ji} \Delta E_{ji}. \quad (2.29)$$

The label X indicates either of C II or O I, x_j is the level population at j , and ΔE_{ji} ($\Delta E_{ji} = h\nu_{ji}$) is the energy difference between levels i and j . The level populations are determined by solving the simultaneous equations of statistical equilibrium

$$x_i \sum_{j \neq i} c_{ij} = \sum_{i \neq j} x_j c_{ji}, \quad (2.30)$$

where

$$c_{ij} \equiv \begin{cases} A_{ij} + \sum_{\lambda} \gamma_{ij}^{\lambda} n_{\lambda} & \text{for } (i > j) \\ \sum_{\lambda} \gamma_{ij}^{\lambda} n_{\lambda} & \text{for } (i < j) \end{cases}. \quad (2.31)$$

We treat these line emissions as optically thin for simplicity in this study. Therefore, we omit the calculations of an escaping probability, excitation due to absorption of external radiation, or de-excitation due to induced radiation in Eq.(2.31). Regarding O I cooling, we do not explicitly take into account O I photoionization in our chemistry model. Atomic oxygen might be ionized in H II regions, and this would reduce the O I cooling rate. We approximately incorporate this effect into the O I cooling rate by setting O I abundance to $y_{\text{OI}}(1 - y_{\text{HII}})$ in H II regions. This approximation could be justified by the similar ionization potentials of atomic hydrogen and atomic oxygen. It would be necessary to treat O I photoionization in detail to model the chemical structure of oxygen. However, adiabatic cooling is dominant in H II regions, and thus this simplification would have little effect on our results.

Line emission associated with rovibrational transitions of H₂ and CO molecules also work as coolants for gas. The cooling rates can be calculated in the same manner as C II and O I line cooling with Eq.(2.29), but in order to save computational cost, we give the cooling rates by using the analytic formula of Galli and Palla (1998) for H₂ cooling and the tabulated values provided by Omukai *et al.* (2010) for CO cooling.

2.2.4 Chemistry Model

We list the chemical reactions incorporated into our simulations in Table 2.2. The chemical network consists of not only collisional reactions but also photochemical reactions: H I photoionization by EUV, H₂ and CO photodissociation by FUV.

H₂ Photodissociation

FUV photons with $11.2 \text{ eV} \lesssim h\nu \lesssim 13.6 \text{ eV}$ pump up H₂ molecules to an upper electronic bound state by absorption. The excited molecules go back to an excited vibrational state of the ground electronic state accompanied by fluorescence emission, or to a continuum vibrational state of the ground electronic state. The molecules going to the bound vibrational state hold the molecular form, while other molecules going to the continuum vibrational state dissociate to form two hydrogen atoms. These transitions are followed by fluorescence emission. Approximately 10–15% of pumped-up H₂ molecules dissociates through this processes.

Dust grains and H₂ molecules themselves are the main absorbers for the dissociating FUV. The shielding effect by H₂ is called self-shielding. We use the functions described in Draine and Bertoldi (1996) to give H₂ photodissociation rates in which the self-shielding is taken into account,

$$R_{\text{H}_2, \text{diss}} = f_{\text{shield}}(N_{\text{H}_2}) e^{-\tau_{\text{d}, 1000}} I_{\text{diss}} n_{\text{H}_2}. \quad (2.32)$$

In the equation, $\tau_{d,1000}$ is optical depth of dust at the wavelength of 1000 \AA , and $I_{\text{diss}} \simeq 4 \times 10^{-11} G_* \text{ s}^{-1}$, where G_* is the unattenuated FUV flux $G_* = L_{\text{FUV}}/(4\pi r^2 F_{\text{ISRF}})$, is the unshielded photodissociation rate. The self-shielding function f_{shield} is

$$f_{\text{shield}} = \begin{cases} 1 & \text{for } N_{\text{H}_2} \leq N_0 \\ \left(\frac{N_{\text{H}_2}}{N_0}\right)^{-0.75} & \text{for } N_{\text{H}_2} \geq N_0 \end{cases}, \quad (2.33)$$

where $N_0 \equiv 10^{14} \text{ cm}^{-2}$.

CO Photodissociation

FUV photodissociates CO molecules with similar processes to H_2 photodissociation, and it is also a line process. FUV is attenuated by dust absorption and the self-shielding effect of CO once the CO column density gets high. In addition, H_2 molecules can protect CO from photodissociation because of line overlap. Note that since H_2 is more abundant than CO, this effect of line overlap can significantly contribute to shielding.

We use a function provided by Lee *et al.* (1996) which gives CO photodissociation rate by taking account of the shielding effects

$$R_{\text{CO,diss}} = G_* p_{\text{diss}} n_{\text{CO}} \Theta_1(N_{\text{CO}}) \Theta_2(N_{\text{H}_2}) \Theta_3(A_V), \quad (2.34)$$

where $p_{\text{diss}} = 1.03 \times 10^{-10} \text{ s}^{-1}$ is the unshielded CO photodissociation rate. The factors Θ_1 , Θ_2 , and Θ_3 account for the effects of the self-shielding, the H_2 shielding, and the dust shielding, respectively. The values of these shielding functions are tabulated in Lee *et al.* (1996).

Carbon Chemistry

Following Richling and Yorke (2000), we assume that carbon atoms produced by CO photodissociation are rapidly ionized by FUV photons. This assumption is based on the fact that the dissociation energy of CO molecules is similar to the ionization energy of carbon atoms. Thus, in our simulations, the CO photodissociation front is identical to the ionization front of atomic carbon.

For the reverse reaction of CO photodissociation and subsequent photoionization, we include a CO-production reaction modeled by Nelson and Langer (1997). In the simplified model, hydrocarbon radicals trigger CO formation with the reaction of $\text{C}^+ + \text{H}_2 \longrightarrow \text{CH}_2^+ + \gamma$ (reaction rate; $k_0 = 5 \times 10^{-16} \text{ cm}^3 \text{ s}^{-1}$). The hydrocarbon ion CH_2^+ is rapidly converted to CH and CH_2 by ion-molecule reactions with H_2 molecules and dissociative recombination with electrons. Then, CO molecules are produced by the reaction between the hydrocarbon radicals and atomic oxygen (reaction rate; $k_1 = 5 \times 10^{-10} \text{ cm}^3 \text{ s}^{-1}$). At the same time, the produced hydrocarbons are photodissociated to become ions (dissociation rate; Γ_{CH_x}). Consequently, the net formation rate of CO molecules per unit volume is

$$R_{\text{CO,form}} = k_0 n_{\text{CII}} n_{\text{H}_2} \frac{k_1 n_{\text{OI}}}{k_1 n_{\text{OI}} + \Gamma_{\text{CH}_x}}, \quad (2.35)$$

(see, e.g., Nomura and Millar (2005), for a detailed derivation). The dissociation rate of hydrocarbons Γ_{CH_x} is set to five times of the CO dissociation rate. These approximations above greatly save computational costs. We have checked the validity of using the simplified chemical network for carbon by postprocess calculations with C I photoionization. The results show that the structure of C I and CO regions is not significantly changed, other than it forms a geometrically thin C I region. The thickness of C I region is less than $\sim 10\%$ of the C II and CO region thicknesses.

2.2.5 Radiative Transfer

Radiative transfer calculations are performed to determine the photochemical reaction rates, photoheating rates, and dust temperatures in a self-consistent manner. We update the column densities at each timestep. Ray-tracing is used for the radiative transfer for UV. The diffuse EUV component is neglected, and the case B recombination is used instead. The diffusion component is expected to be less effective to drive EUV photoevaporation compared to the direct component (Tanaka *et al.* 2013), as discussed in Section 2.3.3. We do not take into account EUV absorption by dust grains. It is not effective to absorb the EUV photons in our computational domain with the adopted EUV luminosity. ^{*2} FUV flux is used in the calculations of photoelectric heating rates, H₂ photodissociation rates, and CO photodissociation rates. The self-shielding effects of H₂ and CO molecules are incorporated as described above. The column densities of these species are also updated at each timestep. A concrete description of radiative transfer for FUV and EUV is given in detail in Section 2.2.3.

Radiative transfer is solved for both of the direct and diffuse components to determine the dust temperatures. A hybrid scheme is adopted; ray tracing is used to calculate the radiative transfer for the direct component (stellar irradiation), while a flux-limited-diffusion (FLD) approximation is used to solve the radiative transfer of the diffusion component coming from thermal (re-)emission by dust. The radiation transport module of Kuiper *et al.* (2010) is used for the radiative transfer calculations. The temperature distribution of dust can be accurately modeled even in an optically-thick region with the hybrid scheme (Kuiper and Klessen 2013). Strictly speaking, the FLD approximation is not valid in optically-thin disk wind regions ($A_V < 1$). However, the stellar irradiation component dominates the local radiation field there. The base region ($A_V \sim 1$) is optically thin to the diffusion component although it partially attenuates the direct component. The dust temperatures in such region are largely set by the direct irradiation as the wind region. We have explicitly checked that including the diffusion component does not change the derived dust temperatures. The difference is only $\sim 2\%$ on average, and at most 6%. Therefore, it is concluded that our radiative transfer calculations can model an accurate temperature distribution of dust grains. We use the opacity table provided by Draine and Lee (1984) for the radiative transfer calculations.

2.2.6 Initial Conditions

In our model, the disk is initially fully molecular, viz. the gas consists of H₂ and CO molecules at $t = 0$.

We set the initial temperatures of dust and gas to $T = T_{\text{dust}} = 100 \text{ K} (R/1 \text{ au})^{-1/2}$ (e.g., Kenyon and Hartmann 1987), except for the $Z = 10^{-4} Z_{\odot}$ case. In the case of $Z = 10^{-4} Z_{\odot}$, we first update the thermochemical structure, fixing the density distribution, for $\sim 1 \text{ Myr}$, and then, we allow the gas to move hydrodynamically. The temperatures of gas and dust do not couple within the timescale of interest, which would be unrealistic, without this procedure.

^{*2} The EUV luminosity yields the maximum density at the ionization front of $n_{\text{H}} \sim 10^6 \text{ cm}^{-3}$ in the innermost region of the computational domain. Atomic hydrogen H I with this density becomes optically thick to EUV within the length of $\sim 0.1 \text{ au}$ at the ionization front. The corresponding H I column density is approximately $N_{\text{HI}} \sim 10^{18} \text{ cm}^{-2}$. Dust becomes effective to absorb EUV photons at much higher column densities ($N_{\text{H}} \sim 10^{21} \text{ cm}^{-2}$). Therefore, the assumption of effectively optically thin dust is valid for $N_{\text{H}} \sim 10^{18} \text{ cm}^{-2}$.

As the initial condition, we give the density distribution of a stratified, hydrostatic disk

$$n_{\text{H}} = n_0 \left(\frac{R}{1 \text{ au}} \right)^{-9/4} \exp \left[-\frac{z^2}{2H^2} \right], \quad (2.36)$$

In the equation, the distance and the height in 2D cylindrical polar coordinates are denoted by R and z , respectively. They are related to r and θ as $(R, z) = (r \sin \theta, r \cos \theta)$. The midplane density at 1 au, n_0 , is set to $n_0 = 10^{14} \text{ cm}^{-3}$ in our model. In Eq.(2.36), the corresponding surface density $\Sigma (\simeq \sqrt{2\pi} h \rho_{\text{m}}; \rho_{\text{m}}$ is the midplane density structure) has the profile of $\Sigma \propto R^{-1}$. The top panel of Figure 2.1 show the initial density distribution.

2.3 Results

Hydrogen atoms absorb EUV photons and eject thermalizing electrons. This works as the dominant photoheating source in H II regions. Dust grains are dominant absorbers for FUV photons. They eject thermalizing electrons by the photoelectric effect. This heating mechanism is referred to grain photoelectric heating, and it dominantly heats the neutral (H I, H₂) regions in PPDs. Hereafter, we simply refer to EUV photoionization heating as EUV heating and FUV photoelectric heating as FUV heating. We observe photoevaporative flows driven by these photoheating in the simulations. The different photoheating sources yield physically different winds. We discuss the physical properties of photoevaporating PPDs with solar metallicity in Section 2.3.1 and with different metallicities in Section 2.3.2. Then, we examine metallicity dependence of the mass-loss rates in Section 2.3.3. In Section 2.3.4, we construct a semi-analytical model to understand the results of our simulations.

2.3.1 Solar-Metallicity Disk Structure

2.3.1.1 Structures of Density, Velocity, and Temperature

The ionized photoevaporative flows are driven by EUV heating, whereas the neutral photoevaporative flows are driven by FUV heating (Figure 2.1). In order to confirm that FUV is actually the cause to excite the neutral flows, we run a simulation in which we first enable FUV heating but is disabled at $t = t_{\text{c}} \equiv 100 \text{ au}/1 \text{ km s}^{-1} \simeq 4.74 \times 10^2 \text{ yr}$. The simulation shows the disappearance of the neutral flows soon after FUV heating is disabled. Thus, FUV has been confirmed to be the driver of the neutral photoevaporative flows in our simulations. Some of the previous studies have predicted the excitation of photoevaporative flows by FUV heating (Gorti and Hollenbach 2009, Owen *et al.* 2012). Our hydrodynamics simulations directly have demonstrated it for the first time. Note that we do not include X-rays, which can also drive neutral flows (Alexander *et al.* 2004, Ercolano *et al.* 2008, 2009, Gorti and Hollenbach 2008, 2009, Owen *et al.* 2010, 2012). X-ray photoevaporation is discussed in Chapter 3.

FUV are able to penetrate the gas columns of $N_{\text{H}} \gtrsim 10^{21} \text{ cm}^{-2}$ for $Z = Z_{\odot}$, whereas EUV is capable of penetrating the H I columns of $N_{\text{HI}} \gtrsim 10^{17} \text{ cm}^{-2}$. This indicates that compared to EUV, FUV generally gets to a denser interior of a PPD and hence drives denser flows. As shown in Figure 2.1, the neutral photoevaporative flows have the density of $n_{\text{H}} \sim 10^5\text{--}10^7 \text{ cm}^{-3}$, which is a few orders of magnitude larger than the density of the EUV-driven ionized flows ($n_{\text{H}} \sim 10^3\text{--}10^4 \text{ cm}^{-3}$).

In the H II region, The dominant sources of heating and cooling are EUV heating and adiabatic cooling associated followed by gas expansion, respectively, in H II regions (the second panel in Figure 2.2). Radiative recombination cooling is weaker there than adiabatic cooling. The crossing time of the ionized gas $t_{\text{II}} \simeq (100 \text{ au}/30 \text{ km s}^{-1}) \sim 16 \text{ yr}$, is shorter than the recombination timescale

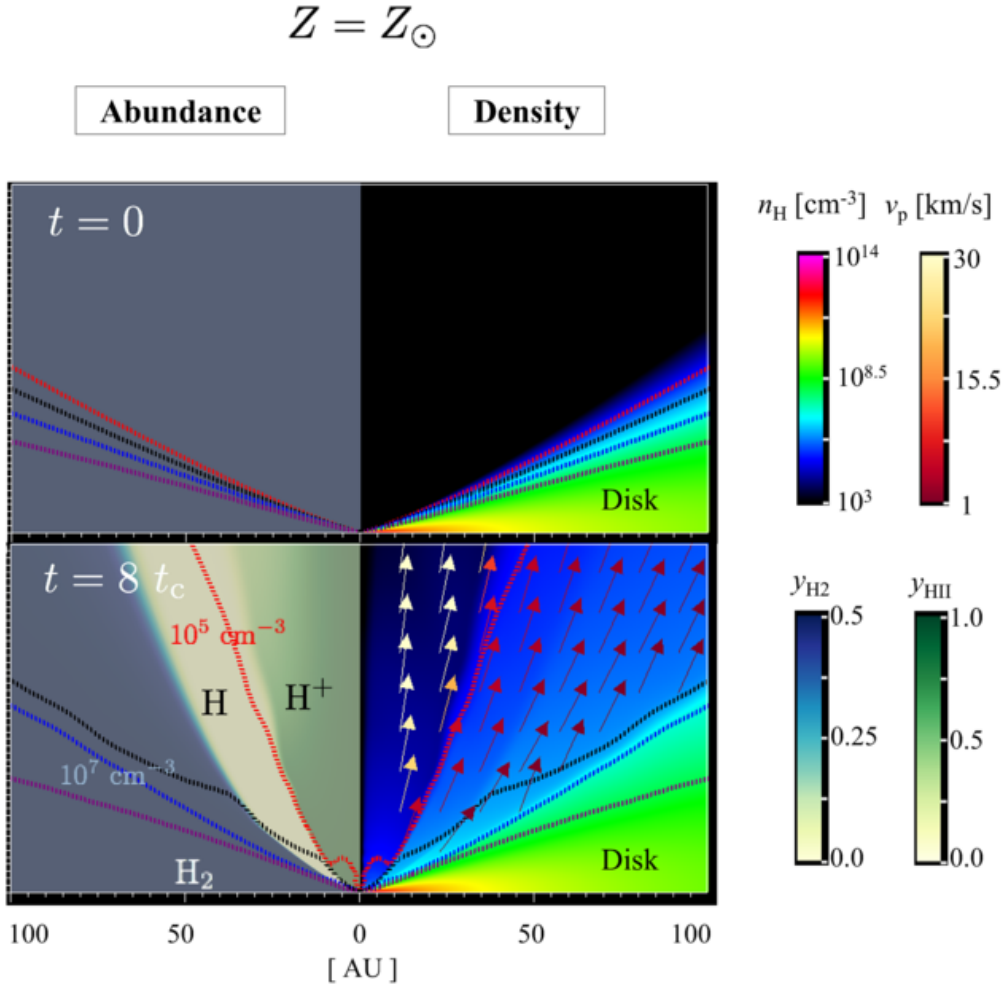


Fig. 2.1 Snapshots of the photoevaporating disk with solar metallicity at $t = 0$ (top) and $t = 8 t_c$ (bottom), where $t_c \equiv 100 \text{ au}/1 \text{ km s}^{-1} \simeq 4.74 \times 10^2 \text{ yr}$ is the typical crossing time of the neutral flow over the computational domain. The left half shows the chemical structure regarding the H-bearing species in each panel. With the color scales shown in the right part, H II-, H I-, and H₂-layers are marked by the different colors of green, white, and blue. The right half shows the density structure and the velocity of the disk. The arrows represent the poloidal velocity $\mathbf{v}_p = (v_r, v_\theta)$ only for $|\mathbf{v}_p| > 0.25 \text{ km s}^{-1}$. The dotted lines are the density contours with $n_{\text{H}} = 10^5 \text{ cm}^{-3}$ (red), 10^6 cm^{-3} (black), 10^7 cm^{-3} (blue), and 10^8 cm^{-3} (purple).

$t_{\text{rec}} \sim 10^2 \text{ yr} (n_{\text{H}}/10^4 \text{ cm}^{-3})^{-1}$. Hydrogen ions get out of the system before they cool gas by radiative recombination.

The ionized flows have a typical temperature of $\sim 10^4 \text{ K}$. It corresponds to the gas sound speed of $c_s \sim 10 \text{ km s}^{-1}$. The photoevaporative flows are thermally driven and are accelerated outward by the pressure gradient. The poloidal velocity $v_p = \sqrt{v_r^2 + v_\theta^2}$ of the ionized flows reaches a few times of the sound speed ($\sim 30 \text{ km s}^{-1}$) as in Figure 2.1. This result is consistent with the previous hydrodynamics simulations (Font *et al.* 2004).

In the neutral region, the dominant heating source is FUV heating, and the dominant coolants are O I cooling, H₂ cooling, and dust-gas collisional cooling. The fine-structure line emission of O I is the most effective cooling source in between the ionization front and photodissociation front of hydrogen. Line emission of H₂ molecules is the dominant source in the H₂ region. Dust-gas

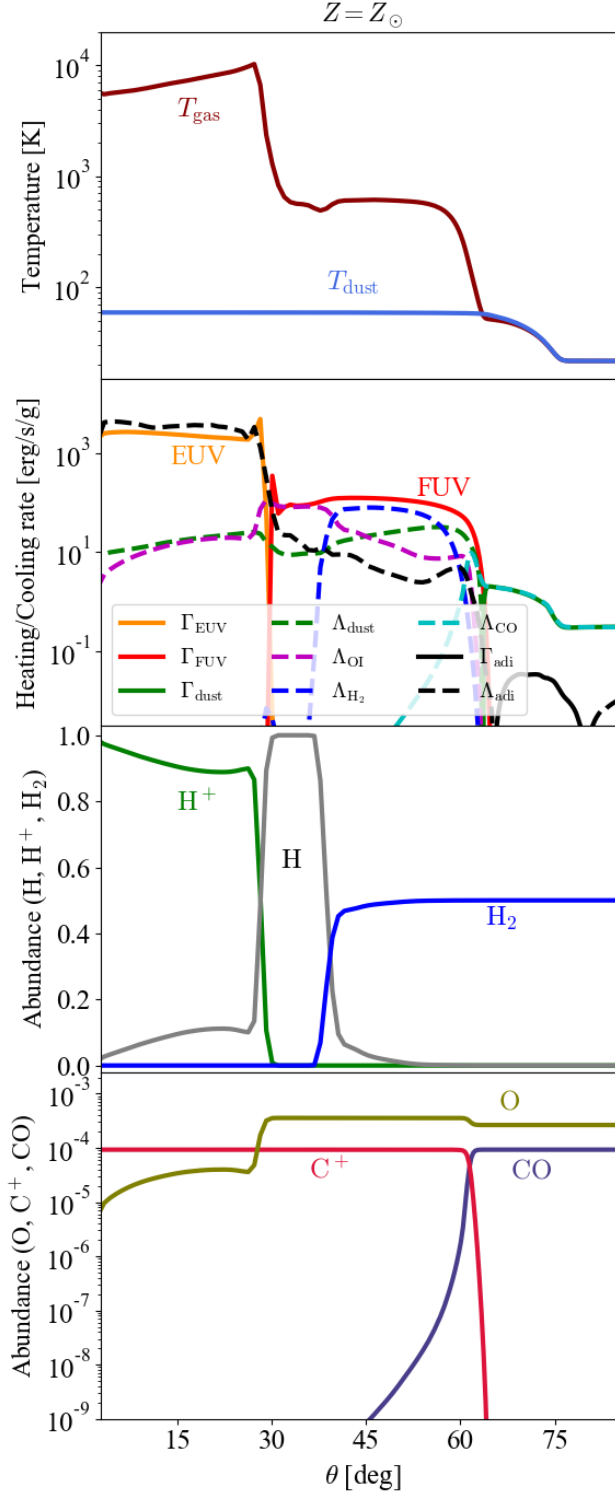


Fig. 2.2 Meridional profiles of physical quantities in the solar-metallicity disk at $r \simeq 80$ au. We show the snapshot at $t = 8 t_c$. (Top panel): Temperatures of the gas T_{gas} and dust T_{dust} . (Second panel): Specific heating and cooling rates of photoionization heating (Γ_{EUV}); photoelectric heating (Γ_{FUV}); dust-gas collisional heating (Γ_{dust}); adiabatic heating ($\Gamma_{\text{adi}} \equiv -P \frac{d}{dt}(1/\rho) = -(P/\rho)\nabla \cdot \mathbf{v}$); dust-gas collisional cooling (Λ_{dust}); line cooling via O I, H₂, and CO (Λ_{OI} , Λ_{H_2} , and Λ_{CO}); and adiabatic cooling ($\Lambda_{\text{adi}} \equiv P \frac{d}{dt}(1/\rho) = (P/\rho)\nabla \cdot \mathbf{v}$). (Third panel): The abundances of the H-bearing species. (Fourth panel): The abundances of the heavy elements.

collisional cooling prevails in much larger-density regions. Similar properties are found in previous studies (e.g., Nomura and Millar 2005, Nomura *et al.* 2007), although H_2 is not included as a coolant. Our simulations directly show that as well as dust-gas collisional cooling and O I cooling, H_2 cooling can be a dominant coolant in the neutral photoevaporative flows.

Adiabatic heating/cooling is subdominant in the neutral photoevaporative flows in contrast to the ionized flows. The resulting temperature is of the order of 10^2 – 10^3 K ($c_s \sim 1$ – 3 km s $^{-1}$). Again, the pressure gradient accelerates the gas outward, and the gas achieves the poloidal velocity of ~ 1 – 5 km s $^{-1}$ while it expands.

2.3.1.2 Hydrogen-bearing Species

We observe the H_2 photoevaporative flows in Figure 2.1. The photoevaporative flows wind H_2 molecules up from the neutral surface of the disk. It replenishes H_2 molecules into the flow region, making the height of the H_2 dissociation front large. Heinzeller *et al.* (2011), where hydrodynamics are not directly incorporated, argued that the H/ H_2 boundary can move upward above a protoplanetary disk owing to the advection associated with winds. Our simulations directly show that the H_2 photodissociation front is indeed raised by the photoevaporation-driven advection from the dense interior of PPDs, where H_2 molecules abundantly exist.

The fact that the H_2 flows remain in the atmosphere implies that dissociating FUV photons are strongly absorbed by dust and/or H_2 molecules themselves at the dissociation front, before reaching in the interior of the molecular flows. For the self-shielding effect of H_2 , we use the function of $f_{\text{shield}} = \min[1, (N_{\text{H}_2}/10^{14} \text{ cm}^{-2})^{-0.75}]$ (Draine and Bertoldi 1996: cf. Eq.(2.33)). The self-shielding effect becomes important for the H_2 column of $N_{\text{H}_2} \gtrsim 10^{14} \text{ cm}^{-2}$. Figure 2.3 shows that the photodissociation front is located at the edge where the shielding factor of the H_2 self-shielding effect (the blue line in the bottom panel of Figure 2.3) sharply declines, i.e. self-shielding effect becomes strong. Hence, the FUV-driven flows continuously replenish H_2 into the flow region, and the H_2 molecules protect themselves from the dissociating photons by the self-shielding effect rather than dust attenuation.

Studies of PPD chemistry have proposed that the self-shielding effect is effective especially in the outer regions (e.g., Voitke *et al.* 2009, Walsh *et al.* 2012). The location of the photodissociation front is much higher in our hydrodynamics simulations than in the previous studies. For instance, the photodissociation front is located at $z \simeq 70$ au with $R = 50$ au in the simulation (see Figure 2.1), while $z \sim 15$ – 20 au at $R \simeq 50$ au in Voitke *et al.* (2009). This shows that the chemical structure of PPDs is strongly influenced by hydrodynamics, and including hydrodynamical effects is important to model the chemical structure of PPDs accurately.

Above the photodissociation front in Figure 2.1, the medium is optically thin to dissociating FUV photons, and the balance between the strong (unshielded) photodissociation and the H_2 formation on dust grains determines the H_2 abundance there. Below the photodissociation front, H_2 molecules are effectively replenished by advection and are formed on grains. In the H I region, the H_2 abundance is set by the balance between photodissociation and H_2 formation catalyzed by dust grains. The H_2 abundance remains largely constant in the region and is typically $y_{\text{H}_2} \lesssim 10^{-5}$.

2.3.1.3 Metal Species

Carbon monoxide molecules are protected against dissociating FUV photons by the self-shielding effect of CO, H_2 shielding, and dust attenuation (see Section 2.2.4 for details). In our simulations, FUV photons dissociate CO molecules to the columns where the dust shielding factor $\Theta_3(A_V)$ declines to be small (Figure 2.4). This indicates the dominance of dust as a shielding source for CO

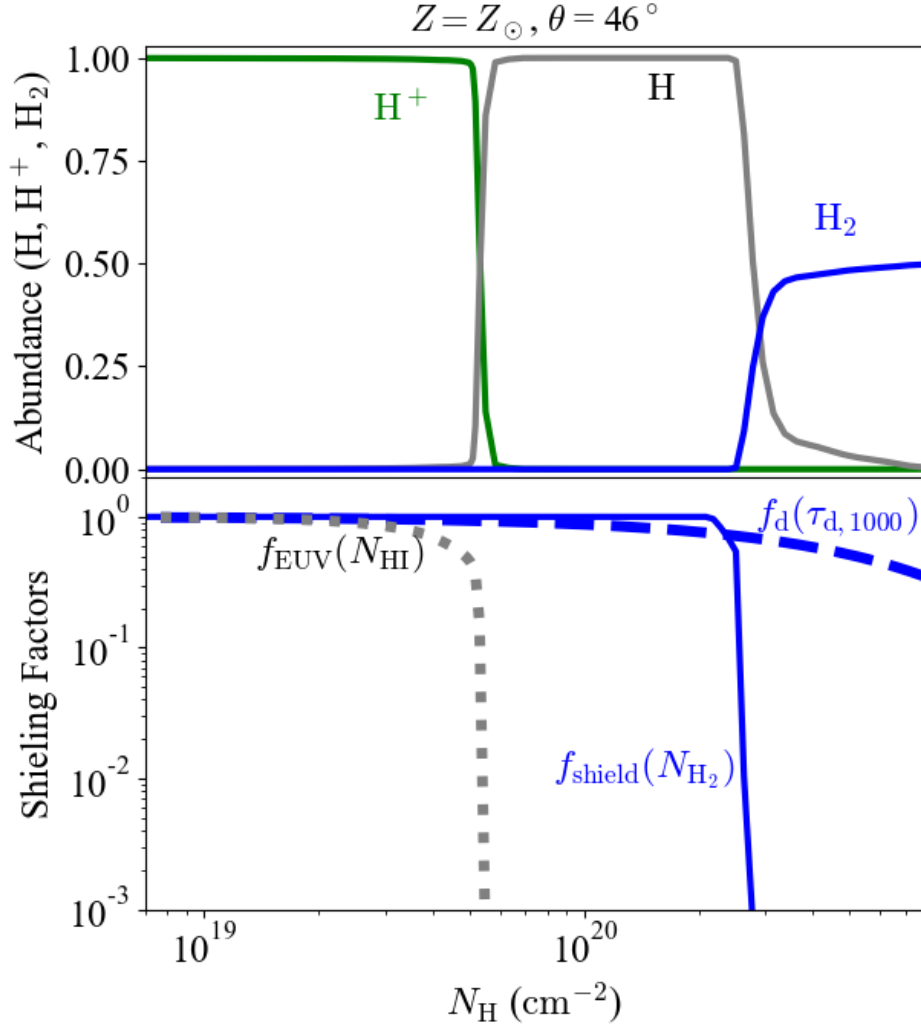


Fig. 2.3 Radial distributions of the H-bearing species (top panel) and the relevant shielding factors (bottom panel) along a ray at $\theta = 46^{\circ}$. The snapshot is taken at $t = 8 t_c$ for the $Z = Z_{\odot}$ disk. The horizontal axis represents the column density of hydrogen nuclei along the line of sight from the central star. In the bottom panel, f_{shield} and $f_{\text{d}}(\tau_{\text{d},1000}) = e^{-\tau_{\text{d},1000}}$ are the H_2 self-shielding and dust attenuation factors against the FUV photons, and $f_{\text{EUV}} = e^{-\tau_{\text{EUV}}}$ is the dust attenuation factor against the EUV photons. The optical depth at the Lyman limit τ_{EUV} is calculated as $\tau_{\text{EUV}} \equiv 6.3 \times 10^{-18} \text{ cm}^2 \times N_{\text{HI}}$.

molecules. Thus, the CO photodissociation front is roughly identical to the edge of the FUV-heated region (see Figure 2.2).

We do not explicitly include the ionization of atomic carbon in our chemistry model but assume that carbon atoms produced by photodissociation are quickly converted to carbon ions by ionizing FUV photons. Thus, the ionization front of carbon is embedded in the higher-density region (the larger θ region in Figure 2.2), compared to the ionization front of hydrogen.

The CO photodissociation front largely corresponds to the edge of the FUV-heated region, and the height of the CO photodissociation front is similar to those in previous hydrostatic studies, in contrast to the case of the H_2 photodissociation front. For instance, the CO photodissociation front

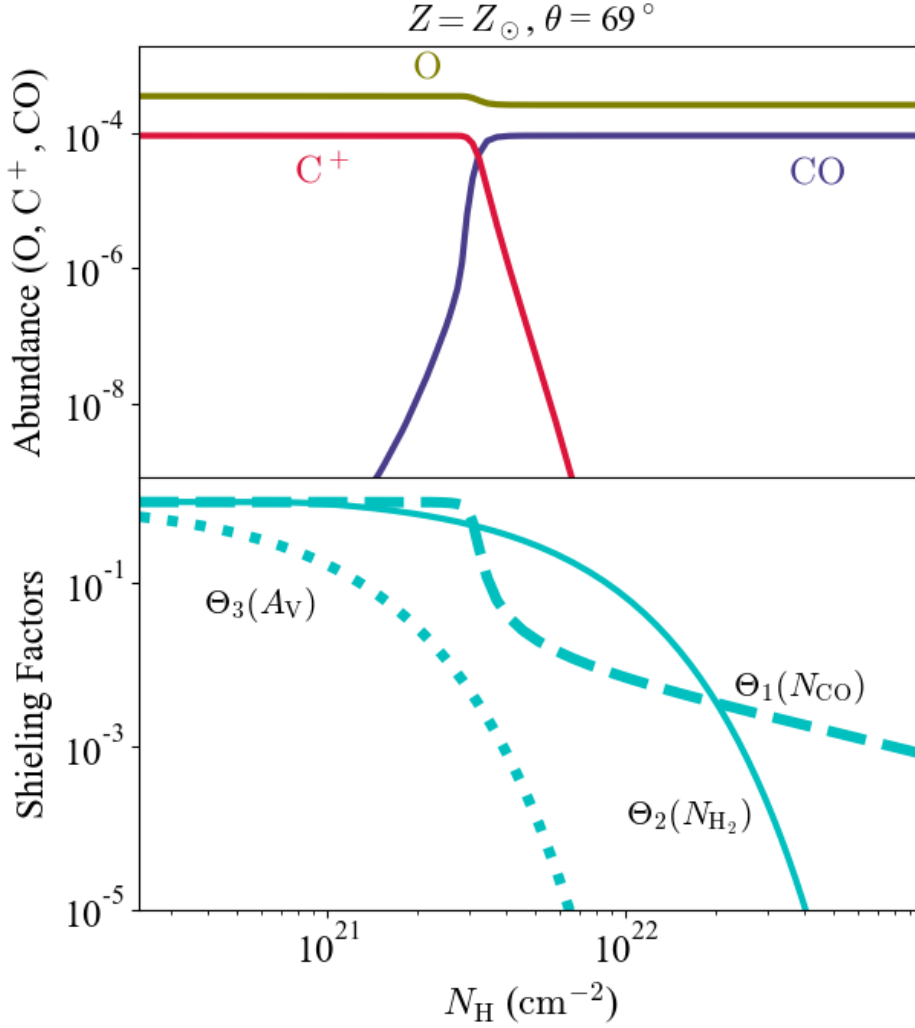


Fig. 2.4 Same as Figure 3 except that it examines heavy elements along a different ray at $\theta = 69^\circ$. In the bottom panel, Θ_1 , Θ_2 , and Θ_3 represent the shielding factors against CO dissociating photons by CO (self-shielding), H_2 , and dust (see also Appendix 2.2.4 for full details for these shielding factors).

is located at $z \simeq 20$ au with $R = 50$ au in our simulation, while $z \sim 15$ au at $R \simeq 50$ au in Woitke *et al.* (2009). Hydrodynamics does not strongly influence the chemical structure of CO molecules as that of H_2 molecules in our model.

2.3.2 Different Metallicities Disks

2.3.2.1 Photoevaporative Flows

the structure of the photoevaporating disks are shown in Figure 2.5 for $Z = 10^{0.5} Z_\odot$, $Z = 10^{-0.5} Z_\odot$, and $Z = 10^{-4} Z_\odot$ (top to bottom). We observe photoevaporative flows in all of the cases. The dense neutral flows are excited only for the higher-metallicity cases of $Z = 10^{0.5} Z_\odot$ and $Z = 10^{-0.5} Z_\odot$. Notably, the density of the neutral flows is higher in the $Z = 10^{-0.5} Z_\odot$ disk than in the $Z = 10^{0.5} Z_\odot$ disk. The typical neutral flow density is $n_{\text{H}} \sim 10^5\text{--}10^6 \text{ cm}^{-3}$ with $Z = 10^{0.5} Z_\odot$, while $n_{\text{H}} \sim$

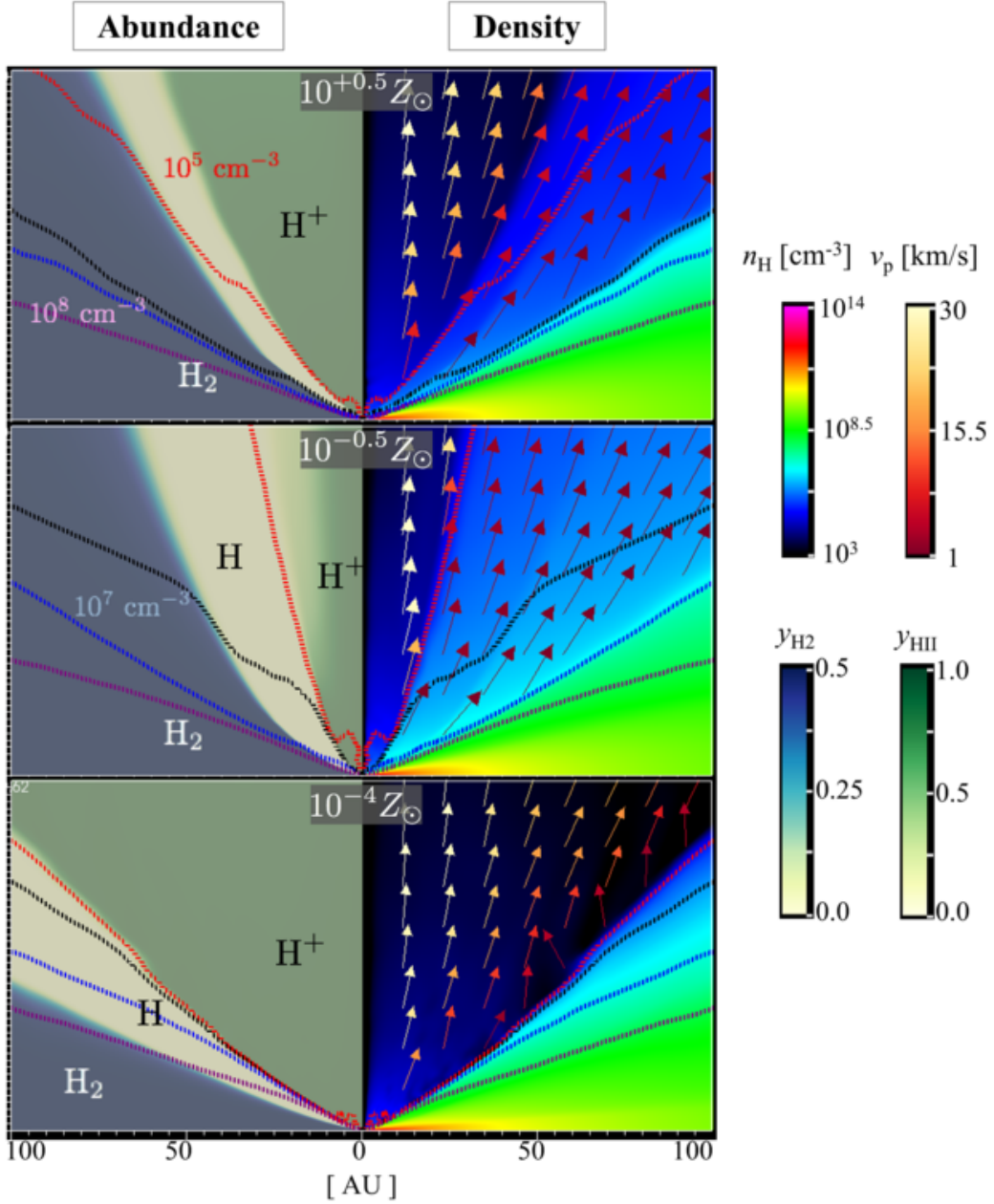


Fig. 2.5 Structure of the photoevaporating disk at $t = 8 t_c$ with different metallicities: $Z = 10^{+0.5} Z_\odot$ (top panel), $Z = 10^{-0.5} Z_\odot$ (middle panel), and $Z = 10^{-4} Z_\odot$ (bottom panel). The disk structure is visualized in the same manner as in Figure 2.1.

10^5 – 10^7 cm^{-3} with $Z = 10^{-0.5} Z_\odot$. It is found that the base density of the neutral photoevaporative flows approximately scales with $\propto Z^{-1}$ in our simulations. The results of the simulations suggest that at least a subsolar metallicity of $Z \gtrsim 10^{-0.5} Z_\odot$ is required to drive the neutral photoevaporative flows by FUV heating, and if excited, the density is higher for lower metallicity disks.

The optical depth for FUV photons is determined by the column density of dust grains along with a ray. The visual extinction A_V effectively provides an optical depth for FUV photons in our simulations. Since the amount of grains proportionally decreases with decreasing metallicity, the visual extinction also decreases as $A_V \propto N_H Z$. The formula describes that a lower-metallicity disk

medium has a smaller optical thickness when it compared at the same column N_{H} . Thus, FUV reaches a denser region of a PPD with low metallicities FUV photons can heat the denser region of the disk with low metallicity, and the higher-density photoevaporative flows excited from the $Z = 10^{-0.5}Z_{\odot}$ disk (Figure 2.5). It is concluded that the decrease of the dust amount is the cause for the higher-density neutral flows in the lower-metallicity disks.

The neutral flows are only weakly driven for even lower-metallicities of $Z \lesssim 10^{-0.5}Z_{\odot}$ and almost cease at the low-metallicity extent $Z = 10^{-4}Z_{\odot}$. FUV heats the gas by ejecting thermalizing electrons from dust grains, and thus the relative amount of dust grains to gas matters to determine the efficiency of FUV heating. We assume the dust-to-gas mass ratio proportional to metallicity. The relative amount decreases with decreasing metallicity, which indicates the decline of the specific FUV heating rate in low-metallicity disks. Moreover, the electron abundance of the neutral region is set by the abundance of ionized carbon under our chemistry model. The neutral region is electron-poor in low-metallicity disks, and it makes the recombination timescale of charged grains longer at a fixed gas density. Dust grains are easy to be positively charged. Thermalizing electrons are hard to be ejected owing to the deepened Coulomb potential of the grains. The photoelectric effect efficiency (cf. Eq.(2.23)) is lowered, and hence the heating efficiency of the photoelectric heating is reduced. This explains the low heating rate in the low-density neutral region close to the ionization front of H II.

Similarly, the specific cooling rates of metal elements of dust decrease with decreasing metallicity. The second row of Figure 2.6 directly shows this behavior; O I cooling, H₂ cooling, and dust-gas collisional cooling rates are the largest in the neutral region for $Z \geq 10^{0.5}Z_{\odot}$, and decrease with decreasing metallicity. Adiabatic cooling is dominant in both the H II and H I regions in the lowest-metallicity disk ($Z = 10^{-4}Z_{\odot}$). In H II regions, EUV heating and adiabatic cooling dominate at any metallicity, and the rates are largely independent of metallicity.

The decrease in the amounts of dust and metal elements reduces the specific heating/cooling rates of FUV heating, O I cooling, and dust-gas collisional cooling. These heating and cooling contribute to determine Figure 2.6 shows a clear decline in the temperatures of the neutral regions, implying that the contribution of coolants is more effective than FUV heating.

In the neutral region dominated by O I cooling and H₂ cooling, the specific FUV heating rate is decreased by the smaller amount of grains and the reduced photoelectric efficiency, as metallicity declines. In contrast, the specific O I cooling rate is decreased owing to the reduced amount of O I, and metallicity does not explicitly affect the H₂ cooling rate. Thus, FUV heating is decreased more efficiently as metallicity lowers, compared with these coolants. In the high-density regions dominated by dust-gas collisional cooling, FUV heating and dust-gas collisional cooling set the temperatures. Since the hydrogen nuclei density and the electron abundance approximately scale with $\sim Z^{-1}$ and Z , respectively, in this region, the photoelectric efficiency hardly varies according to metallicity. Hence, the specific FUV heating rate is almost purely proportional to the amount of grains, i.e. metallicity. By contrast, the specific dust-gas collisional cooling rate is proportional to both Z and n_{H} , and is also dependent on dust temperature. Dust temperatures are set by the balance between the absorption of irradiating photons and (re-)emission by dust grains. Both the absorption and (re-)emission are proportional to the opacities, and the opacities scale with Z . Thus, the distribution of dust temperatures are similar at any metallicity, other than the optically-thick regions are embedded in high-gas-density regions for lower-metallicity disks. Regarding the base gas density, it is inversely proportional to metallicity, so that the specific rate of dust-gas collisional cooling is almost independent of metallicity in the region. The decrease of the dust-gas collisional cooling rate is slower than that of the FUV heating rate, and thus the cooling becomes

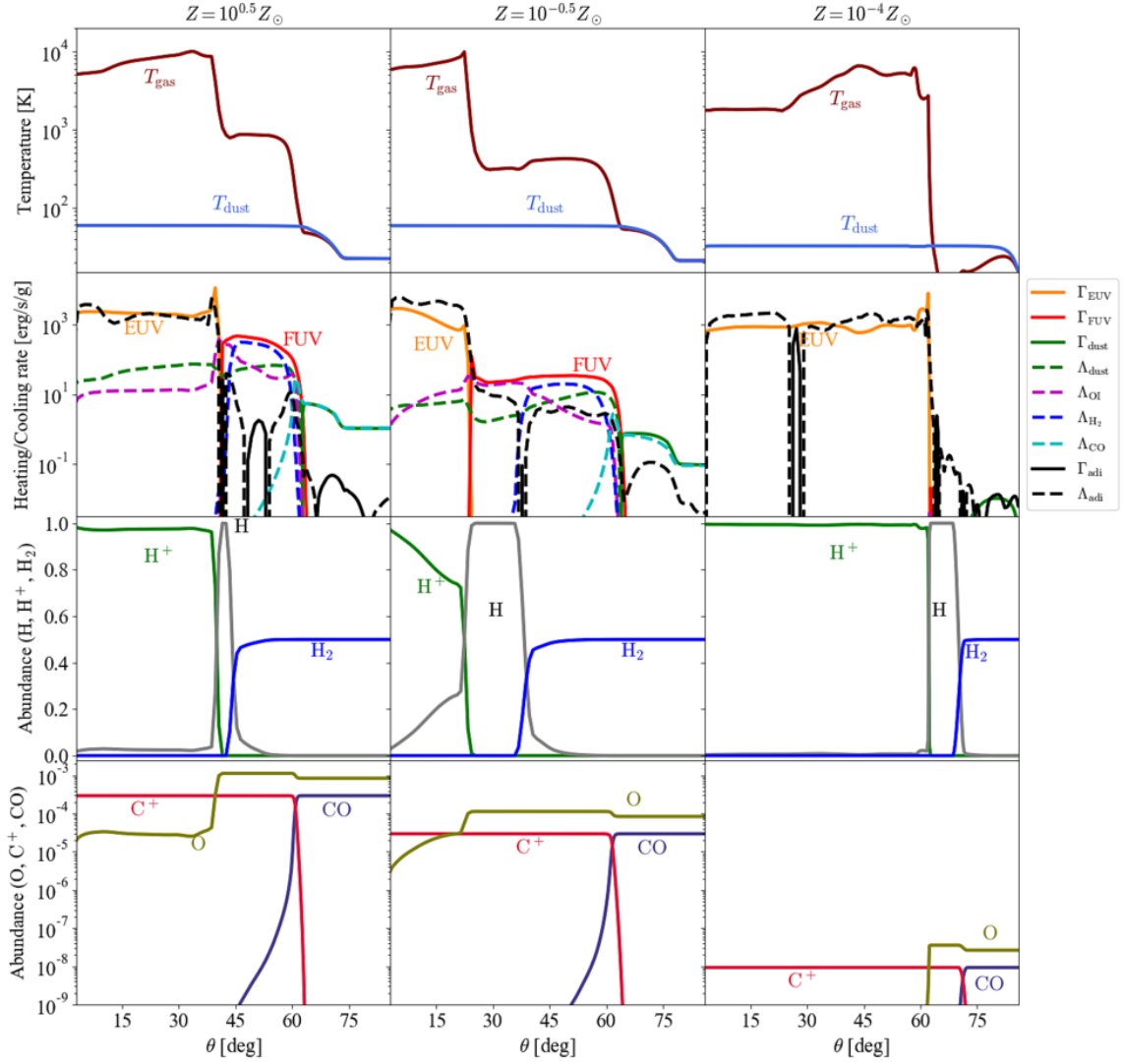


Fig. 2.6 Meridional distributions of various physical quantities at $r \simeq 80$ au in the disks with various metallicities: $Z = 10^{0.5} Z_{\odot}$ (left column), $10^{-0.5} Z_{\odot}$ (middle column), and $10^{-4} Z_{\odot}$ (right column). The snapshots are taken at $t = 8 t_c$. In each column, the profiles are shown in the same manner as in Figure 2.2. We note that, in the second panel for $Z = 10^{-4} Z_{\odot}$, some heating and cooling rates are missing because their values are too small to be plotted.

more efficient compared to FUV heating in lower-metallicity disks. To summarize, as metallicity decreases, O cooling, H_2 cooling, and dust-gas collisional cooling dominantly contribute to thermal balance in the neutral region compared to FUV heating. This results in the lower temperatures of the neutral regions. The reduced FUV heating is ineffective to provide a sufficient energy to the neutral gas for escape from the gravitational binding. For this reason, the neutral photoevaporative flows are even hardly driven in the lowest-metallicity range of $Z \lesssim 10^{-2} Z_{\odot}$.

2.3.2.2 Hydrogen-Bearing Species Distribution

The balance of photodissociation, the photoevaporative advection of H_2 , and H_2 formation on grains determines the chemical structures of H_2 and H I. As discussed in Section 2.3.1, the chemical structures of H_2 and H I is determined by the H_2 advection driven by FUV, H_2 formation on

grains, and photodissociation. The self-shielding effect of hydrogen molecules are effective to protect themselves from the photodissociating FUV at any metallicity (Figure 2.7).

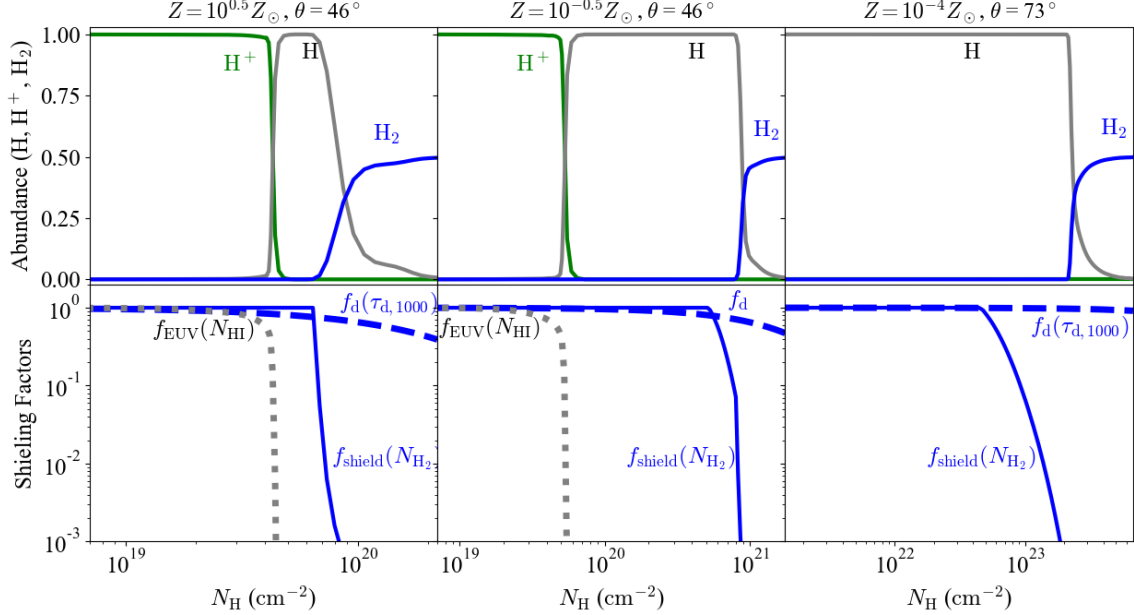


Fig. 2.7 (Top): radial profile of the abundances for the H-bearing species. (Bottom): the shielding factors. These quantities are shown for various metallicity disks with $Z = 10^{0.5} Z_{\odot}$ (left column), $10^{-0.5} Z_{\odot}$ (middle column), and $Z = 10^{-4} Z_{\odot}$ (right column). We take the snapshots at $t = 8 t_c$. The profiles are presented along a different ray at $\theta = 76^{\circ}$ for $Z = 10^{-4} Z_{\odot}$. The panels in each column are shown in the same manner as Figure 2.3.

The balance between H_2 advection and unshielded photodissociation determines the position of the photodissociation front. A sufficient H_2 flows are necessary to be driven to form the photodissociation front in the flow regions. In high-metallicity disks, FUV heating is efficient to yield high gas temperatures in the neutral regions and drives H_2 flows from an inner region of a disk. The FUV-driven H_2 flows have a small density owing to the large dust attenuation at the disk surface. (See also Section 2.3.4 for quantitative discussions.) Therefore, for high metallicity, the efficient FUV heating drives low-density H_2 flows from an inner region, forming the photodissociation front in a low-density region.

The density at the ionization front is determined by the balance of photoionization and recombination. These processes are independent of metallicity. By contrast, the photodissociation front is located in a small-density region for higher metallicities. Hence, the density at the photodissociation front becomes close to that at the ionization front with high metallicity. This forms a geometrically thin H I region in the photoevaporative flows (Figure 2.5).

2.3.2.3 Metal Species Distribution

As the dust amount decreases, dust shielding becomes inefficient to protect CO molecules against the dissociating FUV. Figure 2.8 demonstrates that the dominant shielding source is replaced by H_2 molecules in low-metallicity disks; the dust extinction factor $\Theta_3(A_V)$ is the most important with $Z = 10^{0.5} Z_{\odot}$ and $Z = 10^{-0.5} Z_{\odot}$, whereas the H_2 shielding factor $\Theta_2(N_{H_2})$ controls the total shielding effect with $Z = 10^{-4} Z_{\odot}$. Dust dominantly attenuates CO-dissociating FUV in high-metallicity disks, but the dominant shielding source is switched to molecular hydrogen in low-

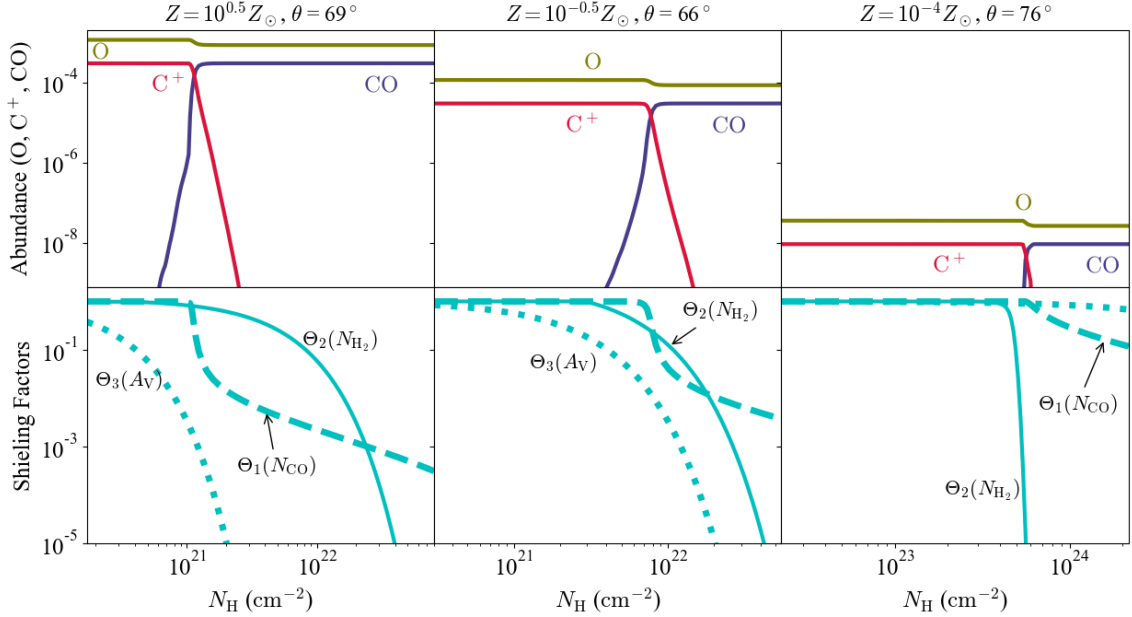


Fig. 2.8 Same as Figure 2.7 but heavy elements are examined (also see Figure 2.4). Note that we show the profiles along the different rays: $\theta = 69^\circ$ for $Z = 10^{0.5} Z_\odot$ (left column), $\theta = 66^\circ$ for $Z = 10^{-0.5} Z_\odot$ (middle column), and $\theta = 76^\circ$ for $Z = 10^{-4} Z_\odot$ (right column).

metallicity disks. Note that hydrogen molecules abundantly exist with any metallicities. The CO photodissociation front is embedded in high-density regions of the disks with all metallicities. This result is similar to that for the solar-metallicity disk in Section 2.3.1.

2.3.3 Photoevaporation Rates and Metallicity Dependence

We measure photoevaporation rates \dot{M}_{ph} by integrating the mass flux component orthogonal to a spherical surface S ,

$$\dot{M}_{\text{ph}} = \int_S d\mathbf{S} \cdot \rho \mathbf{v} = r_S^2 \int_S d\theta d\phi \sin \theta \rho v_r, \quad (2.37)$$

where $d\mathbf{S}$ is an infinitesimal surface element vector normal to the spherical surface, and r_S is the radius of S . We count the gas as unbound as long as the specific enthalpy

$$\eta = \frac{1}{2} \mathbf{v}^2 + \frac{\gamma}{\gamma - 1} c_s^2 - \frac{GM_*}{r}, \quad (2.38)$$

is positive, i.e. we sum up only the gas with $\eta > 0$ in Eq.(2.37). This subtraction can exclude the large contribution from the gas in the bound disk region where the density is significantly high though the velocity is small.

We calculate the resulting photoevaporation rates \dot{M}_{ph} of our simulations with $r_S = 100, 150, 200, 250$ au (Figure 2.9). The photoevaporation rates increase with r_S in general. This trend indicates that the gas always has a positive enthalpy at a larger radius beyond the critical radius, where $\eta = 0$ (Liffman 2003).

The critical radius or the gravitational radius is inversely proportional to the gas temperature (Hollenbach *et al.* 1994, Liffman 2003), that is, the necessary temperature for gas to escape T_{esc} is inversely proportional to the radius. In the case where the base temperature has a smooth profile

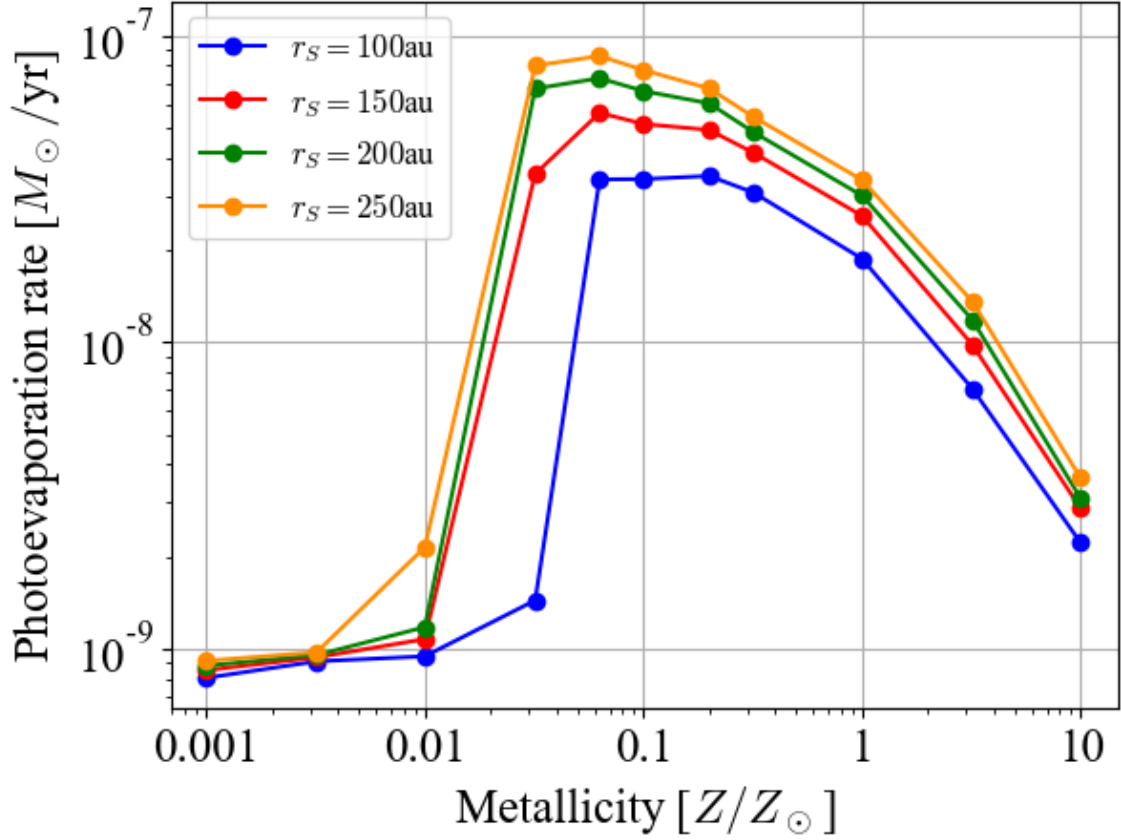


Fig. 2.9 Metallicity dependence of the resulting photoevaporation rates with $r_S = 100, 150, 200, 250$ au. The photoevaporation rates are the time-averaged value from $t = 0$ to $16 t_c \simeq 7.58 \times 10^3$ yr.

as $T_{\text{base}} \propto r^{-\alpha}$ ($0 < \alpha < 1$), $T_{\text{base}} > T_{\text{esc}}$ is always satisfied beyond the radius at which $T_{\text{base}} = T_{\text{esc}}$. Photoevaporative winds are unbound anywhere at the larger radii. This yields \dot{M}_{ph} increasing with r_S , and \dot{M}_{ph} does not converge unless the measuring radius r_S is larger than the disk radius. In our simulations, the base temperature approximately follows $T_{\text{base}} \propto r^{-\alpha}$ ($\alpha < 0.5$). Hence, \dot{M}_{ph} generally increases with the measuring radius r_S at least for $r_S \lesssim 250$ au, as Figure 2.9 shows. The further large r_S is not considered because the increase of \dot{M}_{ph} becomes small for larger r_S . We expect that the bulk of the mass-loss is counted in the resulting photoevaporation rates. In addition, other effects, such as external photoevaporation (e.g., Adams *et al.* 2004, Facchini *et al.* 2016), can affect the evolution of the outer region. Incorporating such effects is out of the scope in this study.

The photoevaporation rates are basically independent of metallicity in the lowest-metallicity range of $10^{-4} Z_{\odot} \leq Z \leq 10^{-2} Z_{\odot}$ (Figure 2.9). Dust-gas collisional cooling is effective to suppress the FUV-driven flows in this metallicity range. (See also the discussion in Section 2.3.2.) The EUV-driven ionized flows are still driven and dominantly contribute to the mass-loss rates. The EUV heating rate does not depend on metallicity, which results in the largely constant rates of \dot{M}_{ph} with the metallicities.

In our simulations, the EUV photoevaporation rate $\dot{M}_{\text{ph,EUV}}$ is estimated to be $\dot{M}_{\text{ph,EUV}} \simeq 1.0 \times 10^{-9} M_{\odot} \text{ yr}^{-1}$ (see \dot{M}_{ph} with $10^{-4} Z_{\odot} \lesssim Z \lesssim 10^{-3} Z_{\odot}$ in Figure 2.9). In Hollenbach *et al.* (1994) and Font *et al.* (2004), the EUV photoevaporation rates are calculated to be $(2.7\text{--}7.3) \times 10^{-10} M_{\odot} \text{ yr}^{-1}$

with $\Phi_{\text{EUV}} = 6 \times 10^{41} \text{ s}^{-1}$ and $M = 0.5 M_{\odot}$. The photoevaporation rate is slightly smaller than our $\dot{M}_{\text{ph,EUV}}$. The previous studies derived $\dot{M}_{\text{ph,EUV}}$ on the basis of the idea that the diffuse EUV component is dominant over the direct EUV component to drive photoevaporation. However, Tanaka *et al.* (2013) recently showed, by solving 2D radiative transfer, that the direct component dominates the EUV radiation rather than the diffusion component. The computational method for the radiative transfer is clearly more accurate than the 1+1D radiative transfer used in Hollenbach *et al.* (1994).^{*3} The resulting photoevaporation rate is about five times of those estimated in Hollenbach *et al.* (1994). This suggests that 1+1D radiative transfer likely leads to underestimating photoevaporation rates. Our study does not incorporate the diffuse EUV component, and thus the resulting photoevaporation rate is consistent with that of Tanaka *et al.* (2013). Note that the geometrical structure of a disk is critical to determine the relative dominance of the EUV components. The differences in $\dot{M}_{\text{ph,EUV}}$ of the previous studies and ours might also result from the distinct structures of the adopted disk models. In order to discuss the relative effectiveness of the EUV components, hydrodynamics studies are necessary with incorporating a self-consistent radiative transfer of the diffuse component.

Both the FUV-driven and EUV-driven flows are constantly excited with $10^{-1} Z_{\odot} \leq Z \leq 10 Z_{\odot}$ (Figure 2.5). As the discussions in Section 2.3.2, FUV heats the dense parts of the low-metallicity disks owing to the reduced amount of dust. The excited neutral photoevaporative flows thus have a higher density as metallicity decreases, and the resulting \dot{M}_{ph} correspondingly becomes larger. A similar dust attenuation effect controls the EUV photoevaporation rates in the study of massive star formation (Tanaka *et al.* 2017).

EC10 showed that the X-ray photoevaporation rate increases for low-metallicity disks. The photoevaporation rates have the scaling of $\dot{M}_{\text{ph}} \propto Z^{\delta}$. The slope δ is derived for -0.77 with $10^{-2} Z_{\odot} \leq Z \leq 2 Z_{\odot}$. In contrast, the metallicity dependence of UV photoevaporation rates in our study scales with $\delta = -0.85 \pm 0.07$ for $10^{-0.5} Z_{\odot} \leq Z \leq 10 Z_{\odot}$. The slopes of EC10 and our study take a similar negative value in spite of the model differences. This suggests that the photoevaporation rates are generally regulated by variations in the opacities of the disk medium.

FUV heating is reduced to be less inefficient than dust-gas collisional cooling in the range of $10^{-2} Z_{\odot} \leq Z \leq 10^{-1} Z_{\odot}$. (See also the discussions in Section 2.3.2.) This leads to lowering the base temperature of the neutral gas. As a result, the neutral flows contribute to the mass loss only from the outer region, where gravity is weak. Therefore, the innermost radius of the unbound neutral flows $r_{\text{min,n}}$ increases as metallicity decreases. Eq.(2.37) discounts the mass loss rate beyond the measuring radius r_S . Hence the sudden decline of \dot{M}_{ph} is found at $Z = 10^{-1.2} Z_{\odot}$ for $r_S = 100 \text{ au}$ and at $Z = 10^{-1.5} Z_{\odot}$ for $r_S = 150, 200, 250 \text{ au}$ in Figure 2.9.

2.3.4 Semi-Analytic Model for Photoevaporation Rates

We construct a semi-analytical model to confirm our interpretation of the numerical results in this section. In Sections 2.3.2 and 2.3.3, we have shown that \dot{M}_{ph} is basically set by the contribution from the FUV-driven neutral flows if excited. We focus on modeling the photoevaporation rates due to the FUV-driven flows $\dot{M}_{\text{FUV}}^{\text{ana}}$ for $10^{-2} Z_{\odot} \lesssim Z \lesssim 10 Z_{\odot}$. We do not model the EUV photoevaporation rate, whose contribution is much less than the FUV-driven flows and do not show a metallicity dependence, but we simply give a constant rate of $\dot{M}_{\text{EUV}}^{\text{ana}} = 1.0 \times 10^{-9} M_{\odot} \text{ yr}^{-1}$. The value is taken from our simulation result in Section 2.3.3.

In our semi-analytic model, a situation as depicted in Figure 2.10 is considered. Here we adopt

^{*3} Font *et al.* (2004) did not solve radiative transfer but performed hydrodynamics simulations, using the results of radiative transfer calculations in Hollenbach *et al.* (1994).

the assumptions:

1. The disk system achieves a steady state.
2. Photoevaporative winds are driven on the surface where $A_V \sim 1/2$.
3. At the base, hydrogen is fully molecular, while CO is completely dissociated.
4. Photoevaporative flows are launched at the speed of $\mathcal{M}c_s$, where $\mathcal{M} = \mathcal{M}(R, Z)$ is the Mach number and R is the distance in cylindrical coordinates. ^{*4}
5. We set azimuthal velocity to $v_\phi \sim \sqrt{GM_*/r}$ at the base.
6. We determine the base temperature by solving the balance equation of the dominant heating and cooling processes: photoelectric heating (FUV heating), O I cooling H₂ cooling, and dust-gas collisional cooling.
7. We count the contribution only from the gas with a positive η (cf. Eq.(2.38); Liffman 2003).
8. The base profile is given by a quadratic function,

$$z = f(R, Z) = a(Z)R^2 + b(Z)R, \quad (2.39)$$

where the coefficients $a(Z)$ and $b(Z)$ are taken from our simulations and are provided later.

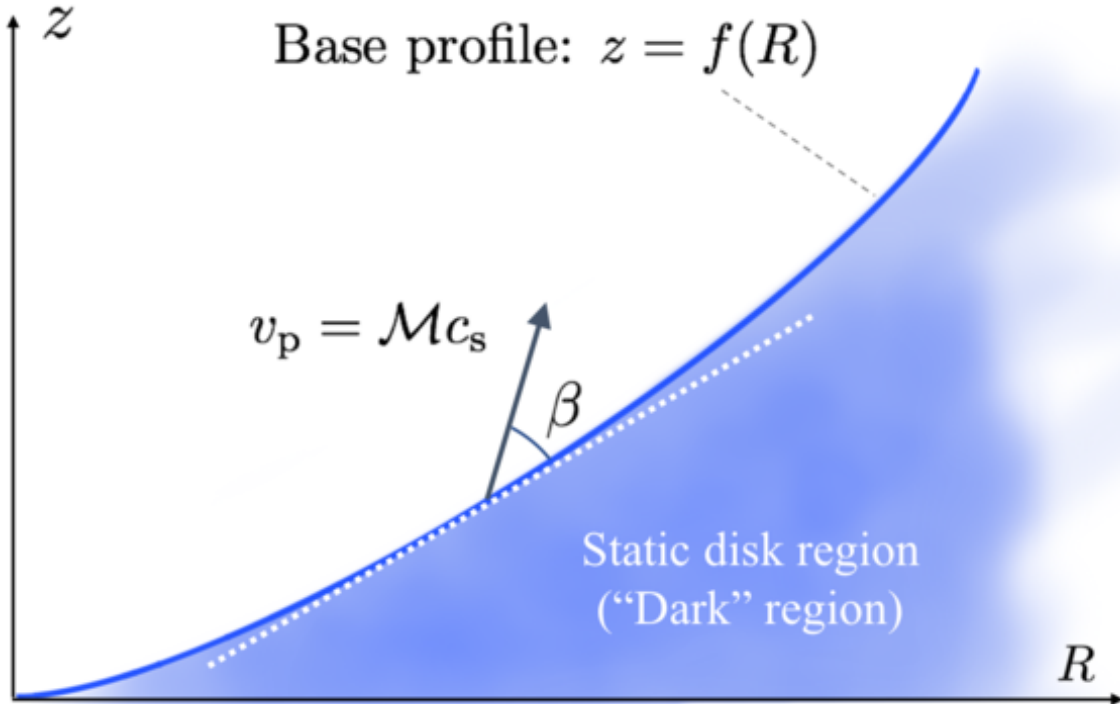


Fig. 2.10 Schematic picture of the situation assumed in our semi-analytic model. The base of the neutral photoevaporative flow is represented by the blue curve, to which the visual extinction along the line of sight from the star reaches $A_V = 1/2$. The profile of the base is simply assumed to be given by an analytic function $z = f(R)$. The photoevaporative flows are launched at a speed of $\mathcal{M}c_s$ in the direction of the angle β . We take the values from the numerical simulations for \mathcal{M} and β .

We adopt $\sim 2A_V$ as the exponent of the dust shielding factor for photoelectric heating (cf.

^{*4} The lowercase letter z is used as the height in cylindrical coordinates to differentiate it from metallicity denoted by the uppercase letter Z .

Eq.(2.23)), and thus the surface where $A_V \sim 1/2$ largely corresponds to the extent that FUV photons reach. The visual extinction is calculated as

$$A_V = \Sigma_d N_H = \Sigma_d \int_{R_*}^r dr' n_H, \quad (2.40)$$

where $\Sigma_d = 5.34 \times 10^{-22}$ mag cm² is the visual extinction per hydrogen nucleon. In Figures 2.1 and 2.5, the density is expected not to significantly change along the ray from the central star. We thus approximate an integral part of Eq.(2.40) as $N_H \sim n_H r$. The visual extinction is approximately reduced to $A_V \sim \Sigma_d (Z/Z_\odot) n_H r$ in our semi-analytic model. With this approximated visual extinction, the base number density is calculated as

$$n_H \sim \frac{1}{2\Sigma_d (Z/Z_\odot) r}. \quad (2.41)$$

We approximately calculate the base density as $\rho_b = m_H / (2\Sigma_d Z/Z_\odot r)$, because hydrogen is dominant in our chemistry model.

Since $A_V = 1/2$ is given, we can calculate the FUV flux at each point of the base. The third assumption and Eq.(2.41) provide the density of each chemical species. The dust temperature is set by the equilibrium between the absorption of the stellar irradiation and (re-)emission, and thus it does not strongly depend on metallicity as discussed in Section 2.3.2.1. We obtain the base dust temperature of $T_{\text{fit,d}} = 120 \text{ K} (r/10 \text{ au})^{-0.35}$ from our simulation results and use it in our analytic model. Under the assumptions above, and following the sixth assumption, we can derive the base temperature by solving a single nonlinear equation of thermal balance. The resulting base temperature is well fitted as

$$T_{\text{fit}} = T_0(Z) \left(\frac{r}{r_0} \right)^{-\alpha(Z)}, \quad (2.42)$$

$$T_0(Z) = 5.20 \times 10^2 \left(\frac{Z}{Z_\odot} \right)^{0.378} \text{ K}, \quad (2.43)$$

$$\begin{aligned} \alpha(Z) = & -6.05 \times 10^{-2} (\log(Z/Z_\odot))^3 + 2.64 \times 10^{-2} (\log(Z/Z_\odot))^2 \\ & + 5.90 \times 10^{-2} \log(Z/Z_\odot) + 3.19 \times 10^{-1}, \end{aligned} \quad (2.44)$$

where $r_0 = 100$ au. The exponent α takes a value in $0.28 < \alpha < 0.40$ with the metallicity range of interest ($10^{-2} Z_\odot \leq Z \leq 10 Z_\odot$).

In our semi-analytic model, the base specific enthalpy can be explicitly written as

$$\eta = \frac{1}{2} v_p^2 + \frac{\gamma}{\gamma-1} c_s^2 - \left(\frac{GM_*}{r} - \frac{1}{2} v_\phi^2 \right) \quad (2.45)$$

$$= \frac{1}{2} \mathcal{M}^2 c_s^2 + \frac{\gamma}{\gamma-1} c_s^2 - \frac{GM_*}{2r}. \quad (2.46)$$

The ‘‘unbound condition’’, $\eta > 0$ (the seventh assumption), reduces to

$$r > r_{\text{min}} \equiv r_0 \left[\frac{\gamma-1}{(1+2\mathcal{M}^{-2})\gamma-1} \frac{\mu m_u GM_*}{\mathcal{M}^2 r_0 k T_0} \right]^{1/(1-\alpha)}. \quad (2.47)$$

The photoevaporative flows are unbound in $r > r_{\text{min}}$.

We obtain the quadratic coefficients in Eq.(2.39) by fitting our simulations,

$$a = \left[-0.303 \{ \log(Z/Z_\odot) + 7.92 \times 10^{-2} \}^2 + 0.534 \right] \times (100 \text{ au})^{-1}, \quad (2.48)$$

$$b = 1.34 \times 10^{-2} (\log(Z/Z_\odot))^3 + 3.26 \times 10^{-2} (\log(Z/Z_\odot))^2 + 4.46 \times 10^{-3} \log(Z/Z_\odot) + 0.421.$$

We can derive $\dot{M}_{\text{FUV}}^{\text{ana}}$ with all of the elements above. It is noteworthy that our semi-analytic model requires one-dimensional radial profiles of the relevant physical quantities on the base; multidimensional assumptions are unnecessary. The model FUV photoevaporation rate is calculated as

$$\dot{M}_{\text{FUV}}^{\text{ana}} = \int_{\eta>0} ds \, 2\pi R \rho v_p \sin \beta, \quad (2.49)$$

where ds is a line element of the base and is given by $ds = dR\sqrt{1+f'^2}$, and $\beta = \beta(R, Z)$ is the angle between the poloidal velocity vector \vec{v}_p and the line element vector $d\vec{s}$. Using the derived elements above reduce Eq.(2.49) to

$$\begin{aligned} \dot{M}_{\text{FUV}}^{\text{ana}} &= 2 \int_{\eta>0} dR \sqrt{1+f'^2} \, 2\pi R \rho \mathcal{M} c_s \sin \beta \\ &= \frac{2\pi}{\Sigma_d(Z/Z_\odot)} \sqrt{\frac{m_{\text{H}} k T_0 r_0^\alpha}{\mu}} \int_{R_{\text{min}}}^{R_{\text{max}}} dR \sqrt{1+f'^2} \frac{R \mathcal{M}}{r^{1+\alpha/2}} \sin \beta, \end{aligned} \quad (2.50)$$

where R_{max} is the maximum distance for the integration. The maximum distance is set to be the real root of $R_{\text{max}}^2 + f(R_{\text{max}})^2 = r_{\text{max}}^2 = r_{\text{S}}^2$ for a direct comparison between the model and the numerical results in Section 2.3.3. The model photoevaporation rate is set to $\dot{M}_{\text{FUV}}^{\text{ana}} = 0$ in the case of $R_{\text{min}} > R_{\text{max}}$, where $R_{\text{min}} (> 0)$ is the real root of the quadratic equation $R_{\text{min}}^2 + f(R_{\text{min}})^2 = r_{\text{min}}^2$. We use an average Mach number $\bar{\mathcal{M}} = 0.6$ and an average launch angle $\bar{\beta} = \pi/6$ rad. The average is taken in the regions that have a positive η .^{*5} Similarly, we average the gradient of the base profile as $\bar{f}' = [f(R_{\text{max}}) - f(R_{\text{min}})] / (R_{\text{max}} - R_{\text{min}})$. Eq.(2.50) is finally rewritten as

$$\begin{aligned} \dot{M}_{\text{FUV}}^{\text{ana}} &\simeq \frac{4\pi}{\Sigma_d(Z/Z_\odot)} \sqrt{\frac{m_{\text{H}} k T_{\text{S}}}{\mu}} \frac{\bar{\mathcal{M}} \sqrt{1+\bar{f}'^2} \sin \bar{\beta}}{2+\bar{f}'(\bar{f}'+b)} \frac{r_{\text{max}}}{1-\alpha/2} \left[1 - \left(\frac{r_{\text{min}}}{r_{\text{max}}} \right)^{1-\alpha/2} \right] \\ &\simeq 1.8 \times 10^{-8} M_\odot \text{ yr}^{-1} \left(\frac{Z}{Z_\odot} \right)^{-1} \left(\frac{T_{\text{S}}}{10^2 \text{ K}} \right)^{1/2} \left(\frac{r_{\text{max}}}{10^2 \text{ au}} \right)^{1/2} \left[1 - \left(\frac{r_{\text{min}}}{r_{\text{max}}} \right)^{1-\alpha/2} \right] \\ &\quad \times \frac{\sqrt{1+\bar{f}'^2}}{[2+\bar{f}'(\bar{f}'+b)] (1-\alpha/2)}, \end{aligned} \quad (2.51)$$

where $T_{\text{S}} \equiv T_{\text{fit}}(r_{\text{max}})$.

The dotted lines in Figure 2.11 show the model photoevaporation rate $\dot{M}_{\text{model}} = \dot{M}_{\text{FUV}}^{\text{ana}} + \dot{M}_{\text{EUV}}^{\text{ana}}$. Our model clearly explains the results of the simulations. The differences between the analytic and numerical \dot{M}_{ph} are relatively large in $Z \lesssim 10^{-1} Z_\odot$. Adiabatic cooling is comparable to or dominant over the other cooling/heating processes in this low metallicity range. It inevitably contributes to determining the base temperature. Since we do not include the contribution from adiabatic cooling in our analytic model, the derived base temperature is higher than those in the simulations. This

^{*5} Though \mathcal{M} and β are generally dependent on both metallicity and radius, their variances are small compared to those of the base density and temperature (cf. Figure 3.8). Thus, we simply take their averages in metallicity and radius and use them in our semi-analytic model.

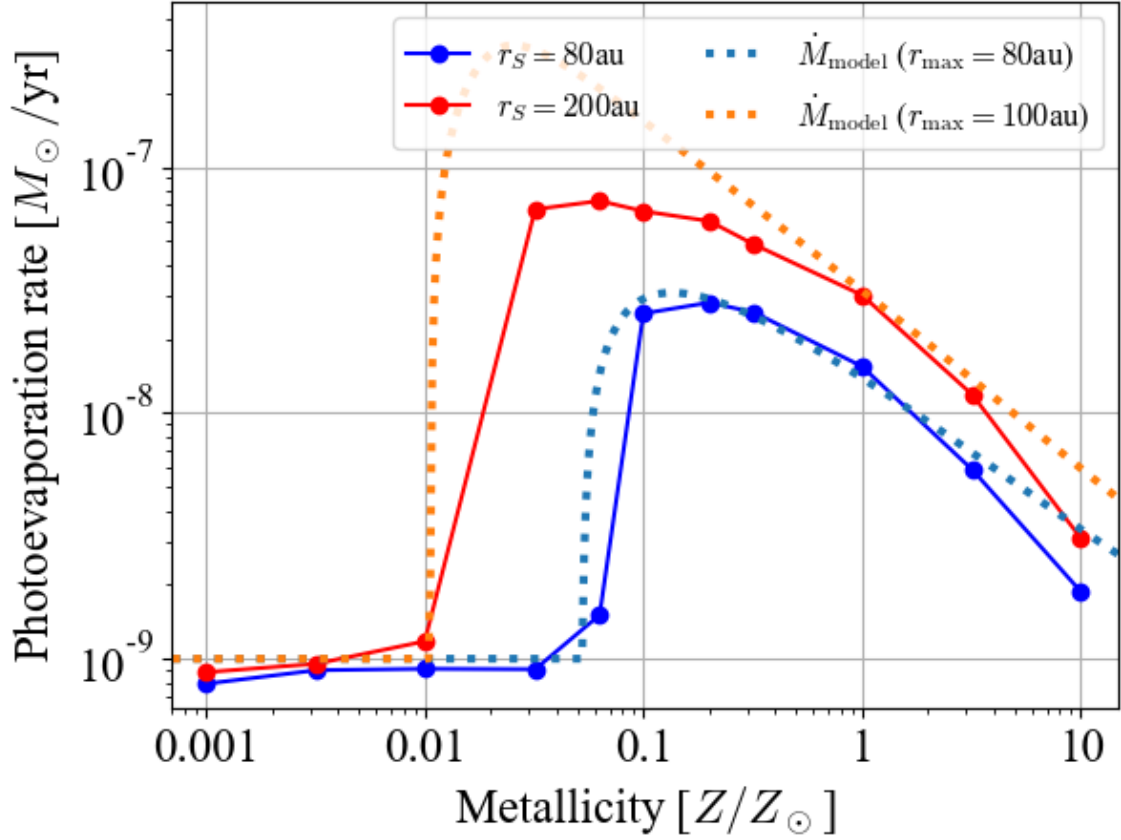


Fig. 2.11 The blue and red dots are \dot{M}_{ph} in the simulations with $r_S = 80$ au, 200 au, respectively. The blue and orange dotted lines represent the model photoevaporation rates (Eq.(2.51)) with $r_{\text{max}} = 80$ and 200 au.

implies that hydrodynamical simulations are required to derive photoevaporation rates accurately, especially when the cooling time is comparable to or longer than the typical dynamical timescale, as in our low-metallicity cases.

The r -dependence of $\dot{M}_{\text{FUV}}^{\text{ana}}$ is also calculated with Eq.(2.51) by replacing r_{max} with r ($r \geq r_{\text{min}}$), and it can be compared with those obtained from the results of the numerical simulations. We use Eq.(2.37) with a small modification:

$$\dot{M}_{\text{FUV}}^{\text{sim}}(r) = r^2 \int_{S_1(r)} d\theta d\phi \sin\theta \rho v_r. \quad (2.52)$$

Here $S_1(r)$ is the region where $y_{\text{HII}} < 0.5$ in the spherical surface with the radius of r . The condition $y_{\text{HII}} < 0.5$ is used to count the contribution from the FUV-driven neutral photoevaporative flows to \dot{M}_{ph} . The radial profile of $\dot{M}_{\text{FUV}}^{\text{ana}}$ is compared with $\dot{M}_{\text{FUV}}^{\text{sim}}(r)$ in Figure 2.12. It is shown that Eq.(2.51) can reproduce the r -dependence of \dot{M}_{ph} as well as the metallicity dependence of \dot{M}_{ph} (Figure 2.11).

Eq.(2.51) gives an approximate form of r_{min} as a function of metallicity $r_{\text{min}} \simeq 12.4 (Z/Z_{\odot})^{-0.55}$ au. The last factor of Eq.(2.51) is also approximated to ~ 0.5 with an error of less than 4%. Using

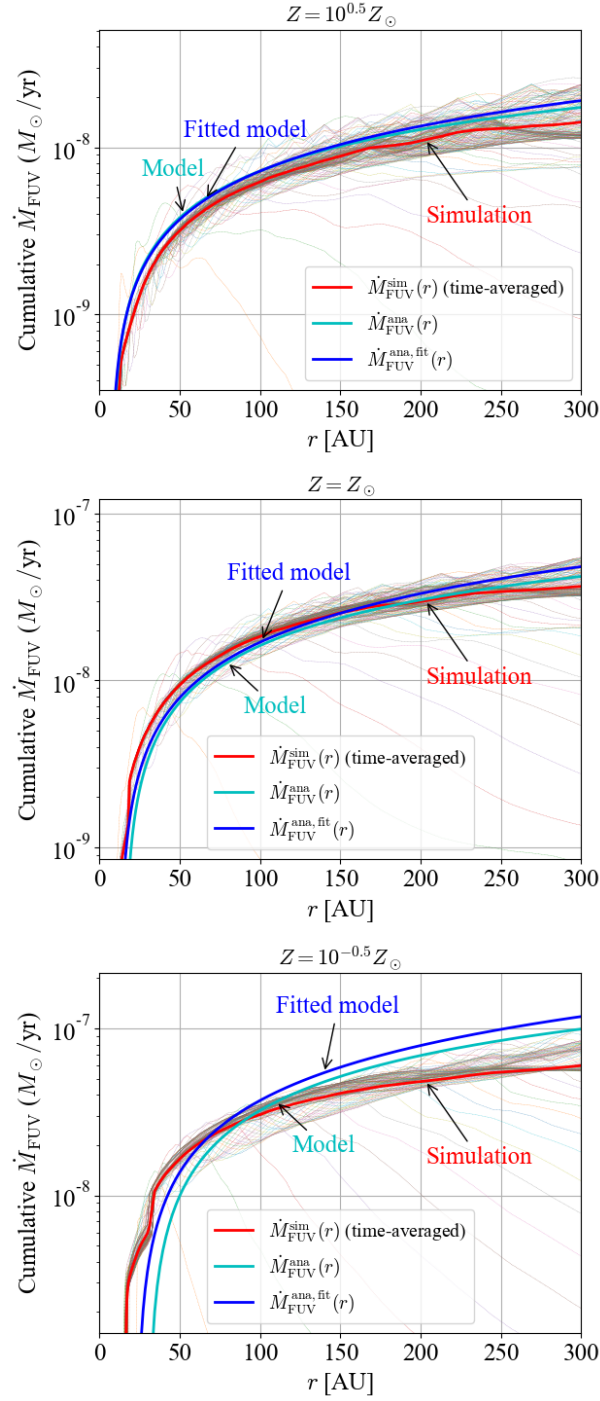


Fig. 2.12 Comparisons between the cumulative FUV photoevaporation rates derived by the analytic model and the numerical simulations. The panels show the different metallicity cases: $Z = 10^{0.5} Z_{\odot}$ (top), $Z = Z_{\odot}$ (middle), and $Z = 10^{-0.5} Z_{\odot}$ (bottom). The snapshots of the profiles taken every $0.1 t_c$ in the simulations are shown by the thin dashed lines, and the averaged profile is represented by the red line. The photoevaporation rates given by Equations 2.51 and 2.53 are shown by the cyan and blue lines, respectively. The range of the vertical axis differs between the top and bottom panels.

these quantities, we can further approximate Eq.(2.51) to a more explicit form:

$$\dot{M}_{\text{FUV}}^{\text{ana,fit}} \simeq 2.1 \times 10^{-8} M_{\odot} \text{ yr}^{-1} \tilde{Z}^{-0.81} \left[\tilde{r}_2^{1-\alpha/2} - \left(0.12 \tilde{Z}^{-0.55} \right)^{1-\alpha/2} \right], \quad (2.53)$$

where $\tilde{r}_2 \equiv r/(100 \text{ au})$ and $\tilde{Z} \equiv (Z/Z_{\odot})$. We plot $\dot{M}_{\text{FUV}}^{\text{ana,fit}}$ (Eq.(2.53)) with the green solid line and compared to $\dot{M}_{\text{FUV}}^{\text{ana}}$ (Eq.(2.51)) represented by the red solid line in Figure 2.12.

2.4 Discussion

2.4.1 Differences from X-Ray Photoevaporation

Our resulting photoevaporation rates increase as metallicity decreases in the metallicity range of $10^{-1} Z_{\odot} \leq Z \leq 10 Z_{\odot}$. The metallicity dependence is similar to that derived in EC10, where EUV/X-ray photoevaporation is investigated. With $10^{-2} Z_{\odot} \leq Z \leq 10^{-1} Z_{\odot}$, our \dot{M}_{ph} decreases with decreasing metallicity, in contrast to EC10. It is clearly worthy to investigate the metallicity dependence of photoevaporation with the effects of X-ray as well as UV. We incorporate X-ray effects in our simulations and investigate UV/X-ray photoevaporation in Chapter 3.

2.4.2 Lifetimes

The lifetimes of PPDs are typically much longer than the crossing time of the photoevaporative flows. This implies that following the global evolution of photoevaporating PPDs is highly computationally expensive. Assuming a simple scaling between the lifetimes and photoevaporation rates as $T_{\text{life}} \propto \dot{M}_{\text{ph}}^{-x}$ ($x > 0$) allows us to calculate the lifetimes approximately. This assumption is well justified by the results of EC10, where it is analytically shown that the lifetimes have an explicit dependence of $T_{\text{life}} \propto \dot{M}_{\text{ph}}^{-2/3}$ when the initial surface density profile $\Sigma \propto R^{-p}$ is set to $p = 1$. However, the formula is derived for the case of X-ray photoevaporation; it would not be applicable to our FUV photoevaporation case, where the profile of photoevaporative flows is different. We simply adopt $T_{\text{life}} \propto \dot{M}_{\text{ph}}^{-1}$ for our analysis in this section. In Figure 2.13, we compare the estimated lifetimes from our photoevaporation rates with the observational lifetimes: $4.9 \pm 1.1 \text{ Myr}$ for the disks with $Z = 1 Z_{\odot}$ and $1.3 \pm 1.9 \text{ Myr}$ for those with $Z = 0.2 Z_{\odot}$ (see Figure 1.3 for the derivation of the observational lifetimes). The formula just provides a simple scaling between T_{life} and \dot{M}_{ph} . Normalization is necessary to give a specific lifetime from \dot{M}_{ph} . We normalize the estimated lifetimes so that it gives the same lifetime as that observationally estimated for $Z = 1 Z_{\odot}$ disks. This enables a direct comparison between the lifetimes of the model and the observations. The estimated lifetime is $\sim 3 \text{ Myr}$ at $Z = 0.2 Z_{\odot}$ in Figure 2.13, which is slightly larger than the observational lifetime 1.3 Myr . The slope of the observational lifetimes is steeper than that of the lifetimes derived with our simulation results for $0.2 Z_{\odot} \lesssim Z \lesssim Z_{\odot}$.

The observational data has only two points in Figure 2.13. More data points are required for a meaningful and sensible comparison with our model. In addition, the accretion process also affects disk lifetimes, but it has not been clearly understood yet. Nevertheless, at least it is found here that our estimated lifetimes have the slope of 0.68 ± 0.09 with $0.2 Z_{\odot} \lesssim Z \lesssim 10^{0.5} Z_{\odot}$, and it is consistent with that of the observational lifetimes, 0.82 . Hence, FUV photoevaporation has the potential to yield the observational trend in disk lifetimes.

The occurrence of gas giants has been observationally known to decrease as the host star’s metallicity decreases for $Z \gtrsim 10^{-0.5} Z_{\odot}$ (so-called “planet-metallicity correlation”, e.g., Gonzalez 1997,

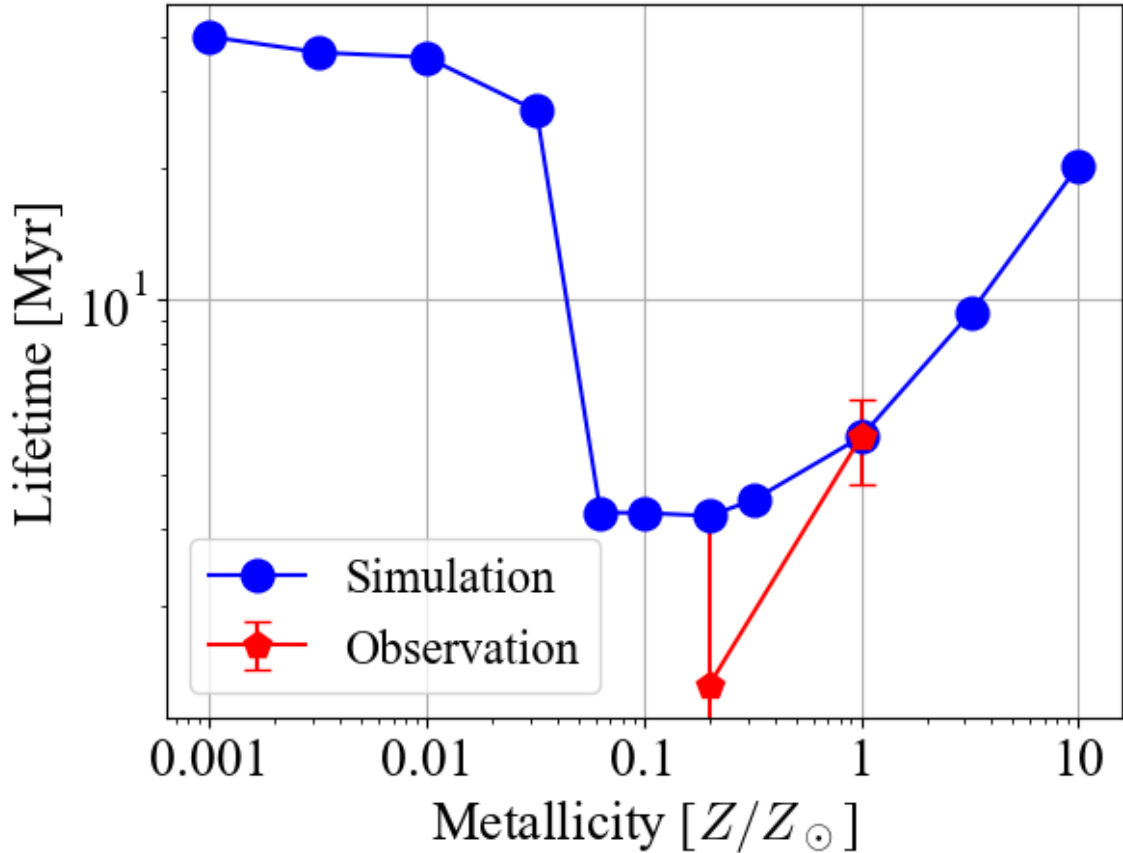


Fig. 2.13 Disk lifetimes estimated with \dot{M}_{ph} measured at $r_S = 100$ au of our simulations (blue dots). The red line represents the observational metallicity dependence of the lifetimes for comparison: 4.9 ± 1.1 Myr at $Z = 1 Z_{\odot}$ (Ribas *et al.* 2014) and 1.3 ± 1.9 Myr at $Z = 0.2 Z_{\odot}$ (Yasui *et al.* 2010). (See Figure 1.3 and Table 1.1.) The disk lifetime T_{life} is converted from \dot{M}_{ph} , using $T_{\text{life}} \propto \dot{M}_{\text{ph}}^{-1}$. The derived lifetimes are normalized so that it coincides with the observationally obtained lifetime at $Z = Z_{\odot}$.

Johnson *et al.* 2010, Mortier *et al.* 2013). The planet-metallicity correlation is considered to originate from inefficient gas-giant formation in low-metallicity PPDs. Interestingly, EC10 showed that rather than the reduced lifetimes due to X-ray photoevaporation, the core accretion scenario can yield a higher occurrence of gas giants owing to the faster core growth caused by a larger amount of dust in a high-metallicity PPD. However, Wang and Fischer (2015) found that the occurrence of terrestrial planets does not strongly depend on metallicity as gas-giants. This would propose that the core growth is not necessarily accelerated in dust-rich environments. If this is the case, the planet-metallicity correlation for gas giants could result from the metallicity-dependent FUV and X-ray photoevaporation.

2.4.3 Dust Grain Effects on FUV-Driven Photoevaporation

Generally, both the local size distribution of dust/PAH grains and the local dust-to-gas mass ratio can change the photoelectric heating rate. We assume a fixed size distribution and a constant dust-to-gas mass ratio throughout the computational domain, but in practice, they can vary in time and

space by settling, grain growth, and entrainment into the disk winds (Takeuchi *et al.* 2005, Owen *et al.* 2011b, Hutchison *et al.* 2016a,b). In fact, the dust-to-gas mass ratio and grain size distribution are observationally found to be variable in both the vertical and radial directions of PPDs (e.g., Pinte *et al.* 2016). Photoevaporation rates and their metallicity dependence can be affected by the spatial distribution, size distribution, and aerodynamics of grains.

The contribution of PAHs to the photoelectric heating is so significant that the abundance can even change FUV photoevaporation rates (Gorti and Hollenbach 2008, 2009). For the PAH abundance, we adopt the ISM value, which might be larger than the observed PAH abundances around T Tauri stars (Geers *et al.* 2007, Oliveira *et al.* 2010, Vicente *et al.* 2013). Though large uncertainties remain in the derived abundances, the influence of the PAH abundance on our results is worthy to be examined.

Bakes and Tielens (1994) showed that approximately 50% of the total photoelectric heating rate is responsible for the small grains with the size of $\lesssim 15 \text{ \AA}$ ($N_C \lesssim 1500$). Following this result, we reduce the FUV heating rate by 50% from that calculated by Eq.(2.23) to approximate a net FUV heating rate without PAHs/small grains. We additionally run simulations with the reduced FUV heating. Figure 2.14 shows the resulting photoevaporation rates. Evidently, even if the contribution

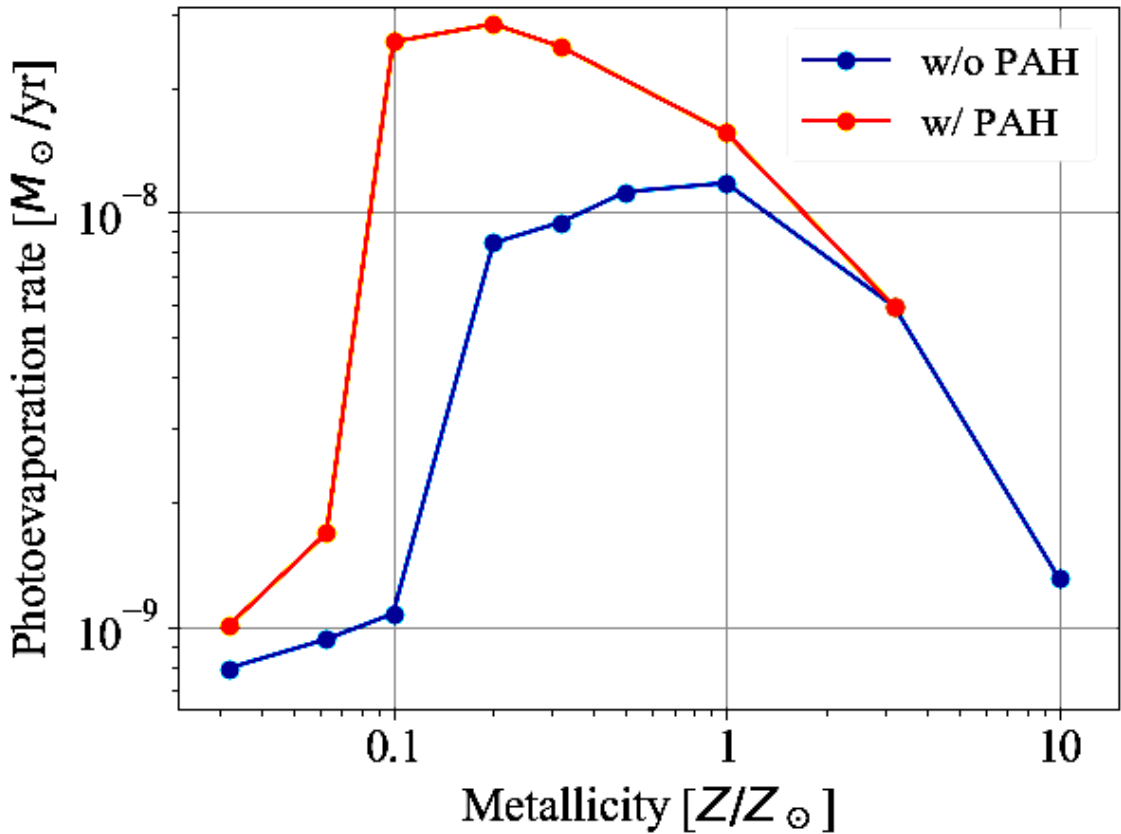


Fig. 2.14 Photoevaporation rates derived in the simulations with no PAH contribution to FUV heating (blue). The photoevaporation rates represented by the red line are those of Figure 2.17, where PAHs contribute to FUV heating. These \dot{M}_{ph} are estimated at $r_S = 80 \text{ au}$ with the outer boundary of $L = 300 \text{ au}$.

from PAHs is neglected, the FUV-driven flows are excited and contribute to \dot{M}_{ph} in the range of

$Z \gtrsim 0.1 Z_{\odot}$.

Although the reduced FUV heating can drive photoevaporative flows, it makes the base temperatures lower. The photoevaporative flows are driven only from the outer region. The reduced FUV heating with $Z \gtrsim Z_{\odot}$ can still yield a sufficiently high base temperature to drive photoevaporative flows from the bulk of the disk surfaces. The resulting photoevaporation rates are not significantly changed by the abundance and the size of PAHs. By contrast, in $0.1 Z_{\odot} \lesssim Z \lesssim Z_{\odot}$, the effective dust-gas collisional cooling suppresses the excitation of photoevaporation. Consequently, \dot{M}_{ph} declines at a high metallicity without the PAH contribution compared to the fiducial case.

As demonstrated, the reduced PAH abundances decrease FUV photoevaporation rates at subsolar metallicities, compared to our fiducial model. Besides the PAH abundances, other effects associated with grains could also have effects on FUV photoevaporation rates (Gorti *et al.* 2015). Dust growth/settling can reduce the disk opacity for UV rays. This enables FUV photons to reach the higher-density interior of a PPD and can correspondingly increase mass-loss rates. Observations have found a low visual extinction $A_V \sim 0.1\text{--}0.2$ in high column density regions of $N_{\text{H}} \sim 10^{22} \text{ cm}^{-2}$ (Vicente *et al.* 2013). They suggest that dust grains with $\sim 0.1 \mu\text{m}$ might be depleted by the effects of grain growth/settling in the neutral region, and the disk opacities to UV would be actually reduced. Thus, in order to study FUV photoevaporation more comprehensively, it is necessary to incorporate the effects of not only the reduced PAH abundance but also other processes which change the size distribution and the spatial distribution, such as grain growth, settling, and dust destruction/fragmentation.

2.4.4 Spurious Reflection at Outer Boundary

The spurious reflection at the outer boundary have influences on the flow profiles and thereby the derived \dot{M}_{ph} , especially if outgoing flows are subsonic. The reflection potentially happens in this study in the region near both the base and the outer boundary, where the flow is not yet supersonic ($\mathcal{M} > 1$). The spurious reflection makes the gas accumulated near the outer boundary and results in smoothing the pressure gradient. Gravity dominates in this case, and the gas is decelerated by the artificial effect.

The velocity of the spurious reflection is set by the sound speed. Therefore, if it happens, it generates some variable features on the timescale of the crossing time in the profiles of photoevaporation and/or \dot{M}_{ph} . This artificial effects would be crucial with a small outer boundary that does not cover transonic surfaces of photoevaporative flows. We examine if the spurious reflection occurs by running test simulations with a smaller outer boundary $L = 100 \text{ au}$. We set the same numbers of the cells as the fiducial model (Section 2.2.1). We derive the resulting \dot{M}_{ph} by Eq.(2.37) with $r_S = 80 \text{ au}$. The time variation are shown in Figure 2.15. The photoevaporation rates are found to vary periodically for $Z \geq 10^{-1.5} Z_{\odot}$. The FUV-driven neutral flows contribute to \dot{M}_{ph} , but they do not exceed $\mathcal{M} > 1$ at the outer boundary and are spuriously reflected. The reflected flows cause oscillational trends in the profiles of photoevaporative flows and the photoevaporation rates. On the other hand, the time evolution of \dot{M}_{ph} is almost independent of metallicity in the range $10^{-4} Z_{\odot} \leq Z \leq 10^{-1.5} Z_{\odot}$. The profiles are largely the same as that of $Z = 10^{-2} Z_{\odot}$ (the magenta line in Figure 2.15). With these low metallicities, only the EUV-driven ionized flows contribute to \dot{M}_{ph} . The flows quickly become supersonic after launched from the base, and therefore the oscillational trend is not observed in \dot{M}_{ph} .

Additional simulations have been performed with $L = 200 \text{ au}$. We have observed the spurious reflection there. We calculate \dot{M}_{ph} for the $Z = Z_{\odot}$ and $Z = 0.1 Z_{\odot}$ disks with $r_S = 80 \text{ au}$. In the case of $L = 200 \text{ au}$, the oscillation of \dot{M}_{ph} with $Z = Z_{\odot}$ damps with time. We interpret this result

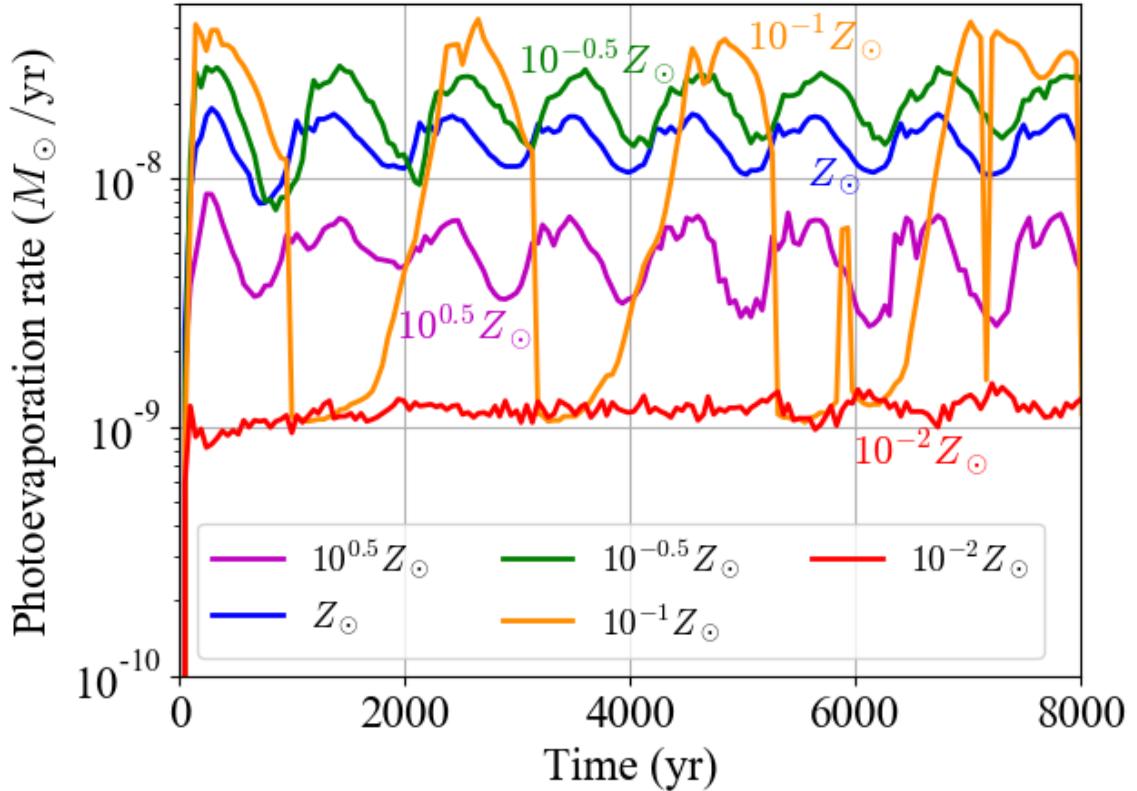


Fig. 2.15 Time evolution of \dot{M}_{ph} with $L = 100$ au at various metallicities $Z = 10^{0.5} Z_{\odot}$ (magenta), Z_{\odot} (blue), $10^{-0.5} Z_{\odot}$ (green), $10^{-1} Z_{\odot}$ (orange), and $10^{-2} Z_{\odot}$ (red). The cases with $Z \leq 10^{-2} Z_{\odot}$ are not plotted because the time evolution is almost the same as for $Z = 10^{-2} Z_{\odot}$.

as that the spurious reflection is disappeared at $r \sim 100$ au, where the neutral subsonic gas significantly contributes to \dot{M}_{ph} , by expanding the computational domain. The oscillation is still found for $Z = 0.1 Z_{\odot}$ with $L = 200$ au. We have further performed test simulations with the larger outer boundaries of $L = 300$ au and 400 au to examine if the artificial oscillation ceases. The extended outer boundaries are sufficiently large to include the transonic surface of the photoevaporative flows. The oscillations disappear as expected, and \dot{M}_{ph} converges after $\sim 10^3$ yr (bottom panel of Figure 2.16). The result clearly indicates that including the transonic surface of photoevaporative flows within the computational domain is necessary to exclude or at least to lessen the artificial effect. This is, in turn, essential to derive physically meaningful photoevaporation rates.

We perform further additional simulations with $L = 100, 200, 300, 400$ au at all the metallicities of interest in this study. We derive the time-averaged \dot{M}_{ph} and the metallicity dependences for the different outer boundaries (Figure 2.17). The resulting photoevaporation rates do not significantly vary according to the outer boundary size with the metallicity of interest, but the spurious reflection affects the behavior of the metallicity dependence, especially in the subsolar metallicity range. With subsolar metallicity, the neutral gas temperature is reduced by the inefficient photoelectric heating, and it yields slow flow velocity. A sufficiently large outer boundary is necessary to obtain a converged \dot{M}_{ph} with the slow flows. The boundary sizes of $L = 300$ and 400 au satisfy this requirement (the red and green lines show in Figure 2.17). It is noteworthy that the photoevaporation rate of the analytic model is in better agreement with \dot{M}_{ph} of the large outer boundaries. This is resulted from the fact

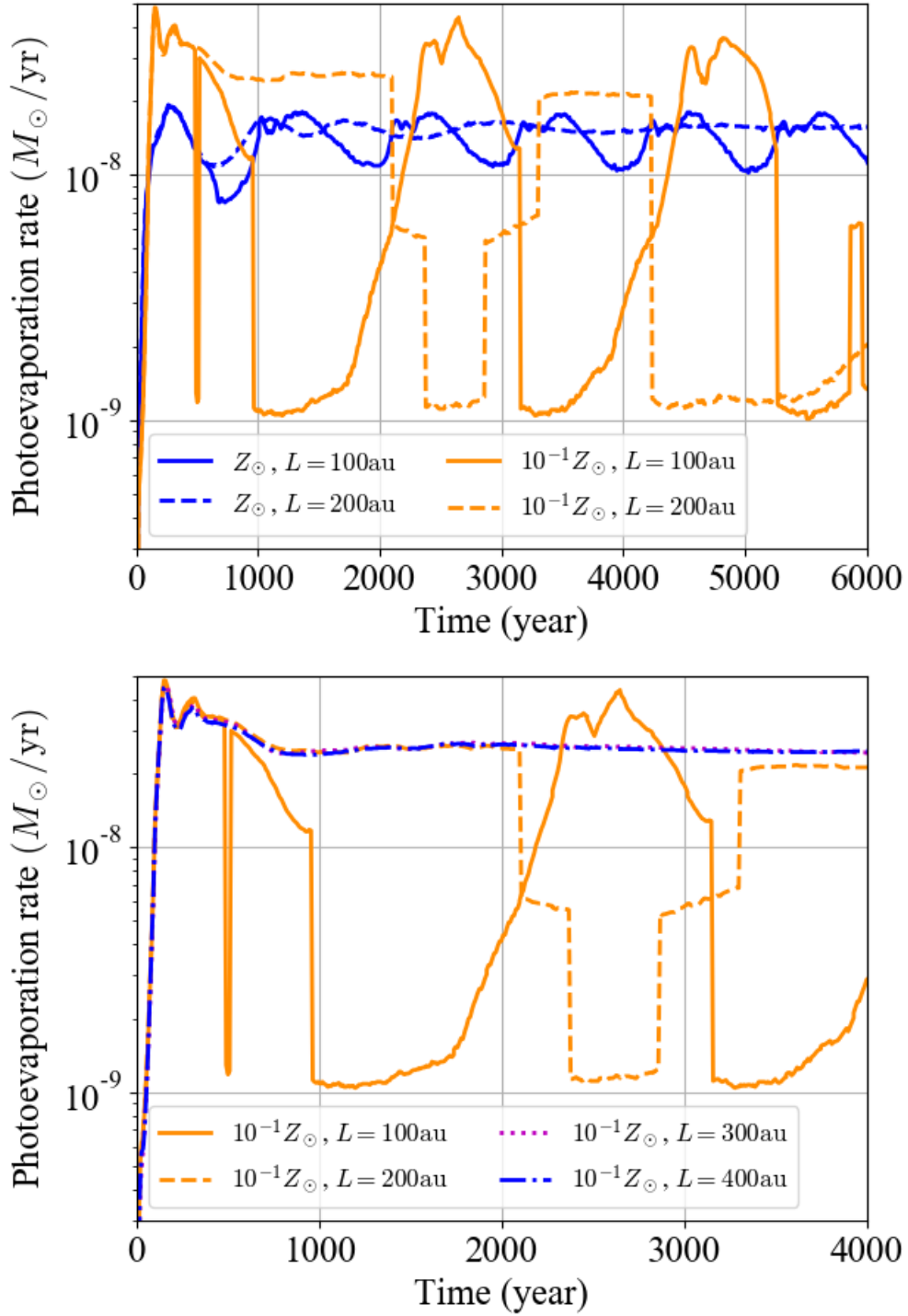


Fig. 2.16 **Top:** time evolution of \dot{M}_{ph} with $Z = Z_{\odot}$ (blue) and $Z = 0.1 Z_{\odot}$ (orange). We compare \dot{M}_{ph} of the simulations with different sizes of the outer boundaries: $L = 100$ au (solid lines) and $L = 200$ au (dashed lines). **Bottom:** time evolution of \dot{M}_{ph} in the $Z = 0.1 Z_{\odot}$ disks. We compare the photoevaporation rates with the different size of the outer boundaries: $L = 100$ au (solid orange line), $L = 200$ au (dashed orange line), $L = 300$ au (dotted purple line), and $L = 400$ au (dot-dashed blue line) Note that the latter two largely overlap.

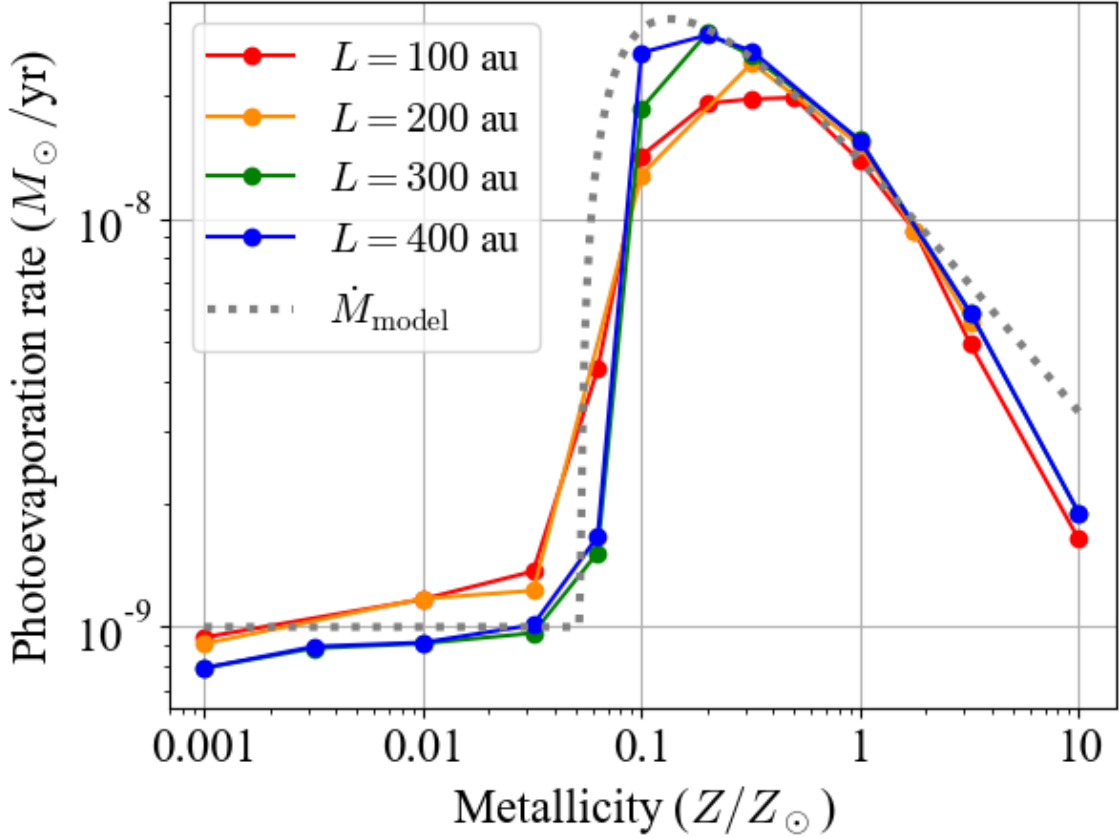


Fig. 2.17 Time-averaged \dot{M}_{ph} measured at $r_S = 80$ au for the different outer extent of the computational domain: $L = 100$ (blue), 200 (orange), 300 (green), and 400 au (red). The photoevaporation rate of the analytic model is also plotted by the black dotted line (cf. Section 2.3.4).

that the simulations reach a steady state, as assumed in the analytic model, by the disappearance of the spurious reflection due to using a large outer boundary.

2.4.5 Measurement of Photoevaporation Rates

In Section 2.3.3, we show that \dot{M}_{ph} increases with the measuring radius r_S . Since $d\dot{M}_{\text{ph}} \propto \rho_{\text{base}} v_{\text{base}} R^2 d(\log R)$, the mass flux is necessary to satisfy $\rho_{\text{base}} v_{\text{base}} \propto R^p$ with $p < -2$ to obtain a converged \dot{M}_{ph} . The radial profile of v_{base} is generally not so strongly dependent on the radius as ρ_{base} , and thus ρ_{base} is basically required to be $\rho_{\text{base}} \propto R^{p'}$ with $p' \lesssim -2$. However, our base density profile has $p' \geq -(1.2 - 1.5)$. It never yields a converged \dot{M}_{ph} until r_S exceeds the disk's outer edge. Tanaka *et al.* (2013) reported a similar result for EUV photoevaporation. The cumulatively increasing photoevaporation rate likely appears in previous studies (see the figures of Gorti and Hollenbach (2009) and Figure 4 of Owen *et al.* (2010)). In Owen *et al.* (2010), which shows X-ray photoevaporation rate increasing with the distance up to 70 au. A converged total photoevaporation rate might be obtained when the computational domain contains the whole disk.

2.4.6 Collisional Excited Lines in H II regions

In H II regions with solar and supersolar metallicities, there can be a significant contribution to cooling from CELs, such as O II (3730 Å, 3727 Å), N II (6585 Å, 6550 Å), O III (88.36 μm, 51.81 μm, 5008 Å, 4960 Å), Ne II (12.81 μm), S II (6733 Å, 6718 Å), and S III (33.48 μm, 18.71 μm, 9071 Å, 9533 Å). We estimate the total cooling rate of CELs $\sim 10^3 (n_{\text{H}}/10^3 \text{ cm}^{-3})(Z/Z_{\odot}) \text{ erg g}^{-1} \text{ s}^{-1}$ with typical parameters of H II regions (Draine 2011). In the present study, we have shown that adiabatic cooling dominantly reduces the temperatures of the ionized photoevaporative gas. The adiabatic cooling rate is approximately estimated as $P(d/dt)(1/\rho) = (P/\rho)\nabla \cdot \mathbf{v} \sim c_s^3/r \sim 10^6 (c_s/30 \text{ km s}^{-1})^3 (r/1 \text{ au})^{-1} \text{ erg g}^{-1} \text{ s}^{-1}$. Thus, instead of adiabatic cooling, the CEL cooling can be dominant in the inner, high-density regions ($r \lesssim 1 \text{ au}$) with a typical base density for the ionized gas of $n_{\text{H}} \sim 10^6 \text{ cm}^{-3} (r/1 \text{ au})^{-1.5}$ (Hollenbach *et al.* 1994, Tanaka *et al.* 2013). The base temperature may be reduced to some extent in such region. Incorporating the CEL cooling could then make the ionized gas even more bound. Nonetheless, the contribution from $r \lesssim 1 \text{ au}$ to \dot{M}_{ph} is negligibly small, as discussed already. Note that the small distance region is out of the computational domain in this study. In the wind region (atmosphere), the adiabatic cooling dominates over the CEL cooling because of the much smaller wind density compared to the base density. Overall, the influence of the CELs is insignificant in our model.

2.5 Chapter Summary

The present study of the chapter is motivated by the recent observation results that PPD lifetimes are suggested to be shorter in low-metallicity environments than in nearby environments. We have performed a suite of self-consistent radiation hydrodynamics simulations of photoevaporating PPDs with nonequilibrium multispecies chemistry. Particularly, we have investigated the photoevaporation of PPDs with a wide variety of metallicities from $10^{-4} Z_{\odot}$ to $10 Z_{\odot}$. Our aims are deriving metallicity dependence, if any, of UV photoevaporation rates and the disk lifetimes. We summarize our major conclusions as follows:

- The low amount of dust reduces the opacity of low-metallicity disks; FUV photons reach and heat denser neutral regions of PPDs. As a result, lower-metallicity disks yield a higher \dot{M}_{ph} in $10^{-1} Z_{\odot} \lesssim Z \lesssim 10 Z_{\odot}$. The estimated lifetimes are consistent with observations.
- FUV photoelectric heating is reduced to be inefficient compared to cooling in neutral regions, as the metallicity decreases. The temperatures of the neutral region drop, and thus photoevaporation is suppressed. The contribution of the FUV-driven flows to \dot{M}_{ph} correspondingly decreases at $10^{-2} Z_{\odot} \lesssim Z \lesssim 10^{-1} Z_{\odot}$.
- The resulting \dot{M}_{ph} peaks at the subsolar metallicity because of the combined effects of the above two.
- The EUV-driven flows primarily contribute to \dot{M}_{ph} in $10^{-4} Z_{\odot} \lesssim Z \lesssim 10^{-2} Z_{\odot}$. The photoevaporation rates are nearly a constant in this extremely low-metallicity environment.
- The semi-analytic model we have developed accurately provides both the metallicity dependence of \dot{M}_{ph} (see Figure 2.9) and the photoevaporative wind profile $\dot{M}_{\text{FUV}}^{\text{sim}}(r)$ (see Figure 2.12).
- A large measuring radius r_S yields a large total photoevaporation rate in a cumulative manner. This indicates that the total photoevaporation rates depend on the disk radius. In order to derive a unique total \dot{M}_{ph} , global simulations are required.

- The spurious reflection is generated at the outer extent of the computational domain in numerical simulations. This affects the resulting profiles of photoevaporative flows and even yield an incorrect \dot{M}_{ph} . The transonic surface should be contained in the computational domain with a sufficiently large outer boundary to avoid it.

Ercolano and Clarke (2010) showed that X-ray photoevaporation also gives a metallicity dependence in photoevaporation rates that is roughly consistent with the observational metallicity dependence of disk lifetimes. They used a hydrostatic method to derive photoevaporation rates, and thus the resulting \dot{M}_{ph} relies on the assumptions on dynamical processes. On the basis of the findings in the study of this chapter, It is necessary to perform hydrodynamics simulations to accurately determine the metallicity dependence of X-ray photoevaporation. We will address this issue in the next chapter.

It is suggested by our simulations and analytic model that FUV photoevaporation has potential to explain the short PPD lifetimes observed in the outer Galaxy. Incorporating the effects of both UV and X-ray, and possibly the magnetohydrodynamics, would be necessary to establish a complete picture of the PPD dispersal.

Chapter 3

Metallicity Dependence of Disk

Photoevaporation Driven by UV and X-Ray

Irradiation from the Central Star: the Influences of X-Ray

3.1 Overview

Generally, X-ray ($0.1 \text{ keV} \lesssim h\nu \lesssim 10 \text{ keV}$) radiation is attenuated by the disk medium at a typical column density of $\sim 10^{21} \text{ cm}^{-2}$. It is comparable to the column densities at which FUV irradiation is attenuated. This indicates that X-ray can reach the dense interior of the disks as FUV does. Several previous studies investigated the X-ray impact on driving photoevaporative flows, but they show diverse results. Some studies suggested X-ray heating as a key process to yield a significant mass loss (Ercolano *et al.* 2009, Owen *et al.* 2010, 2011a, 2012), while others conclude that X-ray is ineffective or at least has only an indirect effect on driving photoevaporation (Alexander *et al.* 2004, Gorti *et al.* 2009, Wang and Goodman 2017). The importance of X-ray is one of the topics under debate in the field. Unfortunately, almost all of these studies do not self-consistently solve the dynamics and radiative transfer. Using a self-consistent calculation method is important to model flow structure and photoevaporation rates accurately. Wang and Goodman (2017) performed radiation hydrodynamics simulations with a self-consistent thermochemistry model, but the adopted X-ray has single energy of 1 keV. Since the X-ray ionization and heating depend on the energy of the photons, taking account of X-ray spectral distribution is necessary to discuss the effectiveness of X-ray on photoevaporation.

In this chapter, we additionally incorporate the X-ray effects of ionization and heating in our chemistry model of Chapter 2 to study X-ray importance and its influence on the UV photoevaporation rates. Again, we self-consistently solve hydrodynamics, radiative transfer, and nonequilibrium thermochemistry and follow long-term evolution of photoevaporating PPDs for over $\sim 5000 \text{ yr}$. The disk metallicity is varied in a wide range of $10^{-3} Z_{\odot} \leq Z \leq 10^{0.5} Z_{\odot}$ to investigate the metallicity dependence of the mass-loss rates and to compare it with the previously obtained metallicity dependence of UV photoevaporation rates in Chapter 2 and X-ray photoevaporation rates in Ercolano and Clarke (2010). In our fiducial case with solar metallicity, the photoevaporation rate is not significantly differed from that in the case of UV photoevaporation (Chapter 2) by including X-ray effects.

As metallicity decreases in the range of $Z \gtrsim 10^{-1.5} Z_{\odot}$, the disk opacity is reduced, and thus the photoevaporation rates increase. The estimated dispersal time is consistent with recent observations in the outer Galaxy. With even lower metallicities of $Z \lesssim 10^{-1.5} Z_{\odot}$, dust-gas collisional cooling becomes relatively efficient compared to FUV heating. This suppresses driving the FUV-driven photoevaporative flow, and hence photoevaporation rates decrease with decreasing metallicity. X-ray indirectly contributes to driving the neutral flows by making electron-rich neutral interiors of the disks and strengthening FUV photoelectric heating. The FUV-driven flows are excited, if X-ray is incorporated, even at the very low metallicities. The indirect X-ray effects significantly increase \dot{M}_{ph} especially at $Z \sim 10^{-2} Z_{\odot}$. We conclude that X-ray itself is not efficient to drive neutral winds, but the strengthening effect is significant to drive the winds by FUV heating with very low metallicities.

The contents in this chapter are based on the published paper, Nakatani et al., the *Astrophysical Journal*, Volume 865, p.75–87, 2018 (Nakatani *et al.* 2018b).

3.2 Methods

We study photoevaporation of PPDs irradiated by UV and X-ray from the central star by performing a suite of radiation hydrodynamics simulations, including self-consistent, nonequilibrium chemistry. We vary disk metallicity in a broad range of $10^{-3} Z_{\odot} \leq Z \leq 10^{0.5} Z_{\odot}$. We use almost the same method as Chapter 2, except that X-ray irradiation effects and chemical reactions involving H_2^+ are incorporated. Here we describe these effects newly added to our chemistry model and briefly review the adopted methods for the simulations. (See also Section 2.2 for the details.)

The irradiating photons from the central stars are composed of FUV, EUV, and X-ray. We list the adopted stellar parameters in Table 3.1. In reality, the stellar properties may be well metallicity-dependent, but the stellar parameters are fixed throughout our simulations to focus our interest on the metallicity dependence of \dot{M}_{ph} caused by the amount of the metal contents in the disks. Note that the UV luminosities and the SED are the same as those used in Chapter 2. We set the

Table 3.1 Properties of the Model

Stellar parameters	
Stellar mass (M_*)	$0.5 M_{\odot}$
Stellar radius (R_*)	$2 R_{\odot}$
FUV luminosity (L_{FUV})	$3 \times 10^{32} \text{ erg s}^{-1}$
EUV photon emission rate (Φ_{EUV})	$6 \times 10^{41} \text{ s}^{-1}$
X-ray luminosity (L_X)	$10^{30} \text{ erg s}^{-1}$
Gas/dust properties	
Species	H, H^+ , H_2 , H_2^+ , CO, O, C^+ , e^-
Carbon abundance (y_{C})	$0.927 \times 10^{-4} \times Z/Z_{\odot}$
Oxygen abundance (y_{O})	$3.568 \times 10^{-4} \times Z/Z_{\odot}$
Dust to gas mass ratio ($\mathcal{D}\mathcal{G}$)	$0.01 \times Z/Z_{\odot}$

X-ray SED to that observed from the TW Hydrae (Nomura *et al.* 2007). A two-temperature thin thermal plasma model (Mewe *et al.* 1985, Liedahl *et al.* 1995) is used to fit the *XMM-Newton* data of the SED. The best-fit plasma temperatures are $kT_1 = 0.8 \text{ keV}$ and $kT_2 = 0.2 \text{ keV}$, and the best-fit foreground interstellar column density is $N_{\text{H}} = 2.7 \times 10^{20} \text{ cm}^{-2}$. We adopt $E_{\text{min}} = 0.1 \text{ keV}$ and

$E_{\max} = 10 \text{ keV}$ as the minimum and maximum energies of the X-ray SED, respectively. ^{*1} The absolute values of the X-ray flux is determined so that the energy integration of the fluxes yields the total X-ray luminosity of $L_X = 1 \times 10^{30} \text{ erg s}^{-1}$.

The disk medium is composed of gas and dust. The gas consists of the eight chemical species: H, H^+ , H_2 , H_2^+ , CO, O, C^+ , and electrons. We add H_2^+ to our chemistry model to follow H_2 ionization by X-rays in the neutral regions of the disks. As in Chapter 2, we set the amounts of the dust grains and heavy elements to the ISM values at solar metallicity, and give those with other metallicities by multiplying the ratio of the metallicity to the local interstellar metallicity Z/Z_\odot , i.e. the dust-to-gas mass ratio is $\mathcal{D}\mathcal{G} = 0.01 Z/Z_\odot$, and the gas-phase elemental abundance of carbon and oxygen are $y_C = 0.927 \times 10^{-4} Z/Z_\odot$ and $y_O = 3.568 \times 10^{-4} Z/Z_\odot$, respectively (Pollack *et al.* 1994, Omukai 2000). We note that these adopted values are the same as those in Chapter 2.

We perform the simulations in 2D spherical polar coordinates (r, θ) . The computational domain extends on $r = [1, 400] \text{ au}$ and $\theta = [0, \pi/2] \text{ rad}$. A sufficiently large outer boundary is chosen to avoid spurious reflection of outflowing gas at the outer boundary. The reflection has potential to yield an unphysical effect to decrease \dot{M}_{ph} (see Section 2.4.4). The disk is symmetric around the rotational axis ($\theta = 0$) and with respect to the midplane ($\theta = \pi/2$). We solve the time evolution of the gas density ρ , radial velocity v_r , meridional velocity v_θ , azimuthal velocity v_ϕ , energy E , and chemical abundances \mathbf{y} (cf. Section 2.2.2). It is noteworthy that the dynamical evolution of the azimuthal velocity is solved as well as the other velocity components regardless of the fact that our simulations are conducted on the 2D plane. In the energy equation, we incorporate relevant heating/cooling sources (Section 2.2.3). We update chemical abundances, taking into account the advection as well as chemical reactions.

For the chemical evolution, we take account of the chemical distribution changes due to both the advection and chemical reactions (Eq.(2.9)). The equation of state is given by Eq.(2.13), but the adiabatic index γ is changed from Eq.(2.14) to consider the contribution of H_2^+ ,

$$\gamma = 1 + \frac{y_{\text{H}} + y_{\text{H}^+} + y_{\text{H}_2} + y_{\text{H}_2^+} + y_{\text{e}}}{\frac{3}{2}y_{\text{H}} + \frac{3}{2}y_{\text{H}^+} + \frac{5}{2}y_{\text{H}_2} + \frac{5}{2}y_{\text{H}_2^+} + \frac{3}{2}y_{\text{e}}}. \quad (3.1)$$

We follow the methods in Chapter 2 to calculate UV transfer. The ray-tracing method is also used for X-ray transfer calculations (the details are described below in Section 3.2.1). Dust temperatures are self-consistently determined by following the radiative transfer of both the irradiation component and the diffuse component due to dust (re-)emission. Again, we use a hybrid scheme of Kuiper *et al.* (2010).

In order to separate the effects of FUV, EUV, and X-ray, we perform three sets of simulations, where (1) all of EUV heating, FUV heating, and X-ray heating are included; (2) FUV heating is disabled; and (3) X-ray heating is disabled (we have already performed this set of simulations in Chapter 2). We compare the resulting photoevaporation rates in these sets of the simulations. Henceforth, a simulation set is labeled based on the incorporated photoheating as ‘‘Run YYY’’. For instance, ‘‘Run FEX’’ represents a simulation with all of the photoheating; ‘‘Run E’’ indicates that only EUV heating is included. Further, we specify the metallicity in a simulation by appending ‘‘/ZC’’ to the label of the simulation sets. The ‘‘/ZC’’ refers to a simulation with $Z = 10^C Z_\odot$. For example, ‘‘Run FX/Z-0.5’’ means a simulation with $Z = 10^{-0.5} Z_\odot$ where FUV and X-ray heating are included.

^{*1} Photons with $h\nu \geq 0.1 \text{ keV}$ are referred to as X-rays in the present study.

3.2.1 X-Ray Heating/Ionization

3.2.1.1 Cross Section

Both light and heavy elements in both gas- and dust-phases are relevant to X-ray absorption. The typical cross section of the dust is a small fraction of the total cross section for the medium (Wilms *et al.* 2000). Therefore, we neglect X-ray absorption by the dust grains in the present study.

Gorti and Hollenbach (2004) (henceforth, GH04) presented a fit of the cross section for the disk medium with solar metallicity. The fitted total cross section per hydrogen nuclei is provided as

$$\sigma_{\text{GH04}}(E) = 1.2 \times 10^{-22} \left(\frac{E}{1 \text{ keV}} \right)^{-2.594} \text{ cm}^2, \quad (3.2)$$

where X-ray photon energy is denoted as E . Eq.(3.2) includes the contribution from both the nonmetal and metal elements, but it is not applicable for the other metallicity disks as it is. Metal elements' contribution is significant for the energy range of $E \geq 0.29 \text{ keV}$, which is the threshold energy of carbon ionization (Wilms *et al.* 2000). In our model, Eq.(3.2) is modified to give an approximate cross section for the disk medium with various metallicities,

$$\sigma_{\text{H}} = 11.55 \times 10^{-24} \left(\frac{E}{1 \text{ keV}} \right)^{-3.4} \text{ cm}^2, \quad (3.3)$$

$$\sigma = \begin{cases} \sigma_{\text{H}} & (0.1 \text{ keV} \leq E \leq 0.29 \text{ keV}) \\ \max \left(\sigma_{\text{H}}, \sigma_{\text{GH04}} \times \frac{Z}{Z_{\odot}} \right) \text{ cm}^2 & (E \geq 0.29 \text{ keV}) \end{cases}. \quad (3.4)$$

Here σ_{H} is the hydrogen cross section per hydrogen nuclei presented in GH04.

Helium has approximately four times larger cross section than hydrogen (Shull and van Steenberg 1985, Gorti and Hollenbach 2004). Atomic helium may contribute to absorbing X-ray photons. The typical helium abundance is 0.1, and thus the absorption rate would increase by $\lesssim 40\%$ if the helium contribution is taken into account in Eq.(3.4). However, the small rise in the absorption rate is expected not to affect our results significantly, and thus we neglect the helium contribution in our chemistry model for the purpose of saving the computational cost.

3.2.1.2 X-Ray Ionization

X-rays ionize elements, depositing the excess energy to the ejected electrons. These free electrons produced by absorption of X-rays are called primary electrons. The primary electrons have such high energy that they ionize ambient neutral elements by collisions. This collisional ionization is referred to as secondary ionization, and the electrons produced by the secondary ionization are called secondary electrons.

In our chemistry model, X-ray ionization of the most abundant neutral species, namely, H_2 and H , is implemented. The total photoionization rate of X-ray is equal to the number of produced primary electrons per unit volume per unit time

$$N_{\text{prim}} = \int_{E_{\text{Emin}}}^{E_{\text{Emax}}} dE \sigma n_{\text{H}} \frac{F(E)}{E} e^{-\tau_{\text{X}}}, \quad (3.5)$$

where τ_{X} is the optical depth of the medium for X-ray defined as $\tau_{\text{X}} = \sigma N_{\text{H}}$. We denote the fraction of the primary electron energy going into secondary ionization as Φ_{H} for atomic hydrogen.

Hence, the energy of $\Phi_{\text{H}}(E - E_{\text{th}})$, where E_{th} is threshold energy to ionize a certain element, is used for secondary ionization per production of a primary electron. The nonthermal primary electron typically has a much larger energy than the threshold energy, and thus the number of secondary electrons produced by ionization of hydrogen is approximately calculated as $\Phi_{\text{H}}E/13.6\text{ eV}$. The secondary ionization rate is

$$\xi_{H,\text{sec}} = \int_{E_{\text{min}}}^{E_{\text{max}}} dE \frac{F(E)}{E} e^{-\tau x} \sigma n_{\text{H}} \left(\frac{\Phi_{\text{H}}E}{13.6\text{ eV}} \right). \quad (3.6)$$

The X-ray photoionization rate of hydrogen is

$$\xi_{H,\text{prim}} = \int_{E_{\text{min}}}^{E_{\text{max}}} dE \frac{F(E)}{E} e^{-\tau x} \sigma_{\text{H}} n_{\text{HI}}. \quad (3.7)$$

The sum of $\xi_{H,\text{prim}}$ and $\xi_{H,\text{sec}}$ provides the total ionization rate associated with X-ray absorption.

$$\begin{aligned} R_{\text{X,H}} &= (\xi_{H,\text{prim}} + \xi_{H,\text{sec}}) / n_{\text{H}} \\ &= \int_{E_{\text{min}}}^{E_{\text{max}}} dE \frac{F(E)}{E} e^{-\tau x} \left[\sigma_{\text{H}} y_{\text{HI}} + \sigma \left(\frac{\Phi_{\text{H}}E}{13.6\text{ eV}} \right) \right]. \end{aligned} \quad (3.8)$$

The fraction Φ_{H} is generally a function of the electron abundance y_{e} and the energy of a primary electron $E - E_{\text{th}} \simeq E$ (Maloney *et al.* 1996). Nevertheless, the dependence on the primary electron energy is usually neglected for simplicity. In electron-poor environments ($y_{\text{e}} \lesssim 0.01$), Φ_{H} is approximately $\Phi_{\text{H}} \simeq 0.35$, i.e. 35% of the primary electron energy goes into secondary ionization (Maloney *et al.* 1996, Gorti and Hollenbach 2004). The neutral regions of PPDs are generally electron-poor ($y_{\text{e}} \ll 1$) even with X-ray ionization. Atomic hydrogen is almost completely ionized ($y_{\text{HI}} \sim 0$) and yields $y_{\text{e}} \sim 1$ in H II regions. The primary electron energy would rapidly thermalize through a frequent Coulomb scattering between electrons, and a small amount of the primary electron energy would go into secondary ionization. The approximation $\Phi_{\text{H}} \simeq 0.35$ is thus not applicable to the gas in this ionized region. In general, Φ_{H} increases as the electron abundance decreases (Shull and van Steenberg 1985). We approximately incorporate the dependence on the electron abundance by setting Φ_{H} to

$$\Phi_{\text{H}} = 0.35 y_{\text{HI}}. \quad (3.9)$$

Eq.(3.8) finally reduces to

$$R_{\text{X,H}} = y_{\text{HI}} \int_{E_{\text{min}}}^{E_{\text{max}}} dE \frac{F(E)}{E} e^{-\tau x} \left[\sigma_{\text{H}} + \sigma \left(\frac{25.7E}{1\text{ keV}} \right) \right]. \quad (3.10)$$

We adopt $2\sigma_{\text{H}}$ for the absorption cross section of H_2 , as used in GH04 (cf. Yan *et al.* 1998, Draine 2011). We note that in the high energy limit, the ratio between the cross sections of molecular and atomic hydrogen is ~ 2.8 (Wilms *et al.* 2000, Yan *et al.* 2001, Draine 2011). The primary ionization rate for molecular hydrogen is

$$\xi_{\text{H}_2,\text{prim}} = \int_{E_{\text{min}}}^{E_{\text{max}}} dE \frac{F(E)}{E} e^{-\tau x} (2\sigma_{\text{H}}) n_{\text{H}_2}. \quad (3.11)$$

The fraction Φ_{H} is also applicable to secondary ionization of molecular hydrogen in electron-poor environments (Maloney *et al.* 1996). The secondary ionization rate of H_2 differs from Eq.(3.6) by the difference in the ionization potentials of atomic and molecular hydrogen. Thus, the secondary

ionization rate of H_2 is calculated as

$$\xi_{\text{H}_2, \text{sec}} = 2y_{\text{H}_2} \int_{E_{\text{min}}}^{E_{\text{max}}} dE \frac{F(E)}{E} e^{-\tau_X} \sigma n_{\text{H}} \left(\frac{13.6 \text{ eV}}{15.4 \text{ eV}} \right) \left(\frac{25.7E}{1 \text{ keV}} \right). \quad (3.12)$$

We use the first factor $2y_{\text{H}_2}$ instead of y_{HI} in Eq.(3.9). Note that the maximum value of molecular hydrogen abundance is $y_{\text{H}_2} = 0.5$. Hence, the total X-ray ionization rate of H_2 is

$$\begin{aligned} R_{\text{X}, \text{H}_2} &= (\xi_{\text{H}_2, \text{prim}} + \xi_{\text{H}_2, \text{sec}}) / n_{\text{H}} \\ &= 2y_{\text{H}_2} \int_{E_{\text{min}}}^{E_{\text{max}}} dE \frac{F(E)}{E} e^{-\tau_X} \left[\sigma_{\text{H}} + \sigma \left(\frac{22.7E}{1 \text{ keV}} \right) \right]. \end{aligned} \quad (3.13)$$

Helium also ejects both the primary and secondary electrons. The fraction of primary electron energy going into secondary ionization is $\Phi_{\text{He}} \sim 0.05$ (Shull and van Steenberg 1985, Gorti and Hollenbach 2004). The value of the fraction is much smaller than that of hydrogen. The smaller fraction and the small value of the helium abundance (~ 0.1) would make the ionization degree of helium smaller than that of hydrogen. There is only a slight difference between the recombination rates of hydrogen and helium (about a factor of two in the range for $10 \text{ K} \leq T \leq 1000 \text{ K}$; McElroy *et al.* 2013), and thus X-ray would yield a smaller, or at least comparable, ionization degree of helium, compared to the ionization degree of hydrogen. Therefore, the electron abundance of the neutral regions may increase by several tens of percent by helium ionization due to X-ray. In the sense that the higher electron abundance strengthens FUV heating more, as discussed in Section 3.3.1, Section 3.3.2, and Section 3.3.3, including X-ray ionization of helium works in a manner to confirm our conclusions. Nonetheless, and so helium ionization by X-ray is not incorporated in our chemistry to save the computational cost for the calculation of the chemistry network. we do not include helium ionization by X-ray in our chemistry network to reduce the computational cost of our simulations.

3.2.1.3 X-Ray Heating

The total energy deposited to primary electrons ejected by X-ray absorption is

$$\epsilon_{\text{tot}} = \int_{E_{\text{min}}}^{E_{\text{max}}} dE F(E) e^{-\tau_X} \sigma n_{\text{H}}. \quad (3.14)$$

The primary electron energy results in gas heating and inducing other physical processes, such as secondary ionization and excitations of the ambient gas. About 10% of the total deposited energy goes into heating in fully atomic gas (Maloney *et al.* 1996). Approximately 40% of the energy works as gas heating in a fully molecular gas. Hence, the X-ray heating rate can be set to

$$\Gamma_{\text{X}} = f_{\text{h}} \epsilon_{\text{tot}} \rho^{-1}, \quad (3.15)$$

$$f_{\text{h}} \equiv \frac{0.1y_{\text{HI}} + 0.4y_{\text{H}_2}}{y_{\text{HI}} + y_{\text{H}_2}}, \quad (3.16)$$

where f_{h} is the heating efficiency of the X-ray heating rate.

3.2.2 Chemistry Model

We incorporate the chemical reactions listed in Table 2.2, and add several reactions involving H_2^+ to our chemical network. The additional reactions are shown in Table 3.2.

Table 3.2 Chemical Reactions Incorporated Additionally in Our Simulations

Label	Reaction	Rate Coefficient	Reference
k9	$\text{H} + \text{H}^+ \longrightarrow \text{H}_2^+$	$10^{-19.38-1.523 \log T+1.118(\log T)^2-0.1269(\log T)^3}$	1
k10	$\text{H}_2^+ + \text{H} \longrightarrow \text{H}_2 + \text{H}^+$	6.4×10^{-10}	1
k11	$\text{H}_2 + \text{H}^+ \longrightarrow \text{H} + \text{H}_2^+$	$3.0 \times 10^{-10} \exp[-2.1050 \times 10^4 \text{ K}/T]$	1
p4	$\text{H} + \gamma \longrightarrow \text{H}^+ + \text{e}$	$R_{\text{X,H}}$ (cf. Eq.(3.10))	2
p5	$\text{H}_2 + \gamma \longrightarrow \text{H}_2^+ + \text{e}$	$R_{\text{X,H}_2}$ (cf. Eq.(3.13))	2

References. (1) Omukai (2000); (2) Gorti and Hollenbach (2004)

3.3 Results

We investigate the structure of PPDs and the photoevaporation rate. The results of the solar metallicity case is first presented in Section 3.3.1. Then, the metallicity dependence is discussed in Section 3.3.2 and Section 3.3.3.

3.3.1 Solar Metallicity Disk

In Figure 3.1, photoevaporative winds are driven in all the cases. We observe dense photoevaporative flows of atomic and molecular hydrogen in Run FEX/Z0 and Run FE/Z0, but not in Run EX/Z0. Photoevaporative flows of ionized hydrogen are excited in all the three cases. The panel of Run EX/Z0 in Figure 3.1 directly shows that X-ray, which heats the neutral regions, is not effective to drive the neutral flows, and only EUV-driven flows are launched at the low-density disk surface. As discussed in Chapter 2, FUV heating is a key process to excite the neutral winds even if X-ray effects are incorporated.

Following Chapter 2, we measure the photoevaporation rate \dot{M}_{ph} with Eq.(2.37)

$$\dot{M}_{\text{ph}} = \int_S d\mathbf{S} \cdot \rho \mathbf{v} = r_S^2 \int_S d\theta d\phi \sin \theta \rho v_r.$$

Again, we regard a gas parcel with a positive total specific enthalpy $\eta > 0$ as unbound (Liffman 2003), and count its contribution to \dot{M}_{ph} . The total specific enthalpy is given by Eq.(2.38)

$$\eta = \frac{1}{2} \mathbf{v}^2 + \frac{\gamma}{\gamma - 1} c_s^2 - \frac{GM_*}{r}.$$

With this condition, we can effectively exclude the contributions from the bound disk region ($\eta < 0$) to the mass-loss rate.

In Section 2.3.3, we show that \dot{M}_{ph} measured by Eq.(2.37) generally increases with r_S because the base temperatures generally have a smoother profile than that of the temperature necessary to escape from the gravity that has the scaling of $\propto r^{-1}$. Thus, \dot{M}_{ph} should be measured with different r_S , otherwise we artificially neglect the contribution. We set $r_S = 20, 100, 200$ au for each of Run FEX, Run FE, and Run EX. As for the solar-metallicity disk, we additionally perform Run X/Z0 to directly examine if X-ray drives the neutral flows, and whether the flows contribute to \dot{M}_{ph} . The photoevaporation rates with $r_S = 20$ au show the contribution from the $r < 20$ au region, while those with $r_S = 100$ au and $r_S = 200$ au show a contribution from the bulk of the disk surface. In

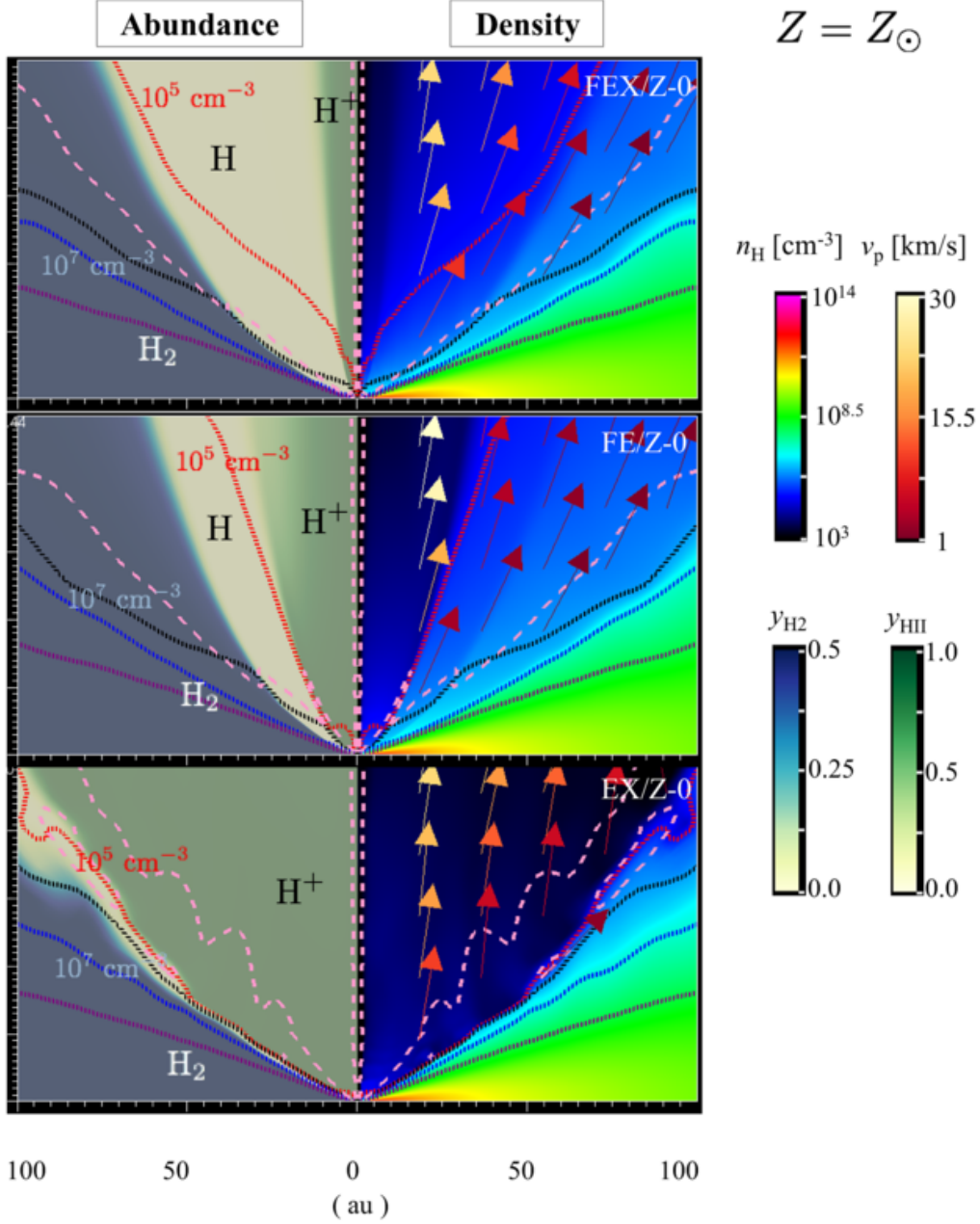


Fig. 3.1 Structures of solar metallicity disks in Run FEX/Z0 (top), Run FE/Z0 (middle), and Run EX/Z0 (bottom). The chemical structures are shown in the left, and the density structure is shown in the right. The poloidal velocity fields are represented by the arrows colored according to the magnitude. Note that we show only arrows with the poloidal velocities of $v_p > 1 \text{ km s}^{-1}$. The density contours are indicated by the dotted lines: $n_H = 10^5 \text{ cm}^{-3}$ (red), $n_H = 10^6 \text{ cm}^{-3}$ (black), $n_H = 10^7 \text{ cm}^{-3}$ (blue), and $n_H = 10^8 \text{ cm}^{-3}$ (purple). The pink dashed lines represent the sonic surface.

the simulations, \dot{M}_{ph} varies in time for the first ~ 5000 years, but then becomes largely constant. Time average of \dot{M}_{ph} is taken over 5000 yr to give a mass-loss rate of the disks. Table 3.3 presents the resulting \dot{M}_{ph} for Run FEX/Z0, Run FE/Z0, Run EX/Z0, and Run X/Z0 with $r_S = 20$ au,

Table 3.3 Resulting Photoevaporation Rates \dot{M}_{ph} of the Solar Metallicity Disk in $M_{\odot} \text{ yr}^{-1}$

r_S	Run FEX/Z0	Run FE/Z0	Run EX/Z0	Run X/Z0
20 au	6×10^{-9}	3×10^{-9}	2×10^{-10}	5×10^{-12}
100 au	2×10^{-8}	2×10^{-8}	1×10^{-9}	1×10^{-11}
200 au	3×10^{-8}	3×10^{-8}	2×10^{-9}	2×10^{-11}

$r_S = 100$ au, and $r_S = 200$ au. (See also the plot in Figure 3.4.)

Note that \dot{M}_{ph} of Run FEX/Z0 is slightly larger than that of Run FE/Z0, and \dot{M}_{ph} of Run EX/Z0 is smaller than those of Run FEX/Z0 and Run FE/Z0 by approximately ten times. A very small \dot{M}_{ph} is found for Run X/Z0. These results confirm that FUV is an important component to yield a high mass-loss rate, while X-ray has little contribution to cause a significant mass loss, though it affects the profile of the neutral flows (see Run FEX/Z0 and Run FE/Z0 in Figure 3.1).

X-ray heating of Run EX/Z0 is weaker than FUV heating of Run FEX/Z0 and Run FE/Z0 (see the second row of Figure 3.2). X-rays do not sufficiently heat the neutral regions up to high temperatures necessary to escape from the gravitational binding of the star. The gas has low temperatures comparable to the dust temperatures in the neutral region (the top right panel of Figure 3.2). Therefore, it is concluded that X-ray heating itself is inefficient to drive the neutral photoevaporative flows. In Run EX/Z0, the EUV-driven ionized flows account for a large portion of the mass-loss rate. The ionized flows have smaller densities than the neutral flows by several orders of magnitude (Figure 3.1), and hence the resulting \dot{M}_{ph} is much smaller than those in Run FEX/Z0 or in Run FE/Z0, where the FUV-driven flows significantly contribute to \dot{M}_{ph} .

In Run FEX/Z0 and Run FE/Z0, the dominant heating source is FUV heating in the neutral regions (Figure 3.2). The FUV heating rate is found to be increased in Run FEX/Z0, compared to in Run FE/Z0, near the ionization front. X-rays weakly ionize the gas and slightly increase the electron abundance there. It makes the recombination of dust grains efficient and reduces the positive charges of the grains. The photoelectric effect efficiency is increased by this effect (Gorti and Hollenbach 2009).

In summary, FUV heating is effectively strengthened by X-ray ionization in the neutral regions by increasing the photoelectric effect efficiency. The higher photoevaporation rate in Run FEX/Z0 than in Run FE/Z0 is resulted from the higher temperatures due to the strengthened FUV heating. The higher temperatures excite neutral photoevaporative flows in the regions close to the central star. Indeed, there exists a large difference in \dot{M}_{ph} with $r_S = 20$ au between Run FE/Z0 and Run FEX/Z0 (Table 3.3). Nevertheless, the contribution from the inner region is responsible for only a small portion of the total photoevaporation rates; outer regions dominantly contribute to the total mass-loss rates. It explains a small difference in the total mass-loss rates between Run FE/Z0 and Run FEX/Z0, when measured with $r_S = 100$ au or $r_S = 200$ au.

3.3.2 Photoelectric Heating in Disks with Low-Metallicities

A lower amount of dust enables FUV photons to reach a deeper interior of PPDs owing to the reduced opacity, and thus photoevaporative flows have a larger density for lower metallicities. By contrast,

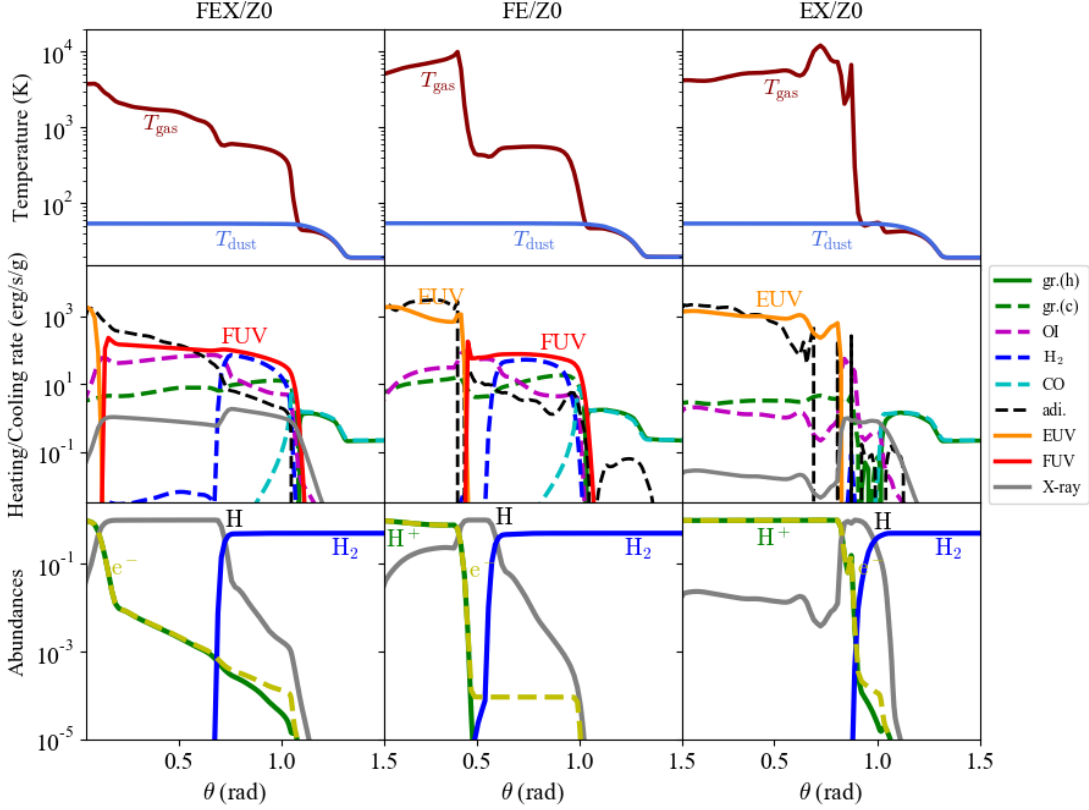


Fig. 3.2 Meridional distributions of the quantities at $r = 100$ au: temperatures of gas and dust (top), specific heating/cooling rates (middle), and chemical abundances of H, H^+ , H_2 , and electrons (bottom). In the middle row, heating rates are represented by the solid lines: EUV (orange), FUV (red), X-ray (grey), and dust-gas collision (green), while cooling rates are shown by the dashed lines: dust-gas collision (green), O I (magenta), H_2 (blue), CO (cyan), and adiabatic cooling (black). The distributions of the physical quantities in Run FEX/Z0, Run FE/Z0, and Run EX/Z0 for solar metallicity disks are shown in the columns from the left to the right.

as metallicity decreases, FUV heating becomes relatively ineffective to determine the temperatures of the neutral gas compared to dust-gas collisional cooling. The inefficient FUV heating decreases the base temperatures, as metallicity decreases. The neutral photoevaporative flows are not driven from such a “cool” disk. In Run FE, the balance of these competing effects results in the increase of \dot{M}_{ph} with $10^{-1} Z_{\odot} \lesssim Z \lesssim 10^{0.5} Z_{\odot}$, and the decrease of \dot{M}_{ph} with $10^{-2} Z_{\odot} \lesssim Z \lesssim 10^{-1} Z_{\odot}$ (see Figure 3.4). We note that the FUV-driven flows have a major contribution in the range of $Z \gtrsim 10^{-2} Z_{\odot}$, while the EUV-driven flows have a dominant contribution in the range of $Z \lesssim 10^{-2} Z_{\odot}$. Since atomic hydrogen is the dominant absorber of EUV, the EUV photoevaporation rates are largely independent of metallicity.

The effects of X-ray change the metallicity dependence of \dot{M}_{ph} (notice the difference between Run FEX and Run FE in Figure 3.4), but the trend is similar to each other; the reduced opacity increases \dot{M}_{ph} of Run FEX with lower metallicities for $Z \gtrsim 10^{-1.5} Z_{\odot}$, and \dot{M}_{ph} declines with decreasing metallicity in the range of $Z \lesssim 10^{-1.5} Z_{\odot}$ owing to the inefficient FUV heating.

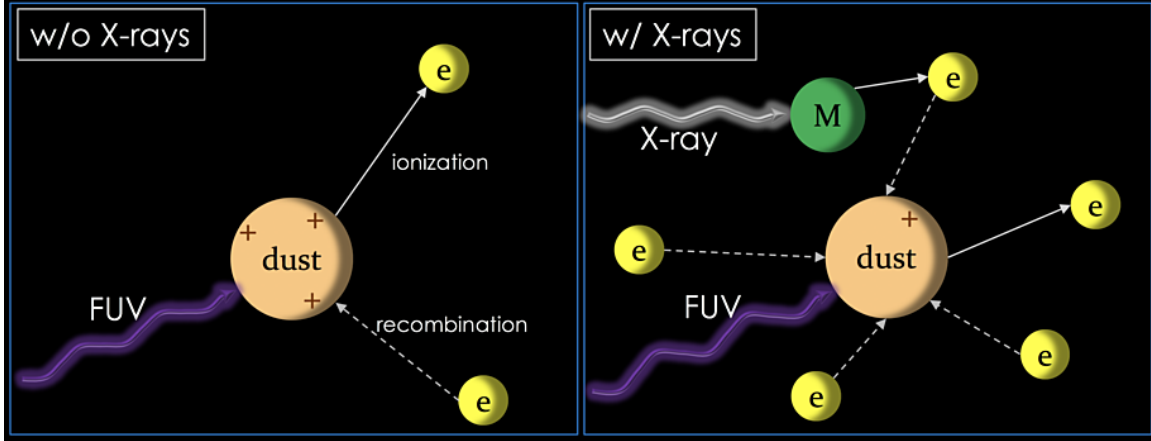


Fig. 3.3 Microscopic views of FUV heating without X-ray effects (left) and with X-ray effects (right). FUV photons are absorbed by the dust grains and produce thermalizing electrons through the photoelectric effect. If X-ray radiation is present as in the right panel, X-ray ionizes atoms (green sphere in the right panel) in the neutral regions. This makes the regions electron-rich and reduces positive charge of the grains there by the efficient recombination. As a result, the efficiency of the photoelectric effect is increased, which leads to a high heating efficiency of FUV.

3.3.3 X-Ray Ionization Effect

The electron abundance of the neutral regions is raised by X-ray ionization, and FUV heating is effectively *strengthened* in Run FEX. The gas temperatures of the neutral region generally become higher compared to Run FE. This yields the neutral photoevaporative flows excited from even inner regions of a disk. For $Z \gtrsim 10^{-1.5} Z_{\odot}$, photoevaporative flows are excited from the bulk of the disk surfaces. The X-ray effect decreases the radius in which all of the gas is gravitationally bound by star's gravity. However, inner regions have only a small contribution to the total photoevaporation rate (Figure 3.4), as discussed in Section 3.3.1. Photoevaporation rates are not significantly increased by the X-ray effect. That is, FUV heating is capable to drive the neutral photoevaporative flows even without the strengthening effect of X-rays in this metallicity range. This is in good contrast to the runs with the very low metallicities $10^{-2.5} Z_{\odot} \lesssim Z \lesssim 10^{-1.5} Z_{\odot}$.

In the metallicity range of $Z \lesssim 10^{-1.5} Z_{\odot}$, \dot{M}_{ph} of Run FEX decreases with decreasing metallicity owing to the inefficient FUV heating relative to dust-gas collisional cooling, but the decline is found to be smoother than in Run FE. In Run FEX, the electron abundance is increased by ionization of the dominant X-ray absorber, hydrogen. Thus, the electron abundance is essentially independent of metallicity in the neutral regions (Figure 3.5). Since the photoelectric effect efficiency varies according to the electron density only through the ratio of the dust/PAH photoionization rate to the dust/PAH recombination rate $\gamma_{\text{pe}} = G_{\text{FUV}}\sqrt{T}/n_e$ (see Eq.(2.24)), metallicity does not, at least explicitly, affect the photoelectric effect efficiency, when hydrogen ionization largely sets the electron abundance. The rich electron abundance makes FUV heating remain effective even at the low metallicities of $Z \lesssim 10^{-1.5} Z_{\odot}$ in Run FEX, which is not the case for Run FE. This explains the smoother decline of \dot{M}_{ph} in Run FEX than in Run FE.

There is a large difference between the photoevaporation rates of Run FEX and Run FE, especially for $10^{-2.5} Z_{\odot} \lesssim Z \lesssim 10^{-1.5} Z_{\odot}$. It can be due to an effect of the partial ionization by X-ray. For instance, in the $Z = 10^{-2} Z_{\odot}$ disk, the electron abundance is larger in Run FEX/Z-2 than in Run

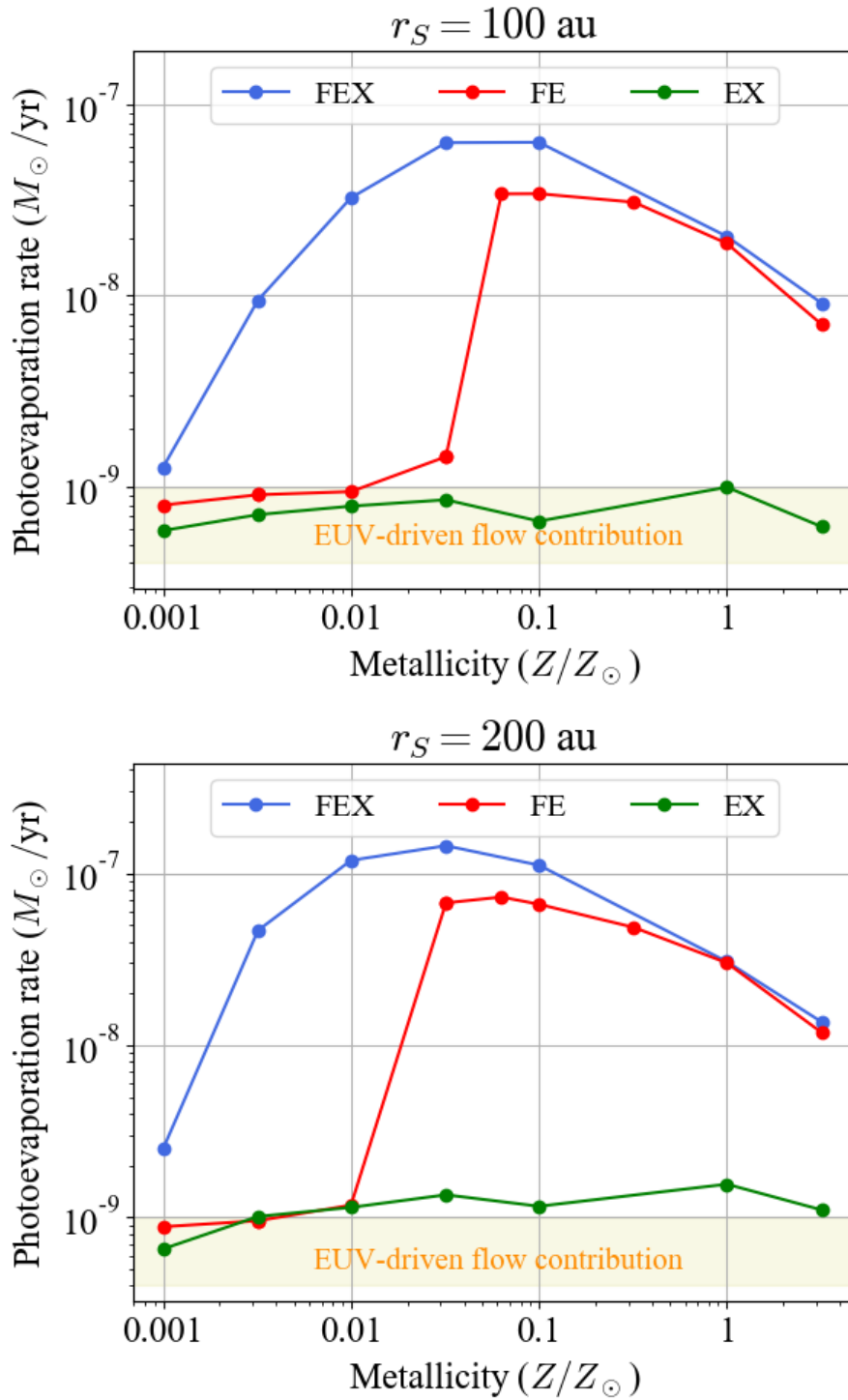


Fig. 3.4 Each panel shows the difference in the metallicity dependences of \dot{M}_{ph} for Run FEX (blue), Run FE (red), and EX (green). The contribution from the EUV-driven flow is approximately represented by the yellow regions ($\dot{M}_{\text{EUV}} \simeq 0.4\text{--}1 \times 10^{-9} M_{\odot} \text{ yr}^{-1}$). It separates the EUV photoevaporation rates from the total photoevaporation rates. The panels show \dot{M}_{ph} calculated with $r_S = 100 \text{ au}$ (top) and $r_S = 200 \text{ au}$ (bottom).

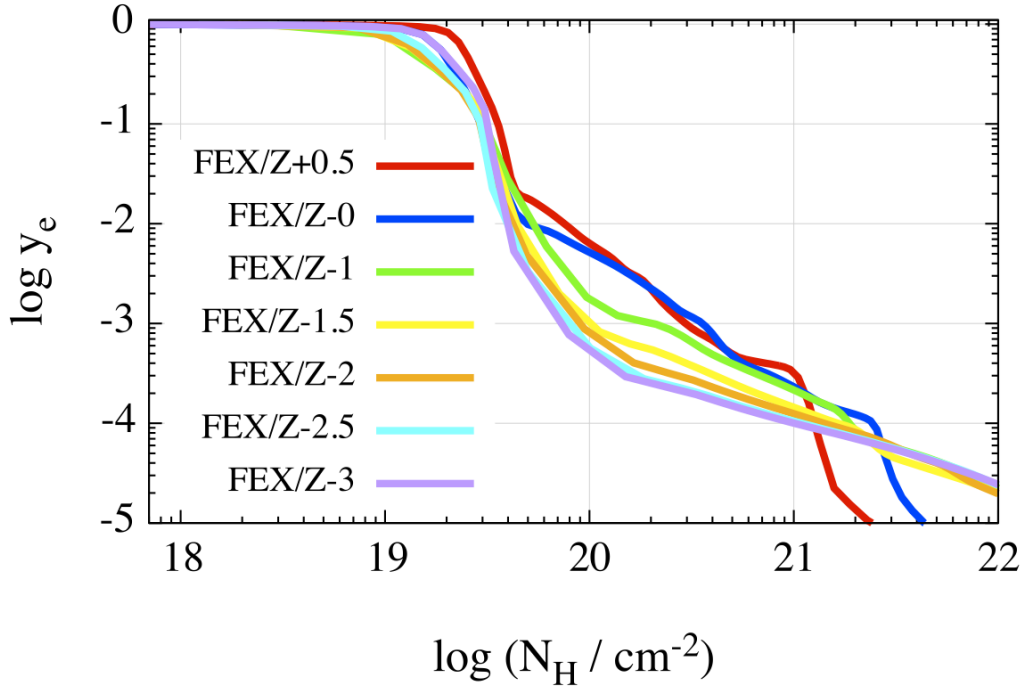


Fig. 3.5 Meridional distributions of electron abundance at $r = 100$ au in the disks with various metallicities. The data are taken from Run FEX. We note that here the horizontal axis indicates hydrogen nuclei column density N_{H} instead of θ unlike in Figure 3.2.

FE/Z-2 by two orders of magnitude in the low-density region ($n_{\text{H}} \sim 10^5\text{--}10^6 \text{ cm}^{-3}$) at ~ 100 au. The ratio $\gamma_{\text{pe}} = G_{\text{FUV}}\sqrt{T}/n_{\text{e}}$ (cf. Eq.(2.24)) is correspondingly small, with the typical value of $\sim 10^3(n_{\text{e}}/100 \text{ cm}^{-3})^{-1}$ in the low-density region. The value is smaller than in Run FE/Z-2 by almost two orders of magnitude. Thus, the photoelectric effect efficiency (Eq.(2.24))

$$\epsilon_{\text{pe}} = \left[\frac{4.87 \times 10^{-2}}{1 + 4 \times 10^{-3} \gamma_{\text{pe}}^{0.73}} + \frac{3.65 \times 10^{-2} (T/10^4 \text{ K})^{0.7}}{1 + 2 \times 10^{-4} \gamma_{\text{pe}}} \right],$$

is approximately an order of magnitude larger (Bakes and Tielens 1994). This increases the temperature by a factor of a few, and then the gas satisfies the “unbound condition” $\eta > 0$. Other regions of the disk are affected by X-rays in a similar manner; the X-ray effect increases the total specific enthalpy η of the gas to be positive. In Figure 3.6, the neutral region of Run FEX/Z-2 partially satisfies the unbound condition $\eta > 0$, whereas the unbound region appears to be almost identical to the H II region in Run FE/Z-2. In runs with $Z = 10^{-2} Z_{\odot}$, enabling X-ray ionization results in exciting the FUV-driven neutral photoevaporative flows that have a significant contribution to the mass-loss rate. The neutral flows, however, are not driven without the X-ray effects, and the mass-loss is mainly contributed by the EUV-driven flows. As a result, the mass-loss rate of Run FEX/Z-2 is significantly larger than that of Run FE/Z-2. The same conclusion holds for Run FEX and Run FE with $10^{-2.5} Z_{\odot} \lesssim Z \lesssim 10^{-1.5} Z_{\odot}$.

With the very low metallicities of $Z \lesssim 10^{-3} Z_{\odot}$, the neutral flows are not excited even with the strengthened FUV heating. Dust-gas collisional cooling is relatively strong compared to the X-ray-strengthened FUV heating. Hence, the mass-loss rates are not significantly different between Run FEX/Z-3 and Run FE/Z-3.

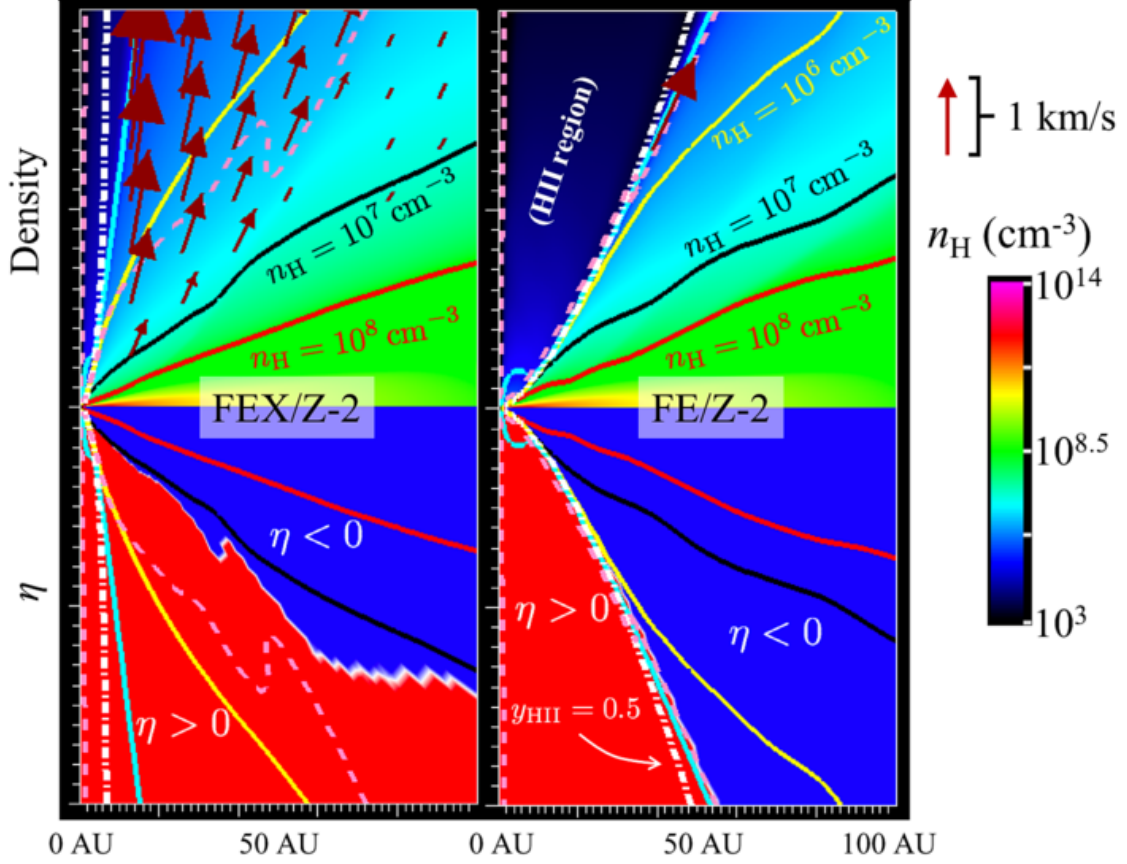


Fig. 3.6 Snapshots of FEX/Z-2 (left) and FE/Z-2 (right). The density distributions are shown in the top panels, and the distributions of η (Eq.(2.38)) are shown in the bottom panels, where the red and blue regions indicate unbound ($\eta > 0$) regions and bound ($\eta < 0$) regions, respectively. The velocity field with $0.25 \text{ km s}^{-1} < v_p < 0.5 \text{ km s}^{-1}$ is indicated by the arrows scaled by its magnitude. The velocity field are not shown in the H II regions ($y_{\text{HII}} > 0.5$) for clarity. The density contours are indicated by the solid lines: $n_{\text{H}} = 10^5 \text{ cm}^{-3}$ (cyan), $n_{\text{H}} = 10^6 \text{ cm}^{-3}$ (yellow), $n_{\text{H}} = 10^7 \text{ cm}^{-3}$ (black), and $n_{\text{H}} = 10^8 \text{ cm}^{-3}$ (red). Note that we draw the velocity arrows and density contours in different manners from Figure 3.1. The white dot-dashed lines represent contours of $y_{\text{HII}} = 0.5$, which is an approximate boundary between the H II region and the other. The sonic surfaces are shown by the pink dashed lines.

3.3.4 Mass-Loss Profile

For a symmetric disk with respect to the rotational axis and the mid-plane, the total photoevaporation rate \dot{M}_{ph} is calculated as the integration of the surface mass-loss rate $\dot{\Sigma}_{\text{ph}}$,

$$\dot{M}_{\text{ph}} = \int 2\pi R \dot{\Sigma}_{\text{ph}} dR. \quad (3.17)$$

The surface mass-loss rate $\dot{\Sigma}_{\text{ph}}$ is also referred to as the mass-loss profile, as it explains the contribution of the mass-loss from a disk annulus at R . The mass-loss profile is especially important to determine the secular viscous evolution of PPDs. In the later stage of the evolution, the surface accretion rate $\dot{\Sigma}_{\text{acc}}$ of a PPD drops below the surface photoevaporation rate $\dot{\Sigma}_{\text{ph}}$ at a certain radius. The disk annulus at the radius loses its mass owing to photoevaporation otherwise it were supplied

to the inner annulus through accretion. The inner annulus also supplies its mass to the further inner annulus but can not gain mass from the outer reservoir. A gap then opens at the radius, and the disk is split into the inner and outer disks. The inner disk clears within the viscous timescale (Eq.(1.33)), leaving a disk with a transitional-disk-like structure (Clarke *et al.* 2001, Alexander *et al.* 2006, Owen *et al.* 2010). The mass-loss profile is thus essential to determine the hole sizes of transitional disks.

The mass-loss profile in Eq.(3.17) gives one-dimensional mass loss rates, i.e. $\dot{\Sigma}_{\text{ph}}$ can be interpreted as the mass loss rates per unit area from an infinitesimally thin disk. In practice, a PPD has a finite scale height H at each R ; $\dot{\Sigma}_{\text{ph}}$ should express the mass flux coming out of the base. Thus,

$$\dot{M}_{\text{ph}} = 2 \int_S \rho_b \vec{v}_p \cdot d\vec{S}, \quad (3.18)$$

where S is the disk surface (base), and $d\vec{S}$ is an infinitesimal surface element vector orthogonal to the base. The first factor of two indicates the contribution from the two sides of the disk surface. In this section, we define the base as the surface where the optical depths for UV and X-ray photons are equal to unity. For instance, the base for EUV and FUV photoevaporative flows are identical with the $\tau_{\text{EUV}} = 1$ and $A_V = 1$ surfaces, respectively. Assuming that the base profile is given by $z = f(R)$ and photoevaporative flows are launched at v_p with β which is the angle between \vec{v}_p and the base (cf. Figure 2.10), Eq.(3.18) reduces to

$$\begin{aligned} \dot{M}_{\text{ph}} &= 2 \int_S \rho_b v_p \sin \beta \sqrt{1 + \left(\frac{df}{dR}\right)^2} R d\phi dR \\ &= 2 \int 2\pi R \rho_b v_p \sin \beta \sqrt{1 + \left(\frac{df}{dR}\right)^2} dR. \end{aligned} \quad (3.19)$$

Hence, for an axisymmetric disk with a finite scale-height, $\dot{\Sigma}_{\text{ph}}$ is defined as

$$\dot{\Sigma}_{\text{ph}} = 2\rho_b v_p \sin \beta \sqrt{1 + \left(\frac{df}{dR}\right)^2}. \quad (3.20)$$

The mass-loss profile depends on the parameters: ρ_b , v_p , β , and f , which are determined by the hydrodynamical profiles of photoevaporative flows. Although the so-called ρc_s model (Hollenbach *et al.* 1994, Ercolano *et al.* 2009, Gorti and Hollenbach 2009, Tanaka *et al.* 2013) is successful to predict photoevaporation rates with a hydrostatic method to some extent, there is no choice but to make assumptions for these parameters. This could yield different $\dot{\Sigma}_{\text{ph}}$ and thereby \dot{M}_{ph} from more accurate ones derived from numerical simulations. In fact, Owen *et al.* (2010) showed that those derived by the ρc_s model and by hydrodynamics simulations have different values. Especially, the launching velocity v_p and angle β are strongly dependent on details of flow structure; it is important to perform hydrodynamics simulations to determine the parameters accurately.

Using the result of the simulation where a solar metallicity disk is illuminated by UV and X-ray, we obtain $\dot{\Sigma}_{\text{ph}}$ for the case of Z0/FEX (the purple crosses in Figure 3.7). The mass-loss profile monotonically decreases toward the larger radii with approximately $\propto R^{-1.56}$ for $R > 1$ au. We compare the profile with that of Owen *et al.* (2012), where the results of the hydrodynamics simulations in Owen *et al.* (2010) and Owen *et al.* (2011a) are used. The mass-loss profile is given

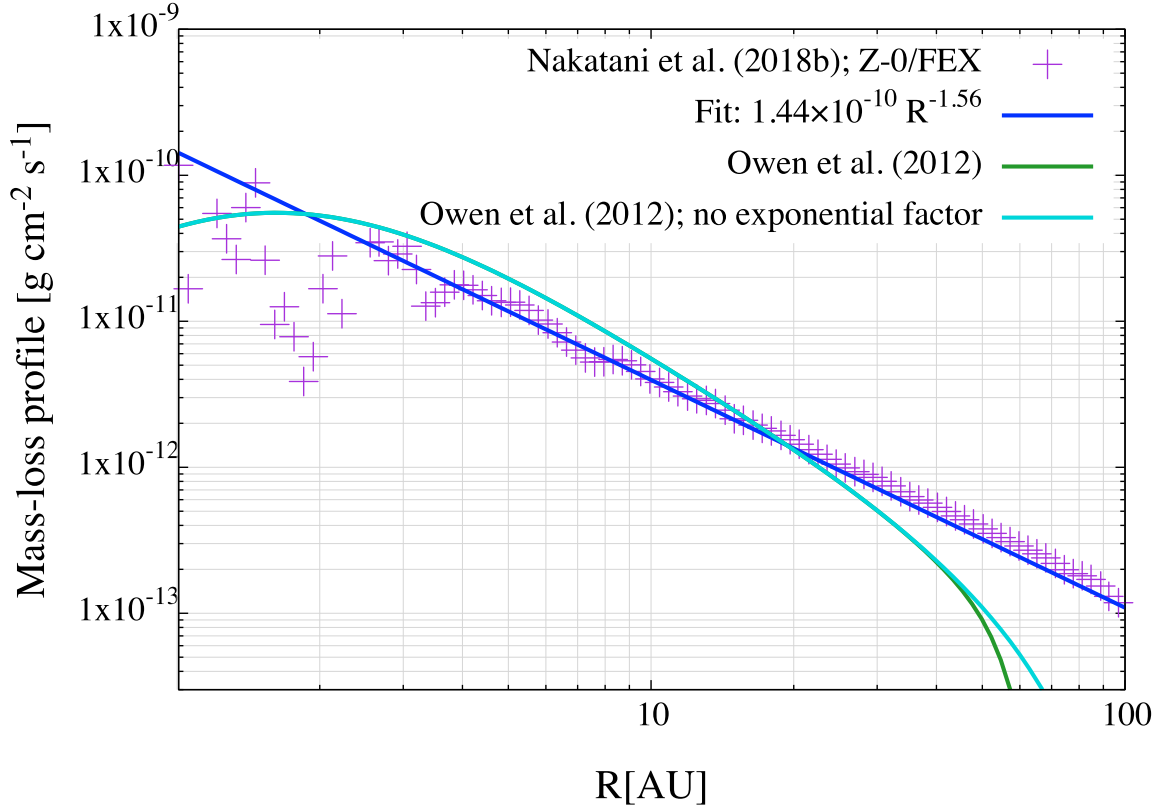


Fig. 3.7 Mass-loss profiles of Z0/FEX (purple crosses) and Owen *et al.* (2012) (green and cyan lines). The green line shows the mass loss profile of Eq.(3.21), and the cyan line shows that without the last exponential factor in Eq.(3.21). Note that the mass-loss profile of Owen *et al.* (2012) is given in arbitrary units, but it is multiplied by $1 \times 10^{-8} \text{ g cm}^{-2} \text{ s}^{-1}$ in this panel to compare our mass-loss profile directly. The blue line is a fit for the mass-loss profile of Z0/FEX within $2.5 \text{ au} \leq R \leq 100 \text{ au}$.

as

$$\begin{aligned} \dot{\Sigma}_w(x > 0.7) = & 10^{0.15138(\log x)^6 - 1.2182(\log x)^5 + 3.4046(\log x)^4 - 3.5717(\log x)^3 - 0.32762(\log x)^2 + 3.6064 \log x - 2.4918} \\ & \times \left[6 \times \frac{0.15138(\log x)^5}{x^2(\ln 10)^7} - 5 \times \frac{1.2182(\log x)^4}{x^2(\ln 10)^6} + 4 \times \frac{3.4046(\log x)^3}{x^2(\ln 10)^5} \right. \\ & \left. - 3 \times \frac{3.5717(\log x)^2}{x^2(\ln 10)^4} - 2 \times \frac{0.32762(\log x)^2}{x^2(\ln 10)^3} + \frac{3.6064}{x^2(\ln 10)^2} \right] \exp \left[- \left(\frac{x}{100} \right)^{10} \right], \\ \text{where } x = & 0.85 \left(\frac{R}{\text{au}} \right) \left(\frac{M_*}{M_\odot} \right)^{-1}, \end{aligned} \quad (3.21)$$

(the green line in Figure 3.7; Owen *et al.* 2012). For $x < 0.7$, $\dot{\Sigma}_w = 0$. We believe that the last exponential factor in Eq.(3.21) would be originated from the adopted computational boundary which only extends to $r = 100 \text{ au}$ in the spherical polar coordinates. Since the base is flared with $\arctan(H/R) \sim 45^\circ$ (see Figure 3.(b) in Owen *et al.* (2010)), the radius is $R \sim 70 \text{ au}$ in the cylindrical polar coordinates at the intersection point of the base and the outer boundary. The mass-loss rates of Owen *et al.* (2010) and Owen *et al.* (2011a) are measured at $r = 85 \text{ au}$ to avoid the effects from spurious reflections on the photoevaporation rates. The total photoevaporation rate contains the

contribution only from $R \lesssim 60$ au. Therefore, we expect that Eq.(3.21) provides the mass-loss profile of X-ray photoevaporation only for $R \lesssim 60$ au. In order to compare the mass loss profiles of ours and Owen *et al.* (2012) at a large distance, we also show the mass-loss profiles of Owen *et al.* (2012) without the last exponential factor (the cyan line in Figure 3.7).

The difference in the mass-loss profiles of Owen *et al.* (2012) our Z0/FEX is within a small factor for $R \lesssim 40$ au, while it becomes larger with R . The difference is almost an order of magnitude at $R = 60$ au. In addition, the mass-loss profile of Owen *et al.* (2012) decreases more rapidly with increasing R than that of Z0/FEX. We discuss several possible origins of these differences in the following.

First, we conclude that FUV is the main driver of photoevaporation and X-ray effect is limited as a driver. Our mass-loss profile is for FUV photoevaporation (Figure 3.7). In contrast, FUV is not incorporated in the simulations of Owen *et al.* (2010) and Owen *et al.* (2011a), and thus the mass-loss profile is for X-ray photoevaporation. The different heating mechanisms of the two studies can yield different base temperatures and mass-loss profiles. In Z0/FEX, the base temperature has a profile of $\propto R^{-0.46}$ (Figure 3.8(c)). The base temperature profile of Owen *et al.* (2010) or Owen *et al.* (2011a) is not provided; we cannot directly compare the profiles of the studies. Instead, we approximately estimate the base temperature of Owen *et al.* (2010) as follows. The base density of Owen *et al.* (2010) is assumed to be similar to that of our Z0/FEX *2

$$n_b \simeq n_1 \left(\frac{R}{\text{au}} \right)^{-\alpha}, \quad (3.22)$$

where $n_1 \sim 10^8 \text{ cm}^{-3}$ is the base density at $R = 1$ au and $\alpha \simeq 1.2-1.5$ is a fitting index. The ionization parameter $\xi = L_X/nr^2$ (Owen *et al.* 2010) is then calculated as

$$\xi \sim 10^{-5}-10^{-4} \left(\frac{L_X}{10^{30} \text{ erg s}^{-1}} \right) \left(\frac{n_1}{10^8 \text{ cm}^{-3}} \right)^{-1} \left(\frac{R}{\text{au}} \right)^{-(2-\alpha)}. \quad (3.23)$$

According to Figure.2(a) of Owen *et al.* (2010), the temperature is approximately scaled as $T \propto \xi^{1.5}$ for the radius range of interest $1 \text{ au} \leq R \leq 100 \text{ au}$ corresponding to $10^{-6} \lesssim \xi \lesssim 10^{-4}$. Consequently, we obtain $T \propto R^{-\beta}$ ($\beta = 1.2-0.75$) as the base temperature profile in Owen *et al.* (2010). The base temperature more rapidly declines with increasing R than that of our Z0/FEX. The rapid decline of the base temperature results in a rapid decrease of $\dot{\Sigma}_{\text{ph}}$ with increasing R : $\dot{\Sigma}_{\text{ph}} \propto n_b c_s \propto R^{-(\alpha+\beta/2)} \simeq R^{-1.9}$. This estimated radius dependence is in good agreement with Eq.(3.21) which gives $\Sigma_w \propto R^{-2}$ in $5 \text{ au} \lesssim R \lesssim 30 \text{ au}$. Hence, we can conclude that the difference in the base temperature profiles due to the different heating would be one of the causes for the different $\dot{\Sigma}_{\text{ph}}$ in Owen *et al.* (2012) and Z0/FEX.

Second, the adopted outer boundary is $r = 400$ au in this study for the same reason as Owen *et al.* (2010). We show that the spurious reflection of subsonic flows at the outer boundary reduces the contribution from the region close to the boundary to the total mass loss rate (Section 2.4.4). The radius where the photoevaporation rates are measured needs to be sufficiently distant from the outer boundary. In Owen *et al.* (2010) and Owen *et al.* (2011a), however, the photoevaporative flows launched from $R \gtrsim 50-60$ au seem not to be accelerated to a supersonic velocity yet before they reach the outer boundary (See Figure 3.(b) in Owen *et al.* (2010)). This could result in underestimation

*2 This assumption would be well reasonable as the definition of the base is similar to ours in Owen *et al.* (2010) and Owen *et al.* (2011a), where it is defined as the surface at which the column to the central star is less than $N_{\text{H}} \leq 10^{22} \text{ cm}^{-2}$.

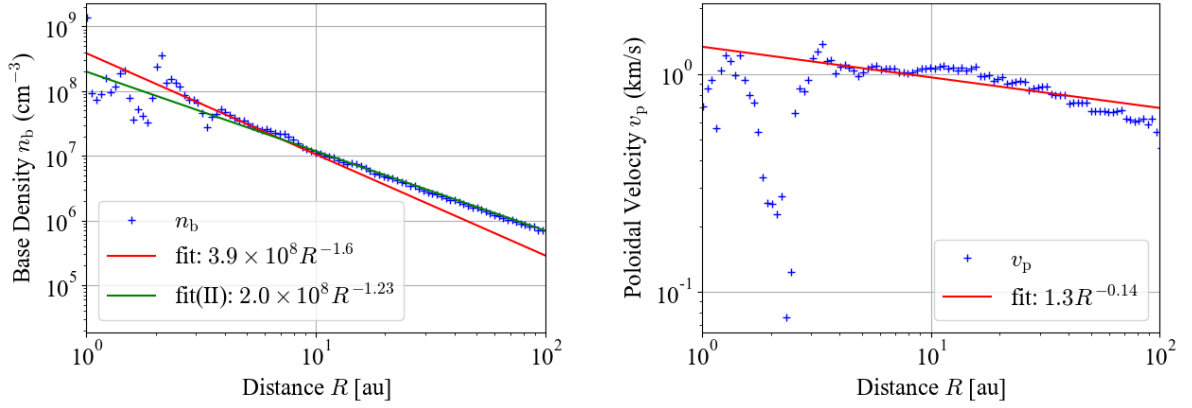
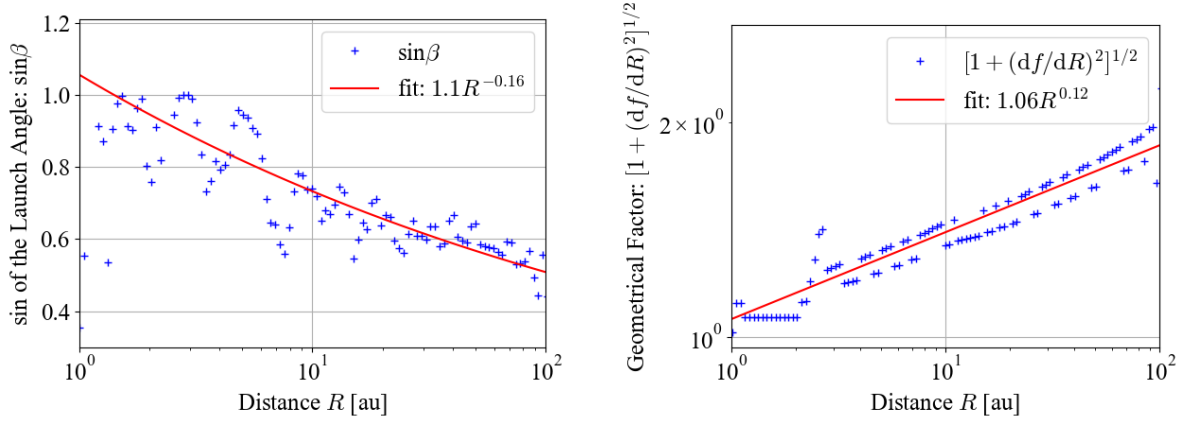
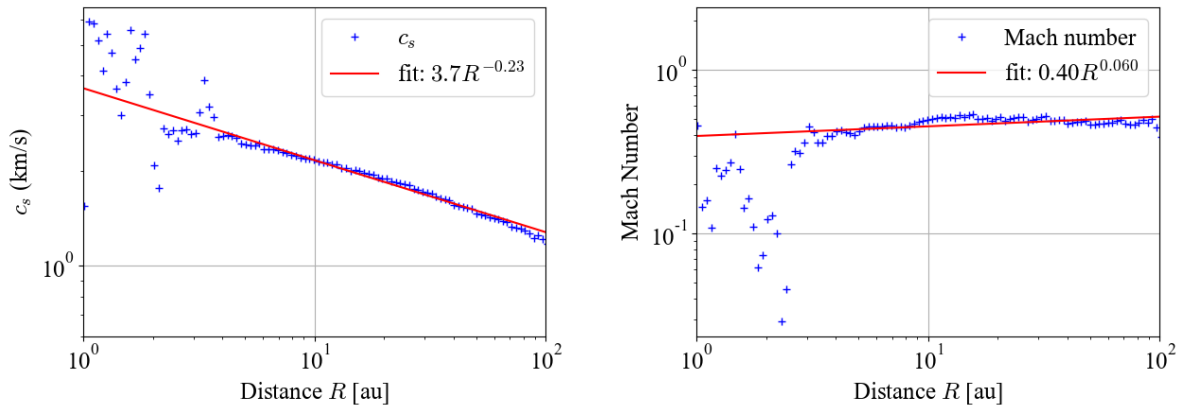
(a) Profiles of density n_b and poloidal velocity v_p (b) Profiles of the launching angle β and the geometrical factor $\sqrt{1 + f'^2}$ (c) Profiles of the sound speed c_s and the mach number \mathcal{M}

Fig. 3.8 Base profiles of Z0/FEX (blue dots). The red solid lines are fits of the profiles for $2.5 \text{ au} \leq R \leq 100 \text{ au}$. Note that a fit for $10 \leq R \leq 100 \text{ au}$ is also presented as the green line in the panel of n_b for comparison.

of the mass-loss from the region (Section 2.4.4).

Finally, the differences in the adopted methods could be other possible causes of the difference in the mass-loss profiles. Owen *et al.* (2010) adopts the “ionization parameter” approach, while we self-consistently solve non-equilibrium chemistry for multi-species, taking account of molecular line cooling due to H₂ and CO, and radiative transfer for photons whose energy ranges from IR to X-ray. This difference may yield differences in thermal structures of the disks even if the same physical processes are considered. The thermal structure sets the disk flaring and thereby the base configuration. Since $d\dot{M}_{\text{ph}} \propto R^2 \dot{\Sigma}_{\text{ph}}(R) d(\ln R)$ (cf. Eq.(3.17)), a larger flaring can reduce $d\dot{M}_{\text{ph}}$ at the same column density N_{H} . This largely sets $\dot{\Sigma}_{\text{ph}}$. Actually, the base flaring in Z0/FEX has a smaller value of $\arctan(H/R) \sim 30^\circ$ than that of Owen *et al.* (2010).

3.3.5 Lifetimes

Typical PPD lifetimes have been suggested to be about 3–6 Myr for solar metallicity disks (Haisch *et al.* 2001, Ribas *et al.* 2014) and ~ 1 Myr for those with $Z = 0.2 Z_\odot$ (Yasui *et al.* 2009, 2010, 2016b,a). Though there are large uncertainties in the observationally estimated lifetimes, we fit the metallicity dependence of the lifetimes as $T_{\text{lif}} \propto Z^{0.82}$ in Section 2.4.2. In this study, the estimated lifetimes of Run FEX have metallicity dependences of $T_{\text{lif}} \propto \dot{M}_{\text{ph}}^{-1} \propto Z^{0.64 \pm 0.07}$ for $0.1 Z_\odot \leq Z \leq 10^{0.5} Z_\odot$ with $r_S = 100$ au, and $T_{\text{lif}} \propto Z^{0.62 \pm 0.09}$ in Run FE. The metallicity dependences of the lifetimes are consistent with the observational metallicity dependence of the PPD lifetimes (Figure 3.9). Note that we currently have only the two data points for observational lifetimes in Figure 3.9. More data points are required for a more meaningful comparison with our model.

We show in the previous three sections that photoevaporative flows are not excited by X-ray heating in a direct manner. EUV-driven photoevaporative flows largely contribute to the total photoevaporation rate in Run EX. Therefore, Run EX does not show a metallicity-independent trend in \dot{M}_{ph} , and \dot{M}_{ph} is much smaller than in Run FEX or Run FE, where the mass loss is contributed by the dense FUV-driven flows. This suggests that when EUV heating dominantly contributes to drive photoevaporative flows as in our Run EX, EUV + X-ray radiation does not yield a metallicity-dependent trend in PPD lifetimes. Hence, given that the metallicity dependence of the PPD lifetimes are originated from the metallicity dependence of photoevaporation rates, our results directly indicate that FUV photoevaporation is the major cause to yield metallicity dependence in the disk lifetimes.

3.4 Discussion

Our conclusion is qualitatively consistent with that of Gorti and Hollenbach (2009) (hereafter, GH09), where it is concluded that although X-ray itself is not so effective heating source, X-ray ionization increases the photoelectric effect efficiency and amplifies the FUV photoevaporation rate. On the other hand, several previous studies have proposed X-ray as an important heating source to drive photoevaporation (Ercolano *et al.* 2008, 2009, Owen *et al.* 2012). However, the results of our self-consistent hydrodynamics simulations show that but our direct comparison shows that X-ray heating is ineffective to excite vigorous photoevaporative winds with a large mass-loss rate. This conclusion is in agreement with those of Alexander *et al.* (2004), Gorti and Hollenbach (2009), and Wang and Goodman (2017). In the following, we discuss the influences of several elements associated with our X-ray radiation model.

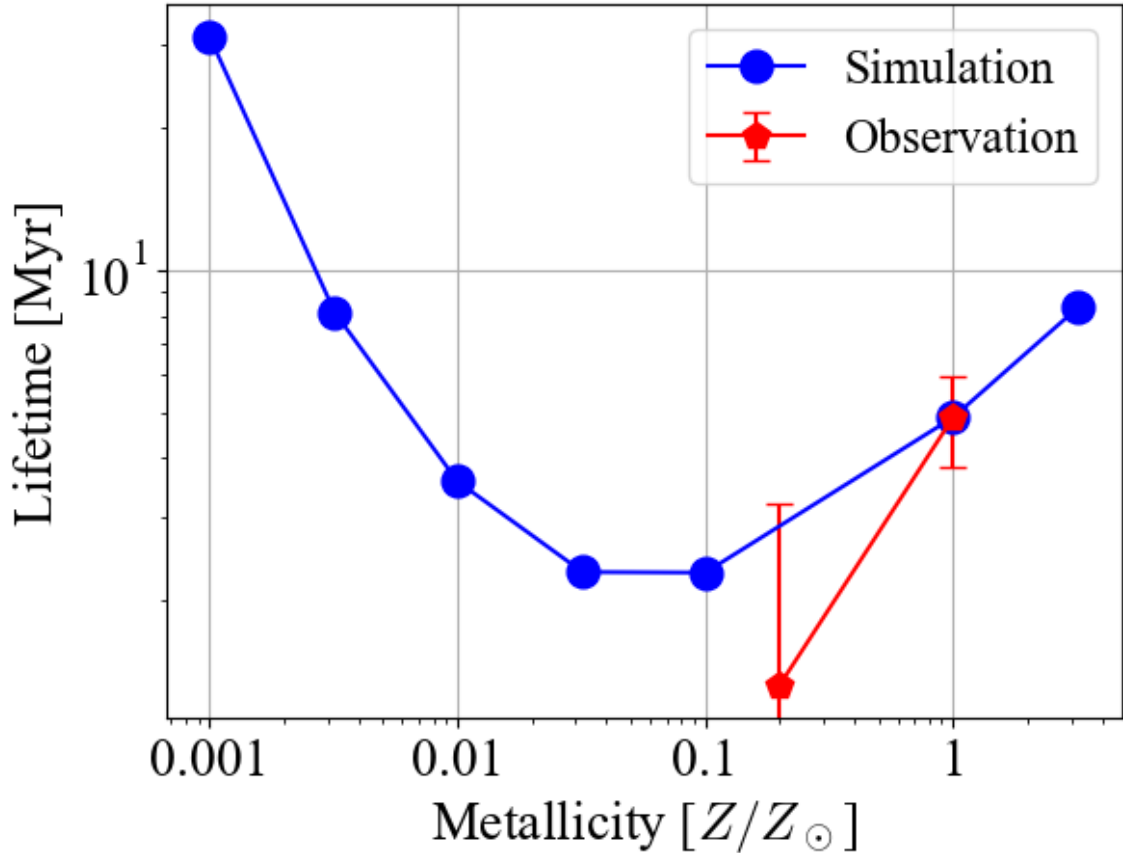


Fig. 3.9 Metallicity dependence of PPD lifetimes. The red points show the observationally estimated lifetimes. Here we adopt 4.9 ± 1.1 Myr at $Z = 1 Z_{\odot}$ and 1.3 ± 1.9 Myr at $Z = 0.2 Z_{\odot}$ (cf. Figure 1.3 and Table 1.1). The blue points show the evaporation timescale defined as $\propto \dot{M}_{\text{ph}}^{-1}$. We use \dot{M}_{ph} measured at $r_S = 100$ au in Run FEX to calculate the evaporation times. They are normalized so that the evaporation time coincides with the observational lifetime at solar metallicity. Note that we show the estimated lifetimes for Run FE in Figure 2.13.

3.4.1 Spectral Hardness of X-ray

The spectral hardness of X-ray generally has a large impact on the resulting photoevaporation rate. Table 1 of Ercolano *et al.* (2009) indicates that using a large “prescreening” column, i.e., increasing the hardness of the EUV + X-ray flux incident on a disk surface, results in a small photoevaporation rate. There are effectively no photons with $\lesssim 0.1$ keV, which are categorized into EUV in Ercolano *et al.* (2009), reaching the surface of a disk with the prescreening column of $N_{\text{H}} \geq 10^{21} \text{ cm}^{-2}$ (see Figure 3 of Ercolano *et al.* 2009). The resulting \dot{M}_{ph} is of the order of $10^{-11} M_{\odot} \text{ yr}^{-1}$ with this spectral hardness, and is two orders of magnitude less than those with the prescreening columns of $N_{\text{H}} \leq 10^{20} \text{ cm}^{-2}$. The incident flux includes the EUV component (≤ 0.1 keV) as well as X-ray with these columns. These results suggest that X-ray photoevaporation is *inefficient* with a hard spectrum, as has been also shown in Gorti *et al.* (2015). Our X-ray spectrum is similar to that with prescreening column of $N_{\text{H}} \sim 10^{21} \text{ cm}^{-2}$ in Ercolano *et al.* (2009), with which \dot{M}_{ph} is as small as $\sim 10^{-11} M_{\odot} \text{ yr}^{-1}$.

We perform additional test simulations in which our fiducial X-ray spectrum is shifted to lower energy ranges in order to examine whether using a harder spectrum actually results in a small \dot{M}_{ph} . Let $F(E)$ the fiducial X-ray spectrum. The shifted spectra have the profiles of $F(E \times \sqrt{10})$ and $F(E \times 10)$. The absolute values of the X-ray fluxes are set so that the total luminosity is fixed at $10^{30} \text{ erg s}^{-1}$. We show the shifted spectra with the yellow and blue lines in Figure 3.10. Henceforth,

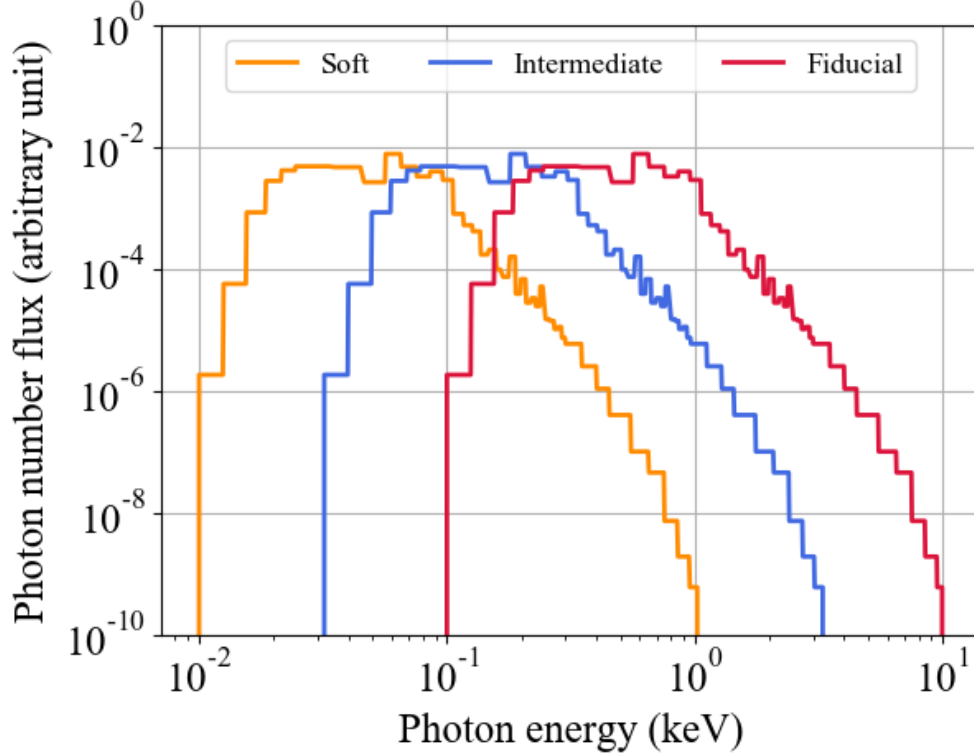


Fig. 3.10 Fiducial X-ray SED (red) and logarithmically shifted SEDs (blue and orange). The shifted SEDs are provided by $F(E \times \sqrt{10})$ (blue) and $F(E \times 10)$ (orange), where $F(E)$ is the fiducial SED function.

we call the shifted spectrum colored in yellow “the soft spectrum”, and the other colored in blue “the intermediate spectrum”. We employ Eq.(3.15) to calculate the photoheating rates as in our fiducial model. The heating efficiency f_{h} is assumed to be given by Eq.(3.16) also for the shifted spectra. The heating efficiency f_{h} is expected to be larger with the softer spectra, because the bulk of the energy deposited to primary electrons goes into heating via Coulomb interactions with the ambient electrons when $y_e \sim 1$ (Maloney *et al.* 1996). However, we neglect the photon energy dependence of the heating efficiency; we run simulations with $f_{\text{h}} = 1$ in Section 3.4.2. This corresponds to the limiting case in which whole deposited energy goes into heating. We do not take into account FUV heating in the test simulations here.

The maximum values of the photoheating rates (the gray lines in Figure 3.11) are larger with the soft and intermediate spectra than with our fiducial spectrum (the right column of Figure 3.2) by approximately an order of magnitude. The specific photoheating rate decreases as the spectral hardness increases. We also see in Figure 3.11 that low-energy photons are absorbed within low-density regions close to the ionization front. These results are attributed to the larger cross-section of the medium to lower energy photons. To summarize, as the cross section gets large, photons are absorbed with small columns, i.e. in low-density regions, but the resulting heating rate becomes

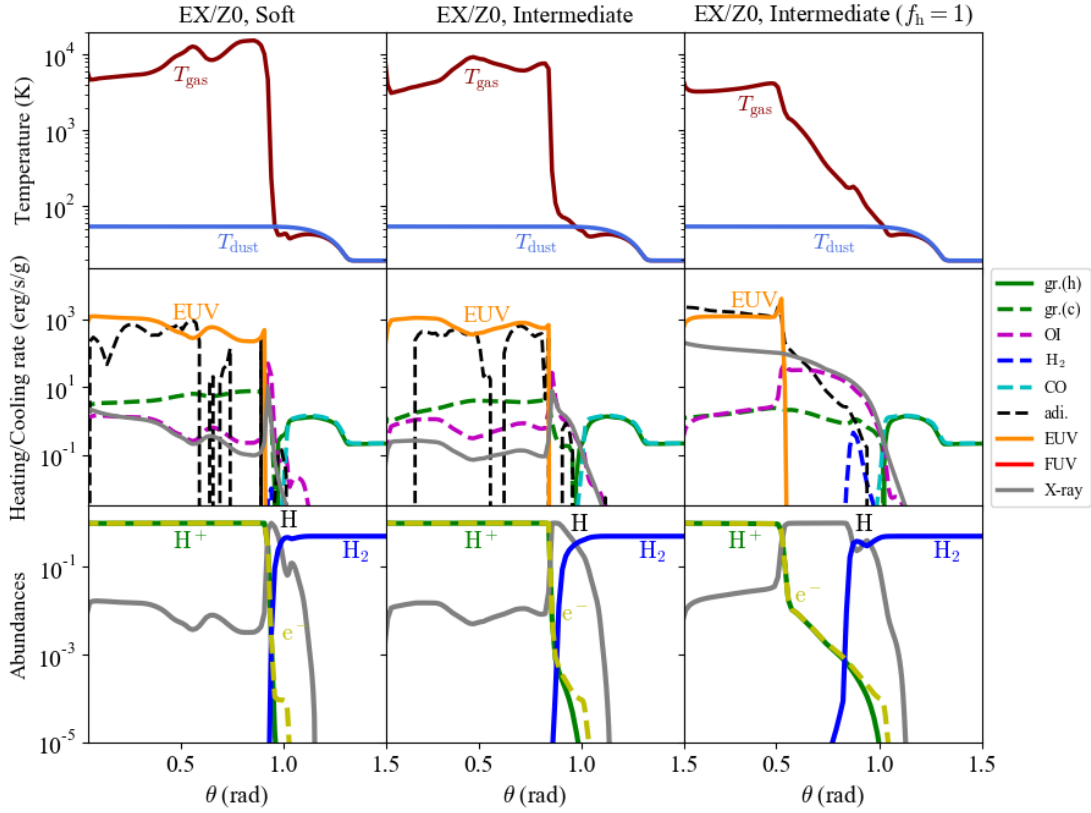


Fig. 3.11 Meridional distributions of the physical quantities at $r = 100$ au in the simulations with the soft spectrum (left), intermediate spectrum (middle), and intermediate spectrum with using $f_h = 1$ (right). The panels are presented in the same manner as Figure 3.2. We note that the photoheating calculated with the spectra is referred to as X-ray heating regardless of the fact that the soft and intermediate spectra technically contain the EUV component ($13.6 \text{ eV} \leq h\nu \leq 100 \text{ eV}$).

higher.

The gas temperature is raised by the photoheating with the soft and intermediate spectra only in the region near the ionization front, whereas it remains low in a large part of the neutral region, as seen in Figure 3.11. The gas is not sufficiently hot to drive neutral evaporative flows, and the EUV-driven flows dominate the mass loss. The resulting photoevaporation rates are compared for the soft, intermediate, and fiducial spectra in Figure 3.12. The photoevaporation rates are not crucially affected by the spectral hardness, though the thermal and chemical structure is changed (Figure 3.11).

3.4.2 Heating Efficiency

The heating efficiency f_h is another important factor to determine the photoheating rate. Using $f_h = 1$ increases the photoheating rate, as clearly seen in Figure 3.11, and makes the neutral region temperature higher than when using f_h of Eq.(3.16) (the left and middle columns in Figure 3.11). As a result, using the intermediate spectrum with $f_h = 1$ yields the highest photoevaporation rate

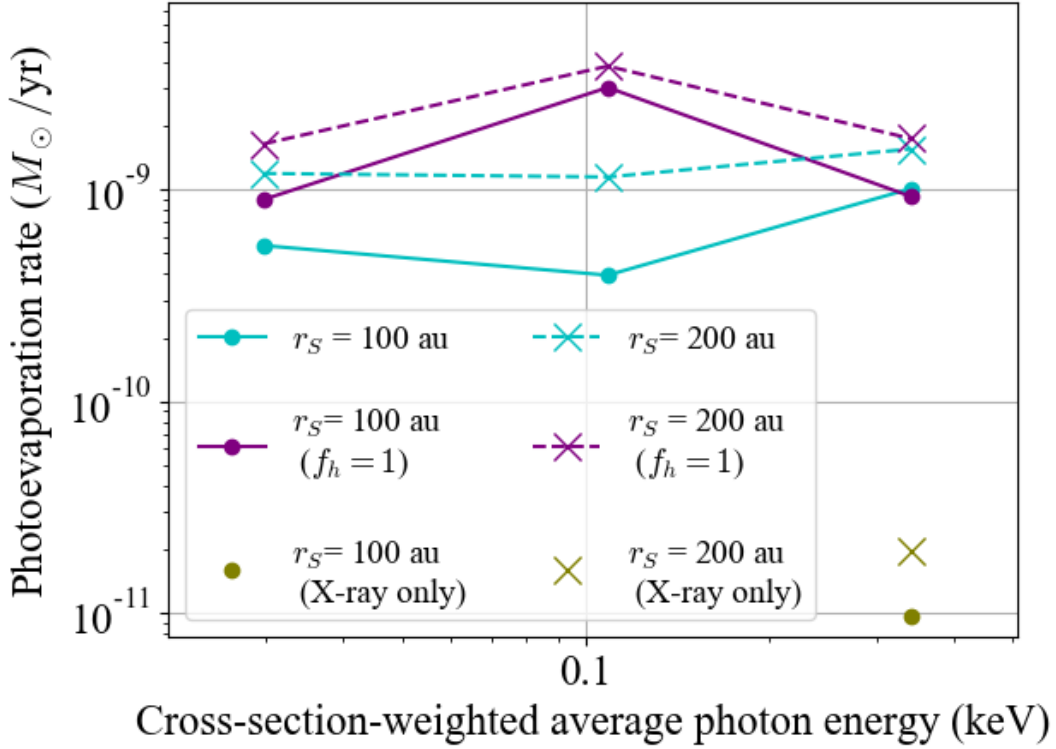


Fig. 3.12 Resulting \dot{M}_{ph} as functions of the cross-section-weighted average photon energy of the soft, intermediate, and fiducial spectra. The cyan and purple lines represent \dot{M}_{ph} derived from the simulations in which f_h is calculated by Eq.(3.16) and f_h is set to unity, respectively. The photoevaporation rates of Run X/Z0 are shown by the yellow points for comparison (cf. Table 3.3).

(Figure 3.12). We note that the cross-section-weighted mean energy \bar{E} is 0.03 keV and 0.11 keV for the soft and intermediate spectra, respectively; it is $\bar{E} = 0.34$ keV for our fiducial spectrum. The specific photoheating rate is still low even with $f_h = 1$ for the fiducial spectrum. The resulting photoevaporation rate is hardly changed from that in our fiducial model. Thus, it is concluded that the high-energy component of $\gtrsim 0.1$ keV is generally ineffective to drive neutral photoevaporative winds. This conclusion also holds for the hard component contained in the soft and intermediate spectra. The results of our test simulations directly indicate that EUV ($13.6 \text{ eV} \leq h\nu \leq 100 \text{ eV}$) is the major component to cause the mass loss, but not X-ray ($0.1 \text{ keV} \leq h\nu \leq 10 \text{ keV}$). Especially, hard EUV photons with $\sim 10^2 \text{ eV}$ are suggested to be the most effective component to cause a significant mass loss. These results confirm our conclusion that X-ray itself is not an efficient heating source for driving photoevaporation.

We directly compare \dot{M}_{ph} in the test simulations with those in Run X/Z0 Figure 3.12. Again, we see that X-ray is ineffective to drive photoevaporative flows. EUV dominantly contributes to the mass loss in the case where FUV heating is absent. Note that our results are consistent with Table 1 of Ercolano *et al.* (2009), in which we have found that the photoevaporation rates are significantly low without the EUV photons incident on the disk (see also Gorti *et al.* (2015)).

In Ercolano *et al.* (2009), the disk surface is irradiated by the EUV component if the prescreening column density is less than 10^{20} cm^{-2} . Our intermediate spectrum is similar to that of Ercolano *et al.* (2009) with $N_{\text{H}} = 10^{19}\text{--}10^{20} \text{ cm}^{-2}$. Their resulting photoevaporation rates are $\dot{M}_{\text{ph}} \simeq 4 \times$

$10^{-9} M_{\odot} \text{ yr}^{-1}$, and are quite similar to our resulting \dot{M}_{ph} of the simulation with the intermediate spectrum and $f_{\text{h}} = 1$ (Figure 3.12). Moreover, there is only a factor of two difference between the photoevaporation rate of Owen *et al.* (2012) and ours. Owen *et al.* (2012) adopt an “ionization parameter” approach in the hydrodynamics simulations, and gas temperatures are determined based on the results of the calculations with the unscreened spectrum in Ercolano *et al.* (2009). It is implied by the agreement between \dot{M}_{ph} in Owen *et al.* (2012) and this study that for a spectrum with a large amount of hard EUV $\sim 0.1 \text{ keV}$ photons, the ionization parameter approach provides essentially the same results as those derived in the simulations where heating and radiative cooling are calculated in a consistent manner. Nevertheless, self-consistent studies such as ours are necessary to examine the relative importance between X-ray and FUV.

In EX/Z0 with the intermediate spectrum and $f_{\text{h}} = 1$, the resulting \dot{M}_{ph} is about a factor of two smaller and the opening angle of the H II region is narrower (see the right column in Figure 3.11) than those in Owen *et al.* (2012). A number of differences in the adopted methods has the potential to cause these differences. This makes it difficult to specify critical causes. Nonetheless, comparing the results between our EX/Z0 with the intermediate spectrum and $f_{\text{h}} = 1$, and with the fiducial f_{h} (Eq.(3.16)) give important clues to understand the causes, because the different f_{h} makes differences in opening angles and \dot{M}_{ph} (Figure 3.11 and Figure 3.12). The comparison suggests that a higher heating efficiency f_{h} yields a larger photoevaporation rate and a narrower H II region, letting us assume that heating efficiency is somehow higher in Owen *et al.* (2012) than in our simulations. In fact, the X-ray-heated region temperature of Owen *et al.* (2012) is typically $\sim 4000\text{--}5000 \text{ K}$ at 2–10 au, whereas it is 2000–4000 K in our EX/Z0 with the intermediate spectrum and $f_{\text{h}} = 1$. Hence, we conclude that a larger heating efficiency may cause the narrower opening angle of Owen *et al.* (2012). Such high heating efficiency can be achieved in an electron-rich neutral region, because Coulomb interactions are efficient between primary electrons and the ambient electrons (Shull and van Steenberg 1985). We do not account for this effect in our test simulations for simplicity. Including the effect could increase X-ray heating rates especially in electron-rich regions. On the other hand, the heating rate can be also lowered in such regions because X-rays are hardly absorbed in a highly ionized medium. Incorporating the electron abundance dependence would raise X-ray heating rates by a small factor with the low electron abundances in the neutral regions of our model $y_{\text{e}} \sim 10^{-4}\text{--}10^{-2}$ (Figure 3.2 and Figure 3.11). Note that comparing Run FEX and Run FE, we actually see a narrower H II region produced by a higher heating rate in Run FEX, where FUV heating is strengthened by X-ray ionization (Figure 3.1 and Figure 3.6).

Wang and Goodman (2017) showed that photoevaporation rates are increased by disabling efficient cooling processes, regardless of the hard X-rays with 1 keV used in the simulations. For the purpose of examining whether it is also the case in our fiducial model, another test simulation is performed. we adopt $f_{\text{h}} = 1$ and the same setup as Run X/Z0, except that we disable all of the line cooling. Indeed, we obtain a modestly larger photoevaporation rate of $5 \times 10^{-9} M_{\odot} \text{ yr}^{-1}$ than our EUV photoevaporation rates. Hence, if all of the deposited energy to the primary electron effectively goes into heating and line cooling processes were inefficient, which might be unrealistic, a relatively efficient mass loss is caused by hard X-rays.

Overall, the heating efficiency f_{h} significantly affects the effectiveness of X-rays to drive photoevaporation. The exact profile of the high energy spectrum especially at $\sim 0.1 \text{ keV}$ also has a major effect on photoevaporation. Modeling a self-consistent heating efficiency and using a realistic spectrum is necessary for a comprehensive study regarding the effectiveness of X-ray (and hard EUV) on photoevaporation.

Finally, it is noteworthy that photoevaporation caused by a hard EUV likely depends on metal-

licity. The efficiency of the metal coolants in the neutral region, such as O I cooling and dust-gas collisional cooling, becomes small as metallicity decreases, and it might cause metallicity dependence of photoevaporation occurring in the neutral region. The exact spectrum profile should be taken into account although observing EUV spectrum is hard because of the extinction by circumstellar and interstellar matters. Similarly, a different \dot{M}_{ph} would be obtained with different FUV spectra. Further studies are warranted to address these issues associated with detailed conditions.

3.4.3 Input Parameter Uncertainties

We have concluded that the dense neutral flows are effectively driven by FUV but X-ray is inefficient to heat the gas. This conclusion is, at least partly, affected by input parameters, such as the abundance of polycyclic aromatic hydrocarbons (PAHs) and spectra/luminosities of FUV/EUV/X-ray. In this section, we discuss the model limitations that possibly arise from such uncertainties in input parameters.

· Grain Properties

Grain photoelectric heating is significantly contributed by PAHs and very small grains, and therefore their abundances are crucial to determine the FUV heating rate (Gorti and Hollenbach 2008, Gorti *et al.* 2009, 2015). The PAH abundances around T Tauri stars is observationally suggested to be smaller than the ISM value, which is adopted in our fiducial model. Though there remain large uncertainties in the observed abundances (Geers *et al.* 2007, Oliveira *et al.* 2010, Vicente *et al.* 2013), we have examined the impact of the PAH abundance on FUV photoevaporation in Section 2.4.3. FUV heating is effectively weakened by the reduced PAH abundance, but still, FUV drives the neutral photoevaporative flow even without the PAH contribution. The resulting photoevaporation rates are reduced but are the same orders of magnitude as the case where the PAH contribution is incorporated.

As well as the PAH abundance, the local size distribution of grains and their amounts have influences on photoelectric heating rates. They can spatially vary in PPDs because of the effects of dust growth/fragmentation, settling, entrainment, and other processes (Owen *et al.* 2011b, Hutchison *et al.* 2016b,a). In fact, observations have detected their variabilities in several PPDs (e.g., Pinte *et al.* 2016). The spatial distribution of grains accordingly changes the disk opacity. This may also strongly affect photoevaporation rates. Hence, it is necessary to take into account not only the reduced abundances of smaller grains but also different spatial distributions of grains with various sizes for accurate modeling of FUV photoevaporation.

· Stellar Luminosities and Spectra

There are also uncertainties in FUV and X-ray luminosities of young stars. A large fraction of FUV photons are considered to be produced in accretion shocks around a T Tauri star. T Tauri stars have a broad range of FUV luminosities with $10^{-6} L_{\odot} \lesssim L_{\text{FUV}} \lesssim L_{\odot}$. The FUV luminosities are known to approximately scale with the accretion rate \dot{M}_{acc} as $L_{\text{FUV}} \propto \dot{M}_{\text{acc}}$ (Gullbring *et al.* 1998, Yang *et al.* 2012). T Tauri stars also show a wide variety of X-ray luminosities with $10^{28} \text{ erg s}^{-1} \lesssim L_{\text{X}} \lesssim 10^{31} \text{ erg s}^{-1}$ (Güdel *et al.* 2007a, Vidotto *et al.* 2014). Typical plasma temperatures are measured to be $(5\text{--}30) \times 10^6 \text{ K}$, corresponding to the peak X-ray energy of $\sim 1 \text{ keV}$ (Güdel and Nazé 2009, Alexander *et al.* 2014). There is also a small number of T Tauri stars showing “soft X-ray excess” with temperatures of a few millions of kelvins (0.3–0.4 keV) (Güdel and Nazé 2009). TW Hya is one of such systems, and we use the observed X-ray spectrum of TW Hya. Therefore, our fiducial X-ray spectra may be relatively soft compared to a typical X-ray spectrum of T Tauri

stars. Even with such a relatively soft X-ray spectrum, X-ray is concluded to be ineffective for exciting photoevaporation in our fiducial model. Since softer components of an X-ray spectrum are important to drive photoevaporative flows as we have shown in Section 3.4.1 and Section 3.4.2, the conclusion would not be changed even if X-ray spectra without the soft X-ray excess are used. Note that X-ray spectra constructed from emission measure data are not necessarily the same as that actually reaching the surfaces of PPDs, considering the screening effect by the circumstellar medium and by the ISM on the line of sight. Note also that FUV and X-ray luminosities would independently vary in time during PPD evolution. Thus, the relative effectiveness of FUV/X-ray on photoevaporation with various luminosities and spectra is worth being examined.

Regarding EUV, the ISM absorption makes direct measurements of EUV luminosity and spectrum significantly difficult, and thus they are hardly constrained. We assume the fiducial EUV spectra to be blackbody radiation with an effective temperature of 10^4 K in our simulations. With this spectrum, more than 90% of the EUV photons are emitted with the energy between $13.6 \text{ eV} \leq h\nu \lesssim 16 \text{ eV}$, i.e. the energy of most EUV is close to Lyman limit. This implies that our combined input spectrum with X-ray have a flux gap in the range of $20 \text{ eV} \lesssim h\nu \lesssim 0.1 \text{ keV}$ (Figure 3.13). The practical spectra of the high-energy radiation from young stars would be continuous from UV

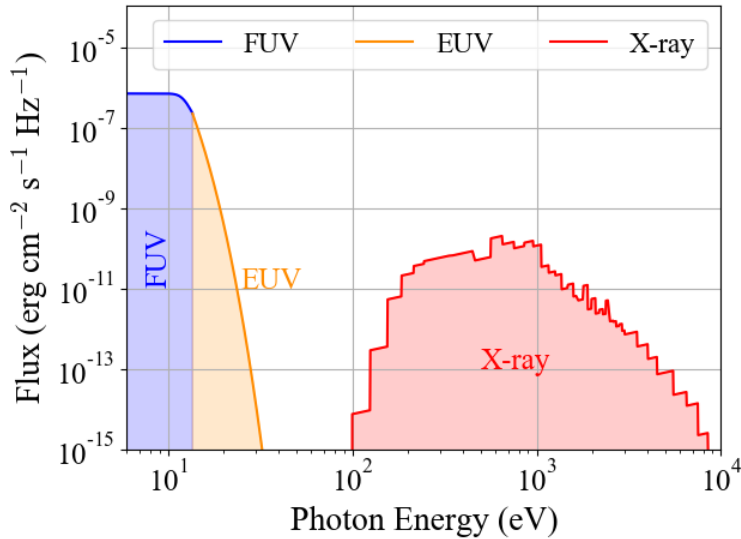


Fig. 3.13 Input spectra of the high-energy radiation in our fiducial model. The spectra of FUV, EUV, and X-ray are indicated by the blue, orange, and red solid lines, respectively. Note that we do not explicitly give the FUV spectrum in our simulations, since assuming FUV spectrum is unnecessary to calculate FUV photodissociation rates and photoelectric heating rates. Here the FUV spectrum is shown in a schematic manner so that it gives the fiducial FUV luminosity $L_{\text{FUV}} = 3 \times 10^{32} \text{ erg s}^{-1}$.

to X-ray, although neither of the actual spectrum nor the emission mechanism is well understood. We have investigated the effect of the spectrum hardness on the resulting photoevaporation rates in Section 3.4.1 and Section 3.4.2, and have shown that hard EUV photons ($h\nu \lesssim 100 \text{ eV}$; see also Figure 3.10) might have potential to increase the resulting photoevaporation rate by a factor (compare the purple dots at the middle and the right in Figure 3.12). Therefore, the lack of hard EUV photons in our fiducial spectrum might miss its contribution to the resulting photoevaporation rates; our photoevaporation rates appear to have uncertainty by a factor because of our adopted spectrum of EUV and X-ray. Nevertheless, since the energy of the hard EUV is less than the threshold energy

($\simeq 0.29$ keV), at which metal species dominantly absorb the high-energy photons, the hard EUV would not directly yield a metallicity-dependent trend. Thus, the resulting metallicity dependence of the photoevaporation rates we have obtained with our fiducial spectra would hold even if we take account of the contribution from the hard EUV component. We note again that detailed modeling of thermochemistry is necessary for the EUV photons with $\gtrsim 35$ eV to determine the heating rate and photoevaporation rates, because the energy partly goes into other processes, such as secondary ionization and exciting neutral gas (Draine 2011).

· Metallicity Dependence of X-ray Radiation

Strong X-ray emission is observed from young stars no matter whether there exists an indication of a strong accretion activity. Therefore, X-ray emission is considered to originate from stellar surface activity involving magnetic field rather than the accreting gas in contrast to the ultraviolet radiation. A sudden energy release due to magnetic reconnection may dominate the source of the strong X-ray emission, as Sun's flare. Observed X-ray spectra are contributed from both continuum and line emission by optically thin thermal plasma with the typical plasma temperature of 10^7 K (Güdel *et al.* 2005, 2007b). Güdel *et al.* (2007b) showed that X-ray spectra of T Tauri stars (DG Tau A, GV Tau, and DP Tau) are well fitted by thermal bremsstrahlung and line emission of metal ions: O III Ly α ($18.97 \text{ \AA} = 0.65$ keV), O VIII Ly β ($14.2 \text{ \AA} = 0.87$ keV), Ne IX ($13.5 \text{ \AA} = 0.92$ keV), Fe XVII ($17 \text{ \AA} = 0.73$ keV, $15 \text{ \AA} = 0.83$ keV, $13.8 \text{ \AA} = 0.9$ keV), and Fe XVIII ($16 \text{ \AA} = 0.78$ keV). Note that Ne X ($12.1 \text{ \AA} = 1.0$ keV), Fe XX ($12.8 \text{ \AA} = 0.97$ keV), and Fe XX–Fe XXIV lines also yield a strong emission at ~ 1 keV, which is often present in active stars having a hot corona (Telleschi *et al.* 2005).

We have used a fixed X-ray spectrum and luminosity for all of the metallicity cases, but in practice, the contribution from the metal lines may be reduced in low-metallicity environments. This effect makes X-ray radiation of the central star further ineffective to drive photoevaporative flows. This confirms our conclusion that X-ray is ineffective to drive photoevaporative flows.

We have shown that X-ray ionization strengthens FUV heating, and this effect is essential to drive a strong photoevaporation with very low metallicities $Z \lesssim 10^{-2} Z_{\odot}$. This X-ray strengthening effect can be decreased by the reduction of metal lines in low-metallicity environments. The metal lines are a relatively softer component ($\lesssim 1$ keV) in the X-ray radiation. Softer X-ray is subject to a larger cross section of the medium (cf. Eq.(3.4)) and is more efficiently attenuated. This indicates that the softer X-ray component is important to ionize the neutral medium in low-density regions of the disk to a relatively high ionization degree ($y_{\text{HII}} \sim 10^{-3}$ – 10^{-2}). Hence, compared to our fiducial case, the reduced line emission can decrease the temperatures of the low-density regions because of the small strengthening effect.

In a region optically thin to X-ray ($\tau_{\text{X}}(E) < 1$), the balance between ionization by unattenuated X-ray and recombination sets the ionization degree of the neutral medium. Thus the ionization degree is calculated as

$$y_{\text{HII}} \simeq \left(\alpha^{-1} n_{\text{H}}^{-1} \int_{E_{\text{min}}}^{E_{\text{max}}} dE \frac{F(E)}{4\pi r^2 E} \sigma \right)^{1/2},$$

where α is the recombination rate. The X-ray flux $F(E)$ decreases to some extent owing to the decline of metal line emission in low-metallicity environments, and the resulting ionization degree is correspondingly reduced. Unfortunately, since it is generally difficult to derive the accurate portion of metal line emission in X-ray flux at each energy bin, it is quite uncertain to what extent X-ray flux should be decreased for low metallicities. Nevertheless, we can, at least, consider a limiting

case, where all of the X-ray photons with ≤ 1 keV were assumed to be contributed from metal line emission, to understand the trend the reduced line emission would yield in the resulting metallicity dependence of the photoevaporation rates in our fiducial model. In the limiting case, the softer component (≤ 1 keV) becomes ineffective to ionize the neutral medium as metallicity decreases. The above equation can be approximated to $y_{\text{HII}} \sim 10^{-4.5}(r/100 \text{ au})^{-1} (\equiv x_{\text{low}})$ in the case of $Z \rightarrow 0$. Note that x_{low} sets the lower limit of the ionization degree in the optically thin regions to X-ray above 1 keV. The value of x_{low} is 10–100 times lower than the ionization degree of the optically thin region in Run FEX/Z0 (see the $\theta \lesssim 0.5$ region in the left bottom panel of Figure 3.2). This can lower the photoelectric efficiency (Eq.(2.24)) and hence FUV heating rate (Eq.(2.23)) by a factor (compare the FUV heating rates of the middle-left and middle-center panels in Figure 3.2). The decline of FUV heating rate would reduce the photoevaporation rates in Run FEX with low metallicities where metal line emission is weak. However, x_{low} is still larger than the electron abundance of the neutral region in Run FE, where we do not include X-ray effects at all, for $Z \lesssim 10^{-0.5} Z_{\odot}$, because in Run FE, electrons are provided only via ionization of atomic carbon whose abundance is given $\sim 10^{-4} Z/Z_{\odot}$. This indicates that FUV heating rates are still larger than those in Run FE for the low metallicities even without the contribution of the metal line emission. Therefore, resulting photoevaporation rates would not fall below those of Run FE. In summary, if we take into account the decline of the metal line emission with decreasing metallicity, the photoevaporation rates are expected to be decreased for low metallicities ($Z \lesssim 10^{-1} Z_{\odot}$) from those of our fiducial Run FEX; still, they are larger than, or at least equal to, the photoevaporation rates in Run FE at each metallicity. Further quantitative discussions would require a detailed modeling of X-ray emission mechanisms, which is clearly beyond the scope of this study.

3.5 Chapter Summary

We have studied photoevaporation of protoplanetary disks irradiated by UV/X-ray from the central star with a suite of radiation hydrodynamics simulations. We have investigated the metallicity dependence of photoevaporation due to those high-energy radiations. Our direct comparison between various cases have shown that X-ray alone does not efficiently heat the gas up to a high temperature necessary to yield a significant mass-loss rate.

Though the net heating effect is insignificant, X-rays efficiently raises the electron abundance in the neutral region by ionization. This makes charged dust grains recombine more efficiently. The fast recombination increases the FUV photoelectric heating efficiency, and the X-ray-strengthened FUV heating raises the temperature of the neutral region. Consequently, the X-ray radiation effects yields a larger photoevaporation rate, than the cases with FUV heating alone.

The disk photoevaporation rate increases as metallicity decreases in the range of $Z \gtrsim 10^{-1.5} Z_{\odot}$ with all of the FUV, EUV, and X-ray radiation. The increase is due to the reduced opacity of the disk medium for FUV photons. At $Z \lesssim 10^{-1.5} Z_{\odot}$, FUV photoelectric heating becomes ineffective compared to dust-gas collisional cooling, and it suppresses photoevaporation. Including X-ray effects is critical to excite FUV-driven photoevaporative winds in this low-metallicity range; otherwise, FUV does not drive winds, and the mass-loss rate is set by the EUV-driven flows. The X-ray effects significantly increase the photoevaporation rate with very low metallicities.

We have derived the metallicity dependence of the resulting photoevaporation rates. The metallicity dependence caused by FUV and strengthened FUV heating is consistent with the observational trend of the PPD lifetimes. Our model predicts that PPDs have longer lifetimes in extremely low-metallicity environments than in solar or subsolar metallicity environments.

Chapter 4

Photoevaporation of Low-Mass Molecular Cloud Cores: Lifetimes and Metallicity Dependence

4.1 Overview

We have investigated the dispersal process of PPDs in the previous two chapters. In this chapter, we extend the scope of our interest to the earlier stage of stellar system formation. We perform a suite of 3D radiation hydrodynamics simulations where a molecular cloud core is illuminated by external massive stars. The intense radiation field excites photoevaporative winds that strip the mass off from the surface of the core. We study the fate of solar-mass cores and derive their lifetimes with varying the core metallicity over a wide range of $10^{-3} Z_{\odot} \leq Z \leq Z_{\odot}$. In our simulations, radiation transfer of far ultraviolet (FUV) and extreme ultraviolet (EUV) is incorporated, and we follow atomic/molecular line cooling and dust-gas collisional cooling. The radiative transfer and hydrodynamics are coupled with nonequilibrium chemistry in a self-consistent manner. Our results show that radiation-driven shocks compress the cores to have a volume set by the pressure-equilibrium with the ambient hot gas. Metal-rich cores condense to have small surface areas, where photoevaporative flows are launched, owing to efficient radiative cooling. For our fiducial set-up with an O-type star at the distance of 0.1 parsecs, the resulting photoevaporation rate is small ($\sim 10^{-5} M_{\odot} \text{ yr}^{-1}$) for metal-rich cores, but is larger for metal-poor cores that have larger launch areas. The cores keep being accelerated away from the external radiation source by the so-called rocket effect and can travel over ~ 1 parsec within the lifetime. We also investigate photoevaporation of cores in a photodissociation region. Grain photoelectric heating is ineffective in metal-poor cores that contain a small amount of grains; they survive for over 10^5 years. It is concluded that the core metallicity significantly affects the lifetime and thus determines the strength of feedback from massive stars in star-forming regions.

The contents in this chapter are based on Nakatani and Yoshida (2018).

4.2 Background

Giant molecular clouds (GMCs) are the largest self-gravitating bodies in galaxies and have masses greater than $\sim 10^4 M_{\odot}$. Line surveys at millimeter and sub-millimeter wavelengths have revealed that GMCs have inhomogeneous clumpy substructures with a broad range of sizes (~ 0.1 – 10 pc) and masses (~ 1 – $10^3 M_{\odot}$) (Bally *et al.* 1987, Bertoldi and McKee 1992, Blitz 1993, Evans 1999, Williams

et al. 2000, Muñoz *et al.* 2007). Typically, most massive clumps are birthplaces of stars in a GMC. Stars form in clusters, which account for a large portion of star formation in GMCs. This suggests that the overall rate and efficiency of star formation may be set by the evolution of stars with the associated clumps in GMCs. It has been of great interest to study the evolution and the destiny of molecular cloud clumps in a star-forming region.

All of the massive star formations take place in GMCs. Newly formed massive stars illuminate the surrounding gas. The radiation is so strong that it can even destruct the parental GMC in about ten million years (e.g. Blitz and Shu 1980, Stahler and Palla 2005). Ultraviolet (UV) radiation from the massive stars chemically and thermally affects the state of the surrounding gas. EUV ionizes hydrogen atoms to form an H II region, and FUV photodissociates molecules to yield a photodissociation region (PDR) around the H II region. Grain photoelectric heating heats the PDR gas to $\sim 100\text{--}1000\text{ K}$, while the gas in H II regions is heated to $\sim 10^4\text{ K}$ by heating followed by hydrogen ionization. The pressure of H II regions is sufficiently high to drive shock waves in the surrounding molecular gas. The process compresses the gas and can make it gravitationally unstable, leading to star formation. Observations have actually found the evidences of such “sequential star formation” (Elmegreen and Lada 1977) in local H II regions (e.g., Deharveng *et al.* 2005, 2008, Miura *et al.* 2010) and in the Large and Small Magellanic Clouds (Contursi *et al.* 2000, Rubio *et al.* 2000, Barbá *et al.* 2003).

The dynamical, chemical, and thermal structure of molecular cloud clumps/cores are significantly influenced by UV radiation from nearby massive OB stars. The EUV heats the surfaces of the molecular clouds, and the high-pressure drives shock in the cool interior of the clouds. The interior gas is compressed by the so-called radiation-driven implosion (e.g., Tenorio-Tagle 1977, Klein *et al.* 1980, Bertoldi 1989, Duvert *et al.* 1990, Lefloch and Lazareff 1994), and can initiate gravitational collapse. After the implosion, the clouds form a cometary structure: a dense core and a prolonged tail in the opposite direction to the radiation source. Such cometary molecular clouds around nearby hot stars are termed “cometary globules” (CGs). CGs are often found near OB associations (e.g., Reipurth 1983), and are considered to be precursors of the Bok globules (Bok and Reilly 1947). There also exist CGs in nearby planetary nebulae, such as Rosette nebula, Helix Nebula, and Gum nebula (Reipurth 1983, O’deH and Handron 1996, O’DeH *et al.* 2002, 2007). Infrared observations have proposed that star formation might be actually occurring in these cometary globules (Sugitani *et al.* 1991, Sugitani and Ogura 1994) and at the bright rims of the globules (Sugitani *et al.* 1995, Megeath *et al.* 1996).

In addition to initiating gravitational collapse and forming CGs, UV radiation drives photoevaporation from the surface of the clouds by their intense heating (e.g. Bertoldi 1989, Bertoldi and McKee 1990). The clouds are gradually eroded from their surfaces, and a significant portion of the mass is lost. Starting with Oort and Spitzer (1955), many of studies have been investigated cloud photoevaporation followed by the radiation-driven implosion and the subsequent CG formation both numerically and analytically. Numerical modeling of the radiation-driven implosion were first carried out with 1D hydrodynamics simulations by Tenorio-Tagle (1977) and with 2D simulations by (Klein *et al.* 1980, Sandford *et al.* 1982, 1984). An approximate analytic model is first developed by Bertoldi (1989) for the radiation-driven implosion and by Bertoldi and McKee (1990) for the cometary structure formation, taking into account the effects of photoevaporation. Lefloch and Lazareff (1994) perform 2D numerical simulations to investigate a detailed evolutionary sequence from the radiation-driven implosion phase to the quasi-static cometary phase. It is shown that a photoevaporating cloud spends $\sim 90\%$ of the lifetime in the cometary phase. Mellema *et al.* (1998) develops a time-dependent analytic model for the evolution of cloud mass and cometary structure

under the effects of photoevaporation. The analytic model is consistent with the analytic solution of Bertoldi and McKee (1990). Mellema *et al.* (1998) also perform 2D radiation-hydrodynamics simulations of photoevaporating clouds with non-equilibrium ion/atom chemistry. The results are consistent with the derived analytic model. The observational features of CGs in the nearby nebulae have been directly compared with these cloud photoevaporation models, and it has been concluded that the models well explain the observational results (López-Martín *et al.* 2001, Williams *et al.* 2001). Other studies investigate cloud photoevaporation due to ionizing radiation with self-gravity (Kessel-Deynet and Burkert 2003, Esquivel and Raga 2007) and with the diffuse EUV (Cantó *et al.* 1998, Pavlakis *et al.* 2001). Cloud photoevaporation with inhomogeneous structures (González *et al.* 2005, Raga *et al.* 2005) and for multi-cloud systems (Raga *et al.* 2009) are also studied by radiation hydrodynamics simulations.

As well as EUV, FUV from nearby massive stars also drives photoevaporation. Johnstone *et al.* (1998) studied FUV effects on spherical gas clouds (and protoplanetary disks) with 1D analytic modeling and numerical simulations. Gorti and Hollenbach (2002) generalized the study of Johnstone *et al.* (1998) and Störzer and Hollenbach (1999), developing a 1D analytical model of FUV photoevaporation that can be applied with various input parameters, such as initial cloud density and cloud temperatures. In the study, it is concluded that shocks develop in strongly FUV-irradiated clouds, and it might trigger gravitational collapse inside the compressed core. The authors estimated the cloud lifetimes to be $\sim 10^4$ – 10^5 yr for solar-mass clouds with using typical parameters in the local star-forming region. More recently, 1D radiation-hydrodynamics simulations with the effects of both FUV and EUV were performed by Decataldo *et al.* (2017) to study cloud photoevaporation around massive stars or quasars. The results are shown to be consistent with those derived in Gorti and Hollenbach (2002).

In these previous studies, an object of interest has been cloud photoevaporation around massive stars in solar-metallicity environments. The evolutionary process and the lifetimes can be different for molecular clouds in low-metallicity star-forming regions, such as, for example, those in the LMC (Minamidani *et al.* 2011) or in the early universe (Shapiro *et al.* 2004). Low-metallicity clouds lack metal coolants, and grain photoelectric heating is inefficient there. Therefore, metallicity is expected to be a key parameter to determine the dynamical/chemical/thermal structure of photoevaporating clouds. In particular, the lifetimes and its metallicity dependence would be an important element, which regulates the efficiency of star formation in high-redshift galaxies. Exploring cloud photoevaporation in various environments is thus important.

4.3 Methods

We set an initially molecular spherical core with decreasing metallicity Z illuminated by an external radiation source (massive star) at distance D (Figure 4.1). The core is exposed to the radiation field from the external source which is assumed to have an FUV luminosity L_{FUV} and an EUV photon emission rate Φ_{EUV} , and correspondingly the FUV and EUV fluxes of $L_{\text{FUV}}/4\pi D^2$ and $\Phi_{\text{EUV}}/4\pi D^2$. A suitably modified version of the publicly available hydrodynamics code PLUTO (Mignone *et al.* 2007) is used for this study. The numerical methods are basically the same as in the previous chapters. In the following, we describe the numerical methods applied to this study in detail with a brief review of the code. Further details are found in Chapter 2, where we have studied the metallicity dependence of PPD photoevaporation.

The molecular cloud cores are made of the ISM consists of dust and gas. The gas is assumed to contain seven chemical species: H, H^+ , H_2 , C^+ , O, CO, e^- . The elemental abundances of carbon

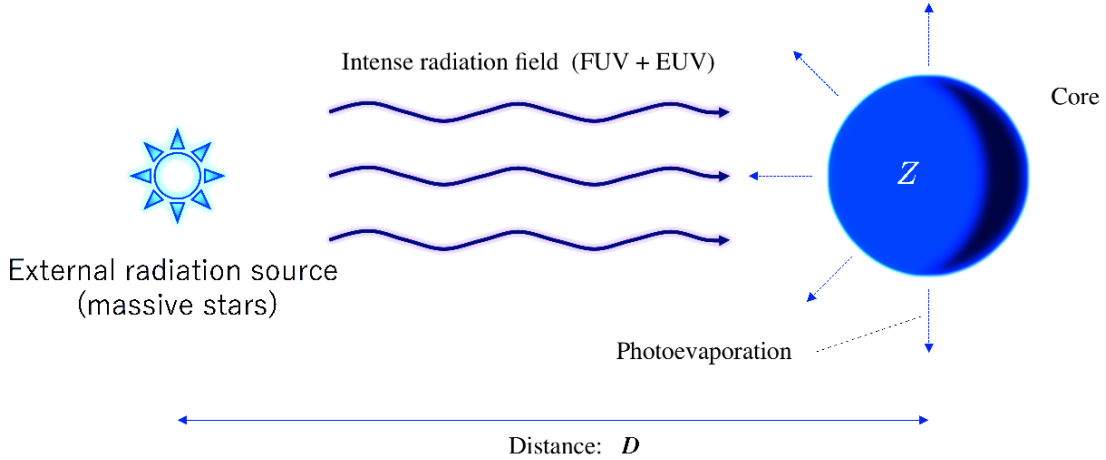


Fig. 4.1 Schematic picture of our simulation configuration. A core, whose metallicity is Z , is irradiated by the plane-parallel UV radiation from the external source placed at the distance D . The intense UV radiation excites photoevaporative flows from the surface of the core.

and oxygen are set to interstellar values $y_C = 0.926 \times 10^{-4} Z/Z_\odot$ and $y_O = 3.568 \times 10^{-4} Z/Z_\odot$, respectively, and the dust-to-gas-mass ratio is set to $0.01 Z/Z_\odot$. We implement photoheating associated with H I photoionization (hereafter EUV heating) and the grain photoelectric effect (hereafter FUV heating; Bakes and Tielens 1994). Radiative transfer of FUV and EUV radiation field are followed at each time step with ray-tracing. Radiative transfer is not solved for the diffuse radiation components. Including the diffuse EUV component can slightly change the geometrical structure of the cloud in the early evolutionary stage, but would not cause crucial differences in the global evolution of the cloud, as demonstrated by Pavlakis *et al.* (2001). One can also naively expect that scattered or diffuse FUV photon might change the chemical and/or thermal structure especially in shadowed regions. However, strong photoevaporative winds are not driven there. It would be ideal to take account of radiation transfer for the diffuse components, but we focus, in this study, on core photoevaporation and lifetimes determined by the effects of the direct UV radiation.

In a fully molecular gas cloud that we consider as the initial condition in this study, Hydrogen molecules can be directly ionized by absorbing EUV photons to produce H_2^+ at the beginning of the clump evolution. The absorption cross section of H_2 is comparable to that of H I, and thus H_2 photoionization can dominate over H_2 photodissociation on the very surface of the initial core. However, the reactions of the dissociative recombination $\text{H}_2^+ + e \longrightarrow \text{H} + \text{H}$ and subsequent H I photoionization are sufficiently rapid processes, so that they immediately convert the produced H_2^+ to H^+ and form an H II region. We have performed test simulations with these processes enabled to examine the effects of H_2 photoionization and the associated photoheating. It has been found that these effects hardly change the evolution of the cores. This allows us to omit the EUV ionization of H_2 in our chemistry model for saving computational cost.

The simulation box is spaced with 3D cartesian coordinates. The core center is initially placed at $\vec{r}_{\text{ini}} \equiv (x, y, z) = (0, 0, 0)$. The computational domain extends from -0.2 pc to 1.0 pc along the x -axis, and from 0.0 pc to 0.2 pc along each of the y - and z -axes; we assume symmetries with respect to both the xy -plane and xz -plane. The computational box is uniformly spaced with the number of the cells $N_x \times N_y \times N_z = 384 \times 64 \times 64$. At $t = 0$, the radiation source is turned on and starts to illuminate the core. The source is located at 0.1 pc from the clump surface. A distant-source

approximation is adopted; a plane-parallel UV radiation field is incident on the side surface of the simulation box at $x = -0.2$ pc. The incident FUV flux and EUV photon number flux are set to be $G_{\text{FUV}} = 6.8 \times 10^3 G_0$ and $F_{\text{EUV}} = 5.9 \times 10^{12} \text{ s}^{-1} \text{ cm}^{-2}$, in which the FUV flux is measured in the unit of the average interstellar flux $G_0 = 1.6 \times 10^{-3} \text{ erg cm}^{-2} \text{ s}^{-1}$. The source luminosities are correspondingly calculated as $L_{\text{FUV}} = 1.3 \times 10^{37} \text{ erg s}^{-1}$ and $\Phi_{\text{EUV}} = 7.0 \times 10^{48} \text{ s}^{-1}$. In Section 4.5.1, lower UV fluxes are considered to study the variation of core lifetimes. Gravity is not incorporated in our simulations, but we refer the readers to our discussion in Section 4.5.3.

We model the initial density distribution of the cloud core as a Bonner-Ebert (BE) sphere (Ebert 1955, Bonnor 1956). We follow Decataldo *et al.* (2017) and adopt $n_{\text{H}}(\vec{r}_{\text{ini}}) = 2 \times 10^4 \text{ cm}^{-3}$, $T_{\text{ini}} = 10 \text{ K}$, and $P_c = 6.9 \times 10^{-12} \text{ erg cm}^{-3}$ as the initial density and temperature at the core center, and the confining pressure, respectively. The corresponding initial core radius is $R_{\text{ini}} = 8.8 \times 10^{-2} \text{ pc}$, and the initial core mass is $M_{\text{ini}} = 0.92 M_{\odot}$. Note that M_{ini} is smaller than the BE mass $M_{\text{BE}} \simeq 1.18 c_s^4 / \sqrt{P_c G^3} \simeq 2 M_{\odot}$.

We run three sets of simulations with (i) both EUV and FUV photons, (ii) only FUV, and (iii) only EUV to examine core photoevaporation in an H II region and in a photodissociation region (PDR) and to study the effects of FUV and EUV separately. Henceforth, the three sets of our simulations are labeled according to the incorporated processes. A set of simulations labeled as “XX” specifies included photoheating sources. For example, “Run FE” indicates simulations with both FUV and EUV, and “Run E” indicates runs with only EUV. In addition, the assumed gas metallicity are specified by appending “ZC” to the labels. This appendix indicates that the molecular cloud core has the metallicity of $Z = 10^C Z_{\odot}$ in the simulation.

4.4 Results

4.4.1 Solar-Metallicity Core

4.4.1.1 Core Evolution and Lifetime

We first describe the evolution of a solar-metallicity core in our simulations. It gives a basic insight into the core evolution with other metallicities. At the beginning of the evolution, H_2 molecules are rapidly dissociated by FUV irradiation in the hemisphere close to the radiation source. The produced atomic hydrogen is then quickly photoionized by EUV. These processes result in the formation of three chemically distinct regions: a molecular region, a geometrically thin H I shell with a typical thickness of $\sim 10^{-2} \text{ pc}$, and an ambient H II region. A bowl-shaped shock develops in the neutral regions and propagates in the medium of the core. The core is compressed to have a small size. This process is called the radiation-driven implosion phase (Lefloch and Lazareff 1994). Henceforth, the shock-induced compression is simply referred to as shock-compression.

The shock converges toward the x -axis (see the snapshots at $t \simeq 1000$ – 5000 yr in Figure 4.2). It has the potential to increase the temperature of the post-shock region, but the cooling time is much shorter than the crossing time of the shock. The temperatures keep a low value at $T \sim 10 \text{ K}$. The line emission of oxygen and dust-gas collisional cooling dominantly contribute to cool the gas in the core. The charge-transfer reaction $\text{H}^+ + \text{O} \longrightarrow \text{H} + \text{O}^+$ could rapidly destroy atomic oxygen in the core (Draine 2011), but it is not effective with the low temperature and low degree of ionization ($< 10^{-5}$) there. The ambient hot medium compresses the cool core after the shock passes. The compressed core forms a stable structure when the internal density becomes high enough to make the internal pressure comparable to the external pressure. The core achieves this approximate pressure equilibrium from the side facing the radiation source. The average density of the neutral

core is raised by the shock-compression and the external pressure in the first ~ 7000 yr. After this compression phase, the core rebounds slightly and then form a cometary structure in the rest frame of the core with the characteristic internal density of $n_{\text{H}} \sim 10^7 \text{ cm}^{-3}$ (Figure 4.2).

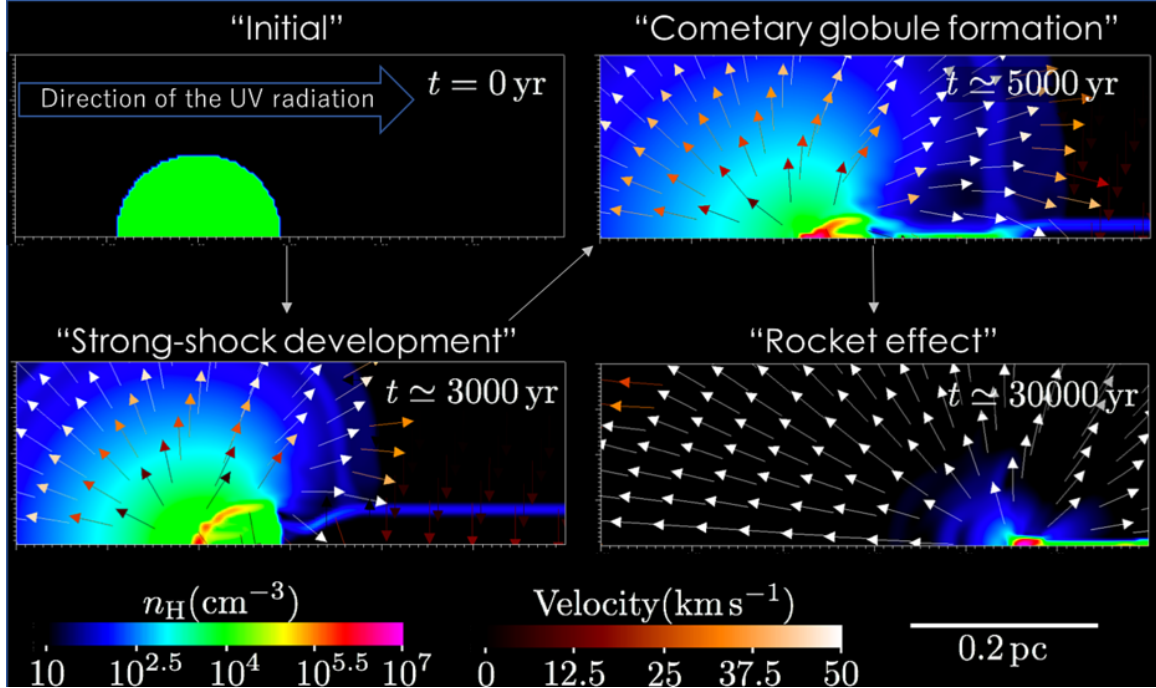


Fig. 4.2 Time evolution of the solar-metallicity core. The FUV and EUV radiation are incident on the computational domain from left to right in the panels. Each color map shows a snapshot of cross-sectional density distribution. The velocity field is represented by the arrows colored according to the magnitude. The physical length scale is presented at the bottom right. The external radiation source is located at the left of the boxes; It is not seen in the frames or in the computational domain.

Photoevaporative winds are driven by the intense UV irradiation at the ionization front (Figure 4.2). They have the launch velocity of $\simeq 10\text{--}30 \text{ km s}^{-1}$ and the typical density of $n_{\text{H}} \sim 10^5 \text{ cm}^{-3}$, stripping the core medium off at the wind base. Throughout this study, the core mass M_c is calculated as

$$M_c = \int_{V(R_c, \mathbf{r}')} \rho dV. \quad (4.1)$$

Here $V(R_c, \mathbf{r}')$ is a spherical volume with the center position \mathbf{r}' and radius R_c . We use $R_{\text{ini}} = R_c$ and set \mathbf{r}' to the center of mass in the “dense” region, which we define as

$$n_{\text{H}} > n_d \equiv \min \left(\frac{n_{\text{H}}(\vec{r}_{\text{ini}})}{2}, \frac{n_{\text{max}}}{2} \right). \quad (4.2)$$

Here we have denoted the maximum hydrogen nuclei density in the simulation box as n_{max} . This mass-measuring technique is adopted to estimate the core masses in all the FE, F, and E runs.

The ratio of M_c to the initial core mass $M_{\text{ini}} (= 0.92 M_{\odot})$ is shown in Figure 4.3 as a function of time. The decline of the core mass is monotonic in all the cases of Z0/FE, Z0/F, and Z0/E. In run Z0/FE, about 50% of the initial mass is lost during the implosion phase that lasts for the first $\sim 10^4$ years. The lost mass existed in the part of the core where the R-type ionization front sweeps

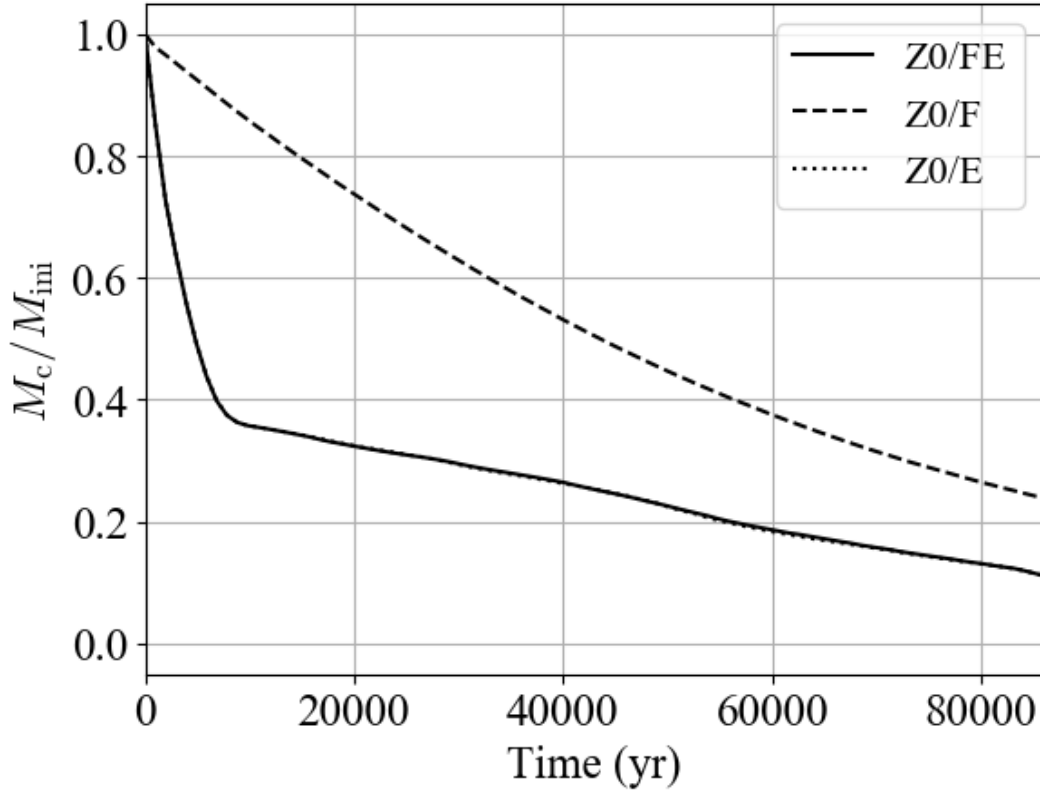


Fig. 4.3 Time evolution of the core mass ratio M_c/M_{ini} . The results for Z0/FE, Z0/F, and Z0/E are represented by the solid, dashed, and dotted lines, respectively. The solid and dotted lines almost overlap.

before it converges to D-type (Spitzer 1978, Shapiro *et al.* 2004). The region is ionized and heated, and then evaporates outward from the core center on an approximately crossing time of the ionized flows $R_{\text{ini}}/10 \text{ km s}^{-1} \sim 10^4 \text{ yr}$. In run Z0/F, FUV heating yields the temperatures of $\sim 300\text{--}500 \text{ K}$ in nearly the entire hemisphere of the core facing to the external radiation source. The region expands at a velocity of $1\text{--}3 \text{ km s}^{-1}$. The velocity is an order of magnitude smaller than that of the EUV-driven flows. The core survives for a long time compared to Z0/FE or Z0/E (Figure 4.3). In Gorti and Hollenbach (2002), an impulsively FUV-illuminated cloud has bifurcated evolutionary channels, according to the “effective optical depth parameter” η_0 defined as

$$\eta_0 = \frac{R_{\text{ini}} n_0}{N_0}, \quad (4.3)$$

where n_0 is the initial core density and $N_0 \sim 2 \times 10^{21} \text{ cm}^{-2}$ is the typical column at which FUV photons are extinct. In the case of $\eta_0 > 1$, a cloud forms a thin FUV-heated layer on the surface. A shock develops inside the core if FUV heating is sufficiently strong. In the case of $\eta_0 < 1$, FUV heats the core entirely, and the core expands over the crossing timescale. Our cloud core with $\eta_0 \simeq 1$ evolves in an intermediate manner: the almost entire region of the core is heated by FUV. Especially, FUV heats the hemisphere in the side of the external radiation source. Neutral photoevaporative flows are driven there, and a weak shock develops in the interior of the core. The core finally shapes a cometary globule at $t \sim 7 \times 10^4 \text{ yr}$.

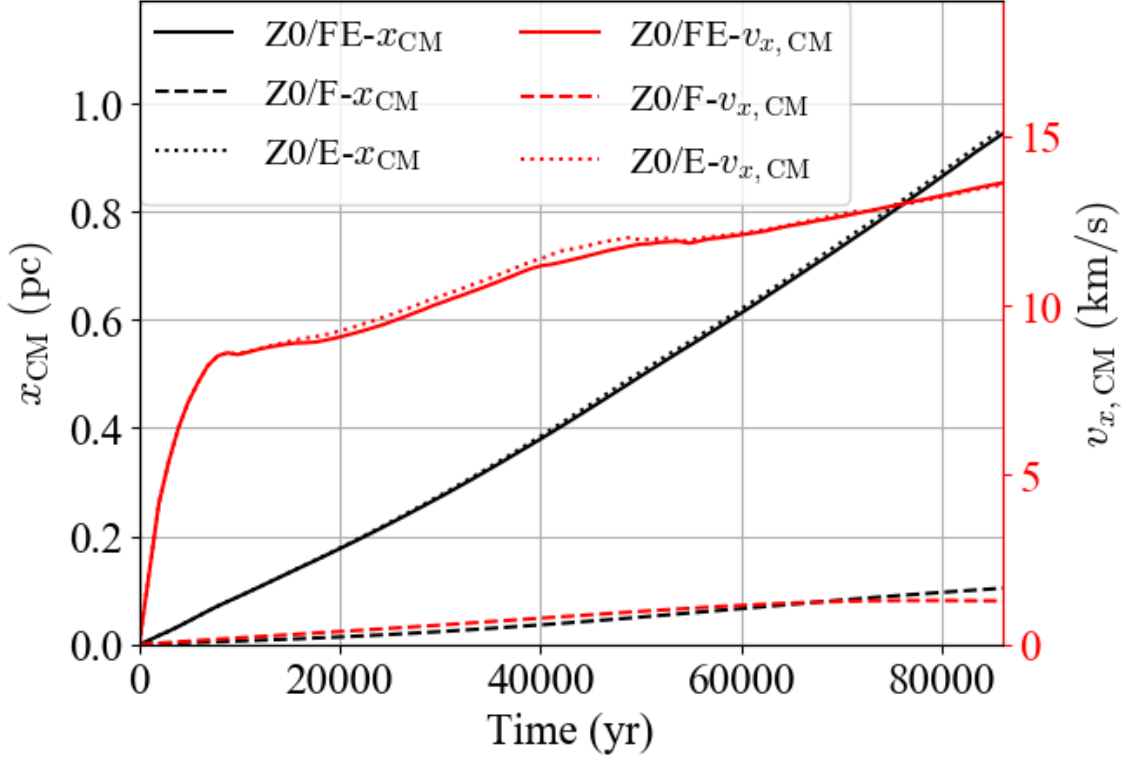


Fig. 4.4 Time evolutions for the mass-center position of the “dense” region along the x -axis ($x_{\text{CM}} = x'$; black) and the bulk velocity of the region ($v_{x,\text{CM}}$; red). Those of Z0/FE, Z0/F, and Z0/E are indicated by the solid, dashed, dotted lines, respectively. Note that the solid and dotted lines almost overlap.

4.4.1.2 The Rocket Effect

Molecular clouds irradiated by external sources acquire momentum from the ejected medium by photoevaporation. The acceleration due to photoevaporation is called the rocket effect (Oort and Spitzer 1955). In our simulations, the rocket effect is observed; the cores move along the x -axis with being accelerated (Figure 4.2 and Figure 4.4). The rocket effect comes from momentum conservation between the core and the ejected medium through photoevaporation. If we assume that photoevaporative flows have the launch density ρ_b and launch velocity v_b at the surface of the hemisphere close to the radiation source, the acceleration is estimated to be

$$\frac{dv_{\text{cl}}}{dt} = \frac{1}{M_{\text{cl}}} \left(\frac{1}{2} S \rho_b v_b^2 \right) \quad (4.4)$$

$$\simeq 4.0 \times 10^{-13} \text{ km s}^{-2} \left(\frac{S}{10^{-4} \text{ pc}^2} \right) \left(\frac{n_b}{10^5 \text{ cm}^{-3}} \right) \left(\frac{v_b}{10 \text{ km s}^{-1}} \right)^2 \left(\frac{M_{\text{cl}}}{M_{\odot}} \right)^{-1}, \quad (4.5)$$

where M_{cl} and S are the shock-compressed core mass and the launch area (base) of the photoevaporative flows. Let m_{H} be the atomic mass of hydrogen, then the base hydrogen nuclei density n_b is calculated as $n_b \simeq \rho_b/m_{\text{H}}$. In Eq.(4.4), the factor of a half in the parenthesis of the right-hand-side is derived from the integration of the momentum flux carried by photoevaporative flows. The right-hand-side shows a net momentum gain of a core through photoevaporation. We take the

values of the core in our Z0/FE run: $S \simeq 0.8 \times 10^{-4} \text{ pc}^2$, $n_b \simeq 1.0 \times 10^5 \text{ cm}^{-3}$, $v_b \simeq 20 \text{ km s}^{-1}$, and $M_{\text{cl}} \simeq 0.38 M_{\odot}$. The acceleration is estimated as $a_{\text{cl}} = 3 \times 10^{-12} \text{ km s}^{-2}$ by substituting the values into Eq.(4.5). After the implosion phase ($t \gtrsim 10^4 \text{ yr}$) in run Z0/FE, the mass center position of the “dense” region x' is well fitted by a quadratic function of time $x' = at^2 + bt$, where $a = 1.1 \times 10^{-12} \text{ km s}^{-2}$ ($= 3.6 \times 10^{-5} \text{ km s}^{-1} \text{ yr}^{-1}$) and $b = 7.6 \text{ km s}^{-1}$ (Figure 4.4). The acceleration a is well explained by the model (Eq.(4.5)). The core velocity at the end of the implosion phase is approximately given by the fitting coefficient b . To summarize, the solar-metallicity core gets a velocity of $\sim 10 \text{ km s}^{-1}$ during the implosion phase and recedes from the external radiation source with being accelerated by the rocket effect due to EUV photoevaporation. The acceleration is of the order of $\sim 10^{-5} \text{ km s}^{-1} \text{ yr}^{-1}$. The core moves the distance of $\sim 1 \text{ pc}$ in $\sim 10^5 \text{ yr}$ by which the mass has decreased to 10% of the initial mass.

4.4.2 Low-Metallicity Cores

4.4.2.1 EUV Effects

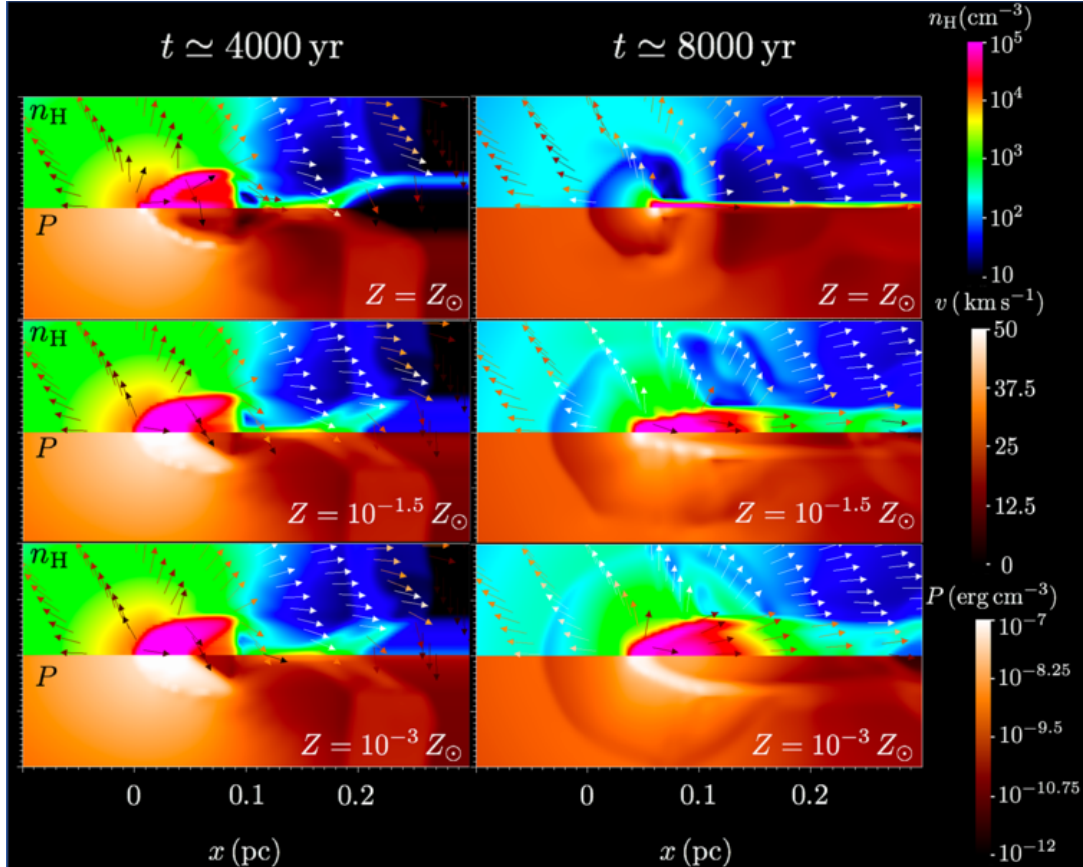


Fig. 4.5 Distributions of the density, velocity, and pressure on the xy -plane. The distributions of density and pressure are shown in the upper and lower half of each panel, respectively. The arrows represent the velocity field and are colored by the magnitude. The distributions at $t \simeq 4000, 8000 \text{ yr}$ are presented in the left and right columns, respectively. Note that the different density scale is used from Figure 4.2 for clarity.

The low-metallicity cores first evolve in a similar manner to the solar-metallicity core. In the hemisphere facing the radiation source, the ionization front develops at the radius of $\sim 0.4 R_{\text{ini}} \simeq$

0.04 pc ($\equiv R_{i,\text{ini}}$) from the core center (cf. Figure 4.2). A bowl-shaped shock (the left column of Figure 4.5) develops in the neutral interior of the core. The shock compression occurs for the first ~ 4000 yr. The timescale corresponds to the shock propagation time $t_{\text{cr}} = R_{i,\text{ini}}/10 \text{ km s}^{-1} \simeq 4 \times 10^3$ yr (the phase (1) in Figure 4.6). The Mach number of the pre-shock region is sufficiently high to yield

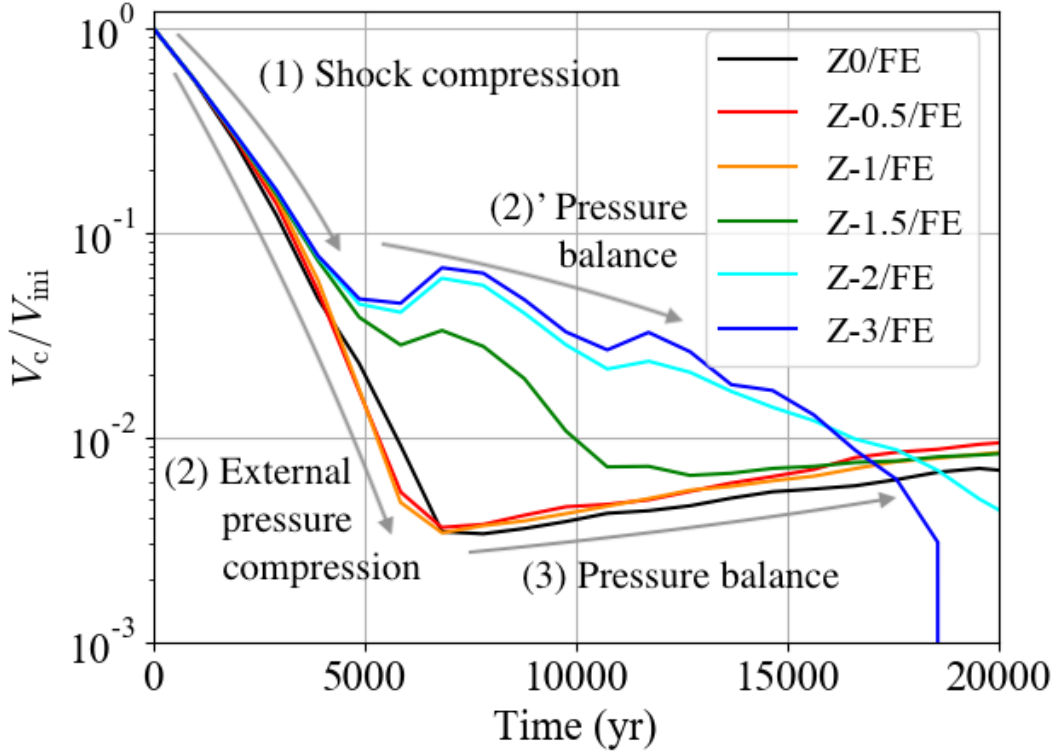


Fig. 4.6 Time evolution of the core volume V_c (Eq.(4.6)) in our FE runs with different metallicities. The core volume V_c is normalized by the initial volume V_{ini} .

a temperature of $\sim 10^4$ K in the post-shock region. The temperature is high enough to balance the internal pressure with the external pressure. For $Z \leq 10^{-2} Z_{\odot}$ cores, the smaller amount of metals and dust reduces the efficiency of radiative cooling processes. The internal temperatures reach $\sim 10^3$ – 10^4 K via the shock compression, yielding a comparable internal pressure to that in the hot ambient gas, and it prevents the cores from shrinking. Thus, the volumes of the lower-metallicity cores remain large even during the implosion phase (the phase (2)' and (3) in Figure 4.6), compared to in run Z0.

The cooling time is much shorter than the crossing time of the shock with $Z \gtrsim 10^{-1} Z_{\odot}$. The neutral region quickly cools to below 10^2 K, allowing the core to shrink until a high internal density is achieved to yield an internal pressure comparable to the hot, ambient gas pressure.

The thermal energy of the gas is lost through atomic/molecular line emission and heat transfer between gas and dust. The O I cooling and dust-gas collisional cooling dominate the cooling processes in the neutral region. The specific rates of these metal cooling processes increase with decreasing metallicity. The time evolution of the “dense” region volume

$$V_c = \int_{n_{\text{H}} > n_{\text{d}}} dV, \quad (4.6)$$

is shown in Figure 4.6. At the early phase of core evolution ($t \lesssim t_{\text{cr}}$; the phase (1) in Figure 4.6), the characteristic cooling time of the dominant coolants is approximately given by

$$t_{\text{c,OI}} \sim 10^2\text{--}10^3 \left(\frac{Z}{Z_{\odot}} \right)^{-1} \text{ yr} \quad (4.7)$$

$$t_{\text{c,dust}} \sim 10^2\text{--}10^3 \left(\frac{Z}{Z_{\odot}} \right)^{-1} \left(\frac{n_{\text{H}}}{10^4 \text{ cm}^{-3}} \right)^{-1} \text{ yr},$$

respectively. They are sufficiently short for the high-metallicity cores with $Z \gtrsim 10^{-1} Z_{\odot}$, compared to t_{cr} . Hence, the internal temperatures of the cores are largely coupled with the dust temperature of $T_{\text{d}} \sim 10 \text{ K}$ at $t \lesssim 1.5 \times 10^4 \text{ yr}$.

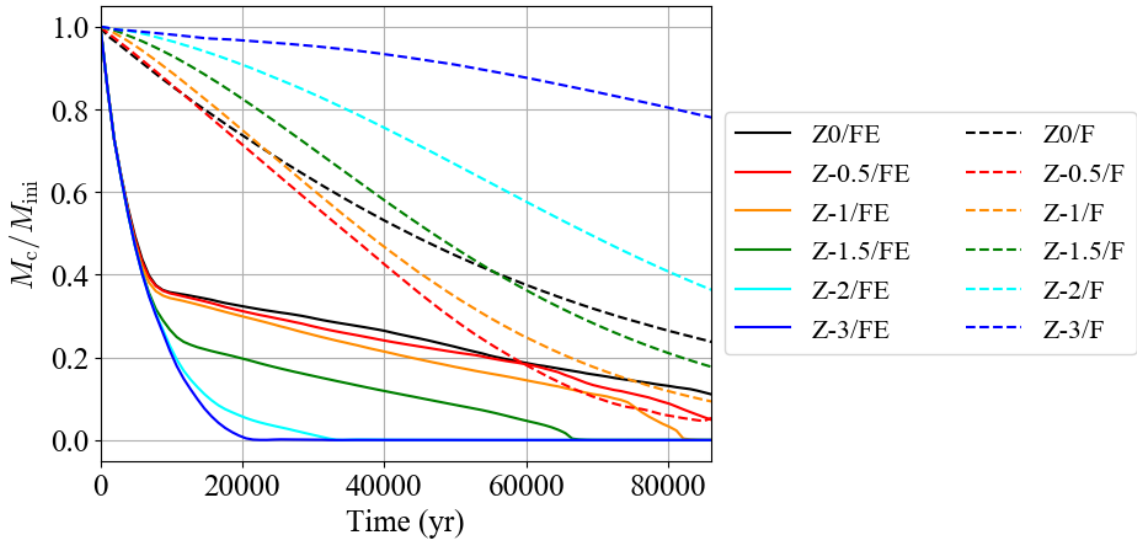


Fig. 4.7 Core mass evolution with various metallicities. The solid and dashed lines correspond to Run FE and Run F, respectively. Note that the core mass is normalized by the initial mass.

Approximately a half of the initial core mass evaporates during the implosion phase in Run FE (solid lines Figure 4.7; see also the discussions in Section 4.4.1). After that, the core mass is gradually decreased by EUV photoevaporation. The mass-loss rate is approximately estimated as

$$\dot{M}_{\text{ph}} \simeq \rho_b v_b S. \quad (4.8)$$

The base density ρ_b does not depend on metallicity because it is set by ionization and recombination of hydrogen whose amount is metallicity-independent. Photoevaporative flows are pressure-driven, and thus the launch velocity v_b is of the order of c_s . For the EUV-driven flows, it is typically $\sim 10 \text{ km s}^{-1}$. The base temperature is determined by EUV heating and radiative recombination cooling. Their rates are independent metallicity, and hence the velocity of the pressure-driven flows are also metallicity-independent. Thus, the difference in the launch area S mainly causes the metallicity dependence of the mass loss rates.

For the high-metallicity cores with $Z \gtrsim 10^{-1} Z_{\odot}$, the launch area S is primarily decreased by compression until the end of the compression phase at $t \sim 6000\text{--}7000 \text{ yr}$. A cometary globule forms afterward (Figure 4.5). The globule is in approximate pressure equilibrium, and thus the surface area is decreased by photoevaporation in this phase. The smaller S of the cometary structure

reduces the mass-loss rate \dot{M} of the cores (the red, blue, and green solid lines in Figure 4.7). For the low-metallicity cores with $Z \lesssim 10^{-2} Z_{\odot}$, the high temperatures of the post-shock region prevent the cores from being compressed by the hot ambient gas. Photoevaporation is the main channel to decrease the surface area S even in the implosion phase. The large surface area correspondingly yields a large EUV photoevaporation rate, and thus the dispersal time of the cores shorter than the high-metallicity cores. The cooling time is comparable to t_{cr} at first but gets shorter as the shock-compression increases the density with $Z \sim 10^{-1.5} Z_{\odot}$ (cf. Eq.(4.7)). The core keeps a large volume for a longer time than the high-metallicity cores (Figure 4.6). Thus, the $Z = 10^{-1.5} Z_{\odot}$ core loses a large amount of mass before evolving to a cometary globule, compared to the $Z \gtrsim 10^{-1} Z_{\odot}$ cores (Figure 4.7). The core has largely the same mass-loss rate as the $Z = 10^{-1} Z_{\odot}$ core afterward. The intermediate-metallicity core has an intermediate evolutionary behavior between the high metallicity ($Z \gtrsim 10^{-1} Z_{\odot}$) cores and the low metallicity ($Z \lesssim 10^{-2} Z_{\odot}$) cores.

The lifetime of a core is defined as the time by which the core mass has decreased to 10% of its initial mass. The lifetime is found to decrease with decreasing metallicity at $10^{-2} Z_{\odot} \leq Z \leq Z_{\odot}$ in

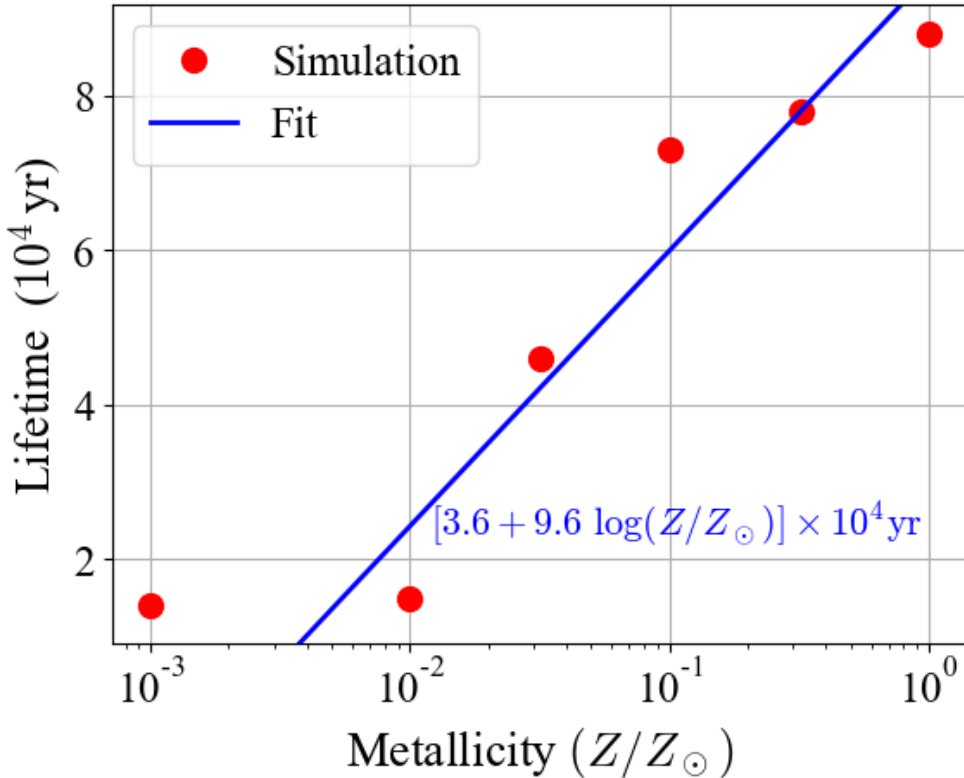


Fig. 4.8 Core lifetimes in Run FE (red dots; cf. Figure 4.7). The blue line is a fit given by $T_{\text{life}} = [9.6 + 3.6 \log(Z/Z_{\odot})] \times 10^4$ yr for $10^{-2} Z_{\odot} \leq Z \leq Z_{\odot}$.

Run FE. We can fit the metallicity dependence as

$$T_{\text{life}} = [9.6 + 3.6 \log(Z/Z_{\odot})] \times 10^4 \text{ yr.} \quad (4.9)$$

The $Z \leq 10^{-2} Z_{\odot}$ cores have lifetimes largely constant with $T_{\text{life}} \simeq 1.4 \times 10^4$ yr. They even completely disperse on the timescale of $\lesssim 3 \times 10^4$ yr. In summary, metal-rich cores have longer lifetimes in H II regions because the efficient cooling result in the smaller core sizes and thereby mass-loss rates.

In order to extract the influences of EUV on the core evolution, we have run the simulations where FUV radiation is disabled (Run E). The overall evolution is found to be almost the same as Run FE. It is concluded that in Run FE, EUV primarily causes the mass loss at any metallicity, and that FUV has only a minor effect on the dynamical evolution of cores. The core evolution is regulated by EUV in H II regions.

4.4.2.2 Photoevaporation Driven by FUV

FUV photons from massive stars penetrate a large column. Molecules are photodissociated, and the gas is heated by the grain photoelectric effect. A photodissociation region (PDR) is formed around H II regions by these effects of FUV. The volume is generally much larger than the inner H II regions, and hence PDRs may contain a number of molecular cloud cores. It is thus also worth studying core photoevaporation purely driven by FUV. For that purpose, we run an additional set of simulations, where a molecular cloud core is exposed to FUV while EUV is disabled (Run F).

A solar-metallicity core is marginally optically thick to FUV in our fiducial setup (Section 4.3). The hemisphere facing the radiation source completely attenuates FUV photons, and the gas temperature reaches 300–500 K. The FUV-driven photoevaporative flows have a typical velocity of 1–3 km s⁻¹. A weak shock is excited, and the core finally shapes a cometary globule.

With $Z \leq 10^{-0.5} Z_{\odot}$, the optical thickness of the cores is so small that FUV can heat the entire regions. The gas temperature is raised to $T_{\text{clump,F}} \simeq 200, 150, 100, 30, 10$ K in the cores with $Z = 10^{-0.5}, 10^{-1}, 10^{-1.5}, 10^{-2}, 10^{-3} Z_{\odot}$, respectively. The cores have the effective optical depth parameter $\eta'_0 < 1$, where we generalize η_0 of Eq.(4.3) to take account of metallicity dependence as

$$\eta'_0(Z) = \eta_0 Z/Z_{\odot}. \quad (4.10)$$

The dynamical evolution of the FUV-heated cores is consistent with the analytic model of Gorti and Hollenbach (2002). The cores spherically expand at the velocity of c_s that is set by $T_{\text{clump,F}}$. We do not observe the shocks in the low-metallicity cores.

Higher-metallicity cores have larger mass-loss rates with $Z \leq 10^{-0.5} Z_{\odot}$. This trend results from the higher $T_{\text{clump,F}}$ (the dashed line in Figure 4.7). With solar-metallicity, photoevaporation takes place only in the hemisphere at the side of the radiation source. As a result, the solar-metallicity core has a smaller \dot{M} than the cores with sub-solar metallicities. Note that the slight mass loss of the $Z = 10^{-3} Z_{\odot}$ core is expected to be caused because gravity is not taken into account in our simulations. We discuss the effect in Section 4.5.3.

4.5 Discussions

4.5.1 Core Photoevaporation with Weaker UV fluxes

Using different assumptions or numerical methods can possibly vary our results. We examine such possible variations in this section. We first investigate the effects of UV flux. We perform other sets of simulations with smaller incident UV fluxes of $(G_{\text{FUV}}, F_{\text{EUV}}) = (8.4 \times 10^2 G_0, 2.1 \times 10^{11} \text{ s}^{-1})$, $(5.7 \times 10^1 G_0, 2.5 \times 10^9 \text{ s}^{-1})$, and compare the results with those of the fiducial model. The weaker flux sets are dubbed the intermediate and weak fluxes to distinguish from the fiducial fluxes. The sets of the fluxes and the corresponding source luminosities are listed in Table 4.1. The luminosities are calculated with assuming that the external source is placed at 0.1 pc from the core surface. Henceforth, a flux set used in a simulation is specified by appending the flux label listed in Table 4.1

Table 4.1 UV Luminosities Used in the Simulations.

Case	Label	$G_{\text{FUV}} (G_0)$	$F_{\text{EUV}} (\text{cm}^{-2} \text{s}^{-1})$	$L_{\text{FUV}} (\text{erg s}^{-1})$	$\Phi_{\text{EUV}} (\text{s}^{-1})$
Fiducial	H	6.8×10^3	5.9×10^{12}	1.3×10^{37}	7.0×10^{48}
Intermediate	M	8.4×10^2	2.1×10^{11}	1.6×10^{36}	2.5×10^{47}
Weak	L	5.7×10^1	2.5×10^9	1.1×10^{35}	3.0×10^{45}

to the simulation label. For example, “Z-0.5/F(M)” indicates a simulation with $Z = 10^{-0.5} Z_\odot$ and the intermediate flux set.

The cores in runs FE(M) and FE(L) evolve in a similar manner to run FE(H). The metallicity dependence of the lifetime is also the same; the lower metallicity core has a shorter lifetime. Luminosity affects the mass-loss rate (Figure 4.9). The shock-compression phase lasts for t_{cr} , which is in

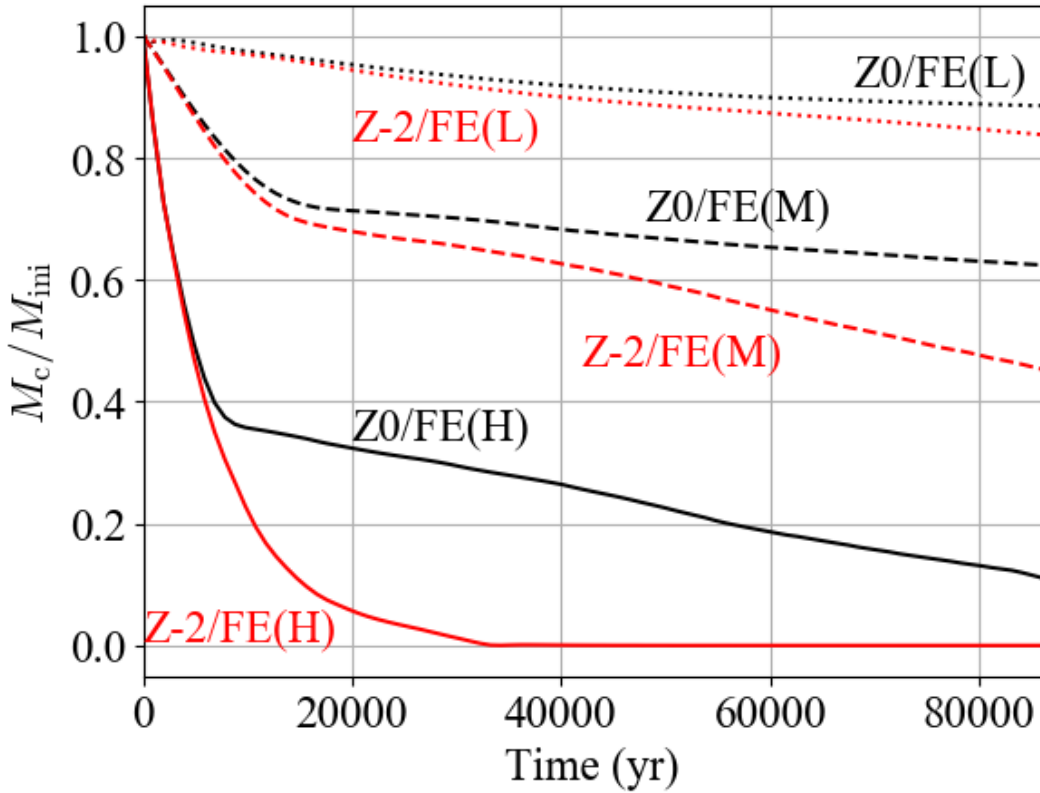


Fig. 4.9 Time evolution of the relative core mass to the initial mass M_c/M_{ini} in Z0/FE and Z-2/FE for each luminosity set. The simulations with the fiducial (H), intermediate (M), and weak (L) luminosity sets are indicated by the solid, dashed, and dotted line, respectively.

proportion to the initial ionization radius $R_{i,\text{ini}}$. Photoionization of H I following photodissociation of H_2 determines $R_{i,\text{ini}}$. The H_2 photodissociation timescale is given as $t_{\text{diss}} \sim 1(G_{\text{FUV}}/10^3)^{-1} \text{yr}$ at the core surface, but the self-shielding effect extends the time in the deeper interior of the core to $t_{\text{diss}} \sim 3 \times 10^4 (G_{\text{FUV}}/10^3)^{-1} (d/10^{-2} \text{pc})$, where d is the physical depth from the core surface; H_2 photodissociation is efficient only in a small H_2 column with a low FUV flux. The produced atomic hydrogen is rapidly photoionized by EUV. These processes increase $R_{i,\text{ini}}$, and thus the shock crossing time is longer with lower fluxes. After the compression phase, the core is eroded from

the surface by EUV photoevaporation with mass-loss rates approximately given by Eq.(4.8). The H II region temperature does not strongly depend on EUV flux, and thus the launch velocity v_b is also $\sim 10 \text{ km s}^{-1}$ with the weaker fluxes. The base density n_b is determined by the balance between ionization and recombination of hydrogen at the ionization front. The bulk of EUV is absorbed by atomic hydrogen residing in the region close to the launch surface. Hence, n_b is nearly in proportion to $\sqrt{F_{\text{EUV}}}$. The launch area S is larger for a lower EUV luminosity because the core volume can remain large in the lower external pressure. The flux dependence of the volume is approximately expressed as $S \propto F_{\text{EUV}}^{-1/3}$ during the cometary phase. Therefore, the EUV photoevaporation rates slightly decline with EUV luminosity as $\dot{M} \propto F_{\text{EUV}}^{1/6}$.

Lefloch and Lazareff (1994) studied the evolution of a neutral globule illuminated by nearby OB stars. They performed 2D hydrodynamics simulations, assuming an isothermal neutral gas, and derived an analytic formula that gives the duration of the cometary phase

$$t_{\text{com}} = 6.5 \left(\frac{M_e}{M_\odot} \right)^{1/3} \left(\frac{F_{\text{EUV}}}{10^7 \text{ cm}^{-2} \text{ s}^{-1}} \right)^{-1/3} \left(\frac{T_n}{100 \text{ K}} \right)^{-2/3} \text{ Myr}. \quad (4.11)$$

Here M_e is the globule mass after the compression phase and T_n is the neutral gas temperature. Using the resulting values of our runs Z-2/FE(H) and Z0/FE(H), we approximately calculate the duration of the cometary phase with Eq.(4.11). The estimated times are $t_{\text{com}} = 5.6 \times 10^4$, 2.6×10^5 yr for Z-2/FE(H) and Z0/FE(H), respectively. The evaporation timescale (= core lifetime) is then calculated as $t_{\text{life}} = t_{\text{cr}} + t_{\text{com}} \simeq 6.0 \times 10^4$ yr, 2.6×10^5 yr, respectively. These are consistent with our simulation results (Figure 4.9). This allows us to employ Eq.(4.11) to estimate the lifetimes of the cores in the simulations with the weaker flux sets, instead of running the simulations until the cores completely disappear. We take the values of t_{cr} , M_e , T_n from runs Z0/FE(M), Z-2/FE(M),

Table 4.2 Adopted Parameters in Eq.(4.11) and the Estimated Lifetimes.

Label	t_{cr} (yr)	M_e (M_\odot)	T_n (K)	t_{life} (Myr)
Z0/FE(M)	1.5×10^4	0.7	10	0.98
Z0/FE(L)	6.0×10^4	0.9	10	4.6
Z-2/FE(M)	1.5×10^4	0.7	100	0.22
Z-2/FE(L)	6.0×10^4	0.9	100	1.0

Z0/FE(L), and Z-2/FE(L), and estimate the core lifetimes. We show the adopted values and the derived lifetimes in Table 4.2. Remarkably, the resulting lifetime is ~ 5 Myr for the weak luminosity with solar metallicity. The EUV flux corresponds to that of an early O-type star at a distance of 10 pc from the core. Since the typical lifetime of such hot stars is a few million years (Stahler and Palla 2005), cores distant from massive stars may survive though the bulk of the mass is lost during their evolution.

With the weaker flux sets, the evolutionary characters of the cores in our Run F are similar to those in our fiducial model. A solar-metallicity core is marginally optically thick to FUV, and thus FUV is excited in the hemisphere at the side of the radiation source. Photoevaporative flows are driven at the velocity comparable to c_s that is set by FUV heating. The temperatures of the FUV-heated regions decrease with FUV fluxes, but not in a significant manner; the FUV-heated region has temperatures varying only by a factor of three, from 100 K to 300 K with the examined FUV luminosities. Thus, the mass-loss rate due to FUV photoevaporative flows monotonically decreases

for a weaker FUV flux, but the flux dependence is weaker than the FE cases (Figure 4.10). Regarding

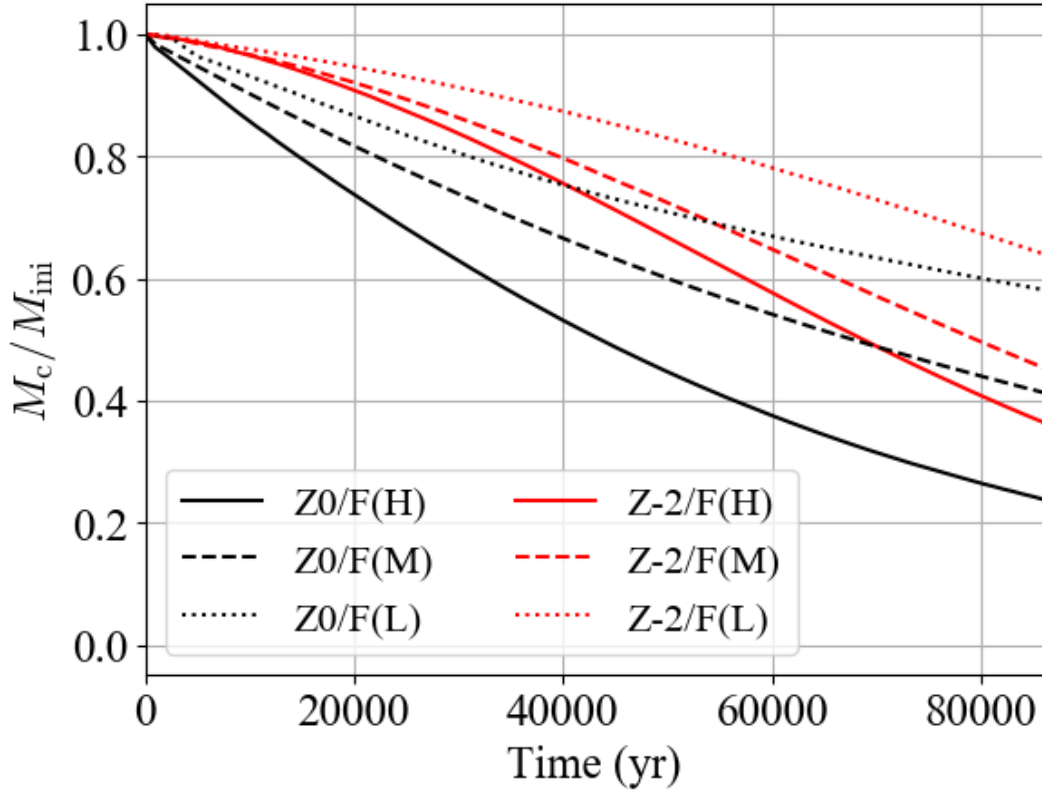


Fig. 4.10 Time evolution of the core mass relative to the initial mass M_c/M_{ini} for Z0/F and Z-2/F with each of the luminosity sets. The simulations with the fiducial (H), intermediate (M), and weaker (L) luminosity sets are indicated by the solid, dashed, and dotted line, respectively.

the lower-metallicity cores with $Z < Z_{\odot}$, FUV entirely heats the optically thin cores. Again, FUV slightly raises the internal temperature with a higher flux. The higher FUV flux yields a higher photoevaporation rate (Figure 4.10).

4.5.2 The Rocket Effect and Star Formation

We have observed in Run FE that photoevaporating molecular cloud cores move outward from the radiation source. Sufficiently long-lived cores can eventually get out of H II regions to enter the surrounding PDRs. Photoevaporation is not so efficient there as in the H II region, and thus the cores may live for an even longer time. Our fiducial EUV luminosity gives the Strömgren radius of the external OB star (radiation source) as $R_S \simeq 14 \text{ pc } (n_{\text{H}}/10 \text{ cm}^{-3})^{-2/3}$, where n_{H} is the average density in an H II region. The effect of dust absorption is neglected in the derivation. ^{*1} The moving cores escape from the intense EUV irradiation at the time of

$$t_{\text{out}} = \frac{R_S}{b} \frac{2}{1 + \sqrt{1 + 4aR_S/b^2}} \quad (4.12)$$

$$\sim 0.63 \left[\left(\frac{n_{\text{H}}}{10 \text{ cm}^{-3}} \right)^{-1/3} - 0.17 \right] \text{ Myr}, \quad (4.13)$$

^{*1} The dust absorption can reduce the Strömgren radius by $\sim 20\%$ owing to (Spitzer 1978).

where $n_{\text{HII}} \lesssim 10^3 \text{ cm}^{-3}$ is assumed. We compare t_{out} with the lifetime of a photoevaporating core t_{ph} by applying the core model of Eq.(4.5) to estimate t_{ph} ,

$$t_{\text{ph}} = \frac{M_{\text{cl}}}{S\rho_{\text{b}}v_{\text{b}}} \sim 0.40 \left(\frac{S}{10^{-4} \text{ pc}^2} \right)^{-1} \left(\frac{n_{\text{b}}}{10^5 \text{ cm}^{-3}} \right)^{-1} \left(\frac{v_{\text{b}}}{10 \text{ km s}^{-1}} \right)^{-1} \left(\frac{M_{\text{cl}}}{M_{\odot}} \right) \text{ Myr}, \quad (4.14)$$

for the solar-metallicity core. Thus, t_{out} is comparable to the photoevaporation time t_{ph} in our model; cores could either evaporate before getting out of the H II region or reach the PDR with small masses. Overall, solar-metallicity cores lose the bulk of the mass while traveling over the H II region. The rocket effect is not so efficient that it allows the cores to escape from the intense EUV irradiation to survive.

If cores could survive in H II regions and enter PDRs, the main heating channel is switched to FUV heating. The cores have experienced the compression and formed the cometary globules in the H II region. The globules are optically thick to FUV (typically, $\eta_0 \sim 2 \times 10^2$), and hence their evolution would differ from the cloud evolution in our Run F discussed in Section 4.4.1. Gorti and Hollenbach (2002) showed that the ratio between the sound speed in the PDR and in the cold cloud interior $\nu \equiv c_{\text{PDR}}/c_{\text{cl}}$ bifurcates the evolution of the clouds with $\eta_0 > 1$. In the case of $\eta_0 < 4\nu^2/3 (\equiv \eta_{\text{crit}})$, FUV produces a PDR “shell” on the surface of the cloud. A shock is excited by the high pressure in the interior. It compresses the cloud until the density becomes high enough to yield the column density equal to η_{crit} . In the case of $\eta_0 > \eta_{\text{crit}}$, an even thinner PDR shell is produced, and the shell expands at the speed of $\sim c_{\text{PDR}}$. The expansion rapidly decreases the pressure of the shell below the cold cloud pressure. It lasts until the internal density is decreased to yield the column density equal to η_{crit} . After the cloud achieves $\eta_0 = \eta_{\text{crit}}$, it evolves, keeping the constant column density at η_{crit} . Photoevaporation occurs during these processes and decreases the cloud volume. The cloud density increases to keep the constant column density during this process. Hence, star formation would occur within long-lived clouds in PDRs Gorti and Hollenbach (2002).

4.5.3 Gravity Effects

We examine possible influences of gravity on our results in this section. UV-heated gas could be bound by gravity, and thus photoevaporation could be suppressed. However, in our simulations, the crossing time of the photoevaporative flows t_{cr} is much shorter than the free fall time

$$t_{\text{ff}} = \sqrt{\frac{3\pi}{32G\rho}} \sim 0.2 \left(\frac{n_{\text{H}}}{10^5 \text{ cm}^{-3}} \right)^{-1/2} \text{ Myr}, \quad (4.15)$$

on the launch surface of the EUV-driven flows. This indicates that the gravity effect is minor to suppress photoevaporation. If self-gravity were incorporated in our simulations, the photoevaporative flows would be driven by EUV in any case. Several previous studies performed 3D simulations with gravity and concluded that the overall evolution is not changed by the gas self-gravity (Kessel-Deynet and Burkert 2003, Esquivel and Raga 2007).

Nevertheless, including self-gravity can change resulting photoevaporation rates to some extent by varying the internal structure of cloud cores. The core gas typically has the ratio of the gravitational

energy to the thermal energy of

$$\psi = \frac{GM_{\text{cl}}}{R_{\text{cl}}c_s^2} \quad (4.16)$$

$$\sim 5 \left(\frac{M_{\text{cl}}}{M_{\odot}} \right) \left(\frac{R_{\text{cl}}}{10^{-2} \text{ pc}} \right)^{-1} \left(\frac{T}{10 \text{ K}} \right)^{-1}. \quad (4.17)$$

Substituting the typical size and temperature of low-metallicity cores with $Z \lesssim 10^{-2} Z_{\odot}$: $R_{\text{cl}} \sim 0.1 \text{ pc}$ and $T \sim 10^3\text{--}10^4 \text{ K}$, respectively, we estimate the ratio ψ to be of the order of $10^{-3}\text{--}10^{-2}$. Thus, gravity would not significantly affect the lifetimes of the low-metallicity cores (Figure 4.8). In contrast, the cores with $Z \gtrsim 10^{-1} Z_{\odot}$ have ψ of the order of unity. The core radius may be reduced by self-gravity, increasing the core density at the center. The gravitationally-reduced surface area of the higher metallicity cores enables them to survive even longer. The internal density profile does not matter to define the base density, because the base density ρ_b is physically determined by the balance of EUV flux and the recombination reaction coefficient.

In the case of FUV photoevaporation, the crossing time of the FUV-driven winds is sufficiently shorter than the free fall time with $Z \gtrsim 10^{-1.5} Z_{\odot}$. FUV photoevaporation can be also excited even if gravity is incorporated. The higher-metallicity cores have a small ratio ψ , and thus the effects of gravity would not significantly change the lifetimes of the higher metallicity cores. By contrast, the free fall time is comparable to the crossing time with the lower metallicities of $Z \lesssim 10^{-2} Z_{\odot}$. The core dispersal would be suppressed by incorporating gravity. Especially, the $Z = 10^{-3} Z_{\odot}$ core likely loses the mass because of neglecting gravity in our model.

4.5.4 Implications to Star Formation

Besides the suppression of photoevaporation, self-gravity is essential for molecular cloud cores to initiate collapse to form stars inside. In this study, the radiation-driven shock compression increases the core density and shortens the free fall time. Thus, the existence of nearby massive stars may have a positive effect on star formation process in star-forming regions (radiation-driven collapse; Esquivel and Raga 2007).

We calculate the free fall time of the highest-density regions in the molecular cloud cores for Run FE and Run F (Figure 4.11). In Run FE, the free fall time is indeed shortened during the shock compression and roughly remains constant afterward for the cores with $Z \gtrsim 10^{-1.5} Z_{\odot}$ (see the left panel in Figure 4.11). The free fall time is of the order of 10^4 yr in the steady cometary phase, and is shorter than the lifetimes. The low-metallicity cores with $Z \lesssim 10^{-2} Z_{\odot}$ have $t_{\text{ff}} \sim 10^5 \text{ yr}$, which is much longer than the lifetimes. In Run F, the solar-metallicity core has the shortest t_{ff} of the order of $10^4\text{--}10^5 \text{ yr}$, and the cores with the other metallicities have $t_{\text{ff}} \gtrsim 10^6 \text{ yr}$. The difference in t_{ff} highlights the different dynamical evolution of the FUV-irradiated cores; the shock compression occurs in the solar-metallicity core, and not in the others. Since the efficient FUV heating due to a larger amount of dust quickly reduces the density of the $Z = 10^{-0.5} Z_{\odot}$ core, the free fall time becomes the longest among the $Z < Z_{\odot}$ cores at the early time. The increase of t_{ff} is delayed in the lower-metallicity cores.

We define the evaporation timescale t_{eva} as

$$t_{\text{eva}} = \left(\frac{1}{M_c} \frac{dM_c}{dt} \right)^{-1}, \quad (4.18)$$

to discuss the possibility of star formation in photoevaporating cores. The evaporation timescale

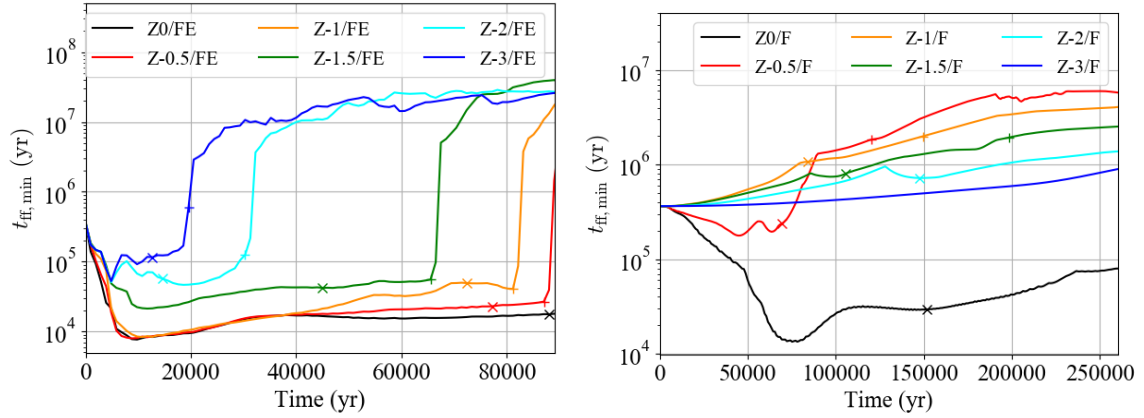


Fig. 4.11 Free fall times t_{ff} in the highest-density regions of the cores. Those of Run FE and Run F are shown in the left and right panels, respectively. The ranges of the vertical and horizontal axes are different between these panels. The points when the core mass decreases to $M_c/M_{\text{ini}} = 0.1, 0.01$ are indicated by the “x” and “+” markers, respectively. Note that the sudden increases of t_{ff} in the left panel implies the disappearance of the cores due to photoevaporation (cf. Figure 4.7); the depicted t_{ff} is physically unimportant after this point.

is defined at each time t , and when $t_{\text{eva}} > t_{\text{ff}}$, the gravitational collapse may take place to form stars before photoevaporation removes the mass. We compare t_{eva} and t_{ff} of the cores for Run FE and Run F in Figure 4.12, defining the region with $t_{\text{eva}} < t_{\text{ff}}$ as the “fast-evaporation region” in the $t_{\text{ff}}-t_{\text{eva}}$ plane. In Run FE, the cores with $Z \gtrsim 10^{-1.5} Z_{\odot}$ get out of the fast-evaporation region

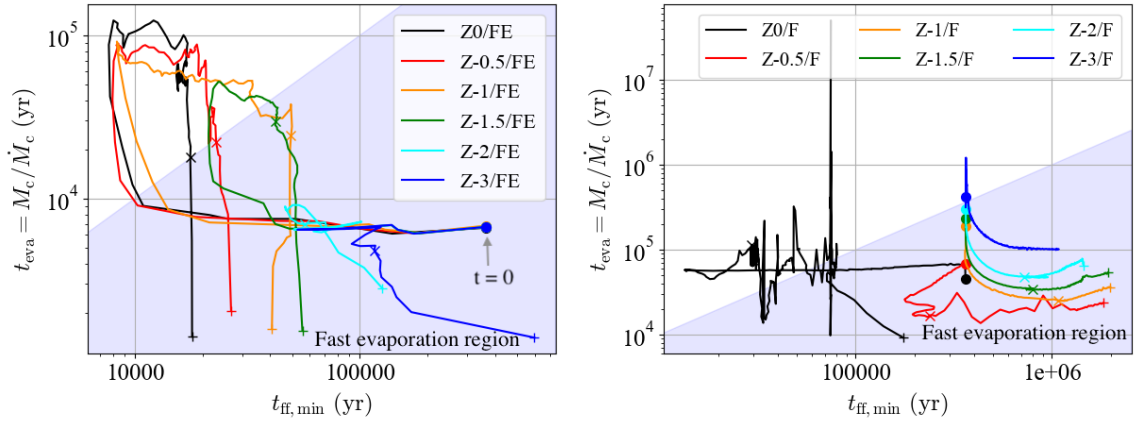


Fig. 4.12 Time evolution of the photoevaporating cores in the $t_{\text{ff}}-t_{\text{eva}}$ plane for Run FE (left) and Run F (right). The initial points are indicated by the dots with the corresponding colors, and they are shared in Run FE. The cross and plus markers are plotted in the same manner as Figure 4.11. The blue regions show the “fast-evaporation regions” where $t_{\text{eva}} < t_{\text{ff}}$. The low-metallicity cores with $Z \leq 10^{-2} Z_{\odot}$ never get out of the fast-evaporation region in Run FE, while only solar-metallicity core gets out of the region for a long time in Run F.

during the evolution, while those with lower metallicities stay in the region. Star formation may be triggered in the cometary cores by the radiation-driven implosion for $Z \gtrsim 0.1 Z_{\odot}$. The evaporation timescale of the $Z = 10^{-1.5} Z_{\odot}$ core is comparable to or less than the free fall time during most of its lifetime. Star formation is possibly suppressed in the cometary core. For the lower metallicities of $Z \lesssim 10^{-2} Z_{\odot}$, the cores never get out of the fast-evaporation region. It indicates that the

intense radiation of nearby massive stars significantly suppresses star formation in low-metallicity environments. Regarding Run F, the solar-metallicity core goes out of the fast-evaporation region, but the others stay in the region with increasing their free fall time. Star formation appears to be relevant only to solar-metallicity cores.

In summary, the radiation-driven shock has an essential effect on star formation, but not necessarily leads to core collapse because of photoevaporation as evidenced by the $Z \lesssim 10^{-2} Z_{\odot}$ cores in Run FE. Star formation can be initiated in $Z \gtrsim 0.1 Z_{\odot}$ cores in H II regions around massive stars, and it is significantly suppressed for $Z \lesssim 10^{-2} Z_{\odot}$. In PDRs around massive stars, at least high-metallicity environments ($Z \gtrsim 1 Z_{\odot}$) are necessary to drive star formation with the intense radiation of the massive stars; otherwise, the FUV radiation negatively affects star formation by reducing the core density. The star formation efficiency around massive stars is directly set by these effects. Hence, it is worth investigating this radiation-triggered star formation by external massive stars in future hydrodynamics simulations.

4.5.5 Metallicity Dependence in the Spectra of High-Energy Radiation

We have used fixed UV luminosity and spectrum of the external radiation source (massive stars) to focus on the variation in the core lifetimes caused by the difference in the amount of the metal content. However, practically, the spectra of stars generally depend on metallicity because the line absorption by metal molecules/atoms/ions (so-called ‘‘line blanketing’’; Milne 1928) is small in the atmosphere of metal-poor stars (e.g, Chamberlain and Aller 1951, McNamara and Colton 1969, Castelli and Cacciari 2001, Christlieb 2003, Castelli and Kurucz 2004, Peterson 2011). The EUV of hot stars, which is the essential component to drive efficient photoevaporation in ambient clouds, is also subject to a strong line blanketing by metal ions (Schaerer and Schmutz 1994, Hillier and Miller 1998, Pauldrach *et al.* 2001, Martins *et al.* 2002), although the direct measurement of the actual spectra is not possible because of the interstellar extinction. Martins *et al.* (2002) showed that including the blanketing effect of metals unnegligibly reduces EUV flux for $\lambda < 500 \text{ \AA}$ ($\gtrsim 25 \text{ eV}$). The reduction even reaches a few orders of magnitude for even hard EUV with $\lambda < 300 \text{ \AA}$ ($\gtrsim 40 \text{ eV}$). We have given $F_{\text{EUV}} = 5.9 \times 10^{12} \text{ cm}^{-2} \text{ s}^{-1}$ for the EUV flux of the external radiation source in our fiducial model. Assuming the source is located at the distance of 0.1 pc from the core surface, the flux corresponds to that of an O7-type star whose typical effective temperature is given by $T_{\text{eff}} \simeq 3.85 \times 10^4 \text{ K}$ (Spitzer 1978). Such stars emit about 91% of EUV photons in $13.6 \text{ eV} \leq h\nu \leq 25 \text{ eV}$, if the intrinsic spectrum is assumed to be given by blackbody with the effective temperature. *2 This indicates that even if we take account of the line blanketing effect, the base density ρ_b , which is set by the balance between EUV flux and the recombination rate, is not significantly changed. Hence, the metallicity dependence of the UV radiation does not strongly affect our results and conclusions regarding the photoevaporation rates, lifetimes, or their metallicity dependence. The spectra of even hotter sources, if exist, would have a strong emission in the high-energy regime $h\nu \geq 25 \text{ eV}$ and may be significantly influenced by metal line absorption. Our conclusions would not hold for such systems. Moreover, not all of the energy of EUV photons with $\gtrsim 35 \text{ eV}$ goes to heating (Draine 2011); our chemistry model is not applicable to cores around the extremely hot sources. Although exploring such systems are beyond our scope in this study, it is also necessary to develop a complete picture of cloud photoevaporation around hot sources, which

*2 In the case where the external source is assumed to be located at $\sim 0.3 \text{ pc}$, the EUV emission rate corresponds to that of O4-type stars with $T_{\text{eff}} \simeq 4.7 \times 10^4 \text{ K}$, and about 84% of EUV belongs to the range of $13.6 \text{ eV} \leq h\nu \leq 25 \text{ eV}$. Note that since we have focused our discussions on the photoevaporation rates resulted from a given flux (or emission rate) but not from a given spectrum, the effective temperature is rather arbitral in our model.

is ubiquitously observed in the universe.

Hot stars with $T_{\text{eff}} \gtrsim 8000$ K (A-, B-, O-type stars) do not have outer convective zones. Dynamo-powered X-ray emission is not expected from massive stars as opposed to solar-type stars. On the other hand, starting with the observations by the *Einstein* observatory (Harnden *et al.* 1979, Seward *et al.* 1979), it has been revealed that O-type stars actually emit strong X-ray whose luminosity is characterized by the relation of $L_X \simeq 10^{-7} L_{\text{bol}}$ (Gagné *et al.* 2011, Nazé *et al.* 2011, Oskinova *et al.* 2011), where L_{bol} is the bolometric luminosity. Though the origin of the X-ray is still under debate, shock-heated plasma in stellar winds (Lucy and White 1980, Lucy 1982, Owocki *et al.* 1988) is considered to be responsible for the emission. X-ray is not incorporated in our model, but it has the potential to affect the thermochemistry of photoevaporating cores. Metal lines contribute to the X-ray emission, and thus its metallicity dependence could bear a metallicity-dependent trend in core lifetimes. Hence, despite the relatively small luminosity of X-ray compared to UV, it would be worth investigating the X-ray effects on cloud photoevaporation. X-ray emission from young low-mass stars has a comparable power in star-forming regions; incorporating their effects would be also necessary for such studies.

4.6 Chapter Summary

We have studied photoevaporation of molecular cloud cores exposed to UV radiation from external massive stars with a suite of 3D radiation hydrodynamics simulations including nonequilibrium thermochemistry. The lifetimes of the cores have been derived for a broad range of metallicities $10^{-3} Z_{\odot} \leq Z \leq Z_{\odot}$.

In our fiducial model, the cores irradiated by EUV are compressed by the radiation-driven shock for the first $t_{\text{cr}} \simeq 4 \times 10^3$ yr. The core loses almost 50% of the initial mass through photoevaporation in this early phase. Afterward, the surface area of the core essentially determines the mass-loss rate. Lower-metallicity cores have higher internal temperatures, and thus remain large in volume, and lose the mass faster. As a result, the cores are shorter-lived with decreasing metallicity in $10^{-2} Z_{\odot} \leq Z \leq Z_{\odot}$. The estimated lifetimes are approximately fitted as $T_{\text{life}} = [9.6 + 3.6 \log(Z/Z_{\odot})] \times 10^4$ yr. The core volume is hardly decreased after the compression phase with $Z \lesssim 10^{-2} Z_{\odot}$. Thus, the lifetime is metallicity-independent and is roughly constant at $T_{\text{life}} \simeq 10^4$ yr.

We have also studied core photoevaporation in an FUV-dominated environment, such as the photodissociation regions, by disabling the EUV radiation in the simulations. The simulations (dubbed Run F) show that the solar-metallicity core is marginally optically thick to FUV photons, so that FUV heats only the hemisphere at the side of the radiation source. The cores are optically thin to FUV photons with the lower-metallicity case $Z < Z_{\odot}$ owing to the reduced amount of dust. FUV heating is efficient in metal-rich cores, and thus evaporation is fastened in the higher-metallicity cores. However, with the metallicity close to $1 Z_{\odot}$, the mass-loss rate is *smaller* than the subsolar cores because photoevaporative winds are driven only in the hemisphere. In Run F, the core is generally long-lived ($\gtrsim 10^5$ yr) than in Run FE.

The molecular cloud cores recede from the radiation source with being accelerated by the rocket effect. The solar-metallicity core has the typical velocity of $\sim 10 \text{ km s}^{-1}$ under the effects of EUV. Without EUV radiation, the velocity is much slower to be $\sim 1 \text{ km s}^{-1}$. Low-metallicity ($Z < Z_{\odot}$) cores also recede at the velocity of $\sim 10 \text{ km s}^{-1}$ in EUV-dominated environments. The rocket effect yields more efficient acceleration owing to the larger launch area of the lower metallicity cores.

In the present-day, local star-forming regions with $Z \gtrsim 10^{-1} Z_{\odot}$, the density enhancement due to the radiation-driven implosion can promote star formation in the H II region around massive

stars. On the other hand, in PDRs, sufficiently high-metallicity ($Z \gtrsim 1 Z_{\odot}$) is necessary for the radiation-driven collapse by FUV; otherwise, FUV-heated cores expand, lowering the density, and thus likely delay or suppress star formation. In low-metallicity environments with $Z \lesssim 10^{-2} Z_{\odot}$, the cores are not compressed by the radiation-driven implosion even in the H II region. In addition, they survive only for a short time. The existence of massive stars strongly suppresses star formation. In the PDRs, FUV heating lowers the core density though it is inefficient. This likely inhibits star formation around massive stars.

Chapter 5

Summary and Concluding Remarks

We have studied photoevaporation of protoplanetary disks and molecular cloud cores with various metallicities, and have derived their metallicity-dependent lifetimes. Protoplanetary disks and molecular cloud cores are the parental bodies of planets and stellar systems. Therefore, the lifetimes set the available time for their formation, and provide important implications to the formation efficiency and clues to understanding the formation processes. Our results can be applied not only to the nearby star-forming regions but also to star-forming regions in various metallicity environments, such as the inner/outer Galaxy and in high-redshift galaxies.

In Chapter 2, we have examined photoevaporation of protoplanetary disks irradiated by ultraviolet radiation from the central star, radiation hydrodynamics simulations including nonequilibrium thermochemistry. Our study is the first to follow the dynamical evolution of photoevaporating protoplanetary disks by employing a self-consistent physics implementation. Especially, none of the previous hydrodynamics studies has modeled dust temperatures by solving a self-consistent radiative transfer. Dust temperature is important to determine the dynamical, chemical, and thermal structure of a disk, and thus they affect resulting photoevaporation rates and lifetimes both directly and indirectly, as we have shown. In our model, FUV drives dense neutral flows that significantly contribute to photoevaporation rates of $\sim 10^{-8} M_{\odot} \text{ yr}^{-1}$ for $Z \gtrsim 0.1 Z_{\odot}$. The resulting photoevaporation rates increase with decreasing disk metallicity in $0.1 Z_{\odot} \lesssim Z \lesssim 10 Z_{\odot}$, while they decline with decreasing metallicity in $0.01 Z_{\odot} \lesssim Z \lesssim 0.1 Z_{\odot}$. Neutral flows are only weakly driven at this low metallicity. For $Z \lesssim 0.01 Z_{\odot}$, EUV-driven flows become dominant over FUV-driven flows to contribute to the mass-loss rate. As a result, the photoevaporation rates are roughly constant at $\sim 10^{-9} M_{\odot} \text{ yr}^{-1}$ with the very low metallicities. We have calculated lifetimes based on the derived photoevaporation rates. The lifetimes show a trend consistent with recent observations, which indicates that UV photoevaporation can be a cause for the metallicity dependence of the lifetimes. Our results predict a longer lifetime of a disk with the very low metallicities.

In Chapter 3, we have studied UV and X-ray photoevaporation of protoplanetary disks. The calculation methods are the same as those of Chapter 2 except that we have implemented X-ray radiation transfer to examine direct influences of X-ray on photoevaporation and its interplay with UV. In our fiducial model, X-ray is ineffective to drive neutral photoevaporative flows by its photoionization heating at any metallicity, but it strengthens FUV photoelectric heating by making the neutral regions electron-rich and thus reducing grain charges via recombination. The strengthened FUV heating excites the neutral photoevaporative flows even at the very low metallicity of $10^{-2.5} Z_{\odot} \lesssim Z \lesssim 10^{-2} Z_{\odot}$, and significantly raises the UV photoevaporation rates of Chapter 2 to be of the order of 10^{-8} – $10^{-7} M_{\odot} \text{ yr}^{-1}$. The slope of the metallicity dependence of the photoevaporation rates is slightly steeper than that of UV photoevaporation for $Z \gtrsim 0.1 Z_{\odot}$, and it makes the estimated lifetimes even more consistent with the observations. It is concluded again that the

strengthened FUV can also explain the observational trend in disk lifetimes. In our model, we have considered spectral energy distribution of X-ray, which has not yet been incorporated in the previous hydrodynamical models. This has led us to find that hard EUV photons with energies ~ 0.1 keV appear to significantly contribute to the mass loss if they reach disk surfaces. Hence, considering the energy distribution is essential to study X-ray photoevaporation.

Dispersal processes of protoplanetary disks have great impacts on planet formation. It sets an available amount of the materials and a time limit to form planets and also sets the initial configuration of primordial planetary systems. Revealing these properties can provide essential implications to future planet-searching missions and practical tools to give explanations for statistical characters of detected planets (e.g., the distribution in the distance-radius plane). To this end, it is worth investigating the dynamical evolution of dust grains growing to larger bodies inside protoplanetary disks under the effects of dispersal processes.

A solar-type pre-main-sequence star has been assumed as the central radiation source in this thesis and in most of the previous works that studied photoevaporation of protoplanetary disks. Since the binding energy and luminosities vary, an appropriate scaling would be necessary to apply our results to the young stellar systems hosting more or less massive stars. In fact, a shorter lifetime has been observationally found for disks around Herbig stars ($> 2 M_{\odot}$) compared to T Tauri disks ($< 2 M_{\odot}$) (Ribas *et al.* 2015). The shorter lifetime has a potential to explain the paucity of hot Jovian planets around the high-mass stars (e.g., Johnson *et al.* 2007) because disk dispersal stops the migration of gas giants. As for less massive stars, many exoplanets have been recently detected around M-dwarf stars ($\lesssim 0.5 M_{\odot}$). Some of the planets reside in the habitable zones as in the TRAPPIST-1 system (Gillon *et al.* 2016), and therefore modeling planet formation in low-mass stellar systems has a great impact especially on the search for habitable planets. There are a number of M-dwarfs, accounting for $\sim 80\%$ of stars in the Milky Way, and habitable planets are easy to be detected owing to the physical characters of the stars. These facts make the low-mass stars a rich target. In particular, infrared-doppler surveys have begun with Subaru telescope; it is expected that a number of planets are detected around M-dwarfs in the next decades. Investigating disk dispersal around the dwarf stars can yield results that can be used to give a possible explanation for observationally obtained trends of M-dwarfs' planets ahead of the surveys.

The shorter lifetimes of the lower-metallicity disks are derived based on the results of near-IR observations for the star-forming regions in the extreme outer galaxies. Near-IR is a tracer for the inner, warm dust at the typical distance of ~ 0.1 au. This implies that the derived lifetimes are not necessarily the dispersal time of outer dust or gas disks, although both gas and dust components are observationally known to disperse within ~ 10 Myr even at large distances in the nearby star-forming regions (Mamaĵek 2009, Ribas *et al.* 2015). Mid- and far-IR telescopes, e.g., *James Webb Space Telescope*, are planned to be used for the observations of the star-forming regions with low metallicities to examine the dispersal time of the outer disk. Whether the lifetime of the outer disks is estimated to be similar to that of the inner disks or not, our results of the subsolar-metallicity disks would give clues to explain these observational results. For a meaningful comparison with the observations, following the global evolution of protoplanetary disks is necessary with subsolar metallicities to obtain the snapshots of the dispersing disks at each evolutionary stage.

We have predicted the lifetimes of the order of 10 Myr for disks with very low metallicities of $Z \lesssim 10^{-2.5} Z_{\odot}$. It would be necessary to observe star-forming regions in such very low-metallicity environments to validate the predicted lifetimes. Unfortunately, known star-forming regions have the metallicity of $\sim 0.1 Z_{\odot}$ at the lowest in the Milky Way, and a comparable metallicity is found in those of LMC and SMC. These facts make it impractical to derive disk lifetimes with $Z \lesssim 10^{-2.5} Z_{\odot}$.

by observing star-forming regions. Instead, our results for the very low-metallicity disks can be applicable to “evolved” disks, viz. protoplanetary disks where the bulk of dust grains has grown to larger bodies and/or dispersed. As we have discussed in Section 2.4.3, small grains have a large contribution to drive neutral photoevaporative flows with FUV, and thus the heating effect of FUV would be weak in evolved disks. In addition, dust settling accompanied by grain growth, which also takes place in young disks, reduces the relative amount of grains to the gas in the regions near disk surfaces. This effect decreases the local metallicity of the FUV-heated region. Such a disk can be effectively regarded as a low-metallicity disk. Debris disks are evolved bodies of protoplanetary disks with the typical age of a few tens of millions of years, and have been considered to consist of dust and planetesimals. However, recent ALMA observations have revealed that roughly one-third of the detected debris disks shows strong CO emission indicating the existence of rich gas content. The physical mechanism to retain the gas for such a long time has not yet been well understood. Photoevaporation models give the dispersal time of the gas much shorter than the age of debris disks. In debris disks, most of the dust grains form larger grains and settle in the midplane, or are dispersed by radiation pressure from the central star and/or by entraining gas outflows. These effects reduce the amount of small grains, which are an important component for FUV heating, in the gas-rich regions, and effectively reduce the metallicity there. The metallicity could locally decrease to the very low-metallicity values. FUV photoevaporation is ineffective but EUV photoevaporation contributes to the mass loss. The predicted lifetime of ~ 10 Myr is in good agreement with the age of the gas-rich debris disks. More detailed studies with ALMA and next-generation telescopes will reveal the spatial distributions of dust and gas in the debris disks and would make it possible to compare our model and the observational results in more detail.

In Chapter 4, we have investigated the extended study: photoevaporation of molecular cloud cores illuminated by external massive stars. Our main focus is to examine lifetimes of the molecular cloud cores and, if any, their metallicity dependence. Although photoevaporation of a molecular cloud core occurs in the early stage of stellar system formation as opposed to the dispersal of a protoplanetary disk, the underlying physics are similar to each other, and thus we have adopted basically the same methods as those in Chapter 2 and Chapter 3. Our study is the first to incorporate multispecies chemistry and the effects of both EUV and FUV in hydrodynamics simulations. We have studied the core photoevaporation in H II regions and in photodissociation regions around massive stars, in which the cores evolve and lose their mass in a dynamically and chemically different manner. In our fiducial set-up, where cores are exposed to FUV/EUV radiation field of an O-type star located at 0.1 pc from the core surface, EUV is relatively more efficient to decrease the core mass through photoevaporation. A solar-metallicity core survives for $\sim 10^5$ yr, and the lifetimes decrease with decreasing metallicity owing to the effects of metal coolants. Molecular cloud cores with $Z \lesssim 0.01 Z_{\odot}$ have a constant lifetime of the order of 10^4 yr. In photodissociation regions, FUV radiation controls the core evolution. More than 80% of the initial mass is lost within 10^5 yr for the cores with $Z \gtrsim 10^{-1.5} Z_{\odot}$, and lower-metallicity cores disperse on the timescale of hundreds of thousands of years. The dispersal time is shorter for *higher*-metallicity cores with $Z < Z_{\odot}$, but a solar-metallicity core has a longer lifetime than the subsolar-metallicity cores, because the launch surface is smaller. We have concluded that in the local star-forming regions ($Z \gtrsim 0.1 Z_{\odot}$), star formation can be triggered by the implosion-driven compression in H II regions but is likely delayed in PDRs because of the core expansion by FUV heating. Note that in metal-rich PDRs with $Z \gtrsim 1 Z_{\odot}$, the radiation-driven implosion occurs and compresses cores, as our model has shown. In low-metallicity environments ($Z \lesssim 0.01 Z_{\odot}$), star formation is significantly suppressed owing to the efficient photoevaporation in H II regions. Molecular cloud cores can survive for a long time in

PDRs, but the free fall time is generally prolonged by FUV heating, implying suppression of star formation.

Massive stars form in star-forming regions of the present-day and high-redshift galaxies. Particularly, metal-poor environments are preferable to form massive stars owing to lack of the coolants. The contribution of massive stars to the star formation efficiency and rate would be especially important in high-redshift galaxies (and in the early period of our galaxy’s history). It is thus intriguing and worth incorporating the radiation-driven effects of massive stars in studies of galaxy formation and evolution. However, the length scale of a single molecular cloud ($\sim 0.1\text{--}10\text{ pc}$) is generally unresolvable in the galaxy simulations; the radiation-driven effects of massive stars on surrounding clouds need to be included in the subgrid models of the simulations. Our study is also necessary for this context, but we should extend our study to make it applicable to photoevaporating cores with other masses in our future work to this end. Once the cloud lifetimes are obtained as a function of the cloud mass, metallicity, and irradiating UV fluxes, we can estimate the amount of surviving molecular clouds and its mass spectrum around luminous sources. This procedure is essential to accurately model and interpret molecular/atomic line emission observed from high-redshift galaxies, and provides essential information to discuss its detectability with ALMA, JWST, and other telescopes starting to operate over the next decade: for instance, ngVLA and SKA. The model and observations are, in turn, required for the estimation of unobservables like dark matter halo mass and total gas mass of galaxies.

Our main interest has been in the formation processes of stellar systems occurring in various metallicity environments throughout this thesis. Metallicity is one of the parameters which can characterize the spatial location of star- and planet-forming bodies within a galaxy and also characterize a certain period of time in the evolutionary history of the universe. Studying stellar system formation with a variety of metallicity is thus indispensable to shed light on the stellar system formation in space and time generally, and to construct a “global” evolutionary scenario since the birth of the universe that follows a larger-scale evolution of galaxies, GMCs, and dark clouds; and a smaller-scale evolution of stars and planets, linking them together. In this thesis, we have studied the dispersal processes of the parental bodies of the stellar systems and planets: namely, molecular cloud cores and protoplanetary disks, bearing the ultimate goals above in mind. Combining the results of the studies presented in this thesis as a whole can give important implications regarding stellar system formation in diverse environments. In the present-day ($\gtrsim 0.1 Z_{\odot}$) GMCs hosting massive stars, star formation can be triggered by the radiation-driven implosion inside low-mass molecular clouds in the H II regions and in the metal-rich ($Z \gtrsim 1 Z_{\odot}$) PDRs. Stars and disks would form from the collapsing cloud cores, and then the disks disperse on the timescale of the lifetimes we have derived. The lifetime is shorter for lower-metallicity disks. In the present-day PDRs with $Z < 1 Z_{\odot}$, star formation might be suppressed by the intense FUV field. If disks were formed, the lifetimes would be similar to those of disks in the H II regions. The formation efficiency of planets, especially for gas giants, could be reduced with decreasing metallicity in both H II regions and PDRs belonging to the GMCs. In metal-poor GMCs ($\lesssim 0.01 Z_{\odot}$), low-mass star formation is significantly suppressed in the H II regions of massive stars. In the PDRs, most of the molecules are destroyed by the intense FUV irradiation, and FUV photoelectric heating is not efficient to drive the radiation-driven implosion in the low-metallicity cores. Although molecular cloud cores survive for a longer time than the free fall time, the lack of the coolants may suppress or delay star formation in the cores. In addition, the inefficient photoelectric heating still works to make the free fall time longer by expanding the core. This also has a negative effect on star formation in the metal-poor PDRs. Therefore, stars and disks rarely form in H II regions and PDRs with the low metallicities. If stellar systems were formed in

surviving cores or molecular regions outside the PDRs, the disk lifetimes would be prolonged from ~ 1 Myr to ~ 10 Myr with decreasing metallicity to the extremely metal-poor range of $\lesssim 10^{-3} Z_{\odot}$. Given that gaseous planets form in the disks, they have plenty of time to grow in mass and to migrate toward the central star. In summary, the metal-poor GMCs hosting massive stars are expected to have a significantly lower formation efficiency of stellar systems in both the H II regions and PDRs than the present-day GMCs. In the present-day star-forming regions, the formation efficiency of massive, close-in gaseous planets would be increased with decreasing metallicity, because long-lived protoplanetary disks provide them an available time to grow in mass and to migrate inward.

Photoevaporation of molecular clouds and protoplanetary disks corresponds to the early and late stages of stellar system evolution, respectively. It is also indispensable to study the mid-stage: the formation of stars and circumstellar disks and their coevolution, with a wide variety of metallicity. Dynamics of dust grains and magnetohydrodynamics effects may play key roles in the processes. We will also explore this stage in future works from both theoretical and observational points of view. The results, combining with those in this thesis, give clues to the formation/evolution histories of galaxies, stars, and planets, including our Milky Way and Solar system, since the beginning of the universe.

References

- Adams, F. C., Hollenbach, D., Laughlin, G. and Gorti, U. (2004). Photoevaporation of Circumstellar Disks Due to External Far-Ultraviolet Radiation in Stellar Aggregates, *ApJ* **611**, pp. 360–379, doi:10.1086/421989.
- Alexander, R., Pascucci, I., Andrews, S., Armitage, P. and Cieza, L. (2014). The Dispersal of Protoplanetary Disks, *Protostars and Planets VI*, pp. 475–496 doi:10.2458/azu_uapress_9780816531240-ch021.
- Alexander, R. D., Clarke, C. J. and Pringle, J. E. (2004). The effects of X-ray photoionization and heating on the structure of circumstellar discs, *MNRAS* **354**, pp. 71–80, doi:10.1111/j.1365-2966.2004.08161.x.
- Alexander, R. D., Clarke, C. J. and Pringle, J. E. (2006). Photoevaporation of protoplanetary discs - II. Evolutionary models and observable properties, *MNRAS* **369**, pp. 229–239, doi:10.1111/j.1365-2966.2006.10294.x.
- André, P., Men'shchikov, A., Bontemps, S., Könyves, V., Motte, F., Schneider, N., Didelon, P., Minier, V., Saraceno, P., Ward-Thompson, D., di Francesco, J., White, G., Molinari, S., Testi, L., Abergel, A., Griffin, M., Henning, T., Royer, P., Merín, B., Vavrek, R., Attard, M., Arzoumanian, D., Wilson, C. D., Ade, P., Aussel, H., Baluteau, J.-P., Benedettini, M., Bernard, J.-P., Blommaert, J. A. D. L., Cambrésy, L., Cox, P., di Giorgio, A., Hargrave, P., Hennemann, M., Huang, M., Kirk, J., Krause, O., Launhardt, R., Leeks, S., Le Penec, J., Li, J. Z., Martin, P. G., Maury, A., Olofsson, G., Omont, A., Peretto, N., Pezzuto, S., Prusti, T., Roussel, H., Russeil, D., Sauvage, M., Sibthorpe, B., Sicilia-Aguilar, A., Spinoglio, L., Waelkens, C., Woodcraft, A. and Zavagno, A. (2010). From filamentary clouds to prestellar cores to the stellar IMF: Initial highlights from the Herschel Gould Belt Survey, *A&A* **518**, L102, doi:10.1051/0004-6361/201014666.
- Andrews, S. M. and Williams, J. P. (2005). Circumstellar Dust Disks in Taurus-Auriga: The Submillimeter Perspective, *ApJ* **631**, pp. 1134–1160, doi:10.1086/432712.
- Anninos, P., Zhang, Y., Abel, T. and Norman, M. L. (1997). Cosmological hydrodynamics with multi-species chemistry and nonequilibrium ionization and cooling, *Nature* **2**, pp. 209–224, doi:10.1016/S1384-1076(97)00009-2.
- Armitage, P. J. (2011). Dynamics of Protoplanetary Disks, *ARA&A* **49**, pp. 195–236, doi:10.1146/annurev-astro-081710-102521.
- Bai, X.-N. (2013). Wind-driven Accretion in Protoplanetary Disks. II. Radial Dependence and Global Picture, *ApJ* **772**, 96, doi:10.1088/0004-637X/772/2/96.
- Bai, X.-N. (2016). Towards a Global Evolutionary Model of Protoplanetary Disks, *ApJ* **821**, 80, doi:10.3847/0004-637X/821/2/80.
- Bai, X.-N. (2017). Global Simulations of the Inner Regions of Protoplanetary Disks with Comprehensive Disk Microphysics, *ApJ* **845**, 75, doi:10.3847/1538-4357/aa7dda.
- Bai, X.-N. and Stone, J. M. (2013). Wind-driven Accretion in Protoplanetary Disks. I. Suppression of the Magnetorotational Instability and Launching of the Magnetocentrifugal Wind, *ApJ* **769**, 76, doi:10.1088/0004-637X/769/1/76.

- Bai, X.-N., Ye, J., Goodman, J. and Yuan, F. (2016). Magneto-thermal Disk Winds from Protoplanetary Disks, *ApJ* **818**, 152, doi:10.3847/0004-637X/818/2/152.
- Bakes, E. L. O. and Tielens, A. G. G. M. (1994). The photoelectric heating mechanism for very small graphitic grains and polycyclic aromatic hydrocarbons, *ApJ* **427**, pp. 822–838, doi:10.1086/174188.
- Balbus, S. A. and Hawley, J. F. (1991). A powerful local shear instability in weakly magnetized disks. I - Linear analysis. II - Nonlinear evolution, *ApJ* **376**, pp. 214–233, doi:10.1086/170270.
- Bally, J., Langer, W. D., Stark, A. A. and Wilson, R. W. (1987). Filamentary structure in the Orion molecular cloud, *ApJ* **312**, pp. L45–L49, doi:10.1086/184817.
- Barbá, R. H., Rubio, M., Roth, M. R. and García, J. (2003). Active Star Formation in the N11B Nebula in the Large Magellanic Cloud: A Sequential Star Formation Scenario Confirmed, *AJ* **125**, pp. 1940–1957, doi:10.1086/368141.
- Barrado y Navascués, D. and Martín, E. L. (2003). An Empirical Criterion to Classify T Tauri Stars and Substellar Analogs Using Low-Resolution Optical Spectroscopy, *AJ* **126**, pp. 2997–3006, doi:10.1086/379673.
- Bertoldi, F. (1989). The photoevaporation of interstellar clouds. I - Radiation-driven implosion, *ApJ* **346**, pp. 735–755, doi:10.1086/168055.
- Bertoldi, F. and McKee, C. F. (1990). The photoevaporation of interstellar clouds. II - Equilibrium cometary clouds, *ApJ* **354**, pp. 529–548, doi:10.1086/168713.
- Bertoldi, F. and McKee, C. F. (1992). Pressure-confined clumps in magnetized molecular clouds, *ApJ* **395**, pp. 140–157, doi:10.1086/171638.
- Bertout, C., Basri, G. and Bouvier, J. (1988). Accretion disks around T Tauri stars, *ApJ* **330**, pp. 350–373, doi:10.1086/166476.
- Blitz, L. (1993). Giant molecular clouds, in E. H. Levy and J. I. Lunine. eds., *Protostars and Planets III*, Tucson, AZ: Univ. of Arizona Press, pp. 125–161.
- Blitz, L. and Shu, F. H. (1980). The origin and lifetime of giant molecular cloud complexes, *ApJ* **238**, pp. 148–157, doi:10.1086/157968.
- Bok, B. J. and Reilly, E. F. (1947). Small Dark Nebulae. *ApJ* **105**, p. 255, doi:10.1086/144901.
- Bonnor, W. B. (1956). Boyle’s Law and gravitational instability, *MNRAS* **116**, p. 351, doi:10.1093/mnras/116.3.351.
- Cantó, J., Raga, A., Steffen, W. and Shapiro, P. R. (1998). Shadows behind Neutral Clumps in Photoionized Regions, *ApJ* **502**, pp. 695–707, doi:10.1086/305946.
- Castelli, F. and Cacciari, C. (2001). Stellar parameters for Pop II A-type stars from IUE spectra and new-ODF ATLAS9 model atmospheres, *A&A* **380**, pp. 630–644, doi:10.1051/0004-6361:20011445.
- Castelli, F. and Kurucz, R. L. (2004). New Grids of ATLAS9 Model Atmospheres, *arXiv Astrophysics e-prints* .
- Chamberlain, J. W. and Aller, L. H. (1951). The Atmospheres of A-Type Subdwarfs and 95 Leonis. *ApJ* **114**, p. 52, doi:10.1086/145451.
- Christlieb, N. (2003). Finding the Most Metal-poor Stars of the Galactic Halo with the Hamburg/ESO Objective-prism Survey (With 6 Figures), in R. E. Schielicke. ed., *Reviews in Modern Astronomy, Reviews in Modern Astronomy*, Vol. 16, New York: Wiley, p. 191, doi:10.1002/9783527617647.ch8.
- Clarke, C. J., Gendrin, A. and Sotomayor, M. (2001). The dispersal of circumstellar discs: the role of the ultraviolet switch, *MNRAS* **328**, pp. 485–491, doi:10.1046/j.1365-8711.2001.04891.x.
- Contursi, A., Lequeux, J., Cesarsky, D., Boulanger, F., Rubio, M., Hanus, M., Sauvage, M., Tran, D., Bosma, A., Madden, S. and Vigroux, L. (2000). Mid-infrared imaging and spectrophotometry

- of N 66 in the SMC with ISOCAM, *A&A* **362**, pp. 310–324.
- Currie, T., Lada, C. J., Plavchan, P., Robitaille, T. P., Irwin, J. and Kenyon, S. J. (2009). The Last Gasp of Gas Giant Planet Formation: A Spitzer Study of the 5 Myr Old Cluster NGC 2362, *ApJ* **698**, pp. 1–27, doi:10.1088/0004-637X/698/1/1.
- Decataldo, D., Ferrara, A., Pallottini, A., Gallerani, S. and Vallini, L. (2017). Molecular clumps photoevaporation in ionized regions, *MNRAS* **471**, pp. 4476–4487, doi:10.1093/mnras/stx1879.
- Deharveng, L., Lefloch, B., Kurtz, S., Nadeau, D., Pomarès, M., Caplan, J. and Zavagno, A. (2008). Triggered massive-star formation on the borders of Galactic H II regions. IV. Star formation at the periphery of Sh2-212, *A&A* **482**, pp. 585–596, doi:10.1051/0004-6361:20079233.
- Deharveng, L., Zavagno, A. and Caplan, J. (2005). Triggered massive-star formation on the borders of Galactic H II regions. I. A search for “collect and collapse” candidates, *A&A* **433**, pp. 565–577, doi:10.1051/0004-6361:20041946.
- Dent, W. R. F., Thi, W. F., Kamp, I., Williams, J. P., Menard, F., Andrews, S., Ardila, D., Aresu, G., Augereau, J.-C., Barrado y Navascues, D., Brittain, S., Carmona, A., Ciardi, D., Danchi, W., Donaldson, J., Duchene, G., Eiroa, C., Fedele, D., Grady, C., de Gregorio-Molsalvo, I., Howard, C., Huélamo, N., Krivov, A., Lebreton, J., Liseau, R., Martin-Zaidi, C., Mathews, G., Meeus, G., Mendigutía, I., Montesinos, B., Morales-Calderon, M., Mora, A., Nomura, H., Pantin, E., Pascucci, I., Phillips, N., Pinte, C., Podio, L., Ramsay, S. K., Riaz, B., Riviere-Marichalar, P., Roberge, A., Sandell, G., Solano, E., Tilling, I., Torrelles, J. M., Vandenbusche, B., Vicente, S., White, G. J. and Woitke, P. (2013). GASPS—A Herschel Survey of Gas and Dust in Protoplanetary Disks: Summary and Initial Statistics, *PASP* **125**, pp. 477–505, doi:10.1086/670826.
- Draine, B. T. (2011). *Physics of the Interstellar and Intergalactic Medium*, Princeton, NJ: Princeton Univ. Press.
- Draine, B. T. and Bertoldi, F. (1996). Structure of Stationary Photodissociation Fronts, *ApJ* **468**, p. 269, doi:10.1086/177689.
- Draine, B. T. and Lee, H. M. (1984). Optical properties of interstellar graphite and silicate grains, *ApJ* **285**, pp. 89–108, doi:10.1086/162480.
- Duvert, G., Cernicharo, J., Bachiller, R. and Gomez-Gonzalez, J. (1990). Star formation in a small globule in IC 1396, *A&A* **233**, pp. 190–196.
- Ebert, R. (1955). Über die Verdichtung von H I-Gebieten. Mit 5 Textabbildungen, *ZAp* **37**, p. 217.
- Elmegreen, B. G. (1979). On the disruption of a protoplanetary disk nebula by a T Tauri like solar wind, *A&A* **80**, p. 77.
- Elmegreen, B. G. and Lada, C. J. (1977). Sequential formation of subgroups in OB associations, *ApJ* **214**, pp. 725–741, doi:10.1086/155302.
- Ercolano, B. and Clarke, C. J. (2010). Metallicity, planet formation and disc lifetimes, *MNRAS* **402**, pp. 2735–2743, doi:10.1111/j.1365-2966.2009.16094.x.
- Ercolano, B., Clarke, C. J. and Drake, J. J. (2009). X-Ray Irradiated Protoplanetary Disk Atmospheres. II. Predictions from Models in Hydrostatic Equilibrium, *ApJ* **699**, pp. 1639–1649, doi:10.1088/0004-637X/699/2/1639.
- Ercolano, B., Clarke, C. J. and Hall, A. C. (2011). The clearing of discs around late-type T Tauri stars: constraints from the infrared two-colour plane, *MNRAS* **410**, pp. 671–678, doi:10.1111/j.1365-2966.2010.17473.x.
- Ercolano, B., Drake, J. J., Raymond, J. C. and Clarke, C. C. (2008). X-Ray-Irradiated Protoplanetary Disk Atmospheres. I. Predicted Emission-Line Spectrum and Photoevaporation, *ApJ* **688**, 398–407, doi:10.1086/590490.

- Ercolano, B. and Pascucci, I. (2017). The dispersal of planet-forming discs: theory confronts observations, *Royal Society Open Science* **4**, 170114, doi:10.1098/rsos.170114.
- Espaillet, C., Muzerolle, J., Najita, J., Andrews, S., Zhu, Z., Calvet, N., Kraus, S., Hashimoto, J., Kraus, A. and D'Alessio, P. (2014). An Observational Perspective of Transitional Disks, *Protostars and Planets VI*, pp. 497–520 doi:10.2458/azu_uapress.9780816531240-ch022.
- Esquivel, A. and Raga, A. C. (2007). Radiation-driven collapse of autogravitating neutral clumps, *MNRAS* **377**, pp. 383–390, doi:10.1111/j.1365-2966.2007.11609.x.
- Evans, N. J., II (1999). Physical Conditions in Regions of Star Formation, *ARA&A* **37**, pp. 311–362, doi:10.1146/annurev.astro.37.1.311.
- Facchini, S., Clarke, C. J. and Bisbas, T. G. (2016). External photoevaporation of protoplanetary discs in sparse stellar groups: the impact of dust growth, *MNRAS* **457**, pp. 3593–3610, doi:10.1093/mnras/stw240.
- Fedele, D., van den Ancker, M. E., Henning, T., Jayawardhana, R. and Oliveira, J. M. (2010). Timescale of mass accretion in pre-main-sequence stars, *A&A* **510**, A72, doi:10.1051/0004-6361/200912810.
- Flaherty, K. M. and Muzerolle, J. (2008). Evidence for Early Circumstellar Disk Evolution in NGC 2068/71, *AJ* **135**, pp. 966–983, doi:10.1088/0004-6256/135/3/966.
- Font, A. S., McCarthy, I. G., Johnstone, D. and Ballantyne, D. R. (2004). Photoevaporation of Circumstellar Disks around Young Stars, *ApJ* **607**, pp. 890–903, doi:10.1086/383518.
- Gagné, M., Fehon, G., Savoy, M. R., Cohen, D. H., Townsley, L. K., Broos, P. S., Povich, M. S., Corcoran, M. F., Walborn, N. R., Remage Evans, N., Moffat, A. F. J., Nazé, Y. and Oskinova, L. M. (2011). Carina OB Stars: X-ray Signatures of Wind Shocks and Magnetic Fields, *ApJS* **194**, 5, doi:10.1088/0067-0049/194/1/5.
- Galli, D. and Palla, F. (1998). The chemistry of the early Universe, *A&A* **335**, pp. 403–420.
- Gammie, C. F. (1996). Layered Accretion in T Tauri Disks, *ApJ* **457**, p. 355, doi:10.1086/176735.
- Geers, V. C., van Dishoeck, E. F., Visser, R., Pontoppidan, K. M., Augereau, J.-C., Habart, E. and Lagrange, A. M. (2007). Spatially extended polycyclic aromatic hydrocarbons in circumstellar disks around T Tauri and Herbig Ae stars, *A&A* **476**, pp. 279–289, doi:10.1051/0004-6361:20078466.
- Gillon, M., Jehin, E., Lederer, S. M., Delrez, L., de Wit, J., Burdanov, A., Van Grootel, V., Burgasser, A. J., TriAUD, A. H. M. J., Opitom, C., Demory, B.-O., Sahu, D. K., Bardalez Gagliuffi, D., Magain, P. and Queloz, D. (2016). Temperate Earth-sized planets transiting a nearby ultracool dwarf star, *Nature* **533**, pp. 221–224, doi:10.1038/nature17448.
- Gonzalez, G. (1997). The stellar metallicity-giant planet connection, *MNRAS* **285**, pp. 403–412, doi:10.1093/mnras/285.2.403.
- González, R. F., Raga, A. C. and Steffen, W. (2005). Numerical Simulations of the Fragmentation of Photoevaporating Nonuniform Clumps, **41**, pp. 443–451.
- Goodman, A. A., Benson, P. J., Fuller, G. A. and Myers, P. C. (1993). Dense cores in dark clouds. VIII - Velocity gradients, *ApJ* **406**, pp. 528–547, doi:10.1086/172465.
- Gorti, U., Dullemond, C. P. and Hollenbach, D. (2009). Time Evolution of Viscous Circumstellar Disks due to Photoevaporation by Far-Ultraviolet, Extreme-Ultraviolet, and X-ray Radiation from the Central Star, *ApJ* **705**, pp. 1237–1251, doi:10.1088/0004-637X/705/2/1237.
- Gorti, U. and Hollenbach, D. (2002). Photoevaporation of Clumps in Photodissociation Regions, *ApJ* **573**, pp. 215–237, doi:10.1086/340556.
- Gorti, U. and Hollenbach, D. (2004). Models of Chemistry, Thermal Balance, and Infrared Spectra from Intermediate-Aged Disks around G and K Stars, *ApJ* **613**, pp. 424–447, doi:10.1086/422406.

- Gorti, U. and Hollenbach, D. (2008). Line Emission from Gas in Optically Thick Dust Disks around Young Stars, *ApJ* **683**, 287–303, doi:10.1086/589616.
- Gorti, U. and Hollenbach, D. (2009). Photoevaporation of Circumstellar Disks By Far-Ultraviolet, Extreme-Ultraviolet and X-Ray Radiation from the Central Star, *ApJ* **690**, pp. 1539–1552, doi: 10.1088/0004-637X/690/2/1539.
- Gorti, U., Hollenbach, D. and Dullemond, C. P. (2015). The Impact of Dust Evolution and Photoevaporation on Disk Dispersal, *ApJ* **804**, 29, doi:10.1088/0004-637X/804/1/29.
- Gorti, U., Liseau, R., Sándor, Z. and Clarke, C. (2016). Disk Dispersal: Theoretical Understanding and Observational Constraints, *Space Sci. Rev.* **205**, pp. 125–152, doi:10.1007/s11214-015-0228-x.
- Gressel, O., Turner, N. J., Nelson, R. P. and McNally, C. P. (2015). Global Simulations of Protoplanetary Disks With Ohmic Resistivity and Ambipolar Diffusion, *ApJ* **801**, 84, doi: 10.1088/0004-637X/801/2/84.
- Güdel, M., Briggs, K. R., Arzner, K., Audard, M., Bouvier, J., Feigelson, E. D., Franciosini, E., Glauser, A., Grosso, N., Micela, G., Monin, J.-L., Montmerle, T., Padgett, D. L., Palla, F., Pillitteri, I., Rebull, L., Scelsi, L., Silva, B., Skinner, S. L., Stelzer, B. and Telleschi, A. (2007a). The XMM-Newton extended survey of the Taurus molecular cloud (XEST), *A&A* **468**, pp. 353–377, doi:10.1051/0004-6361:20065724.
- Güdel, M. and Nazé, Y. (2009). X-ray spectroscopy of stars, *A&A Rev.* **17**, pp. 309–408, doi: 10.1007/s00159-009-0022-4.
- Güdel, M., Skinner, S. L., Briggs, K. R., Audard, M., Arzner, K. and Telleschi, A. (2005). Evidence for an X-Ray Jet in DG Tauri A? *ApJ* **626**, pp. L53–L56, doi:10.1086/431666.
- Güdel, M., Telleschi, A., Audard, M., Skinner, S. L., Briggs, K. R., Palla, F. and Dougados, C. (2007b). X-rays from jet-driving protostars and T Tauri stars, *A&A* **468**, pp. 515–528, doi:10.1051/0004-6361:20065736.
- Gullbring, E., Hartmann, L., Briceño, C. and Calvet, N. (1998). Disk Accretion Rates for T Tauri Stars, *ApJ* **492**, pp. 323–341, doi:10.1086/305032.
- Haisch, K. E., Jr., Lada, E. A. and Lada, C. J. (2001). Disk Frequencies and Lifetimes in Young Clusters, *ApJ* **553**, pp. L153–L156, doi:10.1086/320685.
- Harnden, F. R., Jr., Branduardi, G., Elvis, M., Gorenstein, P., Grindlay, J., Pye, J. P., Rosner, R., Topka, K. and Vaiana, G. S. (1979). Discovery of an X-ray star association in VI Cygni /Cyg OB2/, *ApJ* **234**, pp. L51–L54, doi:10.1086/183107.
- Hartigan, P., Kenyon, S. J., Hartmann, L., Strom, S. E., Edwards, S., Welty, A. D. and Stauffer, J. (1991). Optical excess emission in T Tauri stars, *ApJ* **382**, pp. 617–635, doi:10.1086/170749.
- Hayashi, C. (1981). Structure of the Solar Nebula, Growth and Decay of Magnetic Fields and Effects of Magnetic and Turbulent Viscosities on the Nebula, *Progress of Theoretical Physics Supplement* **70**, pp. 35–53, doi:10.1143/PTPS.70.35.
- Heinzeller, D., Nomura, H., Walsh, C. and Millar, T. J. (2011). Chemical Evolution of Protoplanetary Disks—The Effects of Viscous Accretion, Turbulent Mixing, and Disk Winds, *ApJ* **731**, 115, doi: 10.1088/0004-637X/731/2/115.
- Heithausen, A., Bensch, F., Stutzki, J., Falgarone, E. and Panis, J. F. (1998). The IRAM key project: small-scale structure of pre-star forming regions. Combined mass spectra and scaling laws, *A&A* **331**, pp. L65–L68.
- Hernández, J., Hartmann, L., Megeath, T., Gutermuth, R., Muzerolle, J., Calvet, N., Vivas, A. K., Briceño, C., Allen, L., Stauffer, J., Young, E. and Fazio, G. (2007). A Spitzer Space Telescope Study of Disks in the Young σ Orionis Cluster, *ApJ* **662**, pp. 1067–1081, doi:10.1086/513735.
- Heyer, M. H. and Terebey, S. (1998). The Anatomy of the Perseus Spiral Arm: ^{12}CO and IRAS

- Imaging Observations of the W3-W4-W5 Cloud Complex, *ApJ* **502**, pp. 265–277, doi:10.1086/305881.
- Hillier, D. J. and Miller, D. L. (1998). The Treatment of Non-LTE Line Blanketing in Spherically Expanding Outflows, *ApJ* **496**, pp. 407–427, doi:10.1086/305350.
- Hollenbach, D., Johnstone, D., Lizano, S. and Shu, F. (1994). Photoevaporation of disks around massive stars and application to ultracompact H II regions, *ApJ* **428**, pp. 654–669, doi:10.1086/174276.
- Hollenbach, D. and McKee, C. F. (1989). Molecule formation and infrared emission in fast interstellar shocks. III - Results for J shocks in molecular clouds, *ApJ* **342**, pp. 306–336, doi:10.1086/167595.
- Hollenbach, D. J., Yorke, H. W. and Johnstone, D. (2000). Disk Dispersal around Young Stars, *Protostars and Planets IV*, p. 401.
- Hutchison, M. A., Laibe, G. and Maddison, S. T. (2016a). On the maximum grain size entrained by photoevaporative winds, *MNRAS* **463**, pp. 2725–2734, doi:10.1093/mnras/stw2191.
- Hutchison, M. A., Price, D. J., Laibe, G. and Maddison, S. T. (2016b). On dust entrainment in photoevaporative winds, *MNRAS* **461**, pp. 742–759, doi:10.1093/mnras/stw1126.
- Jayawardhana, R., Coffey, J., Scholz, A., Brandeker, A. and van Kerkwijk, M. H. (2006). Accretion Disks around Young Stars: Lifetimes, Disk Locking, and Variability, *ApJ* **648**, pp. 1206–1218, doi:10.1086/506171.
- Johnson, J. A., Aller, K. M., Howard, A. W. and Crepp, J. R. (2010). Giant Planet Occurrence in the Stellar Mass-Metallicity Plane, *PASP* **122**, p. 905, doi:10.1086/655775.
- Johnson, J. A., Butler, R. P., Marcy, G. W., Fischer, D. A., Vogt, S. S., Wright, J. T. and Peek, K. M. G. (2007). A New Planet around an M Dwarf: Revealing a Correlation between Exoplanets and Stellar Mass, *ApJ* **670**, pp. 833–840, doi:10.1086/521720.
- Johnstone, D., Hollenbach, D. and Bally, J. (1998). Photoevaporation of Disks and Clumps by Nearby Massive Stars: Application to Disk Destruction in the Orion Nebula, *ApJ* **499**, pp. 758–776, doi:10.1086/305658.
- Kataoka, A., Tanaka, H., Okuzumi, S. and Wada, K. (2013). Fluffy dust forms icy planetesimals by static compression, *A&A* **557**, L4, doi:10.1051/0004-6361/201322151.
- Kenyon, S. J. and Hartmann, L. (1987). Spectral energy distributions of T Tauri stars - Disk flaring and limits on accretion, *ApJ* **323**, pp. 714–733, doi:10.1086/165866.
- Kenyon, S. J. and Hartmann, L. (1995). Pre-Main-Sequence Evolution in the Taurus-Auriga Molecular Cloud, *ApJS* **101**, p. 117, doi:10.1086/192235.
- Kessel-Deynet, O. and Burkert, A. (2003). Radiation-driven implosion of molecular cloud cores, *MNRAS* **338**, pp. 545–554, doi:10.1046/j.1365-8711.2003.05737.x.
- Klein, R. I., Sandford, M. T., II and Whitaker, R. W. (1980). Two-dimensional radiation-hydrodynamics calculations of the formation of the O-B associations in dense molecular clouds, *Space Sci. Rev.* **27**, pp. 275–281, doi:10.1007/BF00168309.
- Koepferl, C. M., Ercolano, B., Dale, J., Teixeira, P. S., Ratzka, T. and Spezzi, L. (2013). Disc clearing of young stellar objects: evidence for fast inside-out dispersal, *MNRAS* **428**, pp. 3327–3354, doi:10.1093/mnras/sts276.
- Kramer, C., Stutzki, J., Rohrig, R. and Corneliusen, U. (1998). Clump mass spectra of molecular clouds, *A&A* **329**, pp. 249–264.
- Kuiper, R., Klahr, H., Dullemond, C., Kley, W. and Henning, T. (2010). Fast and accurate frequency-dependent radiation transport for hydrodynamics simulations in massive star formation, *A&A* **511**, A81, doi:10.1051/0004-6361/200912355.
- Kuiper, R. and Klessen, R. S. (2013). The reliability of approximate radiation transport methods

- for irradiated disk studies, *A&A* **555**, A7, doi:10.1051/0004-6361/201321404.
- Lada, C. J. and Adams, F. C. (1992). Interpreting infrared color-color diagrams - Circumstellar disks around low- and intermediate-mass young stellar objects, *ApJ* **393**, pp. 278–288, doi:10.1086/171505.
- Lada, E. A. and Lada, C. J. (1995). Near-infrared images of IC 348 and the luminosity functions of young embedded star clusters, *AJ* **109**, pp. 1682–1696, doi:10.1086/117396.
- Larson, R. B. (1981). Turbulence and star formation in molecular clouds, *MNRAS* **194**, pp. 809–826, doi:10.1093/mnras/194.4.809.
- Lee, H.-H., Bettens, R. P. A. and Herbst, E. (1996). Fractional abundances of molecules in dense interstellar clouds: A compendium of recent model results. *A&AS* **119**, pp. 111–114.
- Lefloch, B. and Lazareff, B. (1994). Cometary globules. 1: Formation, evolution and morphology, *A&A* **289**, pp. 559–578.
- Liedahl, D. A., Osterheld, A. L. and Goldstein, W. H. (1995). New calculations of Fe L-shell X-ray spectra in high-temperature plasmas, *ApJ* **438**, pp. L115–L118, doi:10.1086/187729.
- Liffman, K. (2003). The Gravitational Radius of an Irradiated Disk, *PASA* **20**, pp. 337–339, doi:10.1071/AS03019.
- López-Martín, L., Raga, A. C., Mellema, G., Henney, W. J. and Cantó, J. (2001). Photoevaporating Flows from the Cometary Knots in the Helix Nebula (NGC 7293), *ApJ* **548**, pp. 288–295, doi:10.1086/318654.
- Lucy, L. B. (1982). X-ray emission from the winds of hot stars. II, *ApJ* **255**, pp. 286–292, doi:10.1086/159827.
- Lucy, L. B. and White, R. L. (1980). X-ray emission from the winds of hot stars, *ApJ* **241**, pp. 300–305, doi:10.1086/158342.
- Lynden-Bell, D. and Pringle, J. E. (1974). The evolution of viscous discs and the origin of the nebular variables. *MNRAS* **168**, pp. 603–637, doi:10.1093/mnras/168.3.603.
- Maloney, P. R., Hollenbach, D. J. and Tielens, A. G. G. M. (1996). X-Ray-irradiated Molecular Gas. I. Physical Processes and General Results, *ApJ* **466**, p. 561, doi:10.1086/177532.
- Mamajek, E. E. (2009). Initial Conditions of Planet Formation: Lifetimes of Primordial Disks, in T. Usuda, M. Tamura and M. Ishii. eds., *American Institute of Physics Conference Series, American Institute of Physics Conference Series*, Vol. 1158, Melville, NY: AIP, pp. 3–10, doi:10.1063/1.3215910.
- Martins, F., Schaerer, D. and Hillier, D. J. (2002). On the effective temperature scale of O stars, *A&A* **382**, pp. 999–1004, doi:10.1051/0004-6361:20011703.
- Masunaga, H. and Inutsuka, S.-i. (2000). A Radiation Hydrodynamic Model for Protostellar Collapse. II. The Second Collapse and the Birth of a Protostar, *ApJ* **531**, pp. 350–365, doi:10.1086/308439.
- Mathis, J. S., Ruml, W. and Nordsieck, K. H. (1977). The size distribution of interstellar grains, *ApJ* **217**, pp. 425–433, doi:10.1086/155591.
- McCaughrean, M. J. and O’dell, C. R. (1996). Direct Imaging of Circumstellar Disks in the Orion Nebula, *AJ* **111**, p. 1977, doi:10.1086/117934.
- McElroy, D., Walsh, C., Markwick, A. J., Cordiner, M. A., Smith, K. and Millar, T. J. (2013). The UMIST database for astrochemistry 2012, *A&A* **550**, A36, doi:10.1051/0004-6361/201220465.
- McNamara, D. H. and Colton, D. J. (1969). Line-Blanketing Effects on the uvby β Photometric System, *PASP* **81**, p. 826, doi:10.1086/128855.
- Megeath, S. T., Cox, P., Bronfman, L. and Roelfsema, P. R. (1996). Evidence for ongoing star formation in the Carina nebula. *A&A* **305**, p. 296.
- Mellema, G., Raga, A. C., Canto, J., Lundqvist, P., Balick, B., Steffen, W. and Noriega-Crespo, A.

- (1998). Photo-evaporation of clumps in planetary nebulae, *A&A* **331**, pp. 335–346.
- Mewe, R., Gronenschild, E. H. B. M. and van den Oord, G. H. J. (1985). Calculated X-radiation from optically thin plasmas. V, *A&AS* **62**, pp. 197–254.
- Meyer, M. R., Backman, D. E., Weinberger, A. J. and Wyatt, M. C. (2007). Evolution of Circumstellar Disks Around Normal Stars: Placing Our Solar System in Context, *Protostars and Planets V*, pp. 573–588.
- Mignone, A., Bodo, G., Massaglia, S., Matsakos, T., Tesileanu, O., Zanni, C. and Ferrari, A. (2007). PLUTO: A Numerical Code for Computational Astrophysics, *ApJS* **170**, pp. 228–242, doi:10.1086/513316.
- Milne, E. A. (1928). The total absorption in the Sun’s reversing layer, *The Observatory* **51**, pp. 88–96.
- Minamidani, T., Tanaka, T., Mizuno, Y., Mizuno, N., Kawamura, A., Onishi, T., Hasegawa, T., Tatematsu, K., Takekoshi, T., Sorai, K., Moribe, N., Torii, K., Sakai, T., Muraoka, K., Tanaka, K., Ezawa, H., Kohno, K., Kim, S., Rubio, M. and Fukui, Y. (2011). Dense Clumps in Giant Molecular Clouds in the Large Magellanic Cloud: Density and Temperature Derived from $^{13}\text{CO}(J = 3-2)$ Observations, *AJ* **141**, 73, doi:10.1088/0004-6256/141/3/73.
- Miura, R., Okumura, S. K., Tosaki, T., Tamura, Y., Kurono, Y., Kuno, N., Nakanishi, K., Sakamoto, S., Hasegawa, T. and Kawabe, R. (2010). Aperture Synthesis Observations of CO, HCN, and 89 GHz Continuum Emission Toward NGC 604 in M33: Sequential Star Formation Induced by a Supergiant H II Region, *ApJ* **724**, pp. 1120–1132, doi:10.1088/0004-637X/724/2/1120.
- Mortier, A., Santos, N. C., Sousa, S., Israelian, G., Mayor, M. and Udry, S. (2013). On the functional form of the metallicity-giant planet correlation, *A&A* **551**, A112, doi:10.1051/0004-6361/201220707.
- Motte, F., Andre, P. and Neri, R. (1998). The initial conditions of star formation in the rho Ophiuchi main cloud: wide-field millimeter continuum mapping, *A&A* **336**, pp. 150–172.
- Muñoz, D. J., Mardones, D., Garay, G., Rebolledo, D., Brooks, K. and Bontemps, S. (2007). Massive Clumps in the NGC 6334 Star-forming Region, *ApJ* **668**, pp. 906–917, doi:10.1086/521206.
- Nakatani, R., Hosokawa, T., Yoshida, N., Nomura, H. and Kuiper, R. (2018a). Radiation Hydrodynamics Simulations of Photoevaporation of Protoplanetary Disks by Ultraviolet Radiation: Metallicity Dependence, *ApJ* **857**, 57, doi:10.3847/1538-4357/aab70b.
- Nakatani, R., Hosokawa, T., Yoshida, N., Nomura, H. and Kuiper, R. (2018b). Radiation Hydrodynamics Simulations of Photoevaporation of Protoplanetary Disks. II. Metallicity Dependence of UV and X-Ray Photoevaporation, *ApJ* **865**, 75, doi:10.3847/1538-4357/aad9fd.
- Nakatani, R. and Yoshida, N. (2018). Photoevaporation of Molecular Gas Clumps Illuminated by External Massive Stars: Clump Lifetimes and Metallicity Dependence, *ArXiv e-prints*.
- Natta, A., Testi, L., Muzerolle, J., Randich, S., Comerón, F. and Persi, P. (2004). Accretion in brown dwarfs: An infrared view, *A&A* **424**, pp. 603–612, doi:10.1051/0004-6361:20040356.
- Nazé, Y., Broos, P. S., Oskinova, L., Townsley, L. K., Cohen, D., Corcoran, M. F., Evans, N. R., Gagné, M., Moffat, A. F. J., Pittard, J. M., Rauw, G., ud-Doula, A. and Walborn, N. R. (2011). Global X-ray Properties of the O and B Stars in Carina, *ApJS* **194**, 7, doi:10.1088/0067-0049/194/1/7.
- Nelson, R. P. and Langer, W. D. (1997). The Dynamics of Low-Mass Molecular Clouds in External Radiation Fields, *ApJ* **482**, pp. 796–826, doi:10.1086/304167.
- Nomura, H., Aikawa, Y., Tsujimoto, M., Nakagawa, Y. and Millar, T. J. (2007). Molecular Hydrogen Emission from Protoplanetary Disks. II. Effects of X-Ray Irradiation and Dust Evolution, *ApJ* **661**, pp. 334–353, doi:10.1086/513419.

- Nomura, H. and Millar, T. J. (2005). Molecular hydrogen emission from protoplanetary disks, *A&A* **438**, pp. 923–938, doi:10.1051/0004-6361:20052809.
- O’Dell, C. R., Balick, B., Hajian, A. R., Henney, W. J. and Burkert, A. (2002). Knots in Nearby Planetary Nebulae, *AJ* **123**, pp. 3329–3347, doi:10.1086/340726.
- O’Dell, C. R. and Handron, K. D. (1996). Cometary Knots in the Helix Nebula, *AJ* **111**, p. 1630, doi:10.1086/117902.
- O’Dell, C. R., Henney, W. J. and Ferland, G. J. (2007). Determination of the Physical Conditions of the Knots in the Helix Nebula from Optical and Infrared Observations, *AJ* **133**, pp. 2343–2356, doi:10.1086/513011.
- Oka, T., Hasegawa, T., Sato, F., Tsuboi, M., Miyazaki, A. and Sugimoto, M. (2001). Statistical Properties of Molecular Clouds in the Galactic Center, *ApJ* **562**, pp. 348–362, doi:10.1086/322976.
- Oliveira, I., Pontoppidan, K. M., Merín, B., van Dishoeck, E. F., Lahuis, F., Geers, V. C., Jørgensen, J. K., Olofsson, J., Augereau, J.-C. and Brown, J. M. (2010). A Spitzer Survey of Protoplanetary Disk Dust in the Young Serpens Cloud: How do Dust Characteristics Evolve with Time? *ApJ* **714**, pp. 778–798, doi:10.1088/0004-637X/714/1/778.
- Omukai, K. (2000). Protostellar Collapse with Various Metallicities, *ApJ* **534**, pp. 809–824, doi:10.1086/308776.
- Omukai, K., Hosokawa, T. and Yoshida, N. (2010). Low-metallicity Star Formation: Prestellar Collapse and Protostellar Accretion in the Spherical Symmetry, *ApJ* **722**, pp. 1793–1815, doi:10.1088/0004-637X/722/2/1793.
- Omukai, K., Tsuribe, T., Schneider, R. and Ferrara, A. (2005). Thermal and Fragmentation Properties of Star-forming Clouds in Low-Metallicity Environments, *ApJ* **626**, pp. 627–643, doi:10.1086/429955.
- Oort, J. H. and Spitzer, L., Jr. (1955). Acceleration of Interstellar Clouds by O-Type Stars. *ApJ* **121**, p. 6, doi:10.1086/145958.
- Oskinova, L. M., Hamann, W.-R., Cassinelli, J. P., Brown, J. C. and Todt, H. (2011). X-ray emission from massive stars with magnetic fields, *Astronomische Nachrichten* **332**, p. 988, doi:10.1002/asna.201111602.
- Osterbrock, D. E. (1989). *Astrophysics of gaseous nebulae and active galactic nuclei*, Mill Valley, CA: Univ. Science Books.
- Osterbrock, D. E. and Ferland, G. J. (2006). *Astrophysics of gaseous nebulae and active galactic nuclei*, Mill Valley, CA: Univ. Science Books.
- Ostriker, E. C. (2007). Non-stellar sources of turbulence in the interstellar medium, in B. G. Elmegreen and J. Palous. eds., *Triggered Star Formation in a Turbulent ISM, IAU Symposium*, Vol. 237, Cambridge: Cambridge Univ. Press, pp. 70–75, doi:10.1017/S174392130700124X.
- Owen, J. E., Clarke, C. J. and Ercolano, B. (2012). On the theory of disc photoevaporation, *MNRAS* **422**, pp. 1880–1901, doi:10.1111/j.1365-2966.2011.20337.x.
- Owen, J. E., Ercolano, B. and Clarke, C. J. (2011a). Protoplanetary disc evolution and dispersal: the implications of X-ray photoevaporation, *MNRAS* **412**, pp. 13–25, doi:10.1111/j.1365-2966.2010.17818.x.
- Owen, J. E., Ercolano, B. and Clarke, C. J. (2011b). The imprint of photoevaporation on edge-on discs, *MNRAS* **411**, pp. 1104–1110, doi:10.1111/j.1365-2966.2010.17750.x.
- Owen, J. E., Ercolano, B., Clarke, C. J. and Alexander, R. D. (2010). Radiation-hydrodynamic models of X-ray and EUV photoevaporating protoplanetary discs, *MNRAS* **401**, pp. 1415–1428, doi:10.1111/j.1365-2966.2009.15771.x.
- Owocki, S. P., Castor, J. I. and Rybicki, G. B. (1988). Time-dependent models of radiatively driven

- stellar winds. I - Nonlinear evolution of instabilities for a pure absorption model, *ApJ* **335**, pp. 914–930, doi:10.1086/166977.
- Pascucci, I., Gorti, U., Hollenbach, D., Najita, J., Meyer, M. R., Carpenter, J. M., Hillenbrand, L. A., Herczeg, G. J., Padgett, D. L., Mamajek, E. E., Silverstone, M. D., Schlingman, W. M., Kim, J. S., Stobie, E. B., Bouwman, J., Wolf, S., Rodmann, J., Hines, D. C., Lunine, J. and Malhotra, R. (2006). Formation and Evolution of Planetary Systems: Upper Limits to the Gas Mass in Disks around Sun-like Stars, *ApJ* **651**, pp. 1177–1193, doi:10.1086/507761.
- Pauldrach, A. W. A., Hoffmann, T. L. and Lennon, M. (2001). Radiation-driven winds of hot luminous stars. XIII. A description of NLTE line blocking and blanketing towards realistic models for expanding atmospheres, *A&A* **375**, pp. 161–195, doi:10.1051/0004-6361:20010805.
- Pavlakis, K. G., Williams, R. J. R., Dyson, J. E., Falle, S. A. E. G. and Hartquist, T. W. (2001). The modification by diffuse radiation of “cometary tail” formation behind globules, *A&A* **369**, pp. 263–268, doi:10.1051/0004-6361:20010070.
- Peterson, R. C. (2011). The Extreme Overabundance of Molybdenum in Two Metal-poor Stars, *ApJ* **742**, 21, doi:10.1088/0004-637X/742/1/21.
- Pinte, C., Dent, W. R. F., Ménard, F., Hales, A., Hill, T., Cortes, P. and de Gregorio-Monsalvo, I. (2016). Dust and Gas in the Disk of HL Tauri: Surface Density, Dust Settling, and Dust-to-gas Ratio, *ApJ* **816**, 25, doi:10.3847/0004-637X/816/1/25.
- Pollack, J. B., Hollenbach, D., Beckwith, S., Simonelli, D. P., Roush, T. and Fong, W. (1994). Composition and radiative properties of grains in molecular clouds and accretion disks, *ApJ* **421**, pp. 615–639, doi:10.1086/173677.
- Raga, A. C., Henney, W., Vasconcelos, J., Cerqueira, A., Esquivel, A. and Rodríguez-González, A. (2009). Multiple clump structures within photoionized regions, *MNRAS* **392**, pp. 964–968, doi:10.1111/j.1365-2966.2008.14097.x.
- Raga, A. C., Steffen, W. and González, R. F. (2005). 3D Simulations of the Fragmentation of Photoevaporating Clumps Embedded in a Stellar Wind, **41**, pp. 45–55.
- Reipurth, B. (1983). Star formation in BOK globules and low-mass clouds. I - The cometary globules in the GUM Nebula, *A&A* **117**, pp. 183–198.
- Ribas, Á., Bouy, H. and Merín, B. (2015). Protoplanetary disk lifetimes vs. stellar mass and possible implications for giant planet populations, *A&A* **576**, A52, doi:10.1051/0004-6361/201424846.
- Ribas, Á., Merín, B., Bouy, H. and Maud, L. T. (2014). Disk evolution in the solar neighborhood. I. Disk frequencies from 1 to 100 Myr, *A&A* **561**, A54, doi:10.1051/0004-6361/201322597.
- Rice, W. K. M., Wood, K., Armitage, P. J., Whitney, B. A. and Bjorkman, J. E. (2003). Constraints on a planetary origin for the gap in the protoplanetary disc of GM Aurigae, *MNRAS* **342**, pp. 79–85, doi:10.1046/j.1365-8711.2003.06515.x.
- Richling, S. and Yorke, H. W. (1997). Photoevaporation of protostellar disks. II. The importance of UV dust properties and ionizing flux. *A&A* **327**, pp. 317–324.
- Richling, S. and Yorke, H. W. (1998). Photoevaporation of protostellar disks. IV. Externally illuminated disks, *A&A* **340**, pp. 508–520.
- Richling, S. and Yorke, H. W. (2000). Photoevaporation of Protostellar Disks. V. Circumstellar Disks under the Influence of Both Extreme-Ultraviolet and Far-Ultraviolet Radiation, *ApJ* **539**, pp. 258–272, doi:10.1086/309198.
- Rubio, M., Contursi, A., Lequeux, J., Probst, R., Barbá, R., Boulanger, F., Cesarsky, D. and Maoli, R. (2000). Multiwavelength observations of N 66 in the SMC: unveiling photodissociation interfaces and star formation, *A&A* **359**, pp. 1139–1146.
- Salpeter, E. E. (1955). The Luminosity Function and Stellar Evolution. *ApJ* **121**, p. 161, doi:

- 10.1086/145971.
- Sandford, M. T., II, Whitaker, R. W. and Klein, R. I. (1982). Radiation-driven implosions in molecular clouds, *ApJ* **260**, pp. 183–201, doi:10.1086/160245.
- Sandford, M. T., II, Whitaker, R. W. and Klein, R. I. (1984). Radiatively driven dust-bounded implosions - Formation and stability of dense globules, *ApJ* **282**, pp. 178–190, doi:10.1086/162189.
- Santoro, F. and Shull, J. M. (2006). Critical Metallicity and Fine-Structure Emission of Primordial Gas Enriched by the First Stars, *ApJ* **643**, pp. 26–37, doi:10.1086/501518.
- Schaerer, D. and Schmutz, W. (1994). Hydrodynamic atmosphere models for hot luminous stars, *A&A* **288**, pp. 231–254.
- Seward, F. D., Forman, W. R., Giacconi, R., Griffiths, R. E., Harnden, F. R., Jr., Jones, C. and Pye, J. P. (1979). X-rays from Eta Carinae and the surrounding nebula, *ApJ* **234**, pp. L55–L58, doi:10.1086/183108.
- Shakura, N. I. and Sunyaev, R. A. (1973). Black holes in binary systems. Observational appearance. *A&A* **24**, pp. 337–355.
- Shapiro, P. R., Iliev, I. T. and Raga, A. C. (2004). Photoevaporation of cosmological minihaloes during reionization, *MNRAS* **348**, pp. 753–782, doi:10.1111/j.1365-2966.2004.07364.x.
- Shu, F. H. (1977). Self-similar collapse of isothermal spheres and star formation, *ApJ* **214**, pp. 488–497, doi:10.1086/155274.
- Shull, J. M. and van Steenberg, M. E. (1985). X-ray secondary heating and ionization in quasar emission-line clouds, *ApJ* **298**, pp. 268–274, doi:10.1086/163605.
- Simon, J. B., Bai, X.-N., Armitage, P. J., Stone, J. M. and Beckwith, K. (2013a). Turbulence in the Outer Regions of Protoplanetary Disks. II. Strong Accretion Driven by a Vertical Magnetic Field, *ApJ* **775**, 73, doi:10.1088/0004-637X/775/1/73.
- Simon, J. B., Bai, X.-N., Stone, J. M., Armitage, P. J. and Beckwith, K. (2013b). Turbulence in the Outer Regions of Protoplanetary Disks. I. Weak Accretion with No Vertical Magnetic Flux, *ApJ* **764**, 66, doi:10.1088/0004-637X/764/1/66.
- Skrutskie, M. F., Dutkevitch, D., Strom, S. E., Edwards, S., Strom, K. M. and Shure, M. A. (1990). A sensitive 10-micron search for emission arising from circumstellar dust associated with solar-type pre-main-sequence stars, *AJ* **99**, pp. 1187–1195, doi:10.1086/115407.
- Spitzer, L. (1978). *Physical processes in the interstellar medium*, New York: Wiley-Interscience.
- Stahler, S. W. and Palla, F. (2005). *The Formation of Stars*, New York: Wiley-VCH.
- Stahler, S. W., Shu, F. H. and Taam, R. E. (1980). The evolution of protostars. I - Global formulation and results, *ApJ* **241**, pp. 637–654, doi:10.1086/158377.
- Störzer, H. and Hollenbach, D. (1998). On the [O I] λ 6300 Line Emission from the Photoevaporating Circumstellar Disks in the Orion Nebula, *ApJ* **502**, pp. L71–L74, doi:10.1086/311487.
- Störzer, H. and Hollenbach, D. (1999). Photodissociation Region Models of Photoevaporating Circumstellar Disks and Application to the Proplyds in Orion, *ApJ* **515**, pp. 669–684, doi:10.1086/307055.
- Strom, K. M., Strom, S. E., Edwards, S., Cabrit, S. and Skrutskie, M. F. (1989). Circumstellar material associated with solar-type pre-main-sequence stars - A possible constraint on the timescale for planet building, *AJ* **97**, pp. 1451–1470, doi:10.1086/115085.
- Sugitani, K., Fukui, Y. and Ogura, K. (1991). A catalog of bright-rimmed clouds with IRAS point sources: Candidates for star formation by radiation-driven implosion. I - The Northern Hemisphere, *ApJS* **77**, pp. 59–66, doi:10.1086/191597.
- Sugitani, K. and Ogura, K. (1994). A catalog of bright-rimmed clouds with IRAS point sources: Candidates for star formation by radiation-driven implosion. 2: The southern hemisphere, *ApJS*

- 92**, pp. 163–172, doi:10.1086/191964.
- Sugitani, K., Tamura, M. and Ogura, K. (1995). Young Star Clusters in Bright-rimmed Clouds: Small-Scale Sequential Star Formation? *ApJ* **455**, p. L39, doi:10.1086/309808.
- Suzuki, T. K. and Inutsuka, S.-i. (2009). Disk Winds Driven by Magnetorotational Instability and Dispersal of Protoplanetary Disks, *ApJ* **691**, pp. L49–L54, doi:10.1088/0004-637X/691/1/L49.
- Suzuki, T. K., Muto, T. and Inutsuka, S.-i. (2010). Protoplanetary Disk Winds via Magnetorotational Instability: Formation of an Inner Hole and a Crucial Assist for Planet Formation, *ApJ* **718**, pp. 1289–1304, doi:10.1088/0004-637X/718/2/1289.
- Takagi, Y., Itoh, Y. and Oasa, Y. (2014). Disk dissipation timescale of pre-main sequence stars in Taurus*, *PASJ* **66**, 88, doi:10.1093/pasj/psu062.
- Takeuchi, T., Clarke, C. J. and Lin, D. N. C. (2005). The Differential Lifetimes of Protostellar Gas and Dust Disks, *ApJ* **627**, pp. 286–292, doi:10.1086/430393.
- Tanaka, K. E. I., Nakamoto, T. and Omukai, K. (2013). Photoevaporation of Circumstellar Disks Revisited: The Dust-free Case, *ApJ* **773**, 155, doi:10.1088/0004-637X/773/2/155.
- Tanaka, K. E. I., Tan, J. C. and Zhang, Y. (2017). The Impact of Feedback During Massive Star Formation by Core Accretion, *ApJ* **835**, 32, doi:10.3847/1538-4357/835/1/32.
- Telleschi, A., Güdel, M., Briggs, K., Audard, M., Ness, J.-U. and Skinner, S. L. (2005). Coronal Evolution of the Sun in Time: High-Resolution X-Ray Spectroscopy of Solar Analogs with Different Ages, *ApJ* **622**, pp. 653–679, doi:10.1086/428109.
- Tenorio-Tagle, G. (1977). The time evolution of a globule immersed in an H II region, *A&A* **54**, pp. 517–524.
- Testi, L. and Sargent, A. I. (1998). Star Formation in Clusters: A Survey of Compact Millimeter-Wave Sources in the Serpens Core, *ApJ* **508**, pp. L91–L94, doi:10.1086/311724.
- Turner, N. J., Fromang, S., Gammie, C., Klahr, H., Lesur, G., Wardle, M. and Bai, X.-N. (2014). Transport and Accretion in Planet-Forming Disks, *Protostars and Planets VI*, pp. 411–432, doi:10.2458/azu_uapress_9780816531240-ch018.
- Vicente, S., Berné, O., Tielens, A. G. G. M., Huélamo, N., Pantin, E., Kamp, I. and Carmona, A. (2013). Polycyclic Aromatic Hydrocarbon Emission in the Proplyd HST10: What is the Mechanism behind Photoevaporation? *ApJ* **765**, L38, doi:10.1088/2041-8205/765/2/L38.
- Vidotto, A. A., Gregory, S. G., Jardine, M., Donati, J. F., Petit, P., Morin, J., Folsom, C. P., Bouvier, J., Cameron, A. C., Hussain, G., Marsden, S., Waite, I. A., Fares, R., Jeffers, S. and do Nascimento, J. D. (2014). Stellar magnetism: empirical trends with age and rotation, *MNRAS* **441**, pp. 2361–2374, doi:10.1093/mnras/stu728.
- Walsh, C., Nomura, H., Millar, T. J. and Aikawa, Y. (2012). Chemical Processes in Protoplanetary Disks. II. On the Importance of Photochemistry and X-Ray Ionization, *ApJ* **747**, 114, doi:10.1088/0004-637X/747/2/114.
- Wang, J. and Fischer, D. A. (2015). Revealing a Universal Planet-Metallicity Correlation for Planets of Different Sizes Around Solar-type Stars, *AJ* **149**, 14, doi:10.1088/0004-6256/149/1/14.
- Wang, L., Bai, X.-N. and Goodman, J. (2018). Global Simulations of Protoplanetary Disk Outflows with Coupled Non-ideal Magnetohydrodynamics and Consistent Thermochemistry, *arXiv e-prints*.
- Wang, L. and Goodman, J. (2017). Hydrodynamic Photoevaporation of Protoplanetary Disks with Consistent Thermochemistry, *ApJ* **847**, 11, doi:10.3847/1538-4357/aa8726.
- Weidenschilling, S. J. (1977). The distribution of mass in the planetary system and solar nebula, *Ap&SS* **51**, pp. 153–158, doi:10.1007/BF00642464.
- White, R. J. and Basri, G. (2003). Very Low Mass Stars and Brown Dwarfs in Taurus-Auriga, *ApJ*

- 582**, pp. 1109–1122, doi:10.1086/344673.
- Williams, J. P., Blitz, L. and McKee, C. F. (2000). The Structure and Evolution of Molecular Clouds: from Clumps to Cores to the IMF, *Protostars and Planets IV*, p. 97.
- Williams, R. J. R., Ward-Thompson, D. and Whitworth, A. P. (2001). Hydrodynamics of photoionized columns in the Eagle Nebula, *MNRAS* **327**, pp. 788–798, doi:10.1046/j.1365-8711.2001.04757.x.
- Wilms, J., Allen, A. and McCray, R. (2000). On the Absorption of X-Rays in the Interstellar Medium, *ApJ* **542**, pp. 914–924, doi:10.1086/317016.
- Woitke, P., Kamp, I. and Thi, W.-F. (2009). Radiation thermo-chemical models of protoplanetary disks. I. Hydrostatic disk structure and inner rim, *A&A* **501**, pp. 383–406, doi:10.1051/0004-6361/200911821.
- Yan, M., Sadeghpour, H. R. and Dalgarno, A. (1998). Photoionization Cross Sections of He and H₂, *ApJ* **496**, pp. 1044–1050, doi:10.1086/305420.
- Yan, M., Sadeghpour, H. R. and Dalgarno, A. (2001). Erratum: Photoionization Cross Sections of He and H₂, *ApJ* **559**, pp. 1194–1194, doi:10.1086/322775.
- Yang, H., Herczeg, G. J., Linsky, J. L., Brown, A., Johns-Krull, C. M., Ingleby, L., Calvet, N., Bergin, E. and Valenti, J. A. (2012). A Far-ultraviolet Atlas of Low-resolution Hubble Space Telescope Spectra of T Tauri Stars, *ApJ* **744**, 121, doi:10.1088/0004-637X/744/2/121.
- Yasui, C., Kobayashi, N., Saito, M. and Izumi, N. (2016a). Low-metallicity Young Clusters in the Outer Galaxy. II. Sh 2-208, *AJ* **151**, 115, doi:10.3847/0004-6256/151/5/115.
- Yasui, C., Kobayashi, N., Tokunaga, A. T., Saito, M. and Izumi, N. (2016b). Low-metallicity Young Clusters in the Outer Galaxy. I. Sh 2-207, *AJ* **151**, 50, doi:10.3847/0004-6256/151/3/50.
- Yasui, C., Kobayashi, N., Tokunaga, A. T., Saito, M. and Tokoku, C. (2009). The Lifetime of Protoplanetary Disks in a Low-metallicity Environment, *ApJ* **705**, pp. 54–63, doi:10.1088/0004-637X/705/1/54.
- Yasui, C., Kobayashi, N., Tokunaga, A. T., Saito, M. and Tokoku, C. (2010). Short Lifetime of Protoplanetary Disks in Low-metallicity Environments, *ApJ* **723**, pp. L113–L116, doi:10.1088/2041-8205/723/1/L113.
- Yorke, H. W., Bodenheimer, P. and Laughlin, G. (1995). The formation of protostellar disks. 2: Disks around intermediate-mass stars, *ApJ* **443**, pp. 199–208, doi:10.1086/175514.
- Yorke, H. W. and Welz, A. (1996). Photoevaporation of protostellar disks. I. The evolution of disks around early B stars. *A&A* **315**, pp. 555–564.